Ternary group 11/15 iodido metalates as building blocks for new materials

Kumulative Dissertationsschrift

zur Erlangung des akademischen Grades eines
Doktors der Naturwissenschaften (Dr. rer. nat.)
des Fachbereichs Chemie der Philipps-Universität Marburg
Hochschulkennziffer 1180

Vorgelegt von

Jakob Möbs

aus Leonberg

Marburg 2023

Erstgutachterin:	Dr. Johanna Heine
Zweitgutachter:	Prof. Dr. Sangam Chatterjee
Einreichungstermin:	14.06.2023
Disputationstermin:	26.07.2023

Die vorliegende Arbeit entstand in der Zeit von Februar 2019 bis Juni 2023 unter Betreuung von Dr. Johanna Heine am Fachbereich Chemie der Philipps-Universität Marburg.

Diese veröffentlichte Version der Dissertation ist gekürzt um Danksagung, Lebenslauf sowie die Elektronischen Zusatzinformationen zu den einzelnen Publikationen. Die elektronischen Zusatzinformationen sind online bei den entsprechenden Verlagen kostenfrei verfügbar.
Darüber hinaus wurden in Kapitel 1 einige Tippfehler entfernt und in Kapitel 3.6 das in der ursprünglichen Fassung der Dissertation noch unveröffentlichte Manuskript durch die inzwischen veröffentlichte Fassung ersetzt. Die Publikationsliste (Anhang A) wurde entsprechend angepasst.

This thesis has been created between February 2019 and June 2023 under the supervision of Dr. Johanna Heine at the Department of Chemistry, Philipps-Universität Marburg.

This published version of the dissertation is shortened by the Words of Thanks, Curriculum Vitae and Electronic Supplementary Information on the individual publications. The Electronic Supplementary Information is available free of charge from the respective publishers.
Furthermore, in Chapter 1 some typing errors have been removed and in Chapter 3.6 the manuscript that was still unpublished in the original version of the dissertation was replaced by the version that has since been published. The list of publications (Appendix A) has been adjusted accordingly.

Erklärung

Ich erkläre, dass eine Promotion noch an keiner anderen Hochschule als der Philipps-Universität Marburg, Fachbereich Chemie, versucht wurde. Weiterhin versichere ich, dass ich die vorliegende Dissertation

„Ternary group 11/15 iodido metalates as building blocks for new materials“

selbstständig und ohne unerlaubte Hilfe Dritter angefertigt und nicht andere als die in ihr angegebenen Quellen oder Hilfsmittel benutzt habe. Alle Stellen, die wörtlich oder sinngemäß aus veröffentlichten oder unveröffentlichten Schriften entnommen sind, habe ich als solche kenntlich gemacht. Dritte waren an der inhaltlich-materiellen Erstellung der Dissertation nicht beteiligt; insbesondere habe ich hierfür nicht die Hilfe eines Promotionsberaters in Anspruch genommen. Kein Teil dieser Arbeit ist in einem anderen Promotions- oder Habilitationsverfahren verwendet worden. Mit dem Einsatz von Software zur Erkennung von Plagiaten bin ich einverstanden.

Ort, Datum	Jakob Möbs

"The reason they [parallel universes] are not universes is that any given universe is not actually a thing as such, but is just a way of looking at what is technically known as the WSOGMM, or Whole Sort of General Mish Mash. The Whole Sort of General Mish Mash doesn't actually exist either, but is just the sum total of all the different ways there would be of looking at it if it did."

- *Douglas Adams: Mostly Harmless, Chapter 3*[1]

Contents

List of Figures

List of figures

List of abbreviations

AM	air mass
Bu	butyl
Bz	benzyl
CBM	conduction band minimum
DABCO	1,4-diazabicyclo[2.2.2]octane
dme	1,2-dimethoxy-ethane
DSSC	dye-sensitized solar cell
Et	ethyl
FTO	fluorine-doped indium tin oxide
HOMO	highest occupied molecular orbital
I_{sc}	short circuit current
ITO	indium tin oxide
LUMO	lowest unoccupied molecular orbital
Me	methyl
o-tol	*ortho*-tolyl
PCE	power conversion efficiency (of a solar cell)
Ph	phenyl
Pr	propyl
PSC	perovskite solar cell
py	pyridine
pyz	pyrazine
spiro-OMeTAD	(2,2',7,7'-tetrakis(N,N'-di-p-methoxyphenyl-amine)-9,9'-spirobifluorene
VBM	valence band maximum
V_{oc}	open circuit voltage
VSEPR	valence shell electron pair repulsion

Chapter 1

Introduction

This work is focused on the synthesis and characterization of new halogenido metalates based on bismuth and antimony. This class of materials has received quite a boost of research interest in recent years due to similar optical properties as lead halide perovskites, which, as they are intrinsic semiconductors, have been discovered to be highly efficient as the light absorbing layer in a new generation of solar cells. In the long run, this application is also the target for compounds developed during this work. Therefore, the working principles of the main types of solar cells will be briefly introduced before turning to a more chemical description of perovskites and their derivatives, as well as the current state of research regarding halogenido metalates of the heavy group 15 elements.

1.1 Solar Cells

1.1.1 Silicon based solar cells and basic principles

In 1954, *Chapin*, *Fuller* and *Pearson* reported on "a new silicon *p*-*n* junction photocell for converting solar energy to electrical power"[2], and with that were the first to make use of a silicon *p*-*n* junction for solar energy harvesting. They created a solar cell that achieved around 6 % power conversion efficiency (PCE), far more than ever before, and that was in its principle construction the same as the most common type still used today.
The key part to the success was the *p*-*n* junction, which is a sample of a semiconductor doped in a way that it has a *p*-type region, where there is a large excess of positive charge carriers, *i.e.* "holes", directly in contact with an *n*-type region, with a large excess of negative charge carries, *i.e.* electrons. Most solar cells to date are made out of boron-doped silicon for the *p*-side and phosphorus-doped silicon for the *n*-side. These elements fit into the crystal lattice of silicon forming solid solutions[3] and have one valence electron less, in the case of boron, or one valence electron more in the case of phosphorus. Therefore, there is a lack of electrons on the boron-doped side, meaning an excess of holes, and an excess of electrons on the phosphorus-doped side.

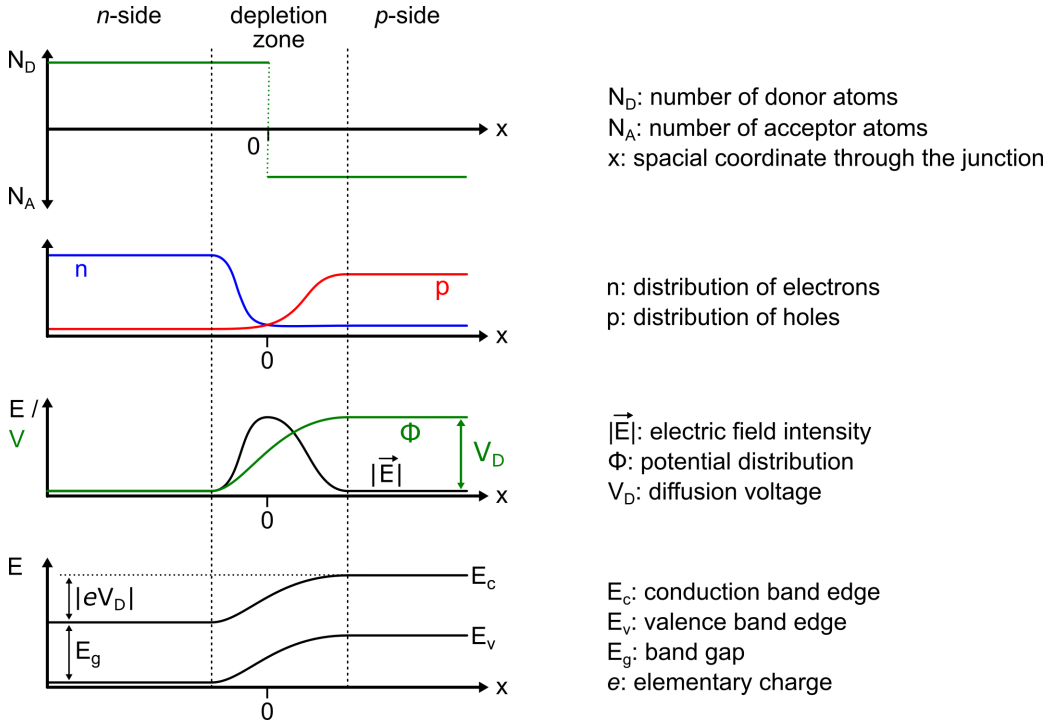

Figure 1.1: Simplified schematics of an unsymmetrical and abrupt p-n junction. Adapted form [4–6].

These charge carriers diffuse through the silicon at temperatures above absolute zero, even without any radiative excitation, and, especially, move away from regions of high concentrations. This means that electrons diffuse from the n-side to the p-side and holes from the p-side to the n-side and, if they meet, combine with one another. This depletes the region around the p-n border of free charge carriers, therefore called the depletion zone, and leaves uncompensated positively charged donor atoms at the n-side and negatively charged acceptor atoms at the p-side. This creates a potential difference—the diffusion voltage V_D—between the two sides, which induces an electric field and with it a drift current opposing the diffusion current, cancelling it out perfectly so that no current flows at equilibrium.
The distance between the edge of the valence band and conduction band, the electrical band gap E_g, is constant throughout the whole semiconductor, but the potential difference between the two sides of the junction causes the bands to bend in the depletion zone so that they are shifted by $|eV_D|$ (e being the elementary charge) to lower energies on the n-side.[4–6] Figure 1.1 gives an overview of this situation in an unsymmetrical and abrupt p-n junction. The words "unsymmetrical" and "abrupt" describe that the dopant levels on both sides are not equal (which is the case in most applications), and that for the sake of simplicity a sudden jump of dopant concentration instead of a gradient between the p- and n-side is assumed.

If radiation of energy larger than E_g is incident on the junction, it ionizes the atoms, creating additional charge carriers in the form of electron-hole pairs. These pairs are separated in the electric field with the electrons getting pushed towards the n-side and the holes getting pushed towards the p-side. This can also be understood as the charge carriers following the curves of the

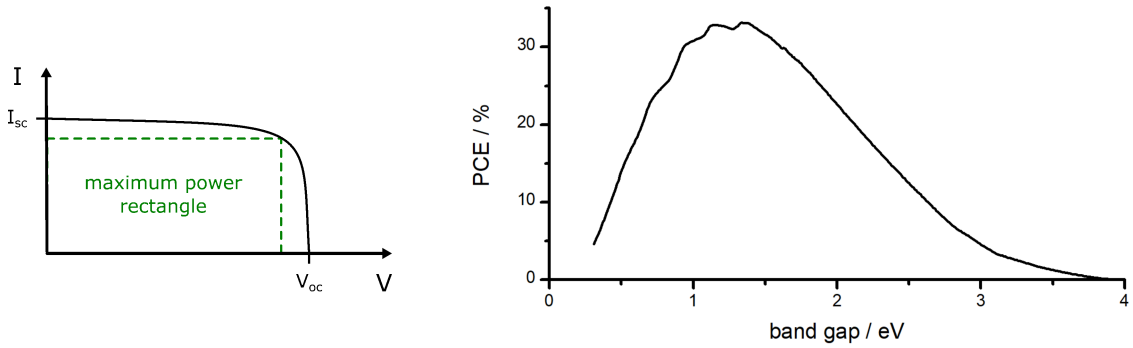

Figure 1.2: Typical current-voltage characteristics of a solar cell under constant irradiation (left, adapted from [7]) and Shockley-Queisser limit at an air mass of 1.5 (right, [9, 10]).

valence and conduction bands: An electron, that gets excited into the conduction band, moves towards the point of lowest energy (to the left in figure 1.1), while the corresponding hole also lets electrons flow to the left in the valence band, therefore moving to the right itself. As a result, a photovoltaic potential is generated and, when the two sides of the junction are connected, a constant current flows (under constant irradiation), which can be harvested.[4, 7]
This means a basic solar cell can be constructed by simply contacting the two differently doped sides of the single crystal that the junction is made out of in a way that light can still reach the crystal. Generally, this is accomplished with normal metal contacts on the back side and thin metal strips or glass with a conductive coating of indium tin oxide (ITO) or fluorine-doped tin oxide (FTO) on the front side.[8] It does not matter if the p- or the n-side is in the front. However, the front layer needs to be thin enough for light to penetrate it and reach the actual junction region, *i.e.* the depletion zone.[2]
Given a defined irradiation power per surface area, the short circuit current I_{sc}, which is the maximum current that flows when the two sides of the junction are shorted, and the open circuit voltage V_{oc}, the maximum voltage when no current flow is allowed, are measurements for the performance of the cell. The output power of a solar cell can never reach $I_{sc} \cdot V_{oc}$. However, as illustrated in figure 1.2, the product $I \cdot V$ can be optimized to above 80 % of $I_{sc} \cdot V_{oc}$. This value, though, is not the overall power conversion efficiency (PCE) of the solar cell. It is only the part of the PCE that can be optimized by technical means like minimizing the resistance of contacts and carefully choosing the load in terms of output current and voltage. [4, 7]
I_{sc} and V_{oc} themselves as well as the curve connecting them in figure 1.2 are strongly dependent on the charge carrier characteristics, such as lifetimes and diffusion length in the p-n junction. In a perfect crystal, these are material constants, but they are also influenced by defects introduced in the fabrication process, which act as recombination sites for electrons and holes.
Another very important factor for the PCE, that is also fairly easy to determine for new materials, is the band gap E_g of the junction material. Only radiation of energy larger than the E_g is able to create electron-hole pairs. Therefore, a smaller band gap leads to more charge carriers being injected into the junction and thus a larger I_{sc}. On the other hand, E_g is also the maximal energy that can be harvested per photon, so a smaller band gap also means a smaller V_{oc}.[7]

Considering the solar spectrum as that of a black body at 6000 K and taking the atmospheric absorption at an air mass of 1.5[1] into account, a theoretical limit for the PCE of solar cells, the Shockley-Quiesser limit, can be calculated.[9, 10] From the diagram in figure 1.2, it is clear that band gaps in the range of 1 eV to 1.6 eV are desirable for the absorption layer of a solar cell. Even if the absorption layer is no *p*-*n* junction, like with other types of solar cells described later, the Shockley-Queisser limit is still applicable and the value of E_g can serve as a useful first assessment for new materials.
For silicon, which has a band gap of $E_g = 1.08$ eV at room temperature, the Shockley-Queisser limit gives a maximum theoretical PCE of 32 %. Through the optimization of parameters like silicon-conductor contacts, layer thickness of the depletion and the p/n-zones as well as anti-reflective coatings, it has been possible to push the actual PCE as high as 26.7 % with an V_{oc} of 0.74 V and a I_{sc} of 42.65 mA per cm^2 front area at AM1.5.[11]
To achieve these values, however, very pure and large single crystals of silicon are needed, which are very expensive in terms of money as well as energy. In the earlier days of silicon solar cells, it even was a major concern, that the cells might not be able to reach the point of positive returns just in terms of energy output during their life time.[4]
Because of that, starting in the 1970s, large efforts were devoted to cells based on thin films of amorphous or microcrystalline silicon. Instead of cutting wafers from large melt-grown crystals, the thin films can be fabricated by decomposing silane gas, SiH_4, and doped by simply adding diborane, B_2H_6, or phosphane, PH_3, to the gas. This saves on energy and material, significantly reducing the overall costs.[12] Unfortunately, with only up to 11.9 % PCE, the performance of such cells remains far behind those of single crystalline silicon cells.[11]
Of course, other common semiconducting materials have been and are being explored as alternatives to silicon. But currently, cells using these materials cannot match crystalline silicon in performance, price, or both. Still, gallium arsenide cells need to be mentioned at this point, as they are the only cells that can outperform crystalline silicon cells with a PCE of 29.1 %, although while being more expensive.[11]

1.1.2 Dye-sensitized solar cells

In search of cheap alternatives to silicon-based solar cells, dye-sensitized solar cells (DSSCs), which have a fundamentally different working principle, emerged in the 1990s.[13] Instead of a *p*-*n* junction made from a small band gap semiconductor, a semiconductor with a very large bandgap, in most cases TiO_2 in its anatase modification ($E_g = 3.2$ eV), is used.[14] Since this band gap is far too large for efficient solar energy harvesting, the semiconductor is "sensitized" with an organic or metal-organic dye optimized for visible light absorption. Put differently, with the help of a large band gap semiconductor the very good absorption properties of (in bulk form) insulating dyes are made usable for solar energy conversion.

[1] Air mass is a term to describe the effect of atmospheric absorption on the solar spectrum. An air mass of 1.5 (AM1.5) corresponds to the sun being 37 ° above the horizon at sea level. The delivered power density under these conditions is nearly exactly 1000 W/m^2. AM0 would be just outside the atmosphere while AM1 would also be at sea level but with the sun directly overhead.[10]

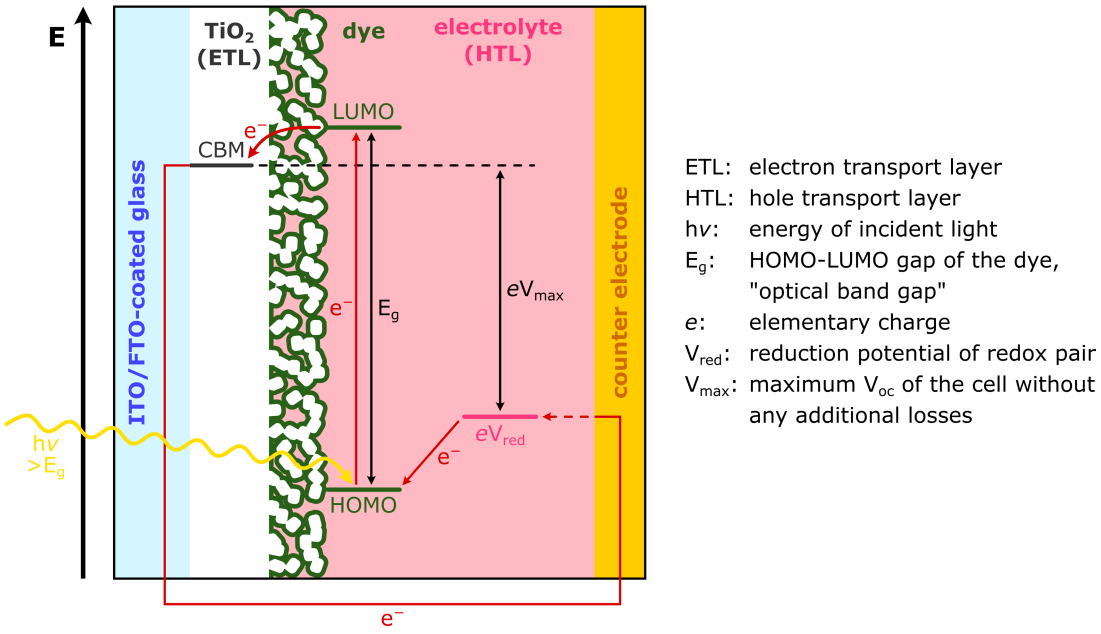

Figure 1.3: Structure and working principle of DSSCs with a porous absorption layer of dye-coated TiO_2-nanoparticles as introduced by *O'Regan* and *Grätzel*. Adapted from [13, 14, 16].

A DSSC is generally built up of five layers: A transparent electrode of ITO/FTO-coated glass, an electron transport layer made from TiO_2 or some other large band gap semiconductor, the dye as the absorption layer, a hole transport layer (some electrolyte), and the counter electrode.[14] The absolute energy levels of the conduction band minimum (CBM) of the semiconductor and the HOMO and LUMO of the dye need to be carefully tuned. The LUMO should be very close to but just above the CBM and the HOMO as far below as possible, while maintaining a good HOMO-LUMO distance for sunlight absorption. The HOMO-LUMO distance is often referred to as the optical band gap E_g, although the dye does not have valence and conduction bands like a classical semiconductor. However, the role of this distance is very similar to that of a semiconductor's band gap in terms of which wavelengths are absorbed and how much energy can at best be harvested per photon.
When the dye is irradiated, an electron is excited from the HOMO to the LUMO and then injected into the conduction band of the semiconductor that makes up the electron transport layer. This leaves the dye in an oxidized state and it needs to be reduced again to be able to absorb more light. This is taken care of by the hole transport layer, which in most cases is an electrolyte solution containing a redox couple like I^-/I_3^- or Br^-/Br_2.[15] This reduces the dye back to its ground state and is itself reduced by electrons from the counter electrode. The reduction potential of the redox couple also needs to be tuned to the HOMO of the dye, so that it is only just able to reduce the dye to minimize energetic losses.[13, 16] A diagram of a DSSC including the working principle is shown in figure 1.3.

Although the basic concepts for dye-based systems have already been known for a long time before the 1990s, the problem preventing DSSCs has been the insulating nature of the dye or, in other words, very poor charge carrier mobility. This makes it necessary for the dye molecules to

be in direct contact with the semiconducting layer to enable the injection of electrons. Unfortunately, such a thin dye layer absorbs less than 1 % of incident light, not nearly enough for efficient solar energy conversion.[13] In 1991, however, *O'Regan* and *Grätzel* were able to combine the electron transport layer and the dye into one porous layer of dye-coated TiO_2-nanoparticles, which are sintered together for conductivity. In combination with a specialized bipyridine/-cyanido ruthenium complex for the dye,[17] they achieved a PCE of over 7 % at AM1.5. This put DSSCs in direct competition with amorphous silicon-based cells.[13]
Since then, large efforts to improve this have been made.[14] Besides optimizing the energetic levels mentioned above, less aggressive solid-state electrolytes/hole transport layers like copper halides or organic materials like spiro-OMeTAD (2,2',7,7'-tetrakis(N,N'-di-p-methoxyphenylamine)-9,9'-spirobifluorene) [18] have been introduced, allowing the use of a much larger variety of dyes and electrode materials. These investigations have been especially fuelled by an estimation by *Snaith*, who predicted that, if the energetic losses due to intrinsic resistance and less than ideal fit of energy levels between CBM, LUMO, HOMO, and reduction potential are minimized, a PCE of above 20 % should be achievable.[16] However, since this educated guess in 2010, only minor improvements in efficiency have been made and the best PCE of a DSSC today is still only 11.9 %.[11] This value is certainly not exceptional but can be considered good enough and definitely very promising when put into the context of production costs. There is no need for costly ultra-high purity silicon wafers, and the efficiency is on par with thin-film silicon cells. In addition, the different layers can simply be printed onto a substrate, immensely reducing production times and costs. In some cases, when an organic polymer is chosen instead of a glass substrate and the generally metallic counter electrode is swapped for a carbon cloth, the devices can even be made flexible.[19, 20]

1.1.3 Perovskite solar cells

Perovskite solar cells (PSCs) started out in 2009 as a subclass of DSSCs and the basic structure is very similar (see figure 1.3). Mainly because of the high absorption coefficients and suitable optical band gaps, *Miyasaka* and co-workers swapped out the common organic dyes for the predominantly inorganic, perovskite-structured methylammonium lead iodide and bromide with the sum formula $(MeNH_3)PbX_3$ (X = I, Br).[21] These two compounds were later expanded to a large range of perovskite-structured lead halide compounds with various small cations.[22] This class of materials will be described in more detail in section 1.2 and for now summarized as halide perovskites.
The first PSCs had efficiencies of 3.1 % to 3.8 % and where thought to function similarly to DSSCs.[21] When different cell architectures were explored, though, it became clear that an ultra-thin perovskite film adsorbed onto a mesoporous TiO_2-layer was not necessary, even counterproductive[23], and that the halide perovskites, in contrast to (metal-)organic dyes, were intrinsic semiconductors, allowing for much better charge transport through the cells. Investigations on cells with TiO_2 as the electron transport layer and the aforementioned spiro-OMeTAD as the hole transport layer revealed that the potential curve across the cell resembles that of a

typical *p*-*n* junction at the TiO_2/$(MeNH_3)PbI_3$ interface very similar to the idealized diagram in figure 1.1.[24] And although the carrier diffusion process is not yet as well understood as for silicon solar cells, the facts that charge carriers *can* diffuse efficiently through the absorption layer, and there is no need for any redox chemistry to happen in the cell, allow for much more flexibility in the design. It is possible to construct PSCs with mesoporous TiO_2 scaffolds or, instead, compact halide perovskite layers and even to completely omit the hole or electron transport layer increasing the maximal obtainable V_{oc}.[25, 26] However, the use of these layers, which are dedicated to efficient charge carrier collection, generally enhances I_{sc} more than their omission enhances V_{oc}. Thus, the most efficient cells commonly make use of them, and the current record PCE of 25.7 % was obtained with a TiO_2/halide perovskite/spiro-OMeTAD setup. This was, however, in a small, experimental cell, but generally, PCEs well above 20 % in larger and scalable devices are possible.[11, 27] These results combined with the still very cheap and fast fabrication methods similar to DSSCs challenge the long-time throne of crystalline silicon cells. But although the efficiencies of silicon and perovskite cells are practically equal and a lot of research effort is being put into halide perovskites, there are still huge problems, that prevent large-scale application.

Problems of PSCs

The strongest concern is, of course, the well-known toxicity of lead, which poses major risks to the environment.[28, 29] Solar cells need to be installed open to the elements for sunlight to be able to reach them and are also expected to have lifetimes of 25 years or longer with little to no need for servicing. Considering the huge scope of possible deployment of solar cells, leakage of lead compounds needs to be completely inhibited. And although the devices can be packed into very rugged encapsulations to withstand all kinds of weather, this drives up the costs. An additional risk, especially in terms of deployment in a private, residential context, are house fires. *Babayigit* and co-workers estimated that in case of large-scale application, 15 tons of lead could be released per year in the form of toxic fumes into residential areas from solar cells on roofs of burning buildings.[30]
Also, before and after the lifetime of a solar cell, the lead content poses a threat. It is not really a problem to take precautions during production to keep toxic substances contained, but the recycling or disposal needs to be controlled as well. A company that produced a cell might not exist anymore at the end of its lifetime to take it back for recycling, or the new owner of a building might be oblivious to the special devices on its roof. Control mechanisms to keep lead-based solar cells from landfills are starting to be implemented by photovoltaic companies, but the progress is still too slow, and legislatory systems are also not keeping up.[28, 30]

All these toxicological issues would not be of such large concern, if $(MeNH_3)PbI_3$ and its relatives were as stable as silicon and just stay where they are, even if the encapsulation is broken. However, this leads to the second major problem of PSCs: The stability of the halide perovskites.
The prototypical $(MeNH_3)PbI_3$ is highly sensitive to moisture and not quite as highly but still

significantly sensitive to atmosphere (O_2, N_2, vacuum).[25] Under humid conditions it first reversibly forms a photovoltaically inactive hydrate that then—irreversibly—decomposes further into lead iodide and methyl ammonium iodide, which can leak from the cell.[31] The atmosphere seems to mostly just influence the surface of the $(MeNH_3)PbI_3$ crystals or films through interactions with defects and alter the luminescence properties, but the influence on photovoltaic performance of this phenomenon is not yet fully investigated.[32–34] However, oxygen, in particular, has been shown to get photo-catalytically reduced to the superoxide radical anion, $O_2^{\bullet -}$, at the perovskite surface and then is able to oxidize the iodide ions in $(MeNH_3)PbI_3$, destroying the compound.[35]
While these issues of external stability can be sorted out by the anyhow necessary encapsulation and are therefore more or less negligible, this is not the case for temperature and light sensitivity. $(MeNH_3)PbI_3$ shows severe decomposition even under dry conditions in air as well as vacuum at temperatures as low as 90 °C.[36] At the moment, this can only to a certain degree be sorted out by substituting part of the methylammonium for other ions (see section 1.2.2). In addition, $(MeNH_3)PbI_3$ is sensitive to UV light, especially in the presence of TiO_2, which acts as a photocatalyst for the degradation reactions. Efforts to mitigate this problem by adding UV blocking layers, special separators between TiO_2 and the perovskite, or moving to other electron transport materials, are showing promising results regarding the stability but also decrease the overall PCE.[37–39] To make matters worse, $(MeNH_3)PbI_3$ has been found to be unstable to electric fields. If a potential is applied, either externally or internally by illumination of the cell, iodide and methylammonium ions migrate through the crystal towards anode or cathode, respectively, also destroying the compound.[40, 41]

All these issues lead to a lifetime of only a few years (extrapolated), during which the cell keeps up at least 80 % of its initial performance with the best estimations being about five years.[42] It goes to show that, despite the immensely promising results of halide perovskite based solar cells concerning their initial PCEs, they might not be the final solution for cheap and accessible photovoltaics, and researchers need to look towards other related but lead-free and hopefully more stable semiconductors for the next generation of solar cells.

1.2 Perovskites

1.2.1 The perovskite structure family

Historically, "Perovskite" is the mineral name of $CaTiO_3$, discovered in 1839 in a collaboration between Russian and Prussian mineralogists *Gustav Rose* and *August Alexander Kämmerer*.[43] As more and more minerals were discovered and characterized though, it became the namesake of a whole family of compounds that feature the same or slightly distorted crystal structure as $CaTiO_3$ and have the general formula ABX_3, where A and B are cations and X is an anion. In this structure, the A and X atoms form a cubic closest packing with the A atoms distributed so that they are always surrounded by a cuboctahedron of twelve X atoms. In that scaffold, the B atoms occupy a quarter of the octahedral holes, exactly those that are completely made up of X atoms. This leads to a network of all corner-sharing $\{BX_6\}$-octahedra like in the ReO_3-structure type with the A atoms again being in the cuboctahedral holes, which would be empty for ReO_3 (see figure 1.4).[44] Ironically, $CaTiO_3$ itself does not crystallize in the ideal cubic perovskite structure (at temperatures below 1600 K) but in the $GdFeO_3$-structure type, a distorted, orthorhombic version with the octahedra slightly tilted.[45, 46] The ideal structure is adopted by the heavier homologue $SrTiO_3$.[47] Still, the $GdFeO_3$-structure type together with other more or less distorted versions of the cubic perovskite type belong to the perovskite structure family.[44]

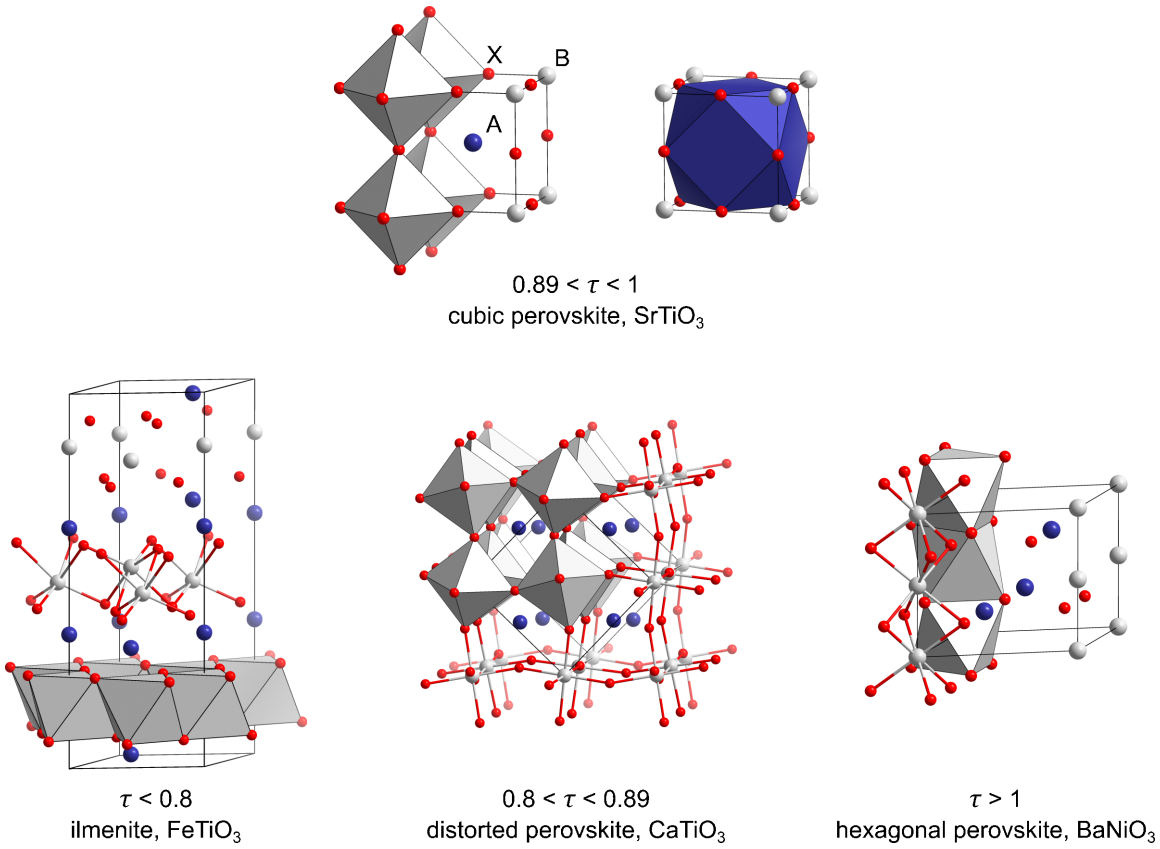

Figure 1.4: Excerpts of crystal structures of the perovskite family and the related ilmenite with corresponding Goldschmidt-factors: $SrTiO_3$ [47], $FeTiO_3$ [48], $CaTiO_3$ [45], $BaNiO_3$ [49].

To predict the adopted structure and estimate the distortion *Goldschmidt* and co-workers developed a tolerance factor based on the ionic radii r of A, B, and X in 1926.[47, 50] Nowadays this factor is mostly referred to as the Goldschmidt-factor τ:

$$\tau = \frac{r_A + r_X}{\sqrt{2}(r_B + r_X)}$$

Of course, τ strongly depends on the ionic radii used, which are not always clear, as the perovskites are not fully ionic crystals but coordination compounds. The Goldschmidt-factor, therefore, can only be a rough estimation. Still, if $0.8 < \tau < 1$, the perovskite structure is generally observed with the ideal cubic structure for $\tau > 0.89$ and distorted versions for smaller values. This is easy to grasp when looking at the radius of A, which, if small, leads to a small τ, and tilting of the $\{BX_6\}$-octahedra decreases the size of the cuboctahedral hole. In extreme cases ($\tau < 0.8$) the octahedra are tilted so far, that they are edge-sharing instead of corner-sharing and the former cuboctahedral hole becomes an octahedral hole, yielding the ilmenite structure type ($FeTiO_3$). If in the contrasting case τ exceeds 1, the hexagonal perovskite structure is observed. Here the A and X atoms form a hexagonal closest packing instead of a cubic one, leading to face sharing $\{BX_6\}$-octahedra.[44] All structural motifs are shown in figure 1.4. It should be noted, that there are many variations of ABX_3 structures based on mixtures of cubic and hexagonal packing of the A and X atoms, which also belong to the perovskite structure family. However, these, as well as the normal hexagonal perovskite, are not relevant to this work. Therefore, the term "perovskite" always refers to the cubic version or one of its distortions from here out.

1.2.2 Perovskite-structured halogenido metalates

Although the examples for perovskites in section 1.2.1 are all oxide-based minerals with ionic charges of +2, +4 and −2 for A, B and X, respectively, it is of course also possible to achieve the ABX_3-formula with charges of +1, +2 and −1. Halide salts with this composition, namely $CsPbX_3$ with X = Cl, Br, I, have been synthesized as early as the late 19th century by *Wells* and co-workers,[51] but were just discovered to adopt the perovskite structure by *Møller* in 1957, since they do so only at elevated temperatures.[52] One year later *Møller* also reported that all three $CsPbX_3$-compounds show photoconductivity, characterizing them as semiconductors and therefore setting them apart from the oxide perovskites, which are mostly insulating and only show, piezo-, pyro- or ferroelectricity.[25, 53] However, the photoconductive behaviour is only observed for the perovskite-structured phases, which are high-temperature phases and at best meta-stable at room temperature. This is also represented in the Goldschmidt-factor of $\tau = 0.8$ for $CsPbCl_3$, just at the lower threshold for perovskite structures and even smaller values for the bromide and iodide.[52] The colour, *i.e.* the optical band gap, of the compounds is determined by the choice of halogen and ranges from light yellow for the chloride to dark red for the iodide.

These halide compounds can generally be classified as halogenido metalates and, in contrast to the oxide perovskites, often be synthesized from solution, allowing for easy variation of cations

and especially the use of organic ones.[54] This led to the synthesis of the today very famous $(MeNH_3)PbI_3$ (Me = methyl, CH_3) as well as its chlorine and bromine homologues in 1978 by *Weber*.[55] Due to the slightly larger size of the methylammonium cation compared to the caesium cation, all three $(MeNH_3)PbX_3$-compounds crystallize in a perovskite structure at room temperature with the I-compound having the smallest Goldschmidt-factor of $\tau = 0.91$. While the Goldschmidt-factor of compounds featuring non-spherical organic ions is even less reliable than for all-inorganic compounds, this fits well with the proposed border of $\tau = 0.89$ between the distorted and ideal cubic regions. Accordingly, the Cl- and Br-compounds adopt the cubic structure, whereas $(MeNH_3)PbI_3$ is found in a slightly distorted tetragonal version that transitions to the cubic phase at 54 °C.[56] The compounds inherit the semiconducting properties of their perovskite-structured caesium relatives. *Weber* also found that it was possible to synthesize mixed halide compounds, which form solid solutions rather than distinctly ordered double anionic structures, and was able to finely tune the colour (optical band gap) by varying the halide ratios.[55]
By the end of the 20th century, many other perovskite-structured group 14 halogenido metalates featuring tin and germanium for the B-site as well as different inorganic and small organic cations for the A-site were synthesized.[54, 57] Despite this early discovery and the very interesting properties regarding optical absorption and also strong and tunable photoluminescence[54], no serious application was under discussion for this family of compounds until the discovery of PSCs.

Starting with *Miyasaka's* publication about the first PSC in 2009[21] the research interest has increased tremendously. Given the success but also the problems of $(MeNH_3)PbI_3$ described in section 1.1.3, the research focused—and still focuses—on two main aspects: Understanding what makes $(MeNH_3)PbI_3$ such a good material for solar absorption and, on this basis, designing more stable and less toxic alternatives.

Properties of $(MeNH_3)PbI_3$

The great qualities of $(MeNH_3)PbI_3$ itself are quite well understood at this point and come down to the composition of valence and conduction band edges. The conduction band minimum (CBM) is mostly made up of unoccupied Pb(p)-orbitals, while the valence band maximum (VBM) comprises occupied I(p)-orbitals with a contribution of the lone pair Pb(s)-orbital (see figure 1.5). The A-site cation (here methyl ammonium) is not found to contribute to the states at the band edges.[58] The composition of the CBM and VBM is somewhat inverted as compared to classical semiconductors like Si or GaAs, where the CBM consists mostly of s- and the VBM of p-orbitals. However, the situation in $(MeNH_3)PbI_3$ results in a good delocalization of the frontier orbitals, which gives rise to exceptional electron as well as hole mobilities and long charge carrier diffusion lengths.[59] In practice, diffusion lengths for both, electrons and holes, of over 100 nm in pure $(MeNH_3)PbI_3$ thin films[60] and over 1 µm in chlorine-doped $(MeNH_3)PbI_3$ thin films[61] have been observed.
It is very surprising that these results are accomplished using solution-processed films, which are

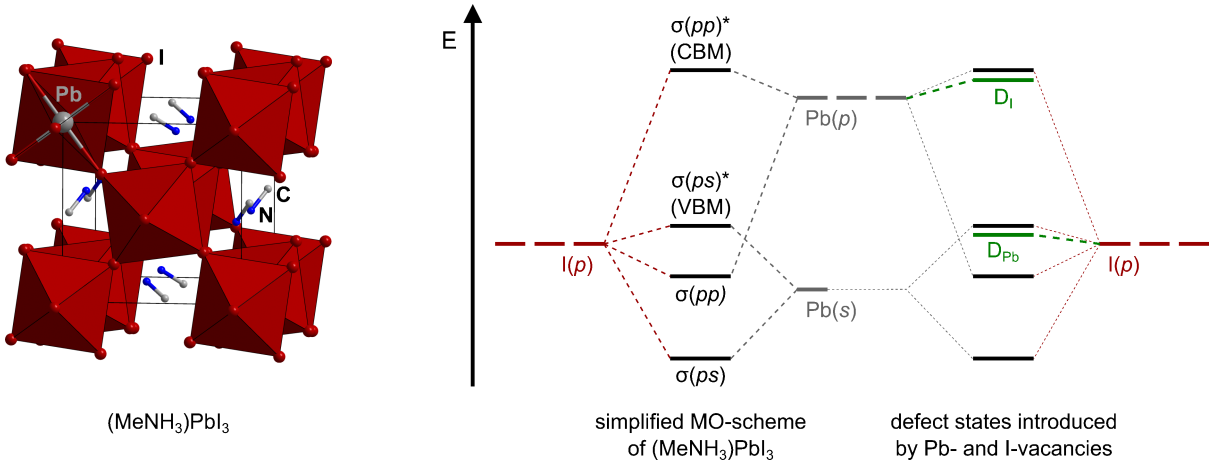

Figure 1.5: Left: Excerpt of the tetragonal distorted perovskite structure of $(MeNH_3)PbI_3$ at room temperature. Hydrogen atoms and disorder of the $(MeNH_3)^+$-ions are omitted.[62] Right: Simplified MO-schemes visualizing the contributions of atomic orbitals to states near the band edges of $(MeNH_3)PbI_3$.[58] D_I and D_{Pb} denote the qualitative energy levels of defect states induced by I- and Pb-vacancies, respectively. As these states are composed mainly of non-bonding atomic orbitals of the residual atoms ("dangling bonds") and the states at both band edges have anti-bonding nature they lie in between the corresponding atomic orbitals and band edges.[59]

generally very prone to defects due to the fast crystallization times and a high number of grain boundaries. Such defects are among the main reasons why the thin film silicon cells mentioned in section 1.1.1 are still showing very low PCEs compared to single crystal silicon cells. The defects introduce additional states in the band gap, where charge carriers can get trapped and recombine, therefore greatly reducing charge carrier diffusion lengths. The phenomenon, that $(MeNH_3)PbI_3$ still features great charge carrier characteristics, is generally summarized under the term "good defect tolerance". *Yan* and co-workers calculated the energy levels of possible defect states as well as their formation energies and analyzed them in great detail.[59] They found that the composition of the band edges leads to the defect states induced by vacancies or interstitial ions being very shallow, meaning they lie close to the band edges, and therefore do not represent good trap sites. For I- and Pb-vacancies this is exemplarily shown in figure 1.5. Defect states caused by ion substitution on the other hand lie deep within the band gap, providing points for non-radiative recombination of charge carriers. However, it turns out that the substitutional defects have very high formation energies, leading to few of the problematic deep states being formed in the first place.
This explains the exceptional behaviour of $(MeNH_3)PbI_3$ thin films regarding charge carrier characteristics and also gives hope that other compounds with similar bonding situations might show good defect tolerance as well.

In addition, $(MeNH_3)PbI_3$ shows an optical band gap between 1.51 - 1.55 eV, depending on sample preparation and measurement setup[21, 63], which fits the range defined by the Shockley-Queisser limit. The absorption coefficients for light of energy larger than E_g are with $4.3 \cdot 10^5\,cm^{-1}$ at 360 nm to $1.3 \cdot 10^5\,cm^{-1}$ at 550 nm even higher than the best performing dyes used in DSSCs[64], and can be explained with the direct nature of the bandgap.[59] Such a high

optical absorption in combination with the long charge carrier diffusion length allows for the fabrication of devices where the absorption layer is as thin as or thinner than the charge carrier diffusion lengths while still absorbing all of the incident light. This leads to an incident photon to electron conversion near 100 % and thus, very high PCEs.

Alternatives for $(MeNH_3)PbI_3$

As mentioned before, the greatest hurdles for the application of $(MeNH_3)PbI_3$ in solar cells concern the stability of the compound. This can be addressed by substituting the methyl ammonium cation to improve the spatial fit as indicated by the Goldschmidt-factor and alter the interactions with the surrounding atoms through changing the cation's dipole moment or hydrogen-bonding options.[54, 65] Such a substitution at the A-site of the perovskite structure should not impact the band structure significantly and therefore maintain the excellent properties.[58, 59] However, finding suitable cations is not easy. In practice, it was found that the most stable and also well-performing compounds are achieved not by substituting methyl ammonium completely, but only partially. It turned out that, if ions of not too different size, like for example formamidinium ($HC(NH_2)_2{}^+$), are used in combination with methyl ammonium, solid solutions $(MeNH_3)_x(HC(NH_2)_2)_{1-x}PbI_3$ can be formed. Here the two A-site cations are statistically distributed throughout the crystal and even the Goldschmidt-factor can be applied to predict stable combinations and ratios of cations, if the ionic radii used for the calculation are weighted according to the percentage of the ions. Of course, the possibilities here are not limited to $(MeNH_3)^+$ and $(HC(NH_2)_2)^+$ or even just two different ions, but so far lead halide perovskites with 60/40 mixtures of methyl ammonium/formamidinium are not only leading stability-wise but also are among the top performing absorber materials in prototypical solar cells.[22, 25]
Aside from the A-site ion, the halide can be substituted in a similar way and with similar results. However, the halide significantly influences E_g with lighter halides raising this value. Therefore, only small amounts of bromide or chloride are used, when the application in PSCs is intended, to remain within the range of the Shockley-Queisser limit.[25] Still, the possibilities of this concept are huge and compositions with up to six different ions distributed over the A- and X-sites are being investigated.[22]

With these methods of mixed-ion-substitution, the stability issues of $(MeNH_3)PbI_3$ can be improved significantly, but not yet sorted out completely, as already mentioned in section 1.1.3. Furthermore, the problem of toxicity remains. A suitable substitute for the Pb^{2+}-ion in the halide perovskite structure not only needs to have a similar size and the same charge but also the same valence electronic structure of unoccupied *p*-orbitals and a fully occupied *s*-orbital, as this is crucial for the outstanding charge carrier characteristics and defect tolerance. This only leaves Sn^{2+} as a substituent. The corresponding $(MeNH_3)SnI_3$ crystallizes similarly to the lead analogue in a tetragonally distorted perovskite structure and also inherits most of its electronic perks while featuring a band gap of 1.25 - 1.3 eV, which is even better suited for solar absorption than that of $(MeNH_3)PbI_3$.[66] Still PCEs of tin-based PSCs remain quite low at

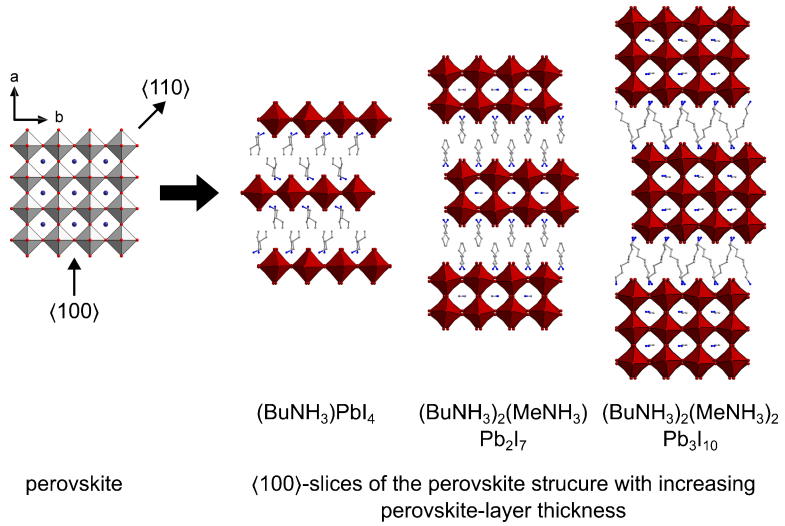

Figure 1.6: Concept of 2d-perovskites, examples for the ⟨100⟩-direction with thickness of the perovskite layer of n = 1 ($(BuNH_3)PbI_4$[74]), n = 2 ($(BuNH_3)_2(MeNH_3)Pb_2I_7$[75]) and n = 3 ($(BuNH_3)_2(MeNH_3)_2Pb_3I_{10}$[75]). For the butylammonium/methylammonium/lead/iodide system all compounds for up to n = 7 are known.[75–77]

only around 8 %[67] which is attributed to poor thin film quality[68] and stability issues due to easy oxidation of Sn^{2+} to Sn^{4+}, which is not a problem for lead.[25, 69] Overall, tin halide perovskites suffer from similar issues as their lead counterparts, but are not yet as well investigated despite $(MeNH_3)SnI_3$ being first reported and characterized by *Weber* in 1978—even before he published his results on $(MeNH_3)PbI_3$ in the same year.[57]

1.2.3 Derivatives of the perovskite structure

In search for more stable alternatives, researchers have also looked beyond the strict perovskite motif and discovered (or rediscovered) a range of compounds whose structures can be derived from perovskite and are therefore hoped to have similarly suitable properties.

The first class of these derivatives are compounds that feature two-dimensional cut-outs of the perovskite motif, which in the community are mostly referred to as layered or 2d-perovskites. There is, however, an ongoing debate about the proper nomenclature of these substances and whether they should or should not be called perovskites.[70–72] Following the majority of publications, they will be referred to as 2d-perovskites in this work.

These compounds can be made by substituting the A-cation of the parent perovskite partly or completely with a much larger organic cation, mostly an ammonium ion with a long organic group attached like *n*-butylammonium or 2-phenylethylammonium. The ammonium groups can interact with the halides of the perovskite via hydrogen bonds while the organic substituents are attracted to one another by van-der-Waals interactions. This leads to the formation of cationic organic layers alternating with layers of perovskite cut-outs. The perovskite layers are mostly slices through the parent structure perpendicular to the simple lattice directions ⟨100⟩, ⟨110⟩ or ⟨111⟩, as shown in figure 1.6, although more complex motifs are known as well.[73]

It should be mentioned that structurally very similar motifs were reported as early as the middle

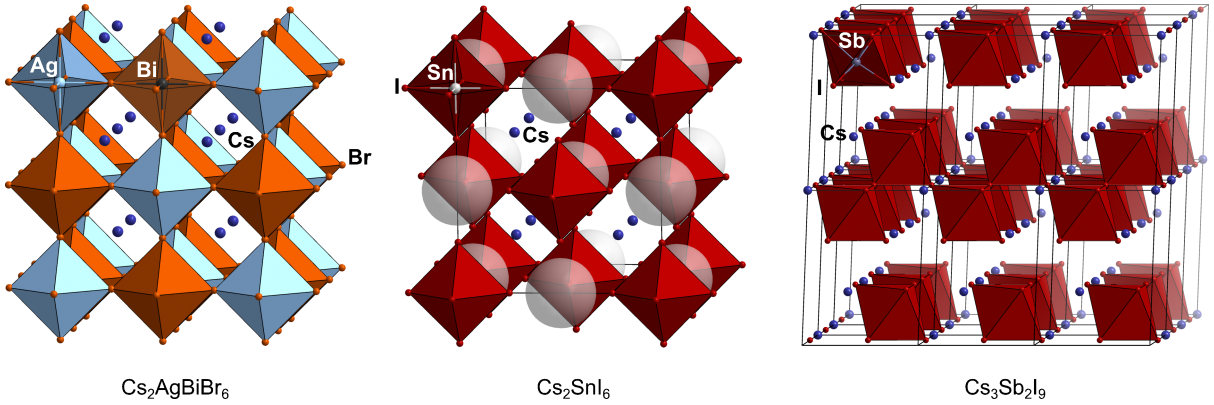

Figure 1.7: Excerpts of crystal structures derived from perovskite: Left: elpasolite-structured $Cs_2AgBiBr_6$.[86] Middle: elpasolite-like vacancy perovskite Cs_2SnI_6 with vacancies highlighted by translucent spheres.[87] Right: layered vacancy perovskite $Cs_3Sb_2I_9$.[88]

of the 20th century in the form of purely inorganic *Ruddlesden-Popper*- and *Dion-Jacobson*-phases, which were oxido or flourido metalates of *d*-block elements similar to the original perovskite.[78–80] When disregarding the organic nature of the cations used today, many of the modern 2d-perovskites can be classified as one of these phases as well.[75]
Interestingly, the thickness of the perovskite layers can often be tuned quite easily by altering the ratio of the small perovskite-A-site cation (Cs^+, $MeNH_3^+$, ...) and the larger layer-dividing cation (n-$BuNH_3^+$, $PhEtNH_3^+$, ...). The higher the amount of the larger cation is, the thinner the perovskite slices become, and with the correct choice of ions, the perovskite can even be "cut down" to 1d-chains or discrete $\{BX_6\}$-octahedra.[54, 73, 81]
Concerning the photovoltaic performance, the 2d-perovskites generally show improved stability as compared to $(MeNH_3)PbI_3$ but also have significantly larger optical band gaps, which leads to a decrease in the PCE of prototypical devices.[81–83] This increase of the band gap is not so large of a problem when moving to tin-based materials, which have a lower E_g, anyway, and for which similar 2d-perovskite structures are accessible. Here, the increase in stability opens a promising path towards stable and lead-free absorber materials.[84]

Another way to overcome lead in perovskites is by heterovalent substitution. This means the bivalent Pb(II) is replaced with equal amounts of a monovalent metal ion and a trivalent metal ion, yielding the general formula $A_2B^IB^{III}X_6$. The resulting structure is a perovskite superstructure, named after the mineral elpasolite, K_2NaAlF_6[85] but sometimes also referred to as double perovskite (see figure 1.7).

To retain the good properties of $(MeNH_3)PbI_3$ it is reasonable to choose ions that also feature the same s^2p^0 valence electronic configuration as lead. Therefore, the obvious choices are its direct neighbours in the periodic table, Bi(III) and Tl(I), or, one period above, Sb(III).[58, 89] For indium and even lighter elements the low oxidation state with s^2p^0 configuration becomes increasingly unstable in halide compounds as compared to the fully oxidized s^0p^0 configuration[90] and the use of highly toxic thallium is somewhat counterproductive to the substitution of lead. This leaves no suitable monovalent *p*-block elements to accompany bismuth or anti-

mony in the elpasolite structure. However, theoretical investigations have predicted that the use of coinage metals (copper, silver, gold) should yield elpasolites with desirable properties as well[91], but so far only the silver compounds, A_2AgEX_6 (E=Sb, Bi, X= Cl, Br) have been synthesized.[86, 92–95] Initially the charge carrier lifetimes seemed favourable in these materials[86], but it quickly turned out that the large and indirect band gaps of around or above 2 eV[96] and the large carrier effective masses, which lead to low charge carrier mobilities[97], result in low PCEs in experimental solar cells.[98] However, the combination of group 15 and group 11 metals in halogenido metalates aside from the perovskite motif is still promising and will be discussed in section 1.3.2.

If the B-site ion in the halide perovskite structure is substituted by an ion with a charge higher than +2, there is also the possibility for the formation of perovskite superstructures with ordered vacancies. In this case, the excess charge is not compensated by an ion of lower charge, like in the elpasolite structure, but by vacancies at a given fraction of the B-sites. This allows for ions of higher charge than +3, like Sn^{4+}, to be incorporated into the perovskite parent structure. For example, Cs_2SnI_6 adopts an elpasolite-like structure where there is a vacancy instead of the lesser charged ion, $Cs_2\square SnI_6$, as shown in figure 1.7. While this compound is not well suited for solar absorption, it has been successfully used as a solid state hole transport layer in DSSCs.[99]
Ions of +3 charge can also lead to vacancy perovskite structures. In this case, one third of the B-sites are vacant and generally 2d layers perpendicular to the perovskite ⟨111⟩-direction are formed. One of the compounds that adopt this structure is $Cs_3Sb_2I_9$, which is also considered as promising for photovoltaic applications.[100] However, more often the group 15 elements adopt motifs different from the perovskite or its relatives, which will be described in the next section.

1.3 Halogenido antimonates and bismuthates

So far the focus of this work has been on the photovoltaic application of perovskite-structured halogenido metalates and their historic development. It has become clear that, while the perovskite motif is very versatile and promising for the intended use case, the amount of perovskite-structured compounds is limited, especially if lead is to be avoided, and a satisfactory material for solar absorption within the halide perovskite family has not been discovered, yet. Therefore structures beyond the perovskite motif need to be explored.

Antimony and bismuth are very close to lead in the periodic table and although their stable +3 oxidation state does not allow the formation of the simple perovskite motif it features the same s^2p^0 valence electronic configuration, that proved crucial for the outstanding photovoltaic performance of $(MeNH_3)PbI_3$. Furthermore, bismuth is well known for its very low toxicity due to low uptake in the human body[101] and while antimony is not quite as benign it still is considered far less problematic than lead.[94, 102]
Similarly to the plumbates, halogenido bismuthates and antimonates generally show strong absorption in or very close to the visible range[103], photoluminescence[104] and in some cases even non-linear optical properties.[105] Because of this, they are under investigation not only for solar absorption but for a wide range of semiconductor applications, such as LEDs[106, 107], lasers[108] and radiation detection.[109, 110] Also similarly to the plumbates, they can be synthesized easily at low temperatures from solutions of the antimony and bismuth tri-halides and monovalent metal or organic halides (*e.g.* CsX, CuX, PPh_4X,...) in solvents like acetonitrile, acetone or aqueous hydrohalic acids. The amount of different anionic motifs that can be obtained through variation of the cation as well as stoichiometry and concentration of the reaction mixture is immense. However, it is near impossible to predict the structure for a new set of reaction conditions as the metal-halide bonds are very labile and the final structure is generally believed to only assemble upon crystallization from the small fragments that exist in solution.[111] Often, the formation energies of different motifs are very close to one another and multiple compounds can be isolated from the same reaction.[112]
In this section, the structural motifs of halogenido antimonates and bismuthates will be elucidated with the exception of the fluorides. For these, the structures can be quite different from the heavier halides and since the preparation also needs specialized equipment due to the reactivity towards glass, fluorides were not investigated in this project.

1.3.1 Antimonates and bismuthates with binary anions

The dominating motif in halogenido antimonates and bismuthates is the $\{EX_6\}$-octahedron (E = Sb, Bi, X = Cl, Br, I) and the isolated, mononuclear $[EX_6]^{3-}$-ion is known for all combinations of E and X in the solid state.[113–116] It is important to note here that the octahedral structure of the $[EX_6]^{3-}$-ion defies the rules of the simple valence shell electron pair repulsion model (VSEPR), which for six ligands and one lone pair at the central atom predicts a coordination polyhedron with seven points, one of which should be vacant or rather

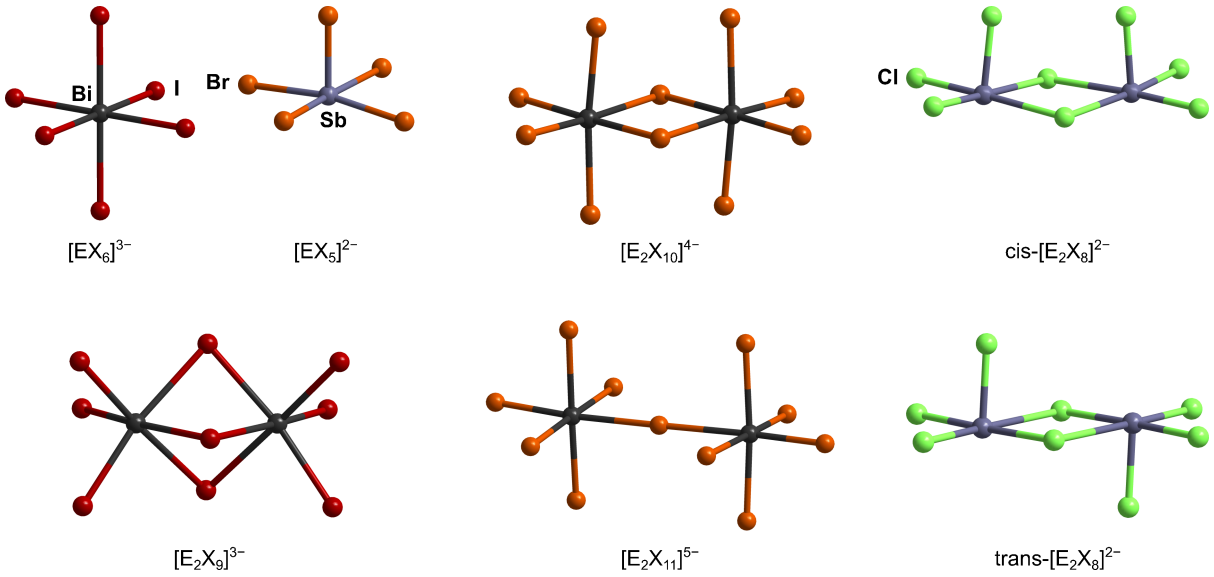

Figure 1.8: Examples for mono- and binuclear motifs of complex halogenido antimonate and bismuthate anions: $[Me_2NH_2]_3[BiI_6]$[118], $[PPh_4]_2[SbBr_5]$[119], $[Et_2NH_2]_3[Bi_2I_9]$[120], $[C_2H_5N_4S]_4[Bi_2Br_{10}]$[121], $[MeNH_3]_5[Bi_2Br_{11}]$[122], $[n Bu_4N]_2[Sb_2Cl_8]$[123] and $[n Pr_4N]_2[Sb_2Cl_8]$[123].

occupied by the lone pair. However, the lone pair has predominantly *s*-character, is therefore spherical and does not point in any specific direction. It is "stereochemically inactive"[117] and thus, an octahedral coordination is observed. For the lighter element combinations (both in terms of the E and X) the octahedron can be distorted, though, as the shift in orbital energy compared to the heavier elements allows for interaction between the group 15 *s*-atomic orbital and the other frontier orbitals. This manifests for example in $[BiCl_6]^{3-}$, where in some (but not all) cases three short and three long Bi-Cl bonds are observed and the lone pair expands towards the face spanned by the three ligands, that are further away.[117] The fact that not all $[BiCl_6]^{3-}$-ions show this distortion and that its amount generally varies quite a lot between different compounds with the same $[EX_6]^{3-}$-ion, can be explained with the energy differences between distorted and undistorted structures being quite small and in the same order of magnitude as crystal packing effects.[116]
While $[EX_6]^{3-}$ is the most common mononuclear motif, $[EX_5]^{2-}$-ions are known as well. Here, a square pyramidal coordination geometry is observed, that, when taking the lone pair into account can also be viewed as pseudo-octahedral—now in accordance with the VSEPR model.
The last possible mononuclear anion is $[EX_4]^-$. It is, however, only known for lighter group 15 elements, for example as $[PCl_4]^-$, where it adopts a structure that can be described as pseudo-trigonal bipyramidal with one of the equatorial positions being occupied by the lone pair.[116]

Starting from these mononuclear motifs, binuclear ones can be constructed by simple dimerisation or through corner-, edge- and face-sharing, yielding the motifs shown in figure 1.8: $[E_2X_9]^{3-}$ with face-sharing octahedra, $[E_2X_{10}]^{4-}$ with edge-sharing octahedra, $[E_2X_{11}]^{5-}$ with point shar-

ing octahedra and $[E_2X_8]^{2-}$, which consists of two $\{EX_5\}$ square pyramids, that share one of their base edges. For $[E_2X_8]^{2-}$, there are two isomers with the axial X ligands being either in cis- or trans-orientation. The trans-variant, however, is more common.[111, 116] Generally, all four compositions are known for all combinations of E and X, with $[E_2X_9]^{3-}$ being most frequent. The only exception is $[E_2X_{11}]^{5-}$, which is not known for the combination Sb/I.[124]

Following the same principles of point-, edge- and face-sharing larger anionic motifs can be obtained as well. As the sheer amount of these motifs is immense and relevant compounds are also discussed in the cumulative part of this work (section 3), it will only be looked at in the form of a few examples. An overview is given in figure 1.9.
One recurring motif for large discrete anions is the arrangement of edge-sharing octahedra analogous to cut-outs of the CdI_2-structure.[44, 125] Two representatives of this class are $[C_9H_{14}N]_4[Bi_4I_{16}]$[126] and $[Fe(C_5H_5)_2][Sb_6I_{22}]$[127]. Another important point to note for multinuclear ions is, that one nominal composition is not restricted to only one motif and for the $[Sb_6I_{22}]^{4-}$-ion for example, four different isomers are known in the literature with a fifth being part of this work (see section 3.2).[112, 127–129]
When looking at polymeric anions, many 1d-motifs are known as well. The structures range from thin chains of point-sharing octahedra with mononuclear repeating units like $[C_{12}H_{14}N_2][BiCl_5]$[130] to thicker motifs with large repeating units like $[C_9H_{18}N_3]_2[Sb_6I_{20}]$, where the monomer again represents a cut-out from the CdI_2-structure type.[131] The comparison of these two anions also points towards a general loose trend that can be observed: The lighter halides tend to form smaller or less closely packed motifs featuring point-sharing octahedra, while the heavy halides prefer more condensed structures with more edge- and face-sharing.[116]
Surprisingly, in contrast to discrete and 1-dimensional anions, 2d-motifs are scarce. Besides two types of ordered or disordered vacancy perovskite derivatives[132, 133] only one bismuthate is known, which features unusual six-membered rings of point- and edge-sharing $\{BiI_6\}$-octahedra.[134]
However, there is a growing class of compounds featuring pseudo-2d structural motifs. Here antimonate and bismuthate anions of low dimensionality are assembled in layers and separated by organic cations. They can be viewed as a combination of the 2d- and vacancy-ordered perovskites described in section 1.2.3 and are obtained by a similar route as the 2d-perovskites: Large organic cations with a polar and an unpolar part tend to order themselves with the unpolar parts pointing towards each other. This templates a structure with separate organic and inorganic layers. The thickness of the organic layer is tunable through the choice of cations and influences the optical properties. In some cases, if the van-der-Waals interactions between the cations are weak, it is even possible to exfoliate the compounds into nanometer-thin mono-layers, making them a new class of 2d-materials[2].[103, 104]

[2]Note the difference between 2d-structural motifs and 2d-materials: Up until this point all mentions of "2d" referred to structural motifs, where some part of a crystal structure (which by definition is periodic in three dimensions) spreads in two dimensions. The term "2d-material", on the other hand, refers to materials that only expand periodically in two dimensions, like for example graphene.

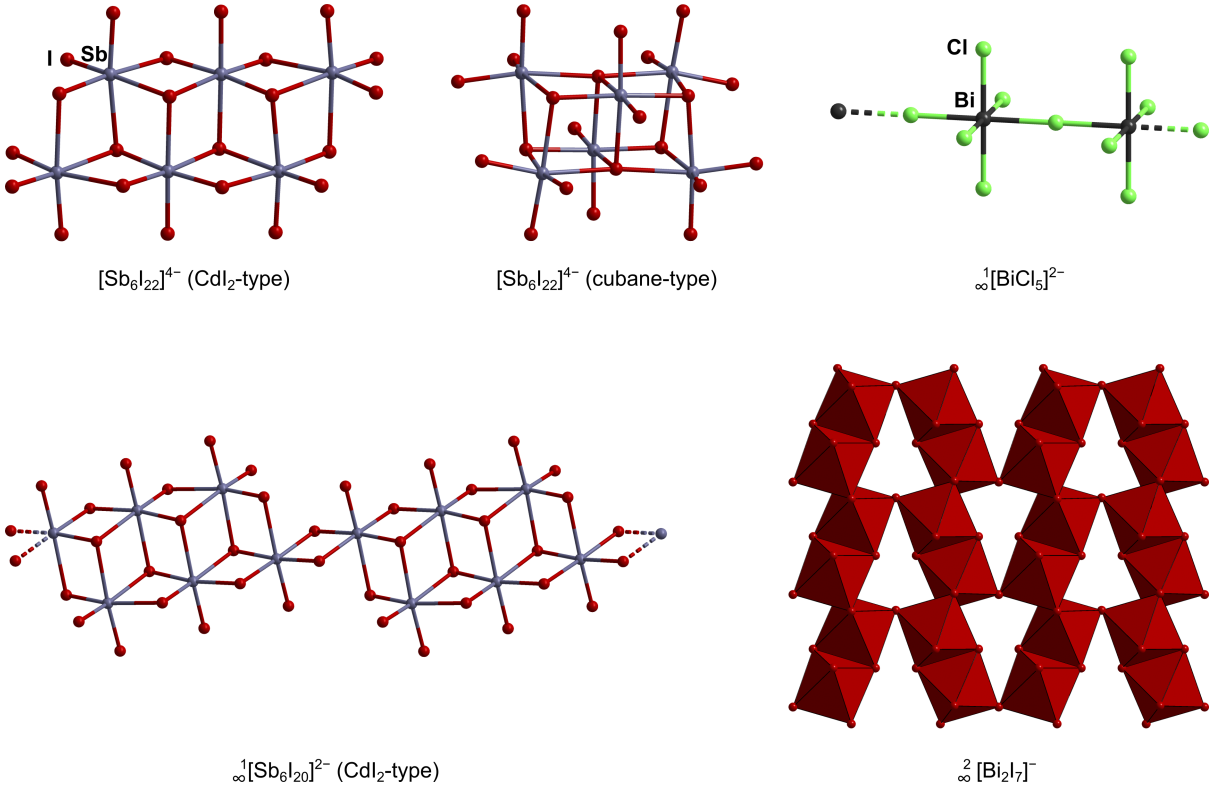

Figure 1.9: Examples for multinuclear and polymeric motifs of complex halogenido antimonate and bismuthate anions: $[Fe(C_5H_5)_2][Sb_6I_{22}]$ with CdI_2 like motif[127], $[Fe(C_{12}H_8N_2)_3]_2[Sb_6I_{22}]$ with a double hetero-cubane like motif[128], chain like, polymeric $[C_{12}H_{14}N_2][BiCl_5]$[130] and $[C_9H_{18}N_3]_2[Sb_6I_{20}]$[131] as well as layered polymeric $[C_5H_{12}N][Bi_2I_7]$[134].

When looking at 3-dimensional anions the number of compounds is even smaller and only chlorido species are known.[135]

As mentioned before, halogenido group 15 metalates show optical properties similar to the group 14 relatives. Especially, the optical band gap is mainly influenced by the halide, with iodine resulting in the smallest and chlorine in the largest band gaps. In contrast to this, the relation between the band gap and the period of the metal atom is inverted between groups 14 and 15. While the halogenido stannates show significantly smaller band gaps than the plumbates, antimonates generally show larger band gaps than bismuthates. It is, however, not possible to derive a strict rule from that, as for example with the vacancy ordered perovskites $Rb_3Sb_2I_9$ and $Rb_3Bi_2I_9$, the antimony compound shows the smaller band gap.[136] Still, in the very most cases, the band gaps of halogenido group 15 metalates become smaller with increasing weight of the elements. A nice example is the isostructural series of $[C_8H_{11}NF]_4[E_2X_{10}]$. Here the optical band gap neatly rises from 2.09 eV to 3.35 eV following the order $[Bi_2I_{10}]^{4-} < [Sb_2I_{10}]^{4-} < [Bi_2Br_{10}]^{4-} < [Sb_2Br_{10}]^{4-} < [Bi_2Cl_{10}]^{4-} < [Sb_2Cl_{10}]^{4-}$.[103] For solar absorption, these values are too high, as even for the combination Bi/I the band gap is well outside the range defined by the Shockley-Queisser limit. However, the comparison of $[C_8H_{11}NF]_4[Bi_2I_{10}]$ with $(MeNH_3)PbI_3$ is not quite fair, as the former features small, discrete anions, while the latter consists of an extended inorganic 3d-network. It is well known that size and dimensionality

of the anionic motif drastically affect the optical band gap of lead perovskites in the way that larger motifs lead to smaller band gaps. The 2d-perovskites with perovskite mono-layers, for instance, show much larger band gaps than $(MeNH_3)PbI_3$ of up to 2.4 eV.[75, 137] Although no comprehensive study exists, it is assumed that this effect also translates to bismuthates and antimonates. In section 3.4, this phenomenon is investigated in detail for a series of iodido antimonates.

When looking at iodido bismuthates of larger anionic dimensionality like the chain-like $[BiI_2(C_{12}H_{24}O_6)][Bi_3I_{10}]$, the comparison with plumbates is much more promising as it shows a band gap of 1.62 eV, close to the arbitrary upper limit of 1.6 eV considered good for solar absorption.[138] Surprisingly, the layered $[C_5H_{12}N][Bi_2I_7]$ features a larger band gap of 1.8 eV despite the higher dimensionality of the anion.[134] However, with so few 2d-bismuthates known, it is impossible to draw conclusions regarding trends.

In general, iodido antimonates and bismuthates also show photoconductivity, even if they contain discrete anions, which is detrimental to charge carrier mobility.[139, 140] And although prototypical solar cells with these materials have low PCEs of 1 - 2 %, they show greatly improved stability over lead-based materials and provide a proof of concept, encouraging further research towards compounds with smaller band gaps as well optimized device architectures.[141, 142]

1.3.2 Metalates with ternary anions

The challenge to find such halogenido antimonates and bismuthates with small band gaps is, however, quite difficult at this point. While it is clear that iodido bismuthates are the most promising of all halogenido pentelates, it still is very much of a guessing game in terms of what cations template large or extended anionic motifs. Therefore, other methods of altering the electronic and optical properties are explored and here the incorporation of hetero-metals has proved promising.

The first example of a compound featuring such a ternary anion was $[Bi_2(C_4H_8O_3H)_3(C_4H_8O_3H_2)][Bi_5CuI_{19}]$ with a chain-like structure, reported well before the rise of perovskite solar cells in 2001 by *Feldmann*.[143] It features $\{Bi_5I_{19}\}$-cut-outs of the familiar CdI_2-structure, which are connected by $\{CuI_4\}$-tetrahedra (see figure 1.10). For a long time, the number of structures with ternary anions remained low, simply due to a lack of research interest. This changed with the success of lead halide perovskites and the subsequent discovery of the whole class of halogenido metalates for semiconductor applications. Today, the number of known compounds is rapidly increasing, and while not yet as large as the number of compounds with binary anions, the known ternary motifs suggest a similar structural diversity.

Fuelled by the success of Bi/Ag-elpasolites, the focus has mainly been on stable and non-toxic silver(I) and copper(I) as hetero-metals, but other elements have been explored as well. Often the ternary anions are composed of subunits known from the binary ones, that are expanded or interconnected by $\{MX_6\}$- or $\{MX_4\}$-units (M = hetero-metal). A very common motif is

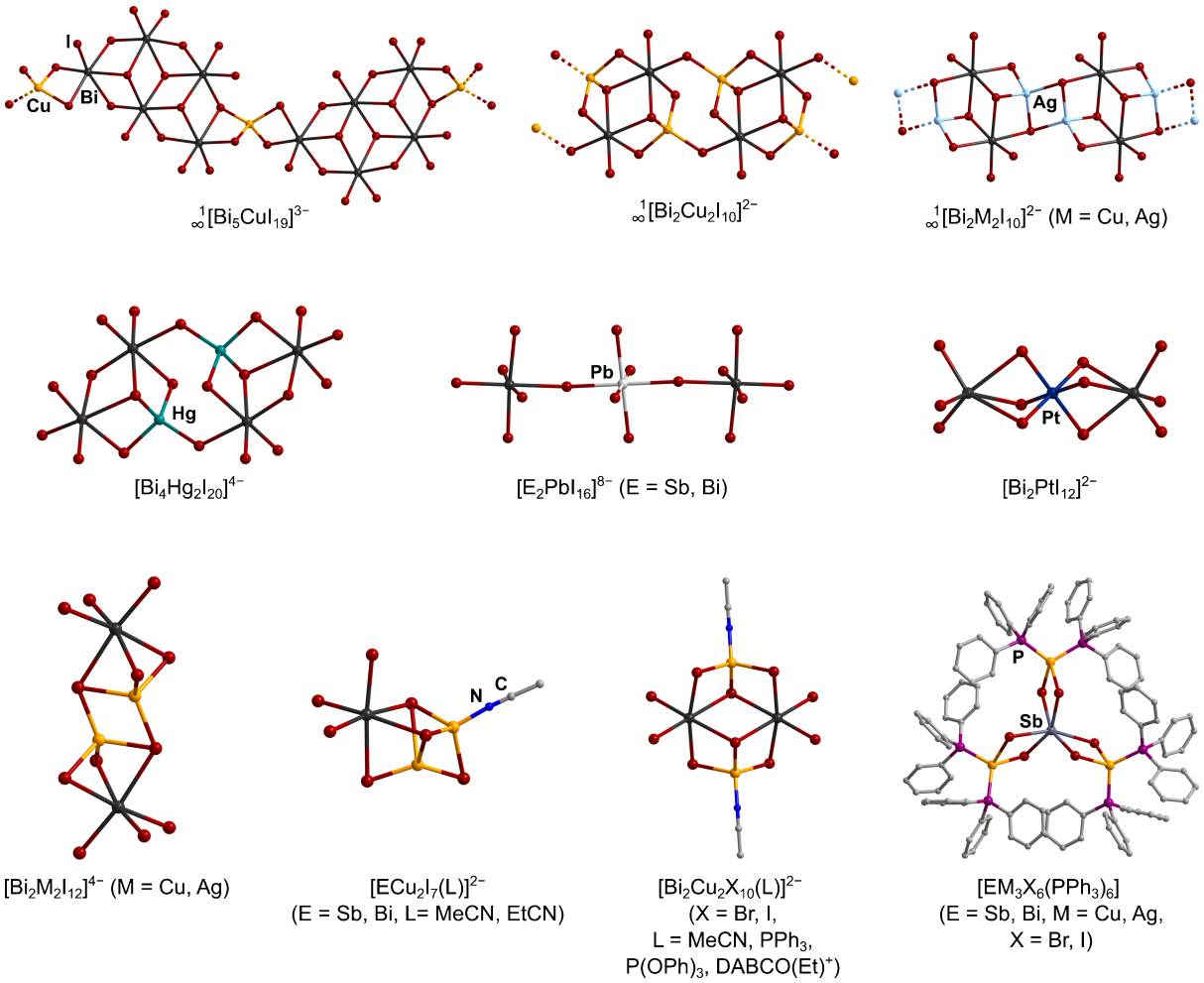

Figure 1.10: Examples for motifs of heterometallic halogenido antimonate and bismuthate anions. Top row: Chain-like anions from $[Bi_2(C_4H_8O_3H)_3(C_4H_8O_3H_2)][Bi_5CuI_{19}]$[143], $[Cu(MeCH_3)_4]_2[Bi_2Cu_2I_{10}]$[144] and $[Et_4N]_2[Bi_2Ag_2I_{10}]$[144, 145]. Middle row: Anions containing hetero-metals other than copper or silver from $(Et_4N)_4(Bi_4Hg_2I_{20})$[146], $[C_9H_{14}N_2]_4[Bi_2PbI_{16}]$[147] and $[Na_4(C_3H_6O)_{15}][Bi_2PtI_{12}]_2 \cdot 3\,(C_3H_6O)$[148]. Bottom row: Discrete complexes containing copper and silver as well as compounds stabilized by organic ligands: $[PPh_4]_4[Bi_2Ag_2I_{12}]$[149], $[PPh_4]_2[BiCu_2I_7(MeCN)]$[150], $[PBz]_2[Bi_2Cu_2I_{10}(MeCN)]$ (Bz = benzyl, DABCO = 1,4-diazabicyclo[2.2.2]octane)[144, 151–153], $[SbCu_3I_6(PPh_3)_6]$[152, 154, 155]. Formulas refer to shown structures, references include all mentioned variations.

$\{Bi_2I_{10}\}$ with two edge-sharing octahedra. It can occur connected into different types of chains, like in $[Cu(MeCH_3)_4]_2[Bi_2Cu_2I_{10}]$[144] or $[Et_4N]_2[Bi_2Ag_2I_{10}]$[145], as well as discrete ions, like in $[Et_4N]_4[Bi_4Hg_2I_{20}]$.[146] When phosphorous or nitrogen-based ligands, especially acetonitrile as the solvent or ammonium ions, that can be deprotonated, are available, the formation of discrete $[Bi_2Cu_2(L)_2X_{10}]^{2-}$ (L = ligand) is also observed frequently.[151–153] Besides that motif, of course, many others are known as well and figure 1.10 gives an overview.

Phosphine ligands are well known to coordinate coinage metals[156], and proved to be able to stabilize a few other discrete motifs resulting in overall neutral complexes in many cases. In this sub-class, especially a series of isostructural compounds for different E/M/X combinations are important. These compounds help verify the trends in band gap energy observed with binary

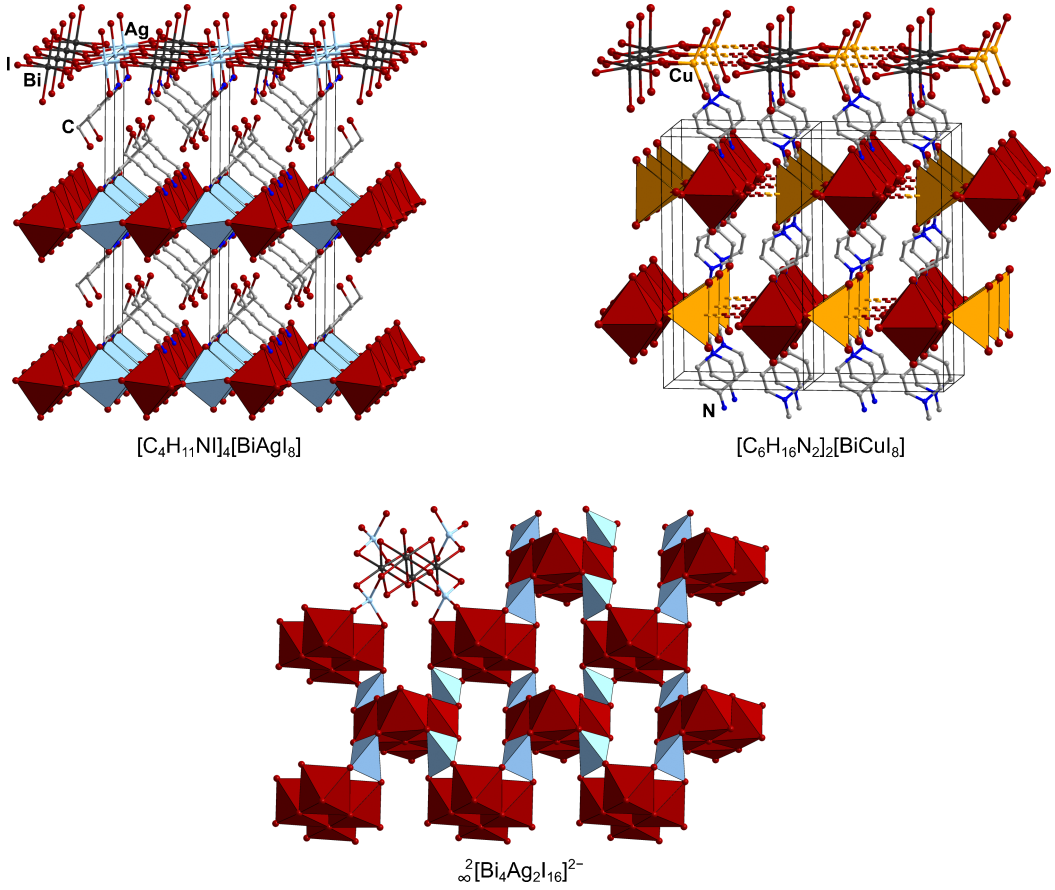

Figure 1.11: Excerpts of the crystal structures of the 2d-elpasolite derivatives $[C_4H_{11}NI]_4[BiAgI_8]$[157] and $C_6H_{16}N_2]_2[BiCuI_8]$[158] as well as anionic motif of $[Et_4N]_2[Bi_4Ag_2I_{16}]$.[145]

metalates with the ternary ones.[154, 155] They also help establish a new trend concerning the influence of the hetero-metal: While silver does not seem to systematically alter the band gap of bismuthates, copper does. Furthermore, it does so in the aimed direction towards narrower gaps. [149, 155] Unfortunately, these are yet only indicative results with a need for broader investigations, especially for antimony, where the number of heterometallic compounds is scarce.

As with the binary anions, two-dimensional anionic motifs are rare. Following the same routes that led to the 2d-perovskite class yields compounds that in comparison can be called 2d-elpasolites with alternating layers of point-sharing bismuth and silver/copper halide polyhedra and organic cations[157, 159]. The analogy to elpasolites works well for most of the silver compounds but is quite far-fetched for the copper ones. There are indeed alternating layers of organic cations and extended, complex, inorganic anions in the crystal structures, but the coordination number of the copper atoms is 4+2 rather than 6. The coordination polyhedron can be viewed as a heavily distorted octahedron but is better described as a tetrahedron. This makes the anionic layer only pseudo-2d with chain-like anions of $\{BiI_6\}$-octahedra and $\{CuI_4\}$-tetrahedra. Still, these copper iodido bismuthates feature small optical band gaps of down to 1.55 eV.[158, 159] Examples for these compounds are shown in figure 1.11.

Besides these 2d-elpasolites, only one compound with a two-dimensional anion is known: $[Et_4N]_2[Bi_4Ag_2I_{16}]$.[145] Here, the CdI_2-like $\{Bi_4I_{16}\}$-motif is connected *via* $\{AgI_4\}$-units into layers. It features a significantly smaller band gap than the related one-dimensional $[Et_4N]_2[Bi_2Ag_2I_2]$, indicating that the trend of larger motifs leading to smaller band gaps also holds true for ternary metalates.[145]

In summary, halogenido antimonates and bismuthates—with or without hetero-metals—show promising behaviour in their semiconductivity, similar to lead halide perovskites and their derivatives. While a huge amount of compounds in this class is known, the systematic investigation towards their application in solar cells or other semiconductor devices is still in its infancy. As with the lead-based compounds, a material suited for the next generation of solar cells needs yet to be discovered, but in contrast to lead halide perovskites, the structural diversity is far from being exhausted and with more trends in the properties being established focused research becomes possible.

Chapter 2

Scope of work

As discussed in the introduction, the heavy group 15 iodido metalates show a huge structural diversity beyond the perovskite derivatives. However, their optical properties and structure-property relationships were only scarcely investigated in the past. Especially, the class of heterometallic metalates, which feature both a heavy group 15 element as well as a transition metal, is still quite small and has only very recently received increased interest. Therefore, three main objectives for this work can be expressed:

1. **Synthesis of new compounds with heterometallic group 15 iodido metalate anions**

   Iodido metalates of group 15 elements or transition metals readily crystallize from solutions of the element iodides and iodides of organic cations in solvents like acetonitrile, acetone, or aqueous hydroiodic acid. If the group 15 and transition metal salts are employed simultaneously, heterometallic metalates can form. Following this simple synthetic route, the aim was to broaden this class of compounds and characterize them regarding their crystal structures, ease of preparation (purity and yield), thermal stability and UV-Vis absorption. For the transition metals, the focus lay on the coinage metals, due to the previous success with bismuth/silver-elpasolites as well as the small optical band gaps observed for bismuth/copper-metalates. The choice of organic cations was based on three main considerations: They should be small to allow for extended anionic networks to form, they should be unusual cations, not used before, and they should be either commercially available or easy to synthesize. Further, in some cases the cations or their corresponding neutral predecessors were chosen for their ability to coordinate to coinage metals to stabilize motifs similar to the phosphine complexes mentioned in section 1.3.2.

2. **Synthesis of new compounds featuring homometallic group 15 iodido metalate anions**

   The exploration of heterometallic systems benefits greatly from knowledge of the homometallic ones. Therefore, the homometallic metalates of the chosen organic cations were to be investigated as well. Here, the focus mainly lay on the relationship between the anionic structure or, more specifically, the size of the anions and the optical band gap.

3. **Identification of new functional materials**

   After the initial characterization, compounds with promising properties, especially with regard to their optical absorption and ease of preparation, were to be further investigated towards their application as functional materials in LEDs or solar cells. For this, luminescence properties and photoconductivity were to be determined in collaboration with physics research groups.

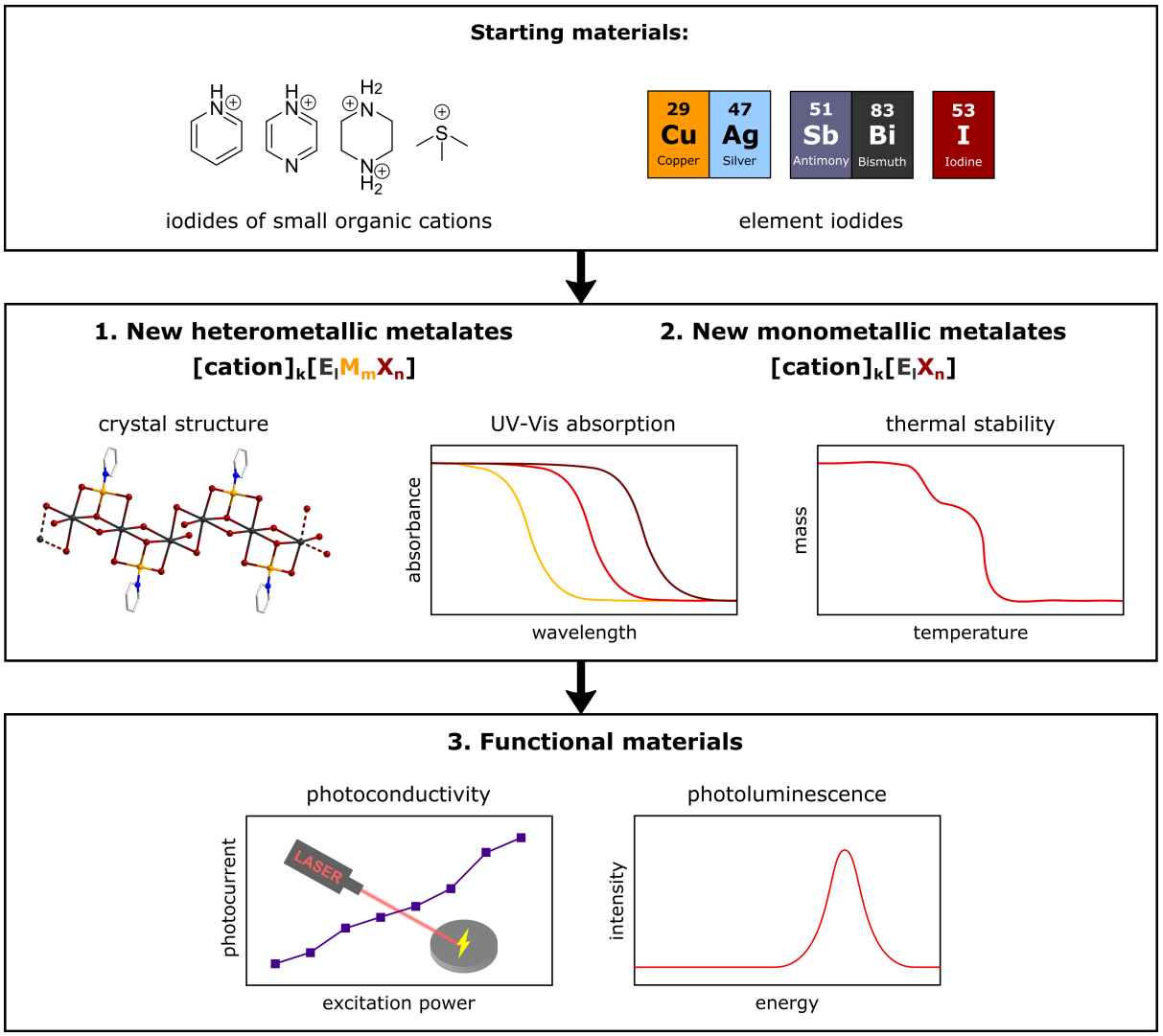

Figure 2.1: Scope of work. (Example crystal structure taken from this project's first publication[160].)

Chapter 3

Cumulative part

This dissertation consists of individual publications, to which I contributed the majority of the work. In the following, the publications are summarized and reprinted with permission from the original publishers. Contributions of the authors are given for each publication. Numbering schemes in the summaries relate to the ones used in the corresponding publication. The supporting/supplementary information can be obtained free of charge from the publishers.

Contents

3.1 $(HPy)_2(Py)CuBi_3I_{12}$, a low bandgap metal halide photoconductor

Jakob Möbs, Marina Gerhard and Johanna Heine, *Dalton Transactions*, **2020**, *49*, 14397-14400, DOI:10.1039/d0dt03427d.

Abstract

Bismuth halides represent an emergent class of materials that combines semiconductor properties with non-toxic constituents. However, many simple bismuth halide compounds feature bandgaps that are significantly higher than those of the lead halide perovskites, which they are supposed to replace. One way to address this issue is the preparation of multinary metal halide materials that feature an additional metal ion. Here, we report on the synthesis and properties of $(HPy)_2(Py)CuBi_3I_{12}$ (**1**) a new copper iodido bismuthate, a photoconductor, which shows a low band gap of 1.59 eV and good thermal and air stability.

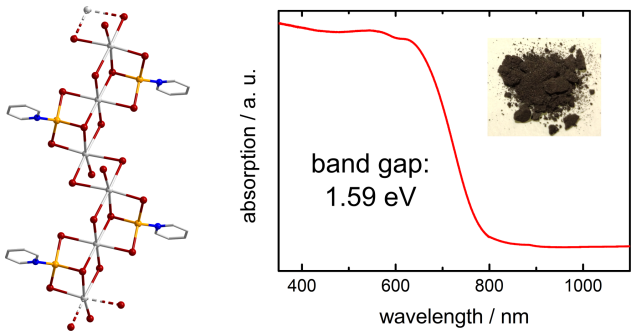

Figure 3.1: Table-of-contents graphic of "$(HPy)_2(Py)CuBi_3I_{12}$, a low bandgap metal halide photoconductor" showing the anionic motif, optical absorption spectrum as well as a photograph of the powder of $(HPy)_2(Py)CuBi_3I_{12}$ (**1**).

Summary

In this communication, a new copper iodido bismuthate with pyridinium counter ions as well as pyridine (py) ligands with the formula $(Hpy)_2(py)CuBi_3I_{12}$ (**1**) is reported. The compound forms in good yields when heating BiI_3, CuI, pyridine (py) and pyridinium iodide in ethanol as a precipitate and also when evaporating the ethanol solution at room temperature, indicating the possibility of thin film preparation. The compound consists of $(Hpy)^+$-cations and chain-like $[(py)CuBi_3I_{12}]^{2-}$-anions. In the anion, trimers of edge-sharing $\{BiI_6\}$-octahedra are connected into chains also *via* edge-sharing. Every trimer is decorated with a $[Cu(py)]^+$-unit. There are two possible positions for each trimer, between which the $[Cu(py)]^+$-unit is distributed equally, leading to only half occupied $[Cu(py)]^+$-positions. Every other half is occupied by a $(Hpy)^+$ion. The anionic chains run along the crystallographic [0 -1 1] direction and are connected into a pseudo-3d network by iodine-iodine contacts well below the double van-der-Waals radius. The pyridinium ions and pyridine ligands are stacked parallel to the chains in a way that suggests π-π interactions.

During the investigations, several other compounds featuring binary group 15 metalate anions were also newly synthesized. Their structures are reported in the supplementary information (see appendix **??**). For one of those, $(Hpy)_3[Bi_2I_9]$ (**2**), the synthesis was optimized to have a compound with discrete binary anions and the same cation as a point of comparison.

Compound **1** is thermally stable up to 150 °C and shows a narrow optical band gap of 1.59 eV. This is surprisingly small when compared to a number of reference compounds, including **2** (E_g = 2.01 eV) and $(Hpy)[BiI_4]$ (E_g = 1.98 eV), which features a binary but also one-dimensional anionic motif. It is even smaller then the band gap of BiI_3 (E_g = 1.69 eV).
Additionally, photoconductivity of **1** was observed under excitation with a helium neon laser, indicating its suitability for future tests in semiconductor devices.

Own contribution

All syntheses were planned and executed by myself. Crystallographic measurements, structure solutions and refinements as well as UV-Vis measurements were carried out by myself. Thermogravimetric measurements were done by Uwe Justus, photocurrent measurements and their analysis by Marina Gerhard. The manuscript was written through contributions of Johanna Heine and myself.

Dalton Transactions

ROYAL SOCIETY OF CHEMISTRY

COMMUNICATION

View Article Online
View Journal | View Issue

Cite this: *Dalton Trans.*, 2020, **49**, 14397

Received 5th October 2020,
Accepted 9th October 2020

DOI: 10.1039/d0dt03427d

rsc.li/dalton

$(HPy)_2(Py)CuBi_3I_{12}$, a low bandgap metal halide photoconductor†

Jakob Möbs, [a] Marina Gerhard [b] and Johanna Heine *[a]

Bismuth halides represent an emergent class of materials that combines semiconductor properties with non-toxic constituents. However, many simple bismuth halide compounds feature bandgaps that are significantly higher than those of the lead halide perovskites, which they are supposed to replace. One way to address this issue is the preparation of multinary metal halide materials that feature an additional metal ion. Here, we report on the synthesis and properties of $(HPy)_2(Py)CuBi_3I_{12}$ (1) a new copper iodido bismuthate, a photoconductor, which shows a low band gap of 1.59 eV and good thermal and air stability.

Main group metal halide semiconductor materials are currently under intense investigation for application in photovoltaics, LEDs and photocatalysis.[1–3] The bulk of this effort is focused on lead halide perovskites $APbX_3$ (A = organic or inorganic cation, *e.g.* $CH_3NH_3^+$ or Cs^+; X = Cl, Br, I) due to their excellent semiconductor properties, ease of fabrication and high defect tolerance.[4] However, concerns about the toxicity of lead have prompted researchers to look beyond this narrowly defined class of compounds.[5] Bismuth, the direct neighbor of lead, shows a related chemistry in its halide compounds,[6–9] but its compounds are of much less environmental concern.[10,11] Along with the rise of lead halide perovskites, bismuth halide compounds have been investigated as well. They typically show better stabilities than their lead counterparts,[12] but fairly low efficiencies in photovoltaics.[13] Instead other semiconductor applications in X-ray detectors,[14] solid state lighting[15] and photocatalysis[16] are much more promising.

One way to significantly alter the electronic properties of bismuth halide compounds is by adding an additional metal. Multinary metalate compounds $A_kM_lBi_mX_n$ (M = metal cation, *e.g.* Cu^+, Ag^+ or Mn^{2+}) can be subdivided into two families. The first family encompasses double perovskites like $Cs_2AgBiBr_6$[17–19] and compounds formally derived from these like <111> perovskites, for example $Cs_4MnBi_2Cl_{12}$[20] or 2D perovskites, for example $[AE2T]_2AgBiI_8$ (AE_2T = 5,5′-diylbis(aminoethyl)-[2,2′-bithiophene])[21] or $(C_3H_9NI)_4AgBiI_8$ (C_3H_9NI = 3-iodopropylammonium).[22] The second family contains "non-perovskite" compounds, which show a rich structural diversity[23] as seen in $(Bi_2(C_4H_8O_3H)_3(C_4H_8O_3H_2))CuBi_5I_{19}$,[24] $(Et_4N)_2Ag_2Bi_4I_{16}$[25] or $(Na_4((CH_3)_2CO)_{15})[PtBi_2I_{12}]_2$.[26] Similar to the chemistry of lead halide perovskites, bismuth iodide materials are of special interest due to their lower band gaps.[27] Formally adding Cu^+ to iodido bismuthates yields copper iodido bismuthates $A_kCu_lBi_mI_n$, which typically have lower band gaps than simple iodido bismuthates $A_kBi_lI_n$ with anions of the same dimensionality.[28–31] The ternary compound $CuBiI_4$ has also been investigated with regard to its semiconductor properties.[31–34] Interestingly, it shows a fairly wide band gap of 2.67 eV. Recent work by the Zheng group has demonstrated the potential of double perovskite derived copper iodido bismuthates for photovoltaic applications.[35,36] Here, materials with band gaps as low as 1.53 eV were obtained – close to the band gap of 1.51 eV reported for $CH_3NH_3PbI_3$, the prototypical lead halide perovskite material.[37] While a low band gap is not the sole criterion when considering the suitability of a material for photovoltaics and other semiconductor applications[38] it is useful as an initial, easy to obtain property before considering more in-depth studies.

Overall, the chemistry of copper iodido bismuthates is still in its infancy and more examples are needed to understand how anion composition, dimensionality and connectivity, as well as additional iodine–iodine interactions can influence the

[a]*Department of Chemistry and Material Sciences Center, Philipps-Universität Marburg, Hans-Meerwein-Straße, 35043 Marburg, Germany. E-mail: johanna.heine@chemie.uni-marburg.de*
[b]*Department of Physics and Material Sciences Center, Philipps-Universität Marburg, Renthof 7, 35032 Marburg, Germany*

† Electronic supplementary information (ESI) available: Experimental procedures and crystallographic details, powder patterns, thermal analysis data, IR spectra, additional UV-Vis spectroscopy data, details of photoconductivity measurements. CCDC 2025569–2025576. For ESI and crystallographic data in CIF or other electronic format see DOI: 10.1039/d0dt03427d

band gap and other optical and electronic properties. In this work, we report on the synthesis and characterization of a new type of copper iodido bismuthate, $(HPy)_2(Py)CuBi_3I_{12}$ (**1**; py = pyridine) which displays good thermal and long-term air stability, a low band gap of 1.59 eV, photoconductive behavior and helps to further understand this promising class of materials.

1 can be prepared in good yield simply by combining pyridine, pyridinium iodide, CuI and BiI_3 in ethanol (see ESI for details†). It is also possible to prepare **1** directly from solution *via* drop-casting, suggesting suitability for thin film preparation. The compound crystallizes in the triclinic space group $P\bar{1}$ in the form of very small black needles. An excerpt of the crystal structure is shown in Fig. 1. **1** is composed of HPy^+ cations and chain-like $[(Py)CuBi_3I_{12}]^{2-}$ anions. The anions feature a partially occupied copper position: the position is only half occupied with a $[(Py)Cu]^+$ unit while the other half is instead occupied by a HPy^+ cation. Many examples of disorder phenomena in iodido cuprates have been described, so it is not unusual to observe it here as well.[39] The iodido bismuthate substructure features a chain-like $[BiI_4]^-$ anion composed of edge-sharing $\{BiI_6\}$-octahedra. While related anion motifs are well-known, for example in $(C_7H_7)BiI_4$[40] the particular connectivity pattern seen here is unique. It is best described as linear $\{Bi_3I_{14}\}$ units connected above and below to neighboring units. $\{(Py)CuI_3\}$ units are then attached *via* edge-sharing. The $[(Py)CuBi_3I_{12}]^{2-}$ strands are running along the [0 −1 1] direction, while pyridine and pyridinium moieties are stacked in parallel.

The pyridinium cation that is not part of the disorder in the copper position is instead disordered across a center of inversion. Significant iodine–iodine interactions below the sum of the van der Waals radii are observed,[41] which interconnect the strands into a pseudo-3D network (see Fig. 2). The parallel stacking of the Py and HPy units indicates that additional offset π–π interactions are present.[42]

1 shows good thermal stability up to 150 °C (see Fig. S13a/b†) and can be stored in air for months without degradation (see Fig. S10†). Its absorption was measured in comparison to a number of reference compounds: $(HPy)BiI_4$ features a strand-like anion composed of edge-sharing $\{BiI_6\}$ octahedra.[43] $(HPy)_3Bi_2I_9$ (**2**), a compound we have newly synthesized during the course of our investigations (see ESI for details†), features molecular $[Bi_2I_9]^{3-}$ anions. BiI_3 was chosen as the parent halide for iodido bismuthates.[44] Fig. 3 shows the corresponding UV-Vis spectra.

Table 1 shows a comparison of the onset of absorption for the materials we have investigated here, as well as some prototypical materials from the literature. It shows that **1** displays a lower onset of absorption than would initially be expected in comparison with other copper iodido bismuthates with chain-like anions, for example $(Cu(CH_3CN)_4)_2Cu_2Bi_2I_{10}$.[28] Two factors could be responsible for this: there are significant iodine–iodine interactions present in **1**, which have been

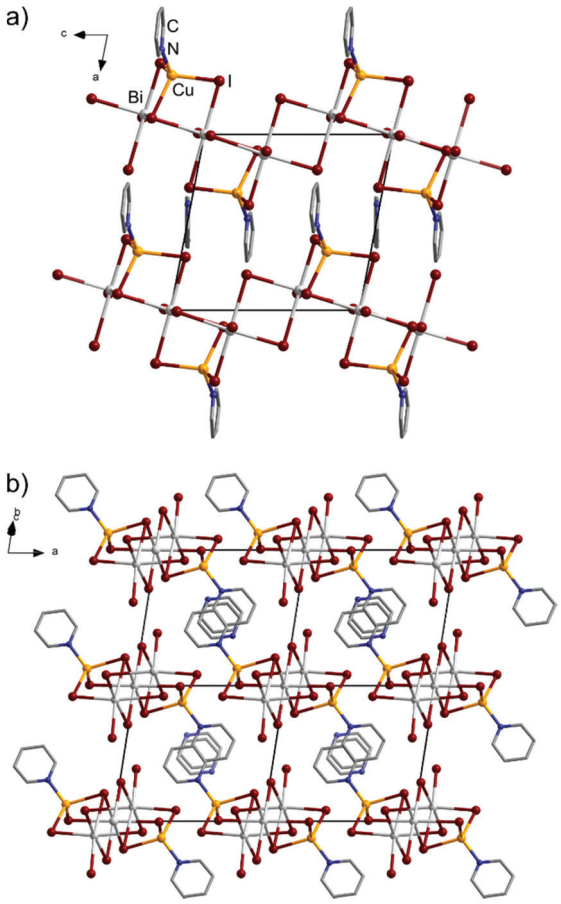

Fig. 1 Excerpts of the crystal structure of **1**: (a) view along the *b* axis. (b) View along the chains along the [0 −1 1] direction.

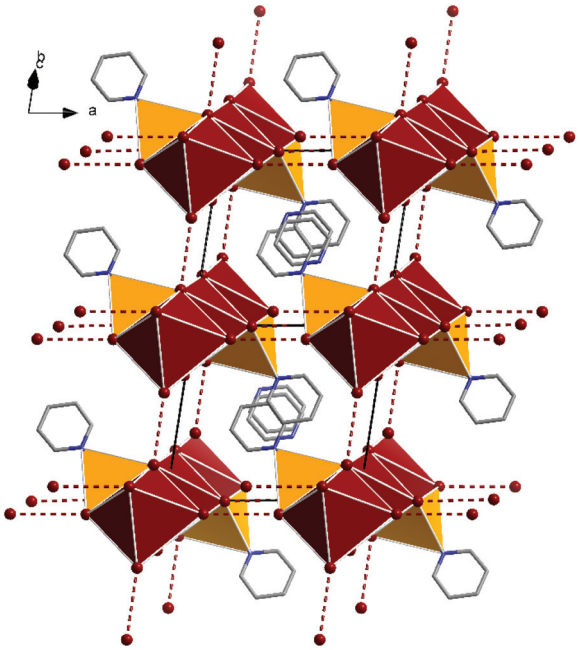

Fig. 2 Excerpts of the crystal structure of **1** showing iodine–iodine interactions below 4 Å (3.88–3.91 Å) as fragmented lines. BiI_6 octahedra are shown as dark red polyhedra, CuI_3N tetrahedra are shown as orange polyhedra. C and N atoms are shown in grey and blue, respectively.

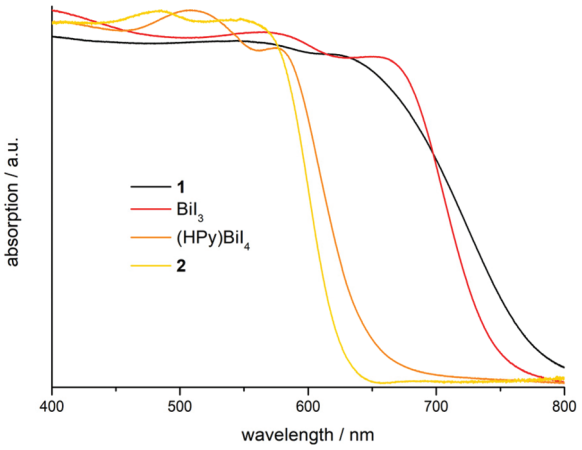

Fig. 3 UV-Vis spectra of **1**, **2** and the reference materials $(HPy)BiI_4$ and BiI_3 recorded in diffuse reflectance.

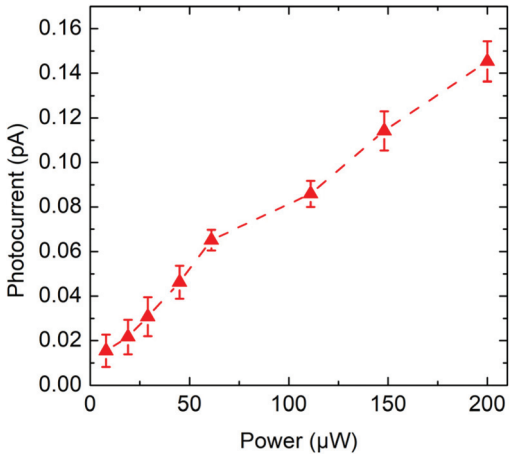

Fig. 4 Photocurrent of **1**, recorded under different excitation powers using a helium neon laser.

Table 1 Onset of absorption for selected organic–inorganic halogenido metalates, sorted from lowest to highest. MPDA = 1-methylpiperidin-4-amine, AMP = 4-aminomethylpiperidine. Note that the parent halide BiI_3 features a neutral, 2D layered structure

	Anion dimensionality	Band gap (in eV)
$(CH_3NH_3)PbI_3$	3	1.51 (ref. 37)
$(MPDA)_2CuBiI_8$	2	1.53 (ref. 36)
$(HPy)_2(Py)CuBi_3I_{12}$ (**1**)	1	1.59
$(AMP)_2CuBiI_8$	2	1.68 (ref. 35)
BiI_3	—	1.69 (ref. 44)
$(Cu(CH_3CN)_4)_2Cu_2Bi_2I_{10}$	1	1.80 (ref. 28)
$(PPh_4)_4Cu_2Bi_2I_{12}$	Molecular	1.80 (ref. 30)
$(Et_4N)_2Cu_2Bi_2I_{10}$	1	1.89 (ref. 28)
$(PPh_4)_2(MeCN)Cu_2BiI_7$	Molecular	1.91 (ref. 28)
$(HPy)BiI_4$	1	1.98 (ref. 43)
$(HPy)_3Bi_2I_9$ (**2**)	Molecular	2.01
$(n\text{-}Bu_4N)_2(CH_3CN)_2Cu_2Bi_2I_{10}$	Molecular	2.06 (ref. 28)

shown to affect the optical properties of iodido bismuthates.[45,46]

Additionally, the comparatively close contact between the anionic substructure and the stacked π-systems of the cations through the $\{CuI_3(Py)\}$ unit might allow a more direct electronic interaction, similar to what was observed in the $(C_7H_7)EX_4$ (E = Sb, Bi; X = Cl, br, I) family of compounds.[40]

To gain further insight into the semiconductor properties of **1**, we have investigated the material's photoconductivity. Under excitation with a helium neon laser (632.8 nm) and a bias of 10 V, a pressed pellet of the material demonstrated a photocurrent increasing linearly with excitation power, as shown in Fig. 4 (see ESI for details†). **1** is not as strongly photoconducting as other copper iodido bismuthates,[35,36] but our measurements confirm the material's basic capability for photoconduction.

In summary, we have presented the facile synthesis and promising properties of a new multinary metal halide photoconductor material, with good stability and an exceptionally low band gap compared to other bismuth halides of the same anion dimensionality. In future work, we will test how $(HPy)_2(Py)CuBi_3I_{12}$ can be integrated into semiconductor devices.

Author contributions

The manuscript was written through contributions of all authors.

Conflicts of interest

There are no conflicts to declare.

Acknowledgements

This research was funded by the German Research Foundation DFG (HE 8018/1). J.H. thanks Prof. Stefanie Dehnen for her support.

Notes and references

1 A. K. Jena, A. Kulkarni and T. Miyasaka, *Chem. Rev.*, 2019, **119**, 3036.
2 L. N. Quan, B. P. Rand, R. H. Friend, S. G. Mhaisalkar, T.-W. Lee and E. H. Sargent, *Chem. Rev.*, 2019, **119**, 7444.
3 H. Huang, B. Pradhan, J. Hofkens, M. B. J. Roeffaers and J. A. Steele, *ACS Energy Lett.*, 2020, **5**, 1107.
4 Z. Xiao, Z. Song and Y. Yan, *Adv. Mater.*, 2019, **31**, 1803792.
5 J. Li, H.-L. Cao, W.-B. Jiao, Q. Wang, M. Wei, I. Cantone, J. Lü and A. Abate, *Nat. Commun.*, 2020, **11**, 310.
6 G. A. Fisher and N. C. Norman, *Adv. Inorg. Chem.*, 1994, **41**, 233.

7 L.-M. Wu, X.-T. Wu and L. Chen, *Coord. Chem. Rev.*, 2009, **253**, 2787.
8 N. Mercier, N. Louvain and W. Bi, *CrystEngComm*, 2009, **11**, 720.
9 S. A. Adonin, M. N. Sokolov and V. P. Fedin, *Coord. Chem. Rev.*, 2016, **312**, 1.
10 R. Mohan, *Nat. Chem.*, 2010, **2**, 336.
11 H. Li, R. Wang and H. Sun, *Acc. Chem. Res.*, 2019, **52**, 216.
12 R. L. Z. Hoye, R. E. Brandt, A. Osherov, V. Stevanovic, S. D. Stranks, M. W. B. Wilson, H. Kim, A. J. Akey, J. D. Perkins, R. C. Kurchin, J. R. Poindexter, E. N. Wang, M. G. Bawendi, V. Bulovic and T. Buonassisi, *Chem. – Eur. J.*, 2016, **22**, 2605–2610.
13 S. M. Jain, D. Phuyal, M. L. Davies, M. Li, B. Philippe, C. De Castro, Z. Qiu, J. Kim, T. Watson, W. C. Tsoi, O. Karis, H. Rensmo, G. Boschloo, T. Edvinsson and J. R. Durrant, *Nano Energy*, 2018, **49**, 614.
14 Y. Zhang, Y. Liu, Z. Xu, H. Ye, Z. Yang, J. You, M. Liu, Y. He, M. G. Kanatzidis and S. Liu, *Nat. Commun.*, 2020, **11**, 2304.
15 Z.-Z. Ma, Z.-F. Shi, L.-T. Wang, F. Zhang, D. Wu, D.-W. Yang, X. Chen, Y. Zhang, C.-X. Shan and X.-J. Li, *Nanoscale*, 2020, **12**, 3637.
16 Y. Dai, C. Poidevin, C. Ochoa-Hernández, A. A. Auer and H. A. Tüysüz, *Angew. Chem., Int. Ed.*, 2020, **59**, 5788.
17 G. Volonakis, M. R. Filip, A. A. Haghighirad, N. Sakai, B. Wenger, H. J. Snaith and F. Giustino, *J. Phys. Chem. Lett.*, 2016, **7**, 1254.
18 A. H. Slavney, T. Hu, A. M. Lindenberg and H. I. A. Karunadasa, *J. Am. Chem. Soc.*, 2016, **138**, 2138.
19 E. T. McClure, M. R. Ball, W. Windl and P. M. Woodward, *Chem. Mater.*, 2016, **28**, 1348.
20 B. Vargas, R. Torres-Cadena, D. T. Reyes-Castillo, J. Rodríguez-Hernández, M. Gembicky, E. Menéndez-Proupin and D. Solis-Ibarra, *Chem. Mater.*, 2020, **32**, 424.
21 M. K. Jana, S. M. Janke, D. J. Dirkes, S. Dovletgeldi, C. Liu, X. Qin, K. Gundogdu, W. You, V. Blum and D. B. Mitzi, *J. Am. Chem. Soc.*, 2019, **141**, 7955.
22 Y. Yao, B. Kou, Y. Peng, Z. Wu, L. Li, S. Wang, X. Zhang, X. Liu and J. Luo, *Chem. Commun.*, 2020, **56**, 3206.
23 N. Dehnhardt, H. Paneth, N. Hecht and J. Heine, *Inorg. Chem.*, 2020, **59**, 3394.
24 C. Feldmann, *Inorg. Chem.*, 2001, **40**, 818.
25 W.-X. Chai, L.-M. Wu, J.-Q. Li and L. Chen, *Inorg. Chem.*, 2007, **46**, 1042.
26 S. A. Adonin, M. N. Sokolov, A. I. Smolentsev, S. G. Kozlova and V. P. Fedin, *Dalton Trans.*, 2013, **42**, 9818.
27 A. García-Fernández, I. Marcos-Cives, C. Platas-Iglesias, S. Castro-García, D. Vázquez-García, A. Fernández and M. Sánchez-Andújar, *Inorg. Chem.*, 2018, **57**, 7655.
28 W.-X. Chai, L.-M. Wu, J.-Q. Li and L. Chen, *Inorg. Chem.*, 2007, **46**, 8698.
29 A. W. Kelly, A. M. Wheaton, A. D. Nicholas, F. H. Barnes, H. H. Patterson and R. D. Pike, *Eur. J. Inorg. Chem.*, 2017, 4990–5000.
30 N. Dehnhardt, H. Borkowski, J. Schepp, R. Tonner and J. Heine, *Inorg. Chem.*, 2018, **57**, 633.
31 N. Dehnhardt, P. Klement, S. Chatterjee and J. Heine, *Inorg. Chem.*, 2019, **58**, 10983.
32 P. H. Fourcroy, D. Carré, F. Thévet and J. Rivet, *Acta Crystallogr.*, 1991, **C47**, 2023.
33 Z. Hu, Z. Wang, G. Kapil, T. Ma, S. Iikubo, T. Minemoto, K. Yoshino, T. Toyoda, Q. Shen and S. Hayase, *ChemSusChem*, 2018, **11**, 2930.
34 H. Yu, B. Zhang, R. Qi, N. Qu, C. Zhao, Y. Lei, X. Yang and Z. Zheng, *Sustainable Energy Fuels*, 2020, **4**, 2800.
35 L.-Y. Bi, L.-Q. Hu, M.-Q. Li, T.-L. Hu, H.-L. Zhang, X.-T. Yin, W.-X. Que, M. S. Lassoued and Y.-Z. Zheng, *J. Mater. Chem. A*, 2019, **7**, 19662.
36 L.-Y. Bi, T.-L. Hu, M.-Q. Li, B.-K. Ling, M. S. Lassoued, Y.-Q. Hu, Z. Wu, G. Zhou and Y.-Z. Zheng, *J. Mater. Chem. A*, 2020, **8**, 7288.
37 T. Baikie, Y. Fang, J. M. Kadro, M. Schreyer, F. Wei, S. G. Mhaisalkar, M. Graetzel and T. J. White, *J. Mater. Chem. A*, 2013, **1**, 5628.
38 T. Kirchartz and U. Rau, *Adv. Energy Mater.*, 2018, **8**, 1703385.
39 H. Hartl and F. Mahdjour-Hassan-Abadi, *Angew. Chem., Int. Ed. Engl.*, 1994, **33**, 1841.
40 I. W. H. Oswald, E. M. Mozur, I. P. Moseley, H. Ahn and J. R. Neilson, *Inorg. Chem.*, 2019, **58**, 5818.
41 S. A. Alvarez, *Dalton Trans.*, 2013, **42**, 8617.
42 D. B. Ninković, J. P. B. Filipović, M. B. Hall, E. N. Brothers and S. D. Zarić, *ACS Cent. Sci.*, 2020, **6**, 420.
43 T. Li, Y. Hu, C. A. Morrison, W. Wu, H. Han and N. Robertson, *Sustainable Energy Fuels*, 2017, **1**, 308.
44 N. J. Podraza, W. Qiu, B. B. Hinojosa, H. Xu, M. A. Motyka, S. R. Phillpot, J. E. Baciak, S. Trolier-McKinstry and J. C. Nino, *J. Appl. Phys.*, 2013, **114**, 033110.
45 A. J. Dennington and M. T. Weller, *Dalton Trans.*, 2018, **47**, 3469.
46 D. B. Mitzi and P. Brock, *Inorg. Chem.*, 2001, **40**, 2096.

3.2 The influence of copper on the optical band gap of heterometallic iodido antimonates and bismuthates

Jakob Möbs, Jan-Niclas Luy, Alena Shlyaykher, Ralf Tonner and Johanna Heine, *Dalton Transactions*, **2021**, *50*, 15855-15869, DOI:10.1039/d1dt02828f.

Abstract

Halogenido metalates of heavy main group elements are versatile semiconductor materials with broad applications. Especially the iodido metalates generally show small optical band gaps, making them suitable for photovoltaics. However, the most promising results have been generated using toxic lead-based materials, raising environmental concerns, while the related and far less toxic bismuth compounds show band gaps too large for direct use in photovoltaics. The introduction of hetero-metals such as copper can significantly lower the band gap of iodido bismuthates and antimonates, but no clear trend could yet be established in this regard. In this work, a short overview of all known copper iodido bismuthates and antimonates is given and this small family of compounds is expanded with nine charged as well as neutral complexes $[E_kM_lI_m(P(R)_3)_n]^{q-}$ (E = Sb, Bi; M = Cu, Ag; R = Ph, *o*-tol). The compounds' crystal structures, stability and optical properties are investigated and compared to the findings of quantum chemical investigations. The main excitation is shown to be a copper-to-antimony or copper-to-bismuth charge transfer while the relative energetic position of the organic ligand orbitals influences the magnitude of the band gap. This reveals that the nature of the ligands and the coordination environment at the copper atom is crucial for designing new copper iodido antimonates and bismuthates with specific band gaps.

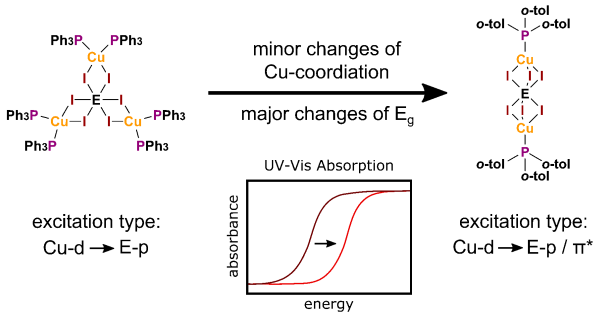

Figure 3.2: Table-of-contents graphic of "The influence of copper on the optical band gap of heterometallic iodido antimonates and bismuthates".

Summary

When looking at the family of heterometallic group 15 metalates for photovoltaic applications, the element combination of bismuth, copper and iodine seems most promising, as it generally leads to the smallest band gaps. However, while the incorporation of copper into iodido bismuthates has been shown to decrease the band gap compared to homometallic bismuthates, the trend is still not very clear as the band gaps in this quite small group of compounds span a

wide range from 1.59 eV to 2.21 eV.
Based on the success of earlier work, where heterometallic complexes were stabilized using triphenylphosphine (PPh_3), a different phosphine ligand with a larger Tolman cone angle, tri(*ortho*-tolyl)phosphine ($P(o\text{-tol})_3$), was used to induce new structural motifs. The change in cone angle from 145 ° for PPh_3 to 194 ° for $P(o\text{-tol})_3$ led to the occurrence of $[M(PR_3)]^+$-fragments (M = Cu, Ag) for R = *o*-tol instead of $[M(PR_3)_2]^+$-fragments, which had been observed with R = Ph. Through variation of solvents and careful control over the availability of protons, ten new compounds featuring $P(o\text{-tol})_3$ with six different structural motifs as well as one additional PPh_3-complex could be obtained.
Under protic conditions, which were ensured by the addition of aqueous hydroiodic acid, $P(o\text{-tol})_3$ is easily protonated to form phosphonium ions. This allowed the formation of $[HP(o\text{-tol})_3][EI_6(Cu(P(o\text{-tol})_3))_2]$ (**1a/b**) and $[Cu(MeCN)_3(P(o\text{-tol})_3)]_3[H(P(o\text{-tol})_3)_2][E_3I_{12}][E_2I_9Cu(P(o\text{-tol})_3)]$ (**2a/b**) in acetone and acetonitrile, respectively, with E = Sb (**a**), Bi (**b**). In **1a/b**, an $\{EI_6\}$-octahedron is capped on opposing sides by $\{Cu(P(o\text{-tol})_3)\}$-fragments to yield $[EI_6(Cu(P(o\text{-tol})_3))_2]^-$-ions, with the charge compensated by simple $[HP(o\text{-tol})_3]^+$. When swapping the solvent for acetonitrile, a compound with three complex ions alongside $[HP(o\text{-tol})_3]^+$ is formed. There is a homometallic $[Cu(P(o\text{-tol})_3)(MeCN)_3]^+$-cation with tetrahedrally coordinated copper, a homometallic $[E_3I_{12}]^{3-}$-anion consisting of three face-sharing octahedra as well as a heterometallic $[E_2I_9CuP(o\text{-tol})_3]^{2-}$-anion consisting of two face-sharing $\{EI_6\}$-octahedra capped at one of the terminal faces by a $\{Cu(P(o\text{-tol})_3)\}$-fragment.
When taking protons out of the equation by working under dry conditions, $[Cu(P(o\text{-tol})_3)(MeCN)_3]_4[E_6I_{22}]$ (**3a/b**) with only homometallic ions is formed in acetonitrile. It features the same complex cation as **2** but a new isomer of the $[E_6I_{22}]^{4-}$-ion in a complicated disordered variation. On the other hand, the neutral complex $[BiI_5(OCMe_2)(Cu(P(o\text{-tol})_3))_2]$ (**4**) crystallizes from acetone under aprotic conditions. It is similar to the anion in **1b** but with one iodide ligand swapped out for acetone. If 1,2-dimethoxy-ethane (dme) is used as a solvent to further prevent the coordination of acetonitrile or acetone, surprisingly, the phosphine is partly oxidized to iodo phosphonium ions, $[IP(o\text{-tol})_3]^+$, in compound **5a/b**. The anion here is $[E_2I_{10}(Cu(P(o\text{-tol})_3))_2]^{2-}$, which features the well known $[E_2X_{10}(M(L))_2]^{2-}$ described in section 1.3.2.

When changing from copper to silver, the first heterometallic iodido antimonate featuring silver aside from the elpasolite structured $(Me_3NH_3)_2SbAgI_6$ could be obtained. $[HP(o\text{-tol})_3]_2[Sb_2I_{10}(Ag(P(o\text{-tol})_3))_2]$ (**6**) also adopts the $[E_2X_{10}(M(L))_2]^{2-}$-motif alongside the simple $[HP(o\text{-tol})_3]^+$-cation. However, due to the bad solubility of AgI no other silver-containing $P(o\text{-tol})_3$-compounds could be synthesized.
Instead, when using PPh_3 in combination with hydroiodic acid, the neutral complex $[Bi_2I_{10}(Ag(PPh_3))_4]\cdot MeCN$ (**7**) was obtained.[3] The structural motif of that compound is similar to $[E_2X_{10}(M(L))_2]^{2-}$ but with two additional $[M(L)^+]$-fragments ($[Ag(PPh_3)]^+$).

[3] In scheme 2 of the published manuscript there is an error. The diagram of **7** is wrongly drawn with $P(o\text{-tol})_3$-ligands.

All compounds except **3a/b** and **7** could be produced in sufficient purity for UV-Vis absorption spectroscopy and their optical band gaps were determined. The most obvious observation to be made here is the shift to smaller band gaps when going from antimony to bismuth in the pairs of isostructural compounds. When looking at the band gap energies in general, however, they lie in the same range as those of homometallic group 15 iodido metalates rather than being significantly smaller, as was expected. This is especially apparent, when comparing **1a/b** and **4** to the structurally very similar literature known PPh_3-complexes $[ECu_3I_6(PPh_3)_6]$ (see figure 1.10). For the same group 15 element, a difference of just below 0.3 eV for the optical band gaps is observed between the PPh_3- and the P(*o*-tol)$_3$-compounds.
To understand this phenomenon, theoretical investigations on these compounds were carried out. In general, the main absorption mechanism proved to be a Cu(*d*)- to E(*p*)-orbital charge transfer, but the ground as well as the excited states are influenced by the phosphine ligands. Of course, with the ground state being mainly Cu(*d*), a dependence on the coordination environment of the copper atoms is clear, but especially for **1a/b** the π*-orbitals of the ligand's aryl groups also significantly contribute to the excited state, which is not the case for $[ECu_3I_6(PPh_3)_6]$.

Own contribution

All syntheses were planned by myself and executed by myself or Alena Shlyaykher under my supervision. Crystallographic measurements, structure solutions and refinements were done by Johanna Heine (single crystals of compounds **1a**, **2a/b** and **6**) or myself (rest and powder diffraction). UV-Vis measurements were carried out by myself or Alena Shlyaykher and analyzed by myself. Thermo-gravimetric measurements were done by Uwe Justus. Computational investigations were carried out by Jan-Niclas Luy and Ralf Tonner-Zech. The manuscript was written through contributions of Johanna Heine, Jan-Niclas Luy, Ralf Tonner-Zech and myself.

Dalton Transactions

ROYAL SOCIETY OF CHEMISTRY

PAPER

View Article Online
View Journal | View Issue

Cite this: *Dalton Trans.*, 2021, **50**, 15855

The influence of copper on the optical band gap of heterometallic iodido antimonates and bismuthates†

Jakob Möbs,[a] Jan-Niclas Luy,[b] Alena Shlyaykher,[a] Ralf Tonner[b] and Johanna Heine *[a]

Received 23rd August 2021,
Accepted 21st October 2021

DOI: 10.1039/d1dt02828f

rsc.li/dalton

Halogenido metalates of heavy main group elements are versatile semiconductor materials with broad applications. Especially the iodido metalates generally show small optical band gaps, making them suitable for photovoltaics. However, the most promising results have been generated using toxic lead-based materials, raising environmental concerns, while the related and far less toxic bismuth compounds show band gaps too large for direct use in photovoltaics. The introduction of heterometals such as copper can significantly lower the band gap of iodido bismuthates and antimonates, but no clear trend could yet be established in this regard. In this work a short overview over all known copper iodido bismuthates and antimonates is given and this small family of compounds is expanded with nine charged as well as neutral complexes $[E_kM_lI_m(P(R)_3)_n]^{q-}$ (E = Sb, Bi; M = Cu, Ag; R = Ph, *o*-tol). The compounds' crystal structures, stability and optical properties are investigated and compared to the findings of quantum chemical investigations. The main excitation is shown to be a copper to antimony or copper to bismuth charge transfer while the relative energetic position of the organic ligand orbitals influences the magnitude of the band gap. This reveals that the nature of the ligands and the coordination environment at the copper atom is crucial for designing new copper iodido antimonates and bismuthates with specific band gaps.

Introduction

Main group metal halide perovskites, most prominently methylammonium lead iodide, $CH_3NH_3PbI_3$, have seen huge research efforts in the last ten years due to their excellent semiconductor properties with a wide range of applications that include photovoltaics, LEDs and photocatalysis.[1–3] Most of these efforts were directed towards lead based materials, especially since the efficiencies of solar cells based on $CH_3NH_3PbI_3$ and related compounds have been rapidly improved from 3.8% in 2009 to more than 22% today.[4,5] However, the toxicity of lead remains a concern[6,7] and thus researchers are searching for suitable alternatives. Here, the heavy group 15 elements bismuth and antimony present promising candidates due to the similar chemistry in their halide compounds[8–10] and—at least in the case of bismuth—a generally low toxicity.[11] Unfortunately, the efficiencies of photovoltaic cells based on halogenido bismuthates and antimonates remain low, due to large, indirect band gaps far from the ideal value of 1.34 eV (ref. 12) and unfavourable defect characteristics.[13] A promising way to change the optical and electronic properties of halogenido bismuthates and antimonates is the incorporation of additional metals. In case of a monovalent metal like silver this even enables the formation of the double perovskite motif, a perovskite superstructure.[14] Heterometallic bismuth and antimony double perovskites, *e.g.* $Cs_2BiAgBr_6$[15–17] or $(CH_3NH_3)_2SbAgI_6$,[18] which are currently under intense investigation,[19–21] are still posing open questions with regard to their optical properties[22] and often feature band gaps too large for direct photovoltaic application, among other issues.[23,24]

Recent advances suggest that the incorporation of copper(I) can lower the optical band gap of iodido group 15 metalates significantly.[25,26] While the double perovskite motif is still out of reach for copper compounds, Zheng and co-workers recently reported a series of layered copper iodido bismuthates, which represent a cut-out of the double perovskite structure and show promising properties for photovoltaic applications

[a]*Department of Chemistry and Material Sciences Center, Philipps-Universität Marburg, Hans-Meerwein-Straße, 35043 Marburg, Germany. E-mail: johanna.heine@chemie.uni-marburg.de*
[b]*Wilhelm-Ostwald-Institut für Physikalische und Theoretische Chemie, Universität Leipzig, Linnéstraße 2, 04103 Leipzig, Germany*

†Electronic supplementary information (ESI) available: Crystallographic details, thermal analysis, powder diffraction patterns, IR spectra, additional UV-Vis spectra. CCDC 2102772–2102774 and 2102776–2102786. For ESI and crystallographic data in CIF or other electronic format see DOI: 10.1039/d1dt02828f

including band gaps as small as 1.53 eV.[27] However, when comparing the overall quite small number of copper iodido bismuthates aside Zheng's series, the band gaps reach from promisingly small 1.59 eV up to 2.21 eV, which is in the same range as monometallic iodido bismuthates and too large for direct photovoltaic applications.[25,26,28–33] The same goes for the antimonates, where even fewer compounds are known. Here the band gaps reach from 1.93 eV to 2.34 eV.[26,30] When looking at the structural motifs and band gaps of these compounds as shown in Scheme 1, no clear relation between the motifs and band gaps can be drawn.

Therefore, we wanted to gain a better understanding of these compounds and shed some light on why the band gap varies so significantly between compounds. To do so, we first needed to broaden the number of compounds for comparison and then investigate their optical properties by experimental and theoretical means.

In a recent work, we looked into the $[EX_6(M(PPh_3)_2)_3]$ (E = Sb, Bi; X = Br, I; M = Cu, Ag) family of compounds, expanding upon earlier work by Fenske[34] and Pike[29] and exploring their potential as model compounds for double perovskites.[26] The good availability of these compounds lead us to swap out PPh_3 for P(*o*-tol)$_3$ (tri(*ortho*-tolyl)phosphine), as it represents a similar monodentate phosphine with a larger Tolman cone angle (145° for PPh_3 *vs.* 194° for P(*o*-tol)$_3$).[35] Judging from the known homometallic complexes $[MX(P(o\text{-tol})_3)]_n$,[36] we surmised that instead of the $[M(PPh_3)_2]^+$ fragment, we would observe a $[M(P(o\text{-tol})_3)]^+$ unit that would enforce the formation of new motifs still similar enough to $[EX_6(M(PPh_3)_2)_3]$ for direct comparison. In this work, we present 10 new complexes featuring this $[M(P(o\text{-tol})_3)]^+$ fragment and an additional compound featuring a $[M(PPh_3)]^+$ fragment. Most of these compounds are anionic complexes, suggesting that neutral motifs are less accessible with P(*o*-tol)$_3$. We discuss the formation and structure of these compounds and explore their stability, thermal decomposition and optical properties in comparison to both other phosphine-decorated heterometallic complexes as well as both simple and multinary iodido antimonates and bismuthates without any additional ligands apart from I^-.

Results and discussion

Synthesis

Initial reactions were performed by combining SbI_3, CuI and P(*o*-tol)$_3$ in acetone or acetonitrile, emulating reaction conditions that successfully lead to $[SbI_6(Cu(PPh_3)_2)_3]$ and related neutral PPh_3 complexes. However, only the formation of $[P(o\text{-tol})_3CuI]$-complexes and a small number of crystals of $[HP(o\text{-tol})_3][SbI_6(Cu(P(o\text{-tol})_3))_2]$ (**1a**) or $[Cu(MeCN)_3(P(o\text{-tol})_3)]_3[H(P(o\text{-tol})_3)_2][Sb_3I_{12}]$ $[Sb_2I_9Cu(P(o\text{-tol})_3)]$ (**2a**) (see Scheme 2) were observed. This suggested that anionic complexes are highly favoured over neutral ones when using P(*o*-tol)$_3$ making the formation of $[CuP(o\text{-tol})_3(MeCN)_3]^+$ or $[HP(o\text{-tol})_3]^+$ as counter ions necessary, if need be from traces of water in the solvent. Thus, in subsequent reactions, HI-solution was used as an additional reagent to enable a quick and quantitative formation of the phosphonium ions, with reaction stoichiometries chosen to target the product composition. By doing so reasonable yields of **1a** and **2a** as well as their bismuthate counterparts (**1b**, **2b**) were achieved. Unfortunately, **1b** only formed as a microcrystalline powder, which was always contaminated with traces of CuI, and no single crystals suitable

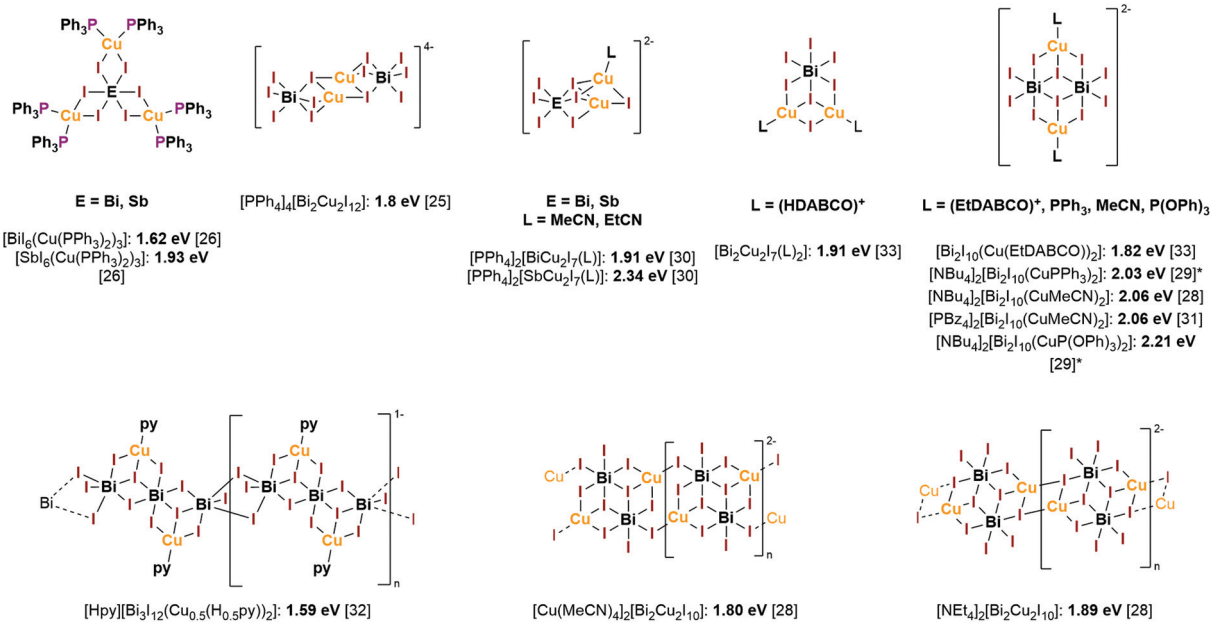

Scheme 1 Overview of the known copper iodido bismuthates and antimonates, sorted according to their published band gaps. Discrete anions above, 1D-anions below. * Reproduced and band gap determined during the preparation of this work for better comparability, see ESI† for details.

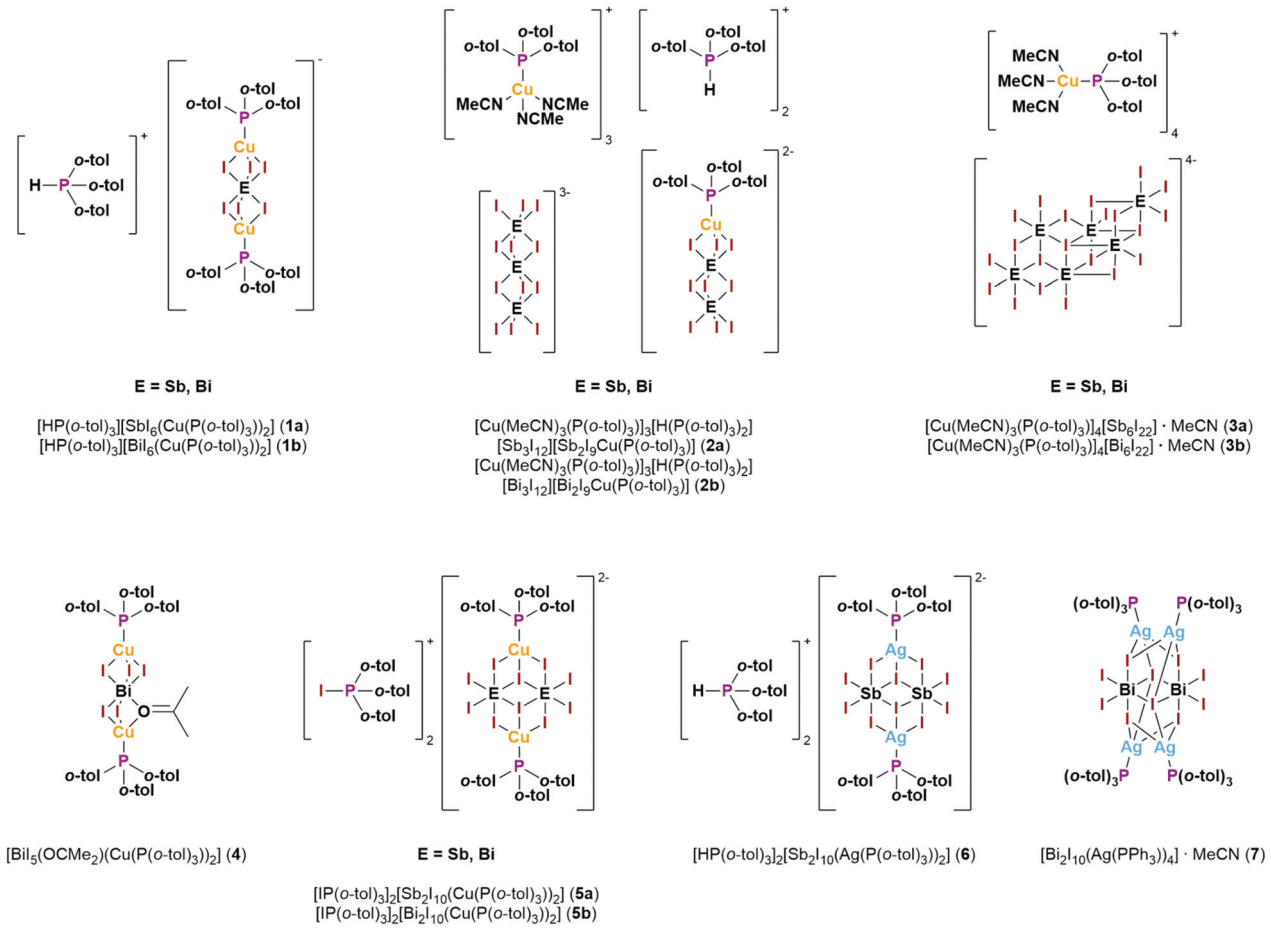

Scheme 2 Overview of the structural motifs of the products.

for X-ray diffraction could be grown. But since **1a** and **1b** are isostructural, it could be identified *via* powder diffraction.

However, the formation of $[CuP(o\text{-tol})_3(MeCN)_3]^+$ and $[HP(o\text{-tol})_3]^+$ pointed towards a strong dependence on the solvent and the availability of protons. Thus, we investigated the influence of different solvents under water-free conditions. Since even the slightest traces of water were found to enable the formation of **1a**/**b** or **2a**/**b** it was necessary to dry the solid reactants directly before starting the reaction inside the reaction vessel at 50 °C under vacuum.

Under these rigorously dry conditions the formation of $[Cu(MeCN)_3(P(o\text{-tol})_3)]_4[E_6I_{22}]\cdot MeCN$ (E = Sb, Bi; **3a**/**b**) was observed in acetonitrile. **3a**/**b** start to decompose as soon as they are taken out of the mother liquor, probably due to the loss of co-crystallized acetonitrile. Powder diffractograms of a few days old samples show the formation of **2a**/**b** which is remarkable since it means that **2a** and **2b** are so stable that even the small amount of protons available through humidity enables their formation (see Fig. S43 and S44 in the ESI†). However, the sensitivity of **3a**/**b** unfortunately prevented further analyses.

While these compounds only feature a non-heterometallic antimonate or bismuthate anion alongside $[CuP(o\text{-tol})_3(MeCN)_3]^+$, a complex with a heterometallic motif $[BiI_5(OCMe_2)(Cu(P(o\text{-tol})_3))_2]$ (**4**), could be obtained under equally dry conditions from acetone. **4** is very similar to the anion in **1b**, with just one iodide ligand replaced by a molecule of acetone. This gives the first overall neutral complex of the series, which—in comparison to **1b**—seems quite straight forward, since the formation of $[HP(o\text{-tol})_3]^+$-counter ions is no longer easily possible. Although both antimony and bismuth variants were accessible for all of the aforementioned compounds, in this case only a bismuth complex is available. Despite the dry conditions, only the formation of **1a**, which still features a $[HP(o\text{-tol})_3]^+$-ion, could be observed for antimony, when using acetone as the solvent. The only source of protons in the reaction mixture is the acetone itself, possibly forming enolate anions.

Since both acetonitrile and acetone obviously took part in the reactions, 1,2-dimethoxy-ethane (dme) was also tested as a solvent. In this case the formation of $[IP(o\text{-tol})_3]_2[E_2I_{10}(Cu(P(o\text{-tol})_3))_2]$ (E = Sb, Bi; **5a**/**b**) was observed. These compounds feature an unexpected, but not unprecedented $(IP(o\text{-tol})_3)^+$-ion, formed through a disproportionation of $P(o\text{-tol})_3$.

Arylphosphanes are known to easily form adducts I_2-$P(Ar)_3$ with diiodine or—in combination with diiodine and a suitable

cation—the corresponding iodo phosphonium salt.[37,38] The oxidation reaction of iodide ions in combination with PPh_3 to iodo phosphonium ions has also been used to carefully reduce uranium(VI) to uranium(V).[39] In our case we believe the oxidizing agent to be remaining P(*o*-tol)$_3$ since we did not observe the formation of elemental metals and no other oxidizing agent was part of the reaction. We also observed a colourless amorphous powder that always formed prior to the formation of **5a**/**b** and should be the side product of that redox reaction. Unfortunately, we were not able to analyse this powder *via* ^{31}P-NMR spectroscopy due to its very low solubility in ethers, pentane and acetone.

In subsequent reactions a stoichiometric amount of diiodine was added to the reaction which resulted in the direct formation of the products.

Additional exploratory reactions with AgI instead of CuI were performed, resulting in the synthesis of $[HP(o\text{-tol})_3]_2[Sb_2I_{10}(Ag(P(o\text{-tol})_3))_2]$ (**6**). Unfortunately, the low solubility of AgI proved to be a major problem and no other compounds could be obtained.

Because of the obviously high stability of the compounds featuring $(HP(o\text{-tol})_3)^+$-ions, we also tried to expand the series of PPh_3-complexes we recently reported on.[26] Therefore HI-solution was added to a reaction mixture of coinage metal iodides, pentele iodides and PPh_3 in MeCN to enable the formation of $(HPPh_3)^+$-ions. However, only a neutral heterometallic compound without the desired phosphonium ions, $[Bi_2I_{10}(Ag(PPh_3))_4]\cdot$MeCN (**7**), could be obtained in form of very few crystals that we were not able to reproduce. This compound stands in direct competition to our previously published $[BiI_6(Ag(PPh_3)_2)_3]$ which also was the main product, when we tried to reproduce **7**, even when HI-solution was added.

Description of crystal structures

Crystal structure of $[HP(o\text{-tol})_3][SbI_6(Cu(P(o\text{-tol})_3))_2]$ (1a). Compounds **1a** and **1b** are isostructural (see ESI† for details). Therefore, only **1a** will be discussed. **1a** crystallizes in the trigonal space group $R\bar{3}$ as yellow blocks. The anionic motif is shown in Fig. 1. Two opposite faces of a $[SbI_6]^{3-}$-octahedron are each capped by a $[CuP(o\text{-tol})_3]^+$-unit resulting in a tetrahedral coordination sphere for the copper atoms. This motif is quite similar to the windmill-like structure of $[SbI_6(Cu(PPh_3)_2)_3]$ we recently reported.[26] The main difference is induced by the large steric bulk of P(*o*-tol)$_3$ compared to PPh_3. It leads to a change in the coordination environment of the copper atoms from two iodide and two phosphine ligands in $[SbI_6(Cu(PPh_3)_2)_3]$ to three iodide and one phosphine ligand in **1a**. However, the Sb–I and Cu–I distances of 3.004 Å and 2.684 Å, respectively, are similar to those found in $[SbI_6(Cu(PPh_3)_2)_3]$ (2.935 Å–3.140 Å and 2.655 Å–2.742 Å). The $(HP(o\text{-tol})_3)^+$-counter ion is disordered over six different positions, linked by the $\bar{3}$ symmetry of the point group (see Fig. S2 in the ESI†). Cations and anions are ordered alternately along the *c*-axis with centroid-to-centroid distances of 4.631 Å to 5.301 Å between the aromatic rings of cations and anions (see Fig. 2). Each cation adopts an edge-to-face coordination between the phenyl groups towards one and an offset-face-to-face coordination towards the other of its neighbouring anions. Arrangements like this were found to be typical for aryl groups in crystals by Dance and Scudder.[40]

Crystal structure of $[Cu(MeCN)_3(P(o\text{-tol})_3)]_3[H(P(o\text{-tol})_3)_2][Sb_3I_{12}][Sb_2I_9Cu(P(o\text{-tol})_3)]$ (2a). Compounds **2a** and **2b** are isostructural (see ESI† for details), therefore, only **2a** will be discussed. **2a** crystallizes in the hexagonal space group $P6_3$ as hexagonal red plates. There are four types of discrete ions to be found in the structure: Two complex anions, $[Sb_3I_{12}]^{3-}$ and $[Sb_2I_9Cu(P(o\text{-tol})_3)]^{2-}$, one complex cation, $[Cu(MeCN)_3P(o\text{-tol})_3]^+$, as well as a simple $(HP(o\text{-tol})_3)^+$-ion. The $[Sb_3I_{12}]^{3-}$-

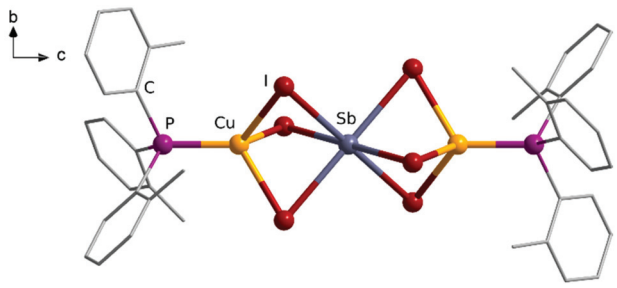

Fig. 1 Anionic $[((P(o\text{-tol})_3)Cu)_2SbI_6]^-$-motif of **1a**. Only carbon positions with an occupancy of 75% are shown.

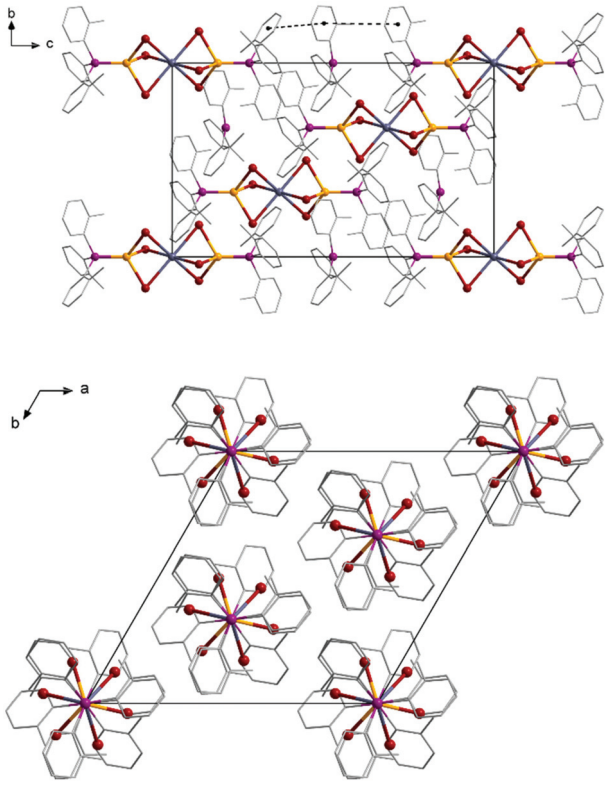

Fig. 2 Packing diagrams of **1a**. Only one orientation is shown for the $(HP(o\text{-tol})_3)^+$-ions.

anion is already known from various different compounds where it forms the sole anion, *e.g.* in $[K(15\text{-crown-}5)_2][Sb_3I_{12}]$.[41] In contrast to the literature known example the ion does not follow an inversion symmetry in **2a** but is distorted along the *c*-axis with the two Sb–Sb distances not being equal but 3.902 Å and 4.018 Å. This is possibly an effect of the I–H interaction between three of the terminal iodide ligands and the proton of a $(HP(o\text{-tol})_3)^+$-ion (see Fig. 3A). The novel $[Sb_2I_9Cu(P(o\text{-tol})_3)]^{2-}$-ion occurs once per formula unit and can be understood as a $[SbI_6]^{3-}$-octahedron which is decorated with one SbI_3-molecule and one $[CuP(o\text{-tol})_3]^{1+}$-unit on opposite faces (see Fig. 3B). The Sb–I distances at the central antimony atom are with 2.964 Å and 3.084 Å similar to those found in $[SbI_6(Cu(PPh_3)_2)_3]$ and **1a**. Also, Cu–I distances of 2.730 Å are within the range of those found in $[SbI_6(Cu(PPh_3)_2)_3]$. However, the Sb–I distances from the second antimony atom to the central $[SbI_6]^{3-}$-unit are with 3.418 Å even longer than the corresponding ones typically found in $[Sb_3I_{12}]^{2-}$-anions.[41] Still, distances of that magnitude are not uncommon and can for example be found in the polymeric $[Sb_{10}I_{34}]^{4-}$-anion.[42]

The $[CuP(o\text{-tol})_3(MeCN)_3]^+$-ion occurs thrice per formula unit, each time with a slightly different orientation of the acetonitrile ligands. Thus, the tetrahedral coordination sphere around the copper atom is more or less distorted. This can be quantified by the P–Cu–N angles, which range from 106.7(6)° to 119.5(7)° (see Fig. 3C). The Cu–N distances and Cu–P distances range from 1.97(2) Å to 2.04(2) Å and 2.22(1) Å to 2.28(1) Å, respectively, which is similar to the distances found in complexes like $[Cu_2I_2(P(o\text{-tol})_3)_2(MeCN)_2]$ or $[Cu_2Br_2(P(o\text{-tol})_3)_2(MeCN)_2]$.[36,43]

As the packing diagrams in Fig. 4 show, the four ion types are stacked in two different kinds of rows in the direction of the *c*-axis. The rows on the edges of the unit cell consist only of alternating $[Sb_2I_9Cu(P(o\text{-tol})_3)]^{2-}$- and $(HP(o\text{-tol})_3)^+$-ions while the two rows in the centre contain the $[Sb_3I_{12}]^{3-}$- and $[CuP(o\text{-tol})_3(MeCN)_3]^+$-ions as well as an additional $(HP(o\text{-tol})_3)^+$.

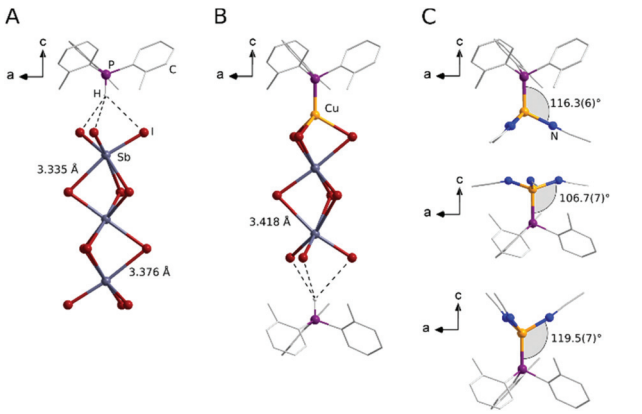

Fig. 3 Structural motifs of **2a**, only phosphorus bonded hydrogen atoms are shown. A: $[Sb_3I_{12}]^{3-}$-anionic motif with neighbouring $(HP(o\text{-tol})_3)^+$-ion. B: $[Sb_2I_9Cu(P(o\text{-tol})_3)]^{2-}$-anionic motif with neighbouring $(HP(o\text{-tol})_3)^+$-ion. C: Three conformers of the $[Cu(MeCN)_3(P(o\text{-tol})_3)]^+$-cation.

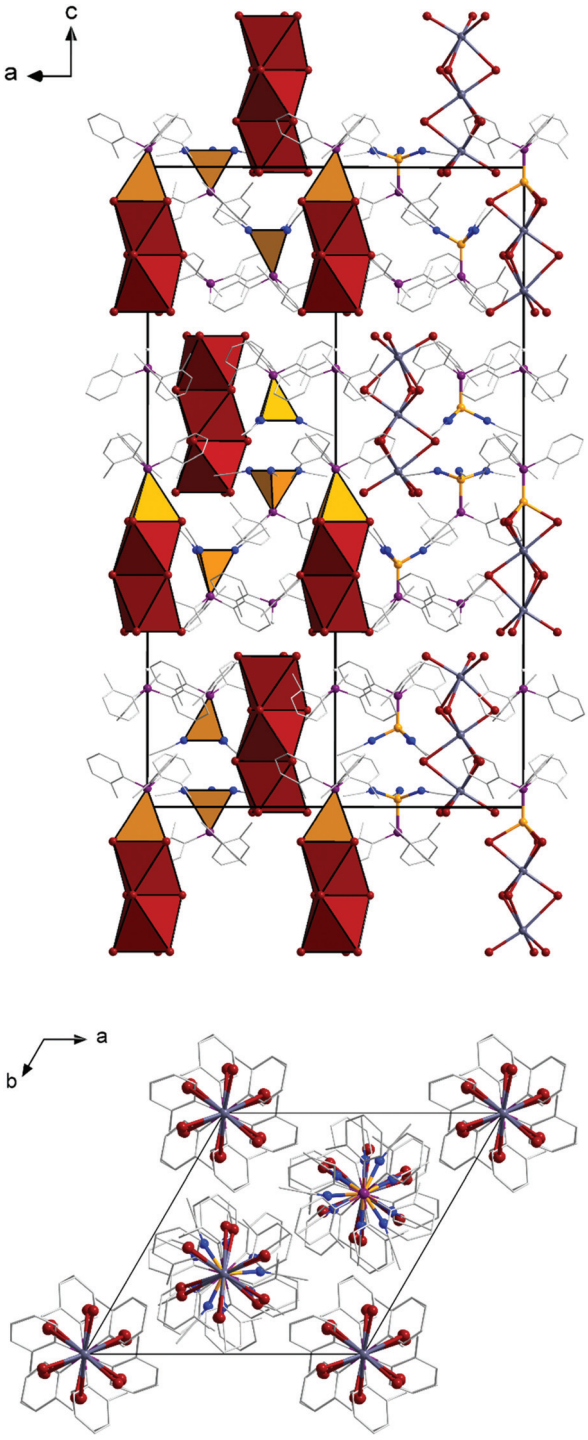

Fig. 4 Packing Diagrams of **2a**. View along the *b*-axis (above) and the *c*-axis (below). The two types of rows can be easily differentiated by the presence or absence of the blue coloured nitrogen atoms of the MeCN-ligands.

On first glance the existence of such multi ion compounds seems a bit surprising. However, while compounds like these are not very common, they are not unknown. For example, Smirani and co-workers found a chlorido antimonate with four

different types of complex $[Sb_nCl_m]^{q-}$-anions in addition to free chloride ions, organic cations and solvate water.[44]

Crystal structure of $[Cu(MeCN)_3(P(o\text{-tol})_3)]_4[Sb_6I_{22}]\cdot MeCN$ (3a). Compounds **3a** and **3b** are isostructural (see ESI† for details), so again only the antimony compound **3a** will be discussed. **3a** crystallizes in the trigonal space group $P\bar{3}$ as orange hexagonal blocks. The anion is a $[Sb_6I_{22}]^{4-}$-ion, disordered over six orientations linked by the $\bar{3}$-symmetry. This gives it the appearance of a Sb_8I_{25} moiety, where only the positions of the outermost SbI_6-octahedra as well as the iodide position in the very centre of the motif are fully occupied. The rest of the atom positions have occupancies of 2/3 or 5/6 (see Fig. 5A). When considering that all antimony atoms should have a complete coordination sphere of six iodide ligands, the actual connectivity of the $[Sb_6I_{22}]^{4-}$-ion can be determined. Although there are many different variations of the $[Sb_6I_{22}]^{4-}$-ion known to literature,[45–48] this particular isomer has not yet been reported. As we have utilized previously, the known $[Sb_6I_{22}]^{4-}$-isomers can be derived from the tetranuclear $[Sb_4I_{16}]^{4-}$-anion by adding neutral SbI_3 units.[42] This is also the case with compound **3a**. However, while with the known examples the SbI_3 units are added to the $[Sb_4I_{16}]^{4-}$-anion on opposing sides, keeping the inversion symmetry of the ion intact, in **3a** they are added on the same side, breaking that symmetry (see Fig. 5B).

Alongside one $[Sb_6I_{22}]^{4-}$-ion crystallize four $[CuP(o\text{-tol})_3(MeCN)_3]^{+}$-ions. There are two different conformers similar to those found in **2a**, although the P–Cu–N-angles here are 114.6(3)° and 122.1(2)°, generally wider than in **2a**. Additionally, two MeCN molecules per formula unit are to be found in the crystal structure. But they are heavily disordered and thus not included in the diagrams (see ESI† for details).

The packing diagram reveals a similar pattern as was observed in **1a** and **2a** with the ions stacked in rows along the *c*-axis. Again, there are two different types of rows. The anions —together with disordered acetonitrile—are stacked along the edges, while two rows of cations and acetonitrile occupy the body of the unit cell (see Fig. 5C).

Crystal structure of $[BiI_5(OCMe_2)(Cu(P(o\text{-tol})_3))_2]$ (4). Compound **4** crystallizes in the orthorhombic space group $Pna2_1$ in the form of thick red needles. The molecular structure is shown in Fig. 6A. As mentioned before the motif is very similar to that of the anion in **1b** with just one of the iodide ligands replaced by an acetone molecule making the complex overall neutral. The acetone ligand has a significant impact on the coordination sphere of one of the copper atoms. It no longer displays a tetrahedral environment but is better

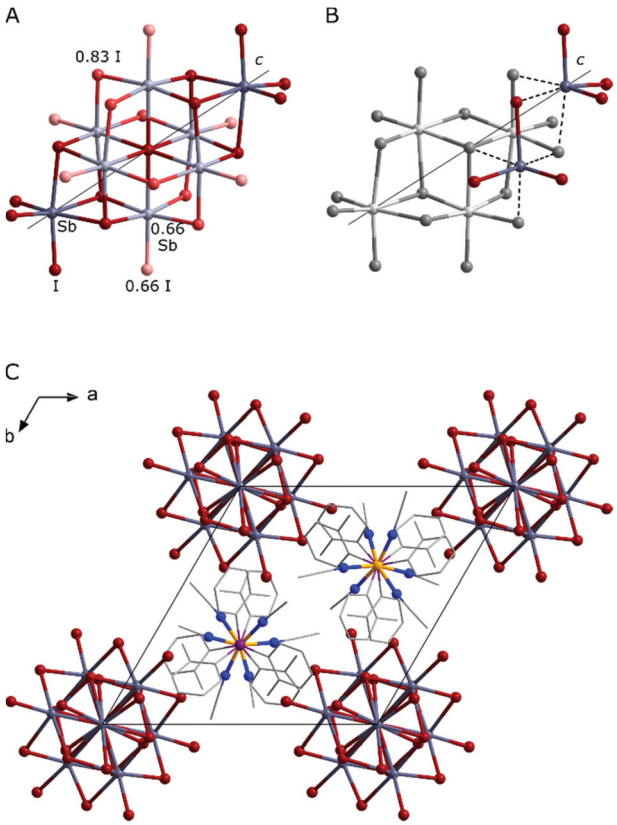

Fig. 5 Excerpts of the crystal structure of **3a**. A: Degrees of occupancy for different atom positions in the disordered $[Sb_6I_{22}]^{4-}$-ion. B: Actual connectivity of the $[Sb_6I_{22}]^{4-}$-ion. The $[Sb_4I_{16}]^{4-}$-ion, from which it can be derived, is highlighted in grey. For ease of viewing the crystallographic *c*-axis is shown as a black line in A and B. C: Packing diagram of **3a**. Disordered MeCN molecules are omitted for clarity.

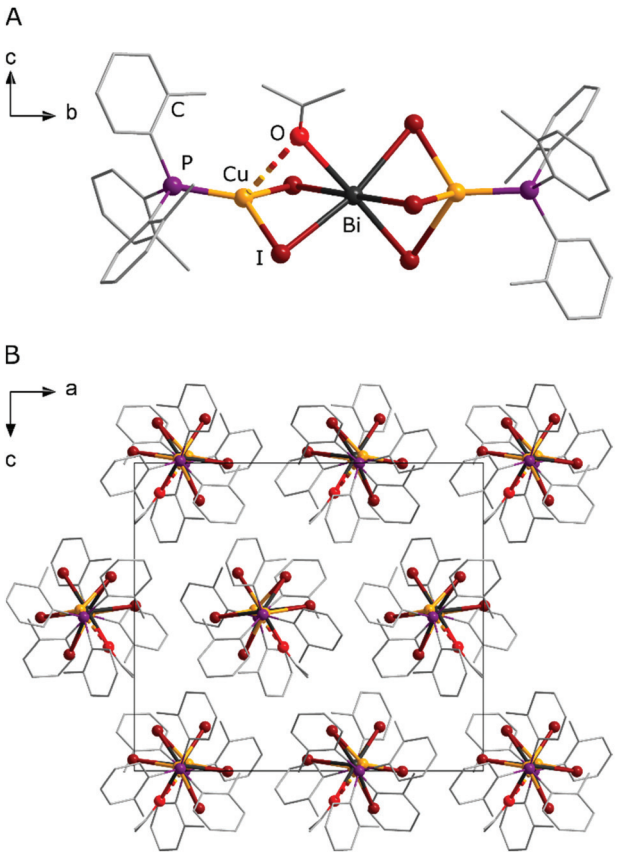

Fig. 6 Molecular structure (A) and unit cell (B) of **4**.

described as a 3 + 1 coordination with a nearly trigonal-planar $[Cu(I)_2(P(o\text{-tol})_3)]$-unit expanded by the acetone ligand, as the copper atom is moved out of the I_2P plane by only 0.285 Å. This also has an effect on the symmetry of the structure overall. The structures discussed before all had trigonal or hexagonal space groups with a threefold axis being induced by a templating effect of the $P(o\text{-tol})_3$-ligand. **4** on the other hand crystallizes in an orthorhombic space group, since the acetone ligand no longer allows for a threefold symmetry of the molecule.

With 2.565 Å and 2.595 Å the Cu–I distances in the trigonal-planar $[Cu(I)_2(P(o\text{-tol})_3)]$-unit are significantly shorter than the ones in the tetrahedral $[Cu(I)_3(P(o\text{-tol})_3)]$-unit in the same molecule (2.699 Å–2.873 Å). While the Cu–O distance is with 2.949 Å quite long, it is well beneath the sum of the van der Waals radii and on the upper end of the range of distances that can be considered as bonding interactions according to Alvarez.[49] The four Bi–I distances perpendicular to the Bi–O bond range from 3.037 Å to 3.099 Å, which is well in line with what is found in $[BiI_6(Cu(PPh_3)_2)_2]$ (3.014 Å–3.181 Å).[29] The distance between the bismuth atom and the iodide ligand opposing the acetone molecule is slightly shorter (2.915 Å), but still longer than the corresponding distance in $[PPh_3Bu][Bi_2I_8(OCMe_2)]$ (2.853 Å), the only other compound featuring a I–Bi–$(OCMe_2)$ unit.[50] On the other hand the Bi–O distance in **4** (2.690 Å) is shorter than in $[PPhh_3Bu][Bi_2I_8(OCMe_2)]$ (2.747 Å).

Crystal structure of $[IP(o\text{-tol})_3]_2[Sb_2I_{10}(Cu(P(o\text{-tol})_3))_2]$ (5a). Compounds **5a** and **5b** are isostructural (see ESI† for details), therefore, only **5a** will be discussed. Compound **5a** crystallizes in the triclinic space group $P\bar{1}$ as orange blocks. The anion is composed of a $[Sb_2I_{10}]^{4-}$-unit, featuring two edge sharing SbI_6-octahedra, that are capped by two $[Cu(P(o\text{-tol})_3)]^+$-groups. Its structure is shown in Fig. 7A. The ion adopts the $\bar{1}$-symmetry with the inversion centre being in the middle between the two antimony positions. A similar PPh_3 complex, but with bismuth instead of antimony was already found by Pike and co-workers.[29] Furthermore, Chen and co-workers as well as our own group already reported on the same $[Bi_2I_{10}Cu_2]^{2-}$-motif as well as the bromido analogue, but with acetonitrile ligands instead of phosphines.[28,31] Still, **5a** is the first compound to feature antimony in this motif. The Sb–I distances for the terminal and μ-bridging iodide ligands (2.850 Å–3.050 Å) as well as the Cu–I distances (2.698 Å–2.736 Å) are well within the ranges previously discussed, while the Sb–μ_3-I distances are significantly elongated (3.269 Å, 3.315 Å), as was also observed with the known bismuth analogues.

What has not been observed with the previous examples of the $[Bi_2I_{10}(Cu(L))_2]^{2-}$-ions is the $[IP(o\text{-tol})_3]^+$-cation and its interaction with the anion as shown in Fig. 7B. The literature-known compounds featured NBu_4^+- or PBz_4^+-cations that show no directional interaction with the anion. The $[IP(o\text{-tol})_3]^+$-cation however is prone to form I–I contacts as can also be seen in the adducts I_2-$P(Ar)_3$ and $[I_3][IP(Ar)_3]$.[37,38] In **5a** an I–I-contact between the cation and the μ-bridging iodide ligand of the anion of 3.471 Å is observed. This is longer than what is found in free I_2-$P(Ar)_3$ (3.124 Å–3.350 Å, depending on Ar) but

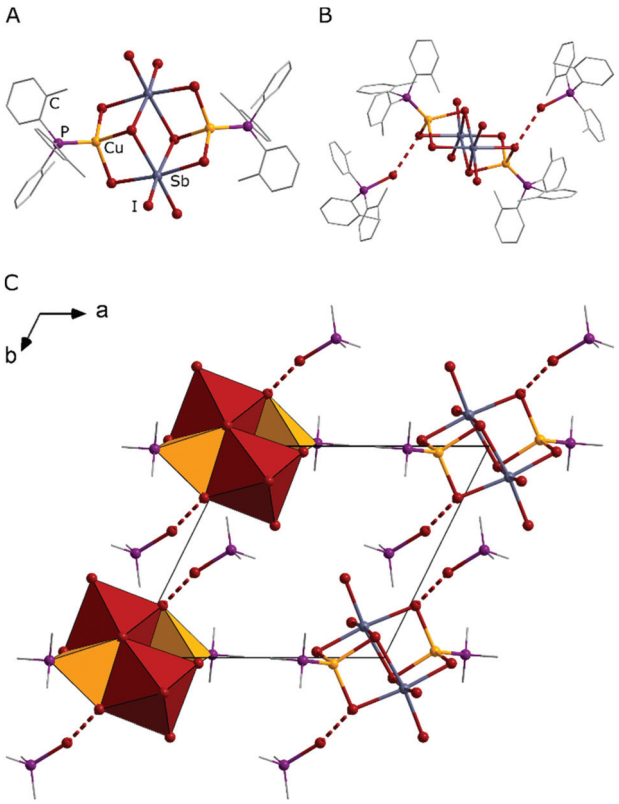

Fig. 7 A: Anionic motif of **5a**. B: Formula unit of **5a** with I–I contacts between anion and cations shown as intercepted bonds. C: Unit cell of **5a**. All but the phosphorous bonded carbon atoms are omitted for clarity.

fits well with the corresponding distances in $[IP(Ar)_3][I_3]$ salts (3.437 Å–3.580 Å) and $[Ph_3PI][U(OSiMe_3)_2I_4]$ (3.480 Å), a rare example of a halide metalate with a $[IP(Ar)_3]^+$-cation.[39]

Despite this short distance which is well below the doubled van der Waals radius of iodine,[49] the contact does not seem to have any effect on the structure of the anion, as no distortion or significant changes of Bi–I or Cu–I distances compared to the known bismuthates can be observed. This fact together with the high number of discovered examples of $[E_2I_{10}(Cu(L))_2]^{2-}$-ions points to a high stability of this particular motif.

Crystal structure of $[HP(o\text{-tol})_3]_2[Sb_2I_{10}(Ag(P(o\text{-tol})_3))_2]$ (6). Compound **6** crystallizes in the triclinic space group $P\bar{1}$ as orange needles. The anionic motif is the same as in **5a** but with silver instead of copper making it is the first multinary silver iodido antimonate ion aside from the three-dimensional anion in the double perovskite $(CH_3NH_3)_2SbAgI_6$.[18] Its structure is shown in Fig. 8A. Similar to its copper analogue, the ion adopts the $\bar{1}$-symmetry with the inversion centre between the two antimony positions.

In contrast to **5a** and the triphenylphosphine coordinated bismuth counterparts reported by Pike and co-workers, the central $[Sb_2I_{10}]^{4-}$-unit in **6** is far more distorted. While the E–μ_3-I distances there are fairly equal, one short and one long

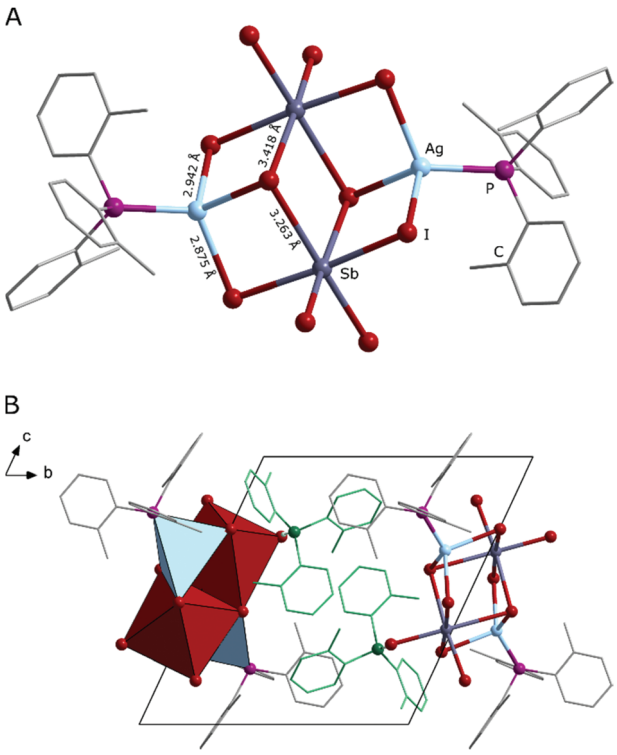

Fig. 8 Anionic motif (A) and unit cell (B) of **6**. Free $(HP(o\text{-tol})_3)^+$-ions are highlighted in green, only phosphorous bonded hydrogen atoms are shown.

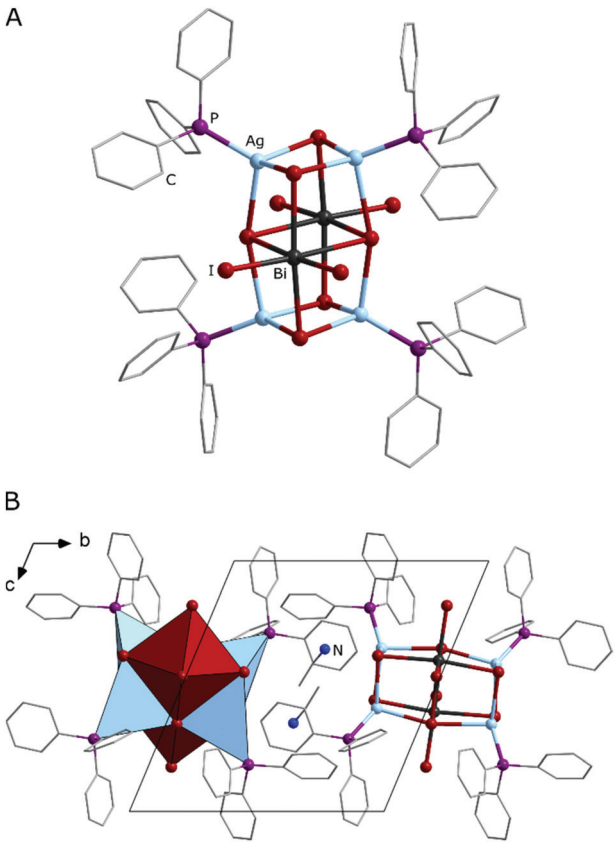

Fig. 9 Molecular motif (A) and unit cell (B) of **7**.

Sb–μ_3-I distance can be found in **6**, being 3.263 Å and 3.418 Å. A similar but less clear-cut observation is made for the Ag–μ-I contacts parallel to the Sb–μ_3-I ones. Here a shorter distance of 2.875 Å and a longer distance of 2.942 Å is found.

The only other $[E_2I_{10}(Cu(L))_2]^{2-}$-ion where a similar observation can be made is the acetonitrile coordinated version $[Bi_2I_{10}(Cu(MeCN))_2]^{2-}$, recently published by our group.[30] Because of this, the distortion can neither be attributed to the enlarged steric bulk of the P(*o*-tol)$_3$-ligand nor to the different ratio between the atomic radii of antimony and silver compared to bismuth and copper.

Crystal structure of $[Bi_2I_{10}(Ag(PPh_3))_4]\cdot MeCN$ (7). Compound **7** crystallizes in the triclinic space group $P\bar{1}$ as red blocks. It features a similar motif as **5a/b** and **6** but here the central $[Bi_2I_{10}]^{4-}$-unit is surrounded by four $[Ag(PPh_3)]^+$ – instead of two $[M(P(o\text{-tol})_3]^+$ – fragments. This leads to an overall neutral molecule with two stacked $Bi_2Ag_2I_6$-cubes in its centre (see Fig. 9). The molecule, too, has an inversion centre between the bismuth positions.

The atom distances as well as the distortion of coordination polyhedra are well in line with what is found in $[BiAg_3I_6(PPh_3)]$ and **5a/b** with the Bi–I distances ranging from 2.870 Å to 3.099 Å for terminal and μ_3-bridging and 3.350 Å to 3.382 Å for the μ_4-bridging iodide ligands. For the μ_4-bridging iodide ligands a similar elongation of the bonds as for the equivalent μ_3-bridging ones in **5a/b** is observed.

Stability and thermal decomposition

Combined TG-DSC measurements were carried out for all products that could be synthesized with sufficient purity (**1a**, **2a/b**, **4**, **5a/b**, **6**). All compounds that do not feature solvent molecules as ligands are stable to about 200 °C and show a sharp peak in the DSC data just before main step of thermal decomposition that most likely corresponds to the melting of the substances. The compounds that do feature acetonitrile or acetone ligands, show a first small loss of mass between 120 °C and 150 °C and then behave similar to the compounds without solvent ligands. PXRD measurements of the residues after the measurement showed the main products to be elemental copper and Cu_3P. For more details see the ESI.†

Optical properties of the copper iodido metalates

UV-Vis absorption spectra measured as diffuse reflectance were obtained for all compounds of the series that could be produced in sufficient amounts and purity. The first prominent observation is a red shift of the onset of absorption when replacing Sb with Bi in the isostructural pairs of compounds. This shift varies from about 0.1 eV for **5a/b** to 0.3 eV for **1a/b** but still always makes a difference from an orange to a deep red colour to the eye (see Fig. 10 and Table 1). This effect of the group 15 element has also been observed with the related PPh_3 complex $[SbI_6(Cu(PPh_3)_2)_3]$ and its Bi counterpart[26] as

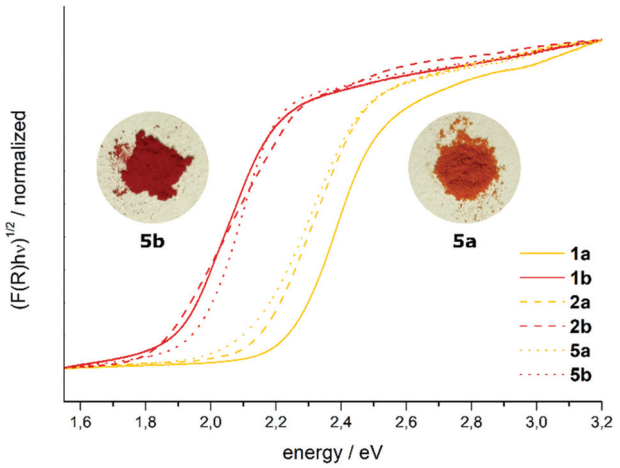

Fig. 10 Tauc-plots from diffuse reflection UV-vis data of **1a/b**, **2a/b** and **5a/b**. Photographs of **5a** and **5b** shown as insets.

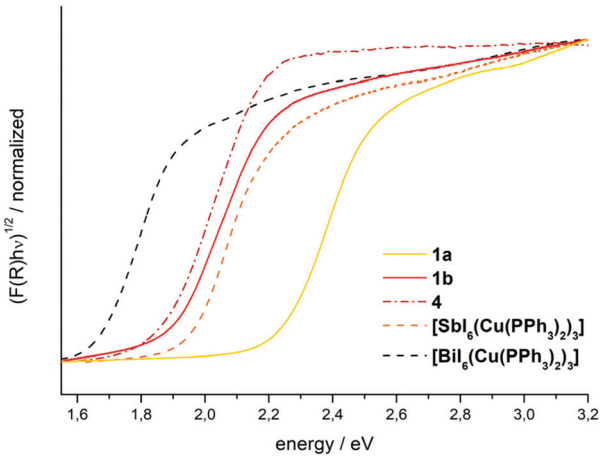

Fig. 11 Tauc-plots from diffuse reflection UV-vis data of **1a/b**, **4** and $[EI_6(Cu(PPh_3)_2)_3]$.

Table 1 Onset of absorption as estimated from Tauc-plots of diffuse reflection UV-Vis data, assuming an indirect allowed transition

		E_{onset}/eV
1a	$[HP(o\text{-tol})_3][SbI_6(Cu(P(o\text{-tol})_3))_2]$	2.24
1b	$[HP(o\text{-tol})_3][BiI_6(Cu(P(o\text{-tol})_3))_2]$	1.91
2a	$[Cu(MeCN)_3(P(o\text{-tol})_3)]_3[H(P(o\text{-tol})_3)_2]$ $[Sb_3I_{12}][Sb_2I_9Cu(P(o\text{-tol})_3)]$	2.16
2b	$[Cu(MeCN)_3(P(o\text{-tol})_3)]_3[H(P(o\text{-tol})_3)_2]$ $[Bi_3I_{12}][Bi_2I_9Cu(P(o\text{-tol})_3)]$	1.85
4	$[BiI_5(OCMe_2)(Cu(P(o\text{-tol})_3))_2]$	1.88
5a	$[IP(o\text{-tol})_3]_2[Sb_2I_{10}(Cu(P(o\text{-tol})_3))_2]$	2.13
5b	$[IP(o\text{-tol})_3]_2[Bi_2I_{10}(Cu(P(o\text{-tol})_3))_2]$	1.98
6	$[HP(o\text{-tol})_3]_2[Sb_2I_{10}(Ag(P(o\text{-tol})_3))_2]$	2.23
	$[SbI_6(Cu(PPh_3)_2)_3]$	1.96 (ref. 26)
	$[BiI_6(Cu(PPh_3)_2)_3]$	1.62 (ref. 26)

well as various iodido metalates with binary anions.[46] However, it is not yet possible to derive a general rule from these findings as the opposite is found with $Rb_3Sb_2I_9$ (1.89 eV) and $Rb_3Bi_2I_9$ (2.06 eV).[51]

Also, comparing the P(*o*-tol)$_3$ complexes to the PPh_3 complexes containing the same elements, it is apparent that E_{onset} is significantly higher for the P(*o*-tol)$_3$ species (see Fig. 11 and S23†). This is especially striking when considering that one reason for introducing copper into iodido pentelates, meaning group 15 metalates, is to lower their optical band gaps. Aside from the neutral PPh_3 complexes this has proven to be successful in a copper iodido bismuthates like $[PPh_4]_4[Cu_2Bi_2I_{12}]$,[25] $[C_6H_{16}N_2]_2[CuBiI_8]$[52] and $[HPy]_2[(Py)CuBi_3I_{12}]$.[32] The onset of absorption for the P(*o*-tol)$_3$ complexes however is well in the range commonly found for the binary iodide pentelates.[46] Naturally, we asked ourselves what the reason for these large differences between the structurally similar compounds **1a/b** and $[SbI_6(Cu(PPh_3)_2)_3]$/$[BiI_6(Cu(PPh_3)_2)_3]$ is. The main difference here is that **1a/b** are charged complexes, while $[SbI_6(Cu(PPh_3)_2)_3]$ and $[BiI_6(Cu(PPh_3)_2)_3]$ feature neutral molecules. However, **4** is a neutral complex that is also structurally quite similar, but still has a high onset of absorption.

Aside from the charge, the coordination environment of the copper atoms changes when looking from the P(*o*-tol)$_3$- to the PPh_3-complexes. While the former feature one phosphine and three iodide ligands the latter have two iodide and two phosphine ligands. We think this to be the major reason for the difference in band gaps, since theoretical investigations have shown a significant influence of the phosphine ligands on the frontier orbitals. However, the electronic situation proved to be very complicated, which is why it is not possible to assign the changes of the band gaps to one or two single parameters (see below).

Optical properties of $[HP(o\text{-tol})_3]_2[Sb_2I_{10}(Ag(P(o\text{-tol})_3))_2]$ (6)

6, which is the first discrete multinary silver iodido antimonate, has an onset of absorption of 2.17 eV (see Fig. 12). This lies in the same range as the binary iodido antimonates mentioned before and fits the trend that is observed when looking at bismuthates with ternary and binary anions, as in contrast

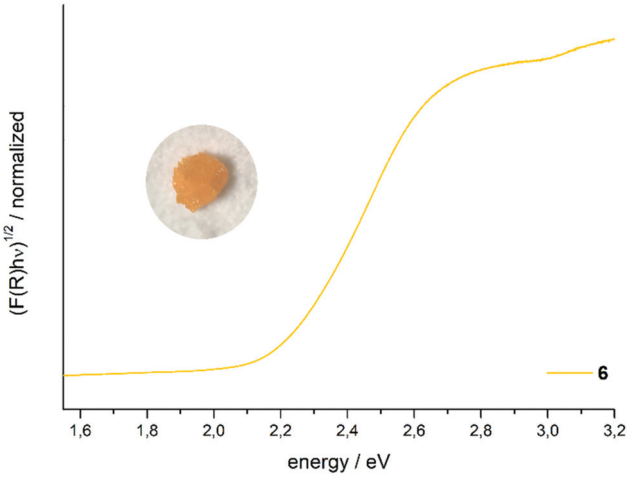

Fig. 12 Tauc-plot from diffuse reflection uv-vis data of **6**. Microscopic photograph of polycrystalline **6** shown as in inset.

to copper, silver does not seem to lower the onset of absorption compared to binary iodido bismuthates.[25,26]

The only other silver iodido antimonate, the double perovskite $(CH_3NH_3)_2SbAgI_6$, shows a bandgap of 1.93 eV.[18] This trend of a small decrease of the band gap when moving to higher dimensional anions, too, fits with the observations at discrete silver iodido bismuthates and the corresponding double perovskites.[25,53]

However, with only **6** as an example at hand it is too soon to draw any conclusions concerning silver iodido antimonates in general.

Theoretical investigations

In order to better understand the different factors determining the band gaps, we calculated excitation energies (Tables S15–23†) of $[SbI_6(Cu(P(o\text{-tol})_3))_2]^-$/$[BiI_6(Cu(P(o\text{-tol})_3))_2]^-$, $[BiI_5(OCMe_2)(Cu(P(o\text{-tol})_3))_2]$ and $[SbI_6(Cu(PPh_3)_2)_3]$/$[BiI_6(Cu(PPh_3)_2)_3]$ using a time-dependent DFT approach (exchange–correlation functional B97-3c[54] with a TZVP-type basis set,[55] TD-approximation and spin–orbit coupling (SOC) based on PBE-D3[56–58] optimized structures, see method section for details). The resulting gap energies of the ground state and the first excited state are shown next to the experimental absorption onset in Table 2.

The TD-DFT results are in good agreement with experimental values discussed above and all observed trends are correctly reproduced. We therefore analyse the first excited SOC states obtained by TD-DFT more closely in the following by investigating the spin-free states making up the SOC state.

The first excited state of the anion of **1b** is a mixture of various triplet states (shown in Table 3). The largest contribution of 35% comes from T_{19} dominated by the excitation from HOMO−1 to LUMO+5. Other contributions also involve HOMO−2 and LUMO+4 which are shown in Fig. 13. The excitation character of all involved spin-free states is Cu-d → Bi-p mediated by lone pairs at iodine atoms. In contrast, the lowlying P(*o*-tol) ligand acceptor orbitals are more active in the Sb analogue complex **1a** (Table S19†). Furthermore, the most active donor orbital is here the HOMO. Additionally, major contributions of T_1 (17%) and T_2 (14%) corresponding to Cu-d → π* character are found (Fig. S52†). When substituting one iodine atom with acetone leading to **4**, the structure of the unoccupied frontier orbitals changes dramatically while the HOMO stays mostly unaltered (Fig. S53†). The Bi-p states interact with $OCMe_2$, shifting them below the organic ligand orbitals in energy. As a result, E_{gap} is reduced.

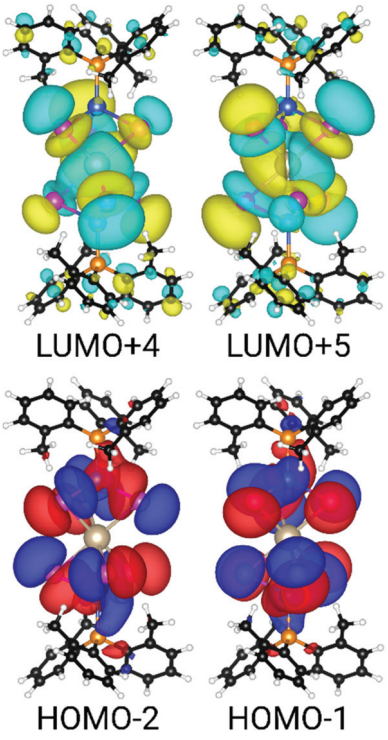

Fig. 13 Relevant molecular orbitals of $[BiI_6(Cu(P(o\text{-tol})_3))_2]^-$.

Table 2 Comparison of theoretical gap (E_{gap}) – and measured absorption onset energies (E_{onset}) of selected complexes

Complex	E_{onset}/eV	E_{gap}/eV
$[SbI_6(Cu(P(o\text{-tol})_3))_2]^-$ (anion of **1a**)	2.24	2.38
$[BiI_6(Cu(P(o\text{-tol})_3))_2]^-$ (anion of **1b**)	1.91	2.03
$[BiI_5(OCMe_2)(Cu(P(o\text{-tol})_3))_2]$ (**4**)	1.88	1.66
$[SbI_6(Cu(PPh_3)_2)_3]$	1.96 (ref. 26)	1.96
$[BiI_6(Cu(PPh_3)_2)_3]$	1.62 (ref. 26)	1.34

Table 3 Contributions of spin-free states to spin–orbit state 1 of $[BiI_6(Cu(P(o\text{-tol})_3))_2]^-$ (anion of **1b**)

Spin-free state (%)	Molecular orbital contributions (%)	Character
T_{19} (35)	HOMO−1 → LUMO+5 (81)	Cu-d → Bi-p
T_{15} (33)	HOMO−1 → LUMO+4 (96)	Cu-d → Bi-p
T_{17} (12)	HOMO-2 → LUMO+5 (94)	Cu-d → Bi-p
T_{16} (10)	HOMO-2 → LUMO+4 (89)	Cu-d → Bi-p

The first SOC state of the "windmill" complex $[BiI_6(Cu(PPh_3)_2)_3]$ is comprised almost equally of triplet states with the HOMO donating into the LUMO (T_1, 29%) and LUMO+1 (T_4, 27%) (Table S18†). Furthermore, there is also a small contribution (S_9, 8%) of a singlet state involving the LUMO+2 acceptor orbital. Similar to the other Bi complexes (**1b**, **4**), the character of all contributions to this excitation can be described as Cu-d → Bi-p (Fig. S51†).

However, the ligand orbitals do not play a role for the excitations in **1b** (Table 3) but contribute significantly to **1a** (Table S20†). In contrast, the Sb windmill complex $[SbI_6(Cu(PPh_3)_2)_3]$ has a stronger contribution of the T_1 state of 45% while contribution of T_4 is reduced slightly to 25% (Table S16†). Furthermore, the LUMO+2 acceptor orbital contributes 7% (T_{11}). The character of all these transitions can be described as Cu-d → Sb-p (Fig. S50†). However, the Sb-s orbital also acts as a donor orbital for the LUMO (T_7, 8%).

In summary, our theoretical investigations highlight why it is so difficult to find simple common descriptors to categorize

the effects of the introduction of copper into iodido pentelates. While the nature of the transition can be broadly described at Cu-d → E-p (E = Sb, Bi) in all investigated cases, both the ground and excited state will be influenced by additional factors: (i) The energy level of the Cu-d ground state will be modified through the coordination environment of the copper atom, *e.g.* the number and nature of the ligands and, in the case of $[SbI_6(Cu(PPh_3)_2)_3]$, by contributions from the Sb-s orbital; (ii) the energy level of the excited state will be influenced by the coordination environment of the E atom, which is comparatively similar throughout the series, but also by additional contributions from Sb-s and π* states, while the latter depend on the nature and arrangement of the phosphine ligands. Nevertheless, our findings suggest that a possible starting point in systematically tuning the absorption properties of copper iodido pentelates lies in controlling the coordination environment of the copper atom. This is underscored by the observation that in the series $A_2[Bi_2I_{10}(Cu(L))_2]$ (A = ammonium or phosphonium cation; L = PR_3 or MeCN)[28,29] the band gap becomes smaller as the electron donor capability of L increases,[59] from 2.21 eV for L = $P(OPh)_3$ (see also Scheme 1) to 1.98 eV for L = P(*o*-tol)$_3$ in compound **5b**.

Conclusions

Overall, we show that numerous new multinary halogenido metalates and metal halide complexes featuring group 11 and group 15 (semi)metals are readily available when using phosphine ligands and phosphonium counterions. This suggests a broad new chemistry in this field, far beyond the small number of current literature examples. We also underscore how complex the interplay between different building units in these materials can be and how simple rationales like 'copper lowers the band gap in iodido bismuthates' fail to capture this. This suggests that in future work, not only the elemental combination can be used to tune the optical properties of materials in this class, but also other factors influencing the electronic situation at individual building units, like ligands at the copper atoms, although more work is still needed to gain a deeper understanding of this.

Experimental

General

SbI_3 and BiI_3 were synthesized from the elements according to literature procedures.[60,61] CuI, AgI, HI (57% solution in water, stabilizer: 0.75% H_3PO_2) and P(*o*-tol)$_3$ were used as supplied from commercial sources unless indicated otherwise. Acetone and acetonitrile were generally flash-distilled prior to use. In cases where rigorously dry conditions were needed, the flash-distilled solvents where stored over molecular sieves for three days and then distilled onto a fresh portion of molecular sieves and stored under argon. 1,2-Dimethoxyethane (dme) was handled the same way, but only used in the dried form and under argon atmosphere since it is prone to the formation of peroxides. For filtration cellulose filters with a pore size of 5–8 μm were used. When dry conditions were needed, glass microfiber filters with a pore size of 1.6 μm which were dried at 120 °C were used. CHN analysis was carried out on an Elementar CHN-analyzer. Thermal analysis was carried out by simultaneous DTA/TG on a NETZSCH STA 409 C/CD in the temperature range of 25 °C to 1000 °C with a heating rate of 10 °C min^{-1} in a constant flow of 80 ml min^{-1} N_2. Powder patterns were recorded on a STADI MP (STOE Darmstadt) powder diffractometer, with CuKα1 radiation with λ = 1.54056 Å at room temperature in transmission mode. IR spectra were measured on a Bruker Tensor 37 FT-IR spectrometer equipped with an ATR-Platinum measuring unit. Optical absorption spectra were recorded on a Varian Cary 5000 UV/Vis/NIR spectrometer in the range of 200–800 nm in diffuse reflectance mode employing a Praying Mantis accessory (Harrick). The raw data was transformed from reflectance R to absorption according to the Kubelka–Munk function $F(R)$ and then plotted as a Tauc-plot, assuming an indirect allowed transition (see ESI† for details).

Synthesis

$[HP(o\text{-tol})_3][SbI_6(Cu(P(o\text{-tol})_3))_2]$ (1a). A total of 37 mg of SbI_3 (0.075 mmol), 19 mg of CuI (0.1 mmol) and 46 mg of P(*o*-tol)$_3$ (0.15 mmol) were suspended in 7.5 mL of acetone. 6.6 μL of HI (57% solution in water, 0.05 mmol) were added under stirring and the mixture was heated to 65 °C for 1.5 h under reflux cooling. The yellow solution with orange precipitate was left to cool to room temperature and then filtered. Within one day orange crystals of **1a** formed in the filtrate. The crystals were collected and washed three times with 3 mL of pentane. Yield: 29 mg (30%). CHN (calculated for $C_{63}H_{64}Cu_2I_6P_3Sb$): C 39.25 (39.28), H 3.430 (3.450), N 0 (0).

Crystal data for 1a. Trigonal, space group $R\bar{3}$ (no. 148), a = 15.8066(5) Å, c = 22.7061(6) Å, V = 4913.0(3) Å^3, Z = 3, T = 100.00 K, μ(MoKα) = 3.991 mm^{-1}, D_{calc} = 1.951 g cm^{-3}, 33 984 reflections measured (4.662° ≤ 2Θ ≤ 50.88°), 2024 unique (R_{int} = 0.0468, R_{sigma} = 0.0168) which were used in all calculations. The final R_1 was 0.0364 ($I > 2\sigma(I)$) and wR_2 was 0.0695 (all data).

$[HP(o\text{-tol})_3][BiI_6(Cu(P(o\text{-tol})_3))_2]$ (1b). A total of 59 mg of BiI_3 (0.1 mmol), 19 mg of CuI (0.1 mmol) and 60 mg of P(*o*-tol)$_3$ (0.2 mmol) were suspended in 9 mL of acetone. 8.6 μL of HI (57% solution in water, 0.06 mmol) were added under stirring and the mixture was heated to 65 °C for 2 h under reflux cooling. After cooling to room temperature the clear solution was stored at 5 °C. Within one week **1b** formed as a red microcrystalline powder. The product was collected and washed three times with 3 mL of pentane. The reaction yielded 45 mg (22%) of the product, but contaminated with traces of CuI, wich could not be removed (see Fig. S40 in the ESI†).

$[Cu(MeCN)_3(P(o\text{-tol})_3)]_3[H(P(o\text{-tol})_3)_2][E_3I_{12}][E_2I_9Cu(P(o\text{-tol})_3)]$ (E = Sb (2a), Bi (2b)). A total of 125 mg of SbI_3 (**2a**) or 148 mg of BiI_3 (**2b**) (0.25 mmol), 38 mg of CuI (0.2 mmol) and 91 mg of P(*o*-tol)$_3$ (0.3 mmol) were dissolved in 10 mL of acetonitrile

by heating the mixture to 95 °C under reflux cooling for 5 min. To the hot solution 13.2 μL of HI (57% solution in water, 0.1 mmol) were added under stirring and the mixture was kept at 95 °C for 45 min under reflux cooling. The clear orange solution was filtered while still hot and left to crystallize at room temperature. Within one day orange crystals of **2a** or red crystals of **2b** formed in the filtrate. The crystals were collected and washed once with 3 mL of cold acetonitrile, twice with 3 mL of methanol and dried under vacuum. Yield: 143 mg (54%) for **2a**, 224 mg (73%) for **2b**. CHN of **2a** (calculated for $C_{144}H_{155}Cu_4I_{21}N_9P_6Sb_5$): C 29.87 (30.21), H 2.673 (2.730), N 2.17 (2.20). CHN of **2b** (calculated for $C_{144}H_{155}Cu_4I_{21}N_9P_6Bi_5$): C 28.19 (28.48), H 2.679 (2.570), N 2.10 (2.08).

Crystal data for 2a. Hexagonal, space group $P6_3$ (no. 173), a = 14.9870(10) Å, c = 44.289(2) Å, V = 8615.0(12) Å^3, Z = 2, T = 100 K, μ(MoKα) = 5.120 mm^{-1}, D_{calc} = 2.207 g cm^{-3}, 123 138 reflections measured (4.836° ≤ 2Θ ≤ 50.722°), 10 521 unique (R_{int} = 0.2247, R_{sigma} = 0.1101) which were used in all calculations. The final R_1 was 0.0681 ($I > 2\sigma(I)$) and wR_2 was 0.1276 (all data).

Crystal data for 2b. Hexagonal, space group $P6_3$ (no. 173), a = 14.9871(5) Å, c = 44.5600(17) Å, V = 8667.8(7) Å^3, Z = 2, T = 100.0 K, μ(MoKα) = 9.378 mm^{-1}, D_{calc} = 2.361 g cm^{-3}, 71 055 reflections measured (4.818° ≤ 2Θ ≤ 50.694°), 10 523 unique (R_{int} = 0.0992, R_{sigma} = 0.0837) which were used in all calculations. The final R_1 was 0.0456 ($I > 2\sigma(I)$) and wR_2 was 0.0766 (all data).

[Cu(P(*o*-tol)$_3$)(MeCN)$_3$]$_4$[E$_6$I$_{22}$]·MeCN (E = Sb (3a), Bi (3b)). The synthesis was carried out completely under an atmosphere of dry Ar. A total of 75 mg of SbI_3 (**3**) or 89 mg of BiI_3 (**3b**) (0.15 mmol), 19 mg of CuI (0.1 mmol) and 30 mg of P(*o*-tol)$_3$ (0.1 mmol) were added to flask and dried at 50 °C and 10^{-3} mbar for one hour. 25 mL of dry acetonitrile were added and the mixture was heated to 95 °C for 45 min under reflux cooling. After cooling to room temperature the solution was filtered and then left for crystallisation at 5 °C. After one week large orange crystals of **3a** or large red crystals of **3b** had appeared, that started to decompose when taken out of the mother liquor.

Crystal data for 3a. Trigonal, space group $P\bar{3}$ (no. 147), a = 14.7250(2) Å, c = 22.9033(6) Å, V = 4300.70(16) Å^3, Z = 1, T = 100 K, μ(CuKα) = 39.543 mm^{-1}, D_{calc} = 2.161 g cm^{-3}, 32 766 reflections measured (6.932° ≤ 2Θ ≤ 151.448°), 5930 unique (R_{int} = 0.0328, R_{sigma} = 0.0286) which were used in all calculations. The final R_1 was 0.0695 ($I > 2\sigma(I)$) and wR_2 was 0.1786 (all data).

Crystal data for 3b. Trigonal, space group $P\bar{3}$ (no. 147), a = 14.6948(7) Å, c = 23.2365(13) Å, V = 4345.4(5) Å^3, Z = 1, T = 100.0 K, μ(MoKα) = 10.512 mm^{-1}, D_{calc} = 2.297 g cm^{-3}, 28 417 reflections measured (3.2° ≤ 2Θ ≤ 53.71°), 6226 unique (R_{int} = 0.0684, R_{sigma} = 0.0591) which were used in all calculations. The final R_1 was 0.0321 ($I > 2\sigma(I)$) and wR_2 was 0.0768 (all data).

[BiI$_5$(OCMe$_2$)(Cu(P(*o*-tol)$_3$))$_2$] (4). The synthesis was carried out completely under an atmosphere of dry Ar. A total of 89 mg of BiI_3 (0.15 mmol), 19 mg of CuI (0.1 mmol), 45 mg of P(*o*-tol)$_3$ (0.15 mmol) were dissolved in 10 mL of dry acetone by heating the mixture to 65 °C for 1 h under reflux cooling. The clear orange solution was left to cool to room temperature and then filtered. Within one day at 5 °C **4** formed as hexagonal plates. The crystals were washed two times with 3 mL of cold acetone and dried on air. Yield: 18 mg (11% with respect to the limiting agent of CuI). CHN (calculated for $C_{45}H_{48}BiCu_2I_5OP_2$): C 32.66 (33.01), H 2.95 (2.95).

Crystal data for 4. Orthorhombic, space group $Pna2_1$ (no. 33), a = 17.9943(12) Å, b = 17.7272(13) Å, c = 15.8671(9) Å, V = 5061.4(6) Å^3, Z = 4, T = 100.0 K, μ(CuKα) = 32.472 mm^{-1}, D_{calc} = 2.149 g cm^{-3}, 126 688 reflections measured (7° ≤ 2Θ ≤ 151.432°), 8754 unique (R_{int} = 0.0486, R_{sigma} = 0.0295) which were used in all calculations. The final R_1 was 0.0241 ($I > 2\sigma(I)$) and wR_2 was 0.0531 (all data).

[IP(*o*-tol)$_3$]$_2$[E$_2$I$_{10}$(Cu(P(*o*-tol)$_3$))$_2$] (E = Sb (5a), Bi (5b)). The synthesis was carried out completely under an atmosphere of dry Ar. A total of 50 mg of SbI_3 (**5a**) or 59 mg of BiI_3 (**5b**) (0.1 mmol), 19 mg of CuI (0.1 mmol), 92 mg of P(*o*-tol)$_3$ (0.3 mmol) and 13 mg of I_2 (0.05 mmol) were suspended in 10 mL of dry dme. After heating the mixture to 85 °C under reflux cooling for 30 min the product had formed as an orange (**5a**) or bright red (**5b**) precipitate. The product was collected, washed once with 3 mL of dry dme, twice with 3 mL of dry pentane. The reaction yielded 70 mg (49%) and 79 mg (52%) of **5a** and **5b**, respectively, but in both cases contaminated with traces of CuI, wich could not be removed (see Fig. S46 and S47 in the ESI†). CHN of **5a** (calculated for $C_{84}H_{84}Cu_2I_{12}P_4Sb_2$): C 31.86 (32.43), H 2.746 (2.720). CHN of **5b** (calculated for $C_{84}H_{84}Cu_2I_{12}P_4Bi_2$): C 30.33 (30.71), 2.612 (2.580).

Initially crystals were grown over the course of four to six weeks from a solution of 75 mg of SbI_3 (**5a**) or 89 mg of BiI_3 (**5b**) (0.15 mmol), 19 mg of CuI (0.1 mmol), 46 mg of P(*o*-tol)$_3$ (0.15 mmol) in dry dme at room temperature.

Crystal data for 5a. Triclinic, space group $P\bar{1}$ (no. 2), a = 14.1928(2) Å, b = 14.5293(2) Å, c = 14.6615(4) Å, α = 117.9820(10)°, β = 104.6040(10)°, γ = 105.1260(10)°, V = 2315.30(8) Å^3, Z = 1, T = 100 K, μ(CuKα) = 37.467 mm^{-1}, D_{calc} = 2.231 g cm^{-3}, 59 560 reflections measured (7.066° ≤ 2Θ ≤ 135°), 8276 unique (R_{int} = 0.0418, R_{sigma} = 0.0341) which were used in all calculations. The final R_1 was 0.0357 ($I > 2\sigma(I)$) and wR_2 was 0.0889 (all data).

Crystal data for 5b. Triclinic, space group $P\bar{1}$ (no. 2), a = 14.2398(3) Å, b = 14.5995(3) Å, c = 14.7020(3) Å, α = 105.454(2)°, β = 117.2590(10)°, γ = 105.296(2)°, V = 2338.21(9) Å^3, Z = 1, T = 100 K, μ(CuKα) = 39.820 mm^{-1}, D_{calc} = 2.333 g cm^{-3}, 59 581 reflections measured (7.036° ≤ 2Θ ≤ 140.204°), 8744 unique (R_{int} = 0.0671, R_{sigma} = 0.0479) which were used in all calculations. The final R_1 was 0.0417 ($I > 2\sigma(I)$) and wR_2 was 0.1069 (all data).

[HP(*o*-tol)$_3$]$_2$[Sb$_2$I$_{10}$(Ag(P(*o*-tol)$_3$))$_2$] (6). A total of 100 mg of SbI_3 (0.2 mmol), 47 mg of AgI (0.2 mmol), 91 mg of P(*o*-tol)$_3$ (0.3 mmol) and 13.2 μL of HI (57% solution in water, 0.1 mmol) were dissolved in 20 mL of acetonitrile by heating the mixture to 95 °C for 2 h under reflux cooling. The yellow

solution with yellow precipitate was left to cool to room temperature and then filtered. Within a few week at 5 °C **6** formed as agglomerates of orange needles alongside a powder of AgI. The AgI was suspended by agitation of the solution and removed together with the liquid. The crystals were washed two times with 3 mL of cold acetonitrile and dried on air. Yield: 30 mg (5% with respect to the limiting agent of HI). CHN (calculated for $C_{84}H_{86}Ag_2I_{10}P_4Sb_2$): C 34.10 (34.23), H 3.012 (2.940).

Crystal data for 6. Triclinic, space group $P\bar{1}$ (no. 2), a = 13.3248(5) Å, b = 14.3029(6) Å, c = 14.7856(6) Å, α = 61.9970(10)°, β = 76.4210(10)°, γ = 66.4810(10)°, V = 2277.38(16) Å^3, Z = 1, T = 100.0 K, μ(MoKα) = 4.510 mm^{-1}, D_{calc} = 2.149 g cm^{-3}, 41 912 reflections measured (4.438° ≤ 2Θ ≤ 50.638°), 8277 unique (R_{int} = 0.0669, R_{sigma} = 0.0506) which were used in all calculations. The final R_1 was 0.0438 ($I > 2\sigma(I)$) and wR_2 was 0.0776 (all data).

$[Bi_2I_{10}(Ag(PPh_3))_4]$·MeCN (7). A total of 100 mg of BiI_3 (0.16 mmol), 50 mg of AgI (0.21 mmol) and 104 mg of PPh_3 (0.4 mmol) were suspended in 10 mL of acetonitrile. 17.2 μL of HI (57% solution in water, 0.13 mmol) were added under stirring and the mixture was heated to 95 °C for 1 h under reflux cooling. The yellow solution with yellow precipitate was filtered while still hot and left for crystallization at 5 °C. Within three weeks red blocks of **7** appeared. Unfortunately, repetition of the synthesis under the same conditions did not yield **7** again, but only produced $[BiI_6(Ag(PPh_3)_2)_3]$.

Crystal data for 7. Triclinic, space group $P\bar{1}$ (no. 2), a = 13.2600(10) Å, b = 14.3061(13) Å, c = 14.5411(11) Å, α = 101.487(6)°, β = 108.303(6)°, γ = 115.047(6)°, V = 2188.6(3) Å^3, Z = 1, T = 100.0 K, μ(MoKα) = 8.522 mm^{-1}, D_{calc} = 2.447 g cm^{-3}, 24 200 reflections measured (3.198° ≤ 2Θ ≤ 53.826°), 9283 unique (R_{int} = 0.0821, R_{sigma} = 0.0983) which were used in all calculations. The final R_1 was 0.0469 ($I > 2\sigma(I)$) and wR_2 was 0.1132 (all data).

Crystallography

Single crystal X-ray determination was performed at 100 K on a Bruker Quest D8 diffractometer with microfocus MoKα radiation and a Photon 100 (CMOS) detector, a STOE StadiVari diffractometer with CuKα radiation and a Detectris Pilatus 300K detector or a STOE IPDS-2/2T diffractometer equipped with an imaging plate detector system using MoKα radiation with graphite monochromatization. Low temperature measurement was chosen to reduce thermal vibrations and to avoid the loss of solvate molecules where necessary.

The structures were solved using direct methods, refined by full-matrix least-squares techniques and expanded using Fourier techniques, using the ShelX software package[62–64] within the OLEX2 suite.[65] All non-hydrogen atoms were refined anisotropically unless otherwise indicated. Hydrogen atoms were assigned to idealized geometric positions and included in structure factors calculations. Pictures of the crystal structures were created using DIAMOND.[66] For additional details on individual refinements, including disorder and twinning found in a number of structures, we refer the reader to the ESI.† The data has been deposited as CCDC 2102772–2102774 and 2102776–2102786.†

Computational methods

Structures of the anionic complexes excluding counterions were extracted from the experimentally determined crystal structures and fully optimized with the exception of **4** for which only positions of hydrogen atoms were relaxed due to large distortions occurring otherwise. Optimizations were performed with TURBOMOLE[67] 7.3 with forces converged to at least 10^{-3} $E_h a_0^{-1}$. The GGA-type exchange–correlation functional PBE[56] was used including the semiempirical dispersion correction DFT-D3[57] with an improved damping function.[58] The self-consistent field energy was converged to 10^{-8} E_h on a fine integration grid (m4) using the def2-TZVPP[68] basis set and corresponding effective core potentials for I, Sb and Bi. Furthermore, the resolution of the identity[69] (RI) approximation was employed throughout.

Time-dependent density functional theory calculations in the Tamm–Dancoff approximation were performed with ORCA 4.2.0[70] using the B97-3c functional[54] and including spin–orbit coupling (SOC) effects. For the purpose of calculating excitation energies, the lowest 20 transitions (roots) were considered. Scalar relativistic effects were treated with the zeroth order regular approximation (ZORA) formalism.[71] The basis set old-ZORA-TZVP,[55] a relativistically recontracted version of the all-electron def2-TZVP[68] basis set was used in conjunction with the auxiliary basis set SARC/J. Due to a missing basis set, SARC-ZORA-TZVP was used for Bi instead. Similar to TURBOMOLE, the RI approximation was used and SCF convergence was set to 10^{-8} E_h on a fine grid (Grid5) while the grid was improved to Grid6 for the final post-SCF evaluation.

Conflicts of interest

There are no conflicts to declare.

Acknowledgements

This research was funded by the German Research Foundation DFG (HE 8018/1). J. H. thanks Prof. Stefanie Dehnen for her support. Computational resources provided by GOETHE-CSC Frankfurt and HLR Stuttgart are gratefully acknowledged.

Notes and references

1 A. K. Jena, A. Kulkarni and T. Miyasaka, *Chem. Rev.*, 2019, **119**, 3036.
2 L. N. Quan, B. P. Rand, R. H. Friend, S. G. Mhaisalkar, T.-W. Lee and E. H. Sargent, *Chem. Rev.*, 2019, **119**, 7444.
3 H. Huang, B. Pradhan, J. Hofkens, M. B. J. Roeffaers and J. A. Steele, *ACS Energy Lett.*, 2020, **5**, 1107.
4 A. Kojima, K. Teshima, Y. Shirai and T. Miyasaka, *J. Am. Chem. Soc.*, 2009, **131**, 6050.

5 M. A. Green, E. D. Dunlop, J. Hohl-Ebinger, M. Yoshita, N. Kopidakis and X. Hao, *Prog. Photovolt. Res. Appl.*, 2021, **29**, 657.
6 J. Li, H.-L. Cao, W.-B. Jiao, Q. Wang, M. Wei, I. Cantone, J. Lü and A. Abate, *Nat. Commun.*, 2020, **11**, 310.
7 A. Babayigit, H.-G. Boyen and B. Conings, *MRS Energy Sustainability*, 2018, **5**, 19.
8 L. M. Wu, X. T. Wu and L. Chen, *Coord. Chem. Rev.*, 2009, **253**, 2787.
9 N. Mercier, N. Louvain and W. Bi, *CrystEngComm*, 2009, **11**, 720.
10 S. A. Adonin, M. N. Sokolov and V. P. Fedin, *Coord. Chem. Rev.*, 2016, **312**, 1.
11 R. Mohan, *Nat. Chem.*, 2010, **2**, 336.
12 S. Rühle, *Sol. Energy*, 2016, **130**, 139.
13 Z. Jin, Z. Zhang, J. Xiu, H. Song, T. Gatti and Z. He, *J. Mater. Chem. A*, 2020, **8**, 16166.
14 N. R. Wolf, B. A. Connor, A. H. Slavney and H. I. Karunadasa, *Angew. Chem.*, 2021, **60**, 16264.
15 G. Volonakis, M. R. Filip, A. A. Haghighirad, N. Sakai, B. Wenger, H. J. Snaith and F. Giustino, *J. Phys. Chem. Lett.*, 2016, **7**, 1254.
16 A. H. Slavney, T. Hu, A. M. Lindenberg and H. I. Karunadasa, *J. Am. Chem. Soc.*, 2016, **138**, 2138.
17 E. T. McClure, M. R. Ball, W. Windl and P. M. Woodward, *Chem. Mater.*, 2016, **28**, 1348.
18 Y.-J. Li, T. Wu, L. Sun, R.-X. Yang, L. Jiang, P.-F. Cheng, Q.-Q. Hao, T.-J. Wang, R.-F. Lu and W.-Q. Deng, *RSC Adv.*, 2017, **7**, 35175.
19 X.-F. Cheng, W.-H. Qian, J. Wang, C. Yu, J.-H. He, H. Li, Q.-F. Xu, D.-Y. Chen, N.-J. Li and J.-M. Lu, *Small*, 2019, **15**, e1905731.
20 Y. Zhang, T. Shah, F. L. Deepak and B. A. Korgel, *Chem. Mater.*, 2019, **31**, 7962.
21 Z. Xu, X. Liu, Y. Li, X. Liu, T. Yang, C. Ji, S. Han, Y. Xu, J. Luo and Z. Sun, *Angew. Chem., Int. Ed.*, 2019, **58**, 15757.
22 A. D. Wright, L. R. V. Buizza, K. J. Savill, G. Longo, H. J. Snaith, M. B. Johnston and L. M. Herz, *J. Phys. Chem. Lett.*, 2021, **12**, 3352.
23 G. Longo, S. Mahesh, L. R. V. Buizza, A. D. Wright, A. J. Ramadan, M. Abdi-Jalebi, P. K. Nayak, L. M. Herz and H. J. Snaith, *ACS Energy Lett.*, 2020, **5**, 2200.
24 G. Longo, S. Mahesh, L. R. V. Buizza, A. D. Wright, A. J. Ramadan, M. Abdi-Jalebi, P. K. Nayak, L. M. Herz and H. J. Snaith, *ACS Energy Lett.*, 2020, **5**, 2200.
25 N. Dehnhardt, H. Borkowski, J. Schepp, R. Tonner and J. Heine, *Inorg. Chem.*, 2018, **57**, 633.
26 J. Möbs and J. Heine, *Inorg. Chem.*, 2019, **58**, 6175.
27 L.-Y. Bi, T. Hu, M.-Q. Li, B.-K. Ling, M. S. Lassoued, Y.-Q. Hu, Z. Wu, G. Zhou and Y.-Z. Zheng, *J. Mater. Chem. A*, 2020, **8**, 7288.
28 W.-X. Chai, L.-M. Wu, J.-Q. Li and L. Chen, *Inorg. Chem.*, 2007, **46**, 8698.
29 A. W. Kelly, A. M. Wheaton, A. D. Nicholas, F. H. Barnes, H. H. Patterson and R. D. Pike, *Eur. J. Inorg. Chem.*, 2017, 4990.
30 N. Dehnhardt, P. Klement, S. Chatterjee and J. Heine, *Inorg. Chem.*, 2019, **58**, 10983.
31 N. Dehnhardt, H. Paneth, N. Hecht and J. Heine, *Inorg. Chem.*, 2020, **59**, 3394.
32 J. Möbs, M. Gerhard and J. Heine, *Dalton Trans.*, 2020, **49**, 14397.
33 Y. Cai, A. M. Chippindale, R. J. Curry and P. Vaqueiro, *Inorg. Chem.*, 2021, **60**, 5333.
34 H. Sommer, A. Eichhöfer and D. Fenske, *Z. Anorg. Allg. Chem.*, 2009, **635**, 1997.
35 J. A. Bilbrey, A. H. Kazez, J. Locklin and W. D. Allen, *J. Comput. Chem.*, 2013, **34**, 1189.
36 G. A. Bowmaker, J. V. Hanna, R. D. Hart, P. C. Healy and A. H. White, *Aust. J. Chem.*, 1994, **47**, 25.
37 F. B. Alhanash, N. A. Barnes, S. M. Godfrey, P. A. Hurst, A. Hutchinson, R. Z. Khan and R. G. Pritchard, *Dalton Trans.*, 2012, **41**, 7708.
38 A. M. Borys and E. R. Clark, *Inorg. Chem.*, 2017, **56**, 4623.
39 J. L. Brown, C. C. Mokhtarzadeh, J. M. Lever, G. Wu and T. W. Hayton, *Inorg. Chem.*, 2011, **50**, 5105.
40 I. Dance and M. Scudder, *CrystEngComm*, 2009, **11**, 2233.
41 B. Borgsen, F. Weller and K. Dehnicke, *Z. Anorg. Allg. Chem.*, 1991, **596**, 55.
42 N. Dehnhardt, A. Böth and J. Heine, *Dalton Trans.*, 2019, **48**, 5222.
43 J. Möbs and J. Heine, *CSD Communication, CCDC 1986611*, 2020.
44 I. Lahbib, A. Valkonen, M. Rzaigui and W. Smirani, *J. Cluster Sci.*, 2017, **28**, 2239.
45 B. Jaschinski, R. Blachnik and H. Reuter, *Z. Anorg. Allg. Chem.*, 1999, **625**, 667.
46 A. J. Dennington and M. T. Weller, *Dalton Trans.*, 2018, **47**, 3469.
47 S. Pohl, D. Haase, R. Lotz and W. Saak, *Z. Naturforsch., B: J. Chem. Sci.*, 1988, **43**, 1033.
48 S. Pohl, M. Peters, D. Haase and W. Saak, *Z. Naturforsch., B: J. Chem. Sci.*, 1994, **49**, 741.
49 S. Alvarez, *Dalton Trans.*, 2013, **42**, 8617.
50 V. V. Sharutin, I. V. Egorova, N. N. Klepikov, E. A. Boyarkina and O. K. Sharutina, *Russ. J. Coord. Chem.*, 2009, **35**, 186.
51 K. M. McCall, C. C. Stoumpos, S. S. Kostina, M. G. Kanatzidis and B. W. Wessels, *Chem. Mater.*, 2017, **29**, 4129.
52 L.-Y. Bi, Y.-Q. Hu, M.-Q. Li, T.-L. Hu, H.-L. Zhang, X.-T. Yin, W.-X. Que, M. S. Lassoued and Y.-Z. Zheng, *J. Mater. Chem. A*, 2019, **131**, 19662.
53 P. Cheng, T. Wu, Y. Li, L. Jiang, W. Deng and K. Han, *New J. Chem.*, 2017, **41**, 9598.
54 J. G. Brandenburg, C. Bannwarth, A. Hansen and S. Grimme, *J. Chem. Phys.*, 2018, **148**, 064104.
55 J. P. Perdew, *Phys. Rev. B: Condens. Matter Mater. Phys.*, 1986, **33**, 8822(R).
56 J. P. Perdew, K. Burke and M. Ernzerhof, *Phys. Rev. Lett.*, 1996, **77**, 3865.
57 S. Ehrlich, J. Moellmann, W. Reckien, T. Bredow and S. Grimme, *ChemPhysChem*, 2011, **12**, 3414.

58 S. Grimme, S. Ehrlich and L. Goerigk, *J. Comput. Chem.*, 2011, **32**, 1456.
59 Q. Teng and H. V. Huynh, *Dalton Trans.*, 2017, **46**, 614.
60 G. Brauer, *Handbuch der Präparativen Anorganischen Chemie*, Ferdinand Enke Verlag, Stuttgart, 3rd edn, 1975, vol. 1, pp 591–592.
61 G. Brauer, *Handbuch der Präparativen Anorganischen Chemie*, Ferdinand Enke Verlag, Stuttgart, 3rd edn, 1975, vol. 1, p. 600.
62 G. M. Sheldrick, *Acta Crystallogr., Sect. A: Found. Crystallogr.*, 2008, **64**, 112.
63 G. M. Sheldrick, *Acta Crystallogr., Sect. A: Found. Adv.*, 2015, **71**, 3.
64 G. M. Sheldrick, *Acta Crystallogr., Sect. C: Struct. Chem.*, 2015, **71**, 3.
65 O. V. Dolomanov, L. J. Bourhis, R. J. Gildea, J. A. K. Howard and H. Puschmann, *J. Appl. Crystallogr.*, 2009, **42**, 339.
66 K. Brandenburg, *Diamond*, Crystal Impact GbR, Bonn, Germany, 2005.
67 F. Furche, R. Ahlrichs, C. Hättig, W. Klopper, M. Sierka and F. Weigend, *Wiley Interdiscip. Rev.: Comput. Mol. Sci.*, 2013, **4**, 91.
68 F. Weigend and R. Ahlrichs, *Phys. Chem. Chem. Phys.*, 2005, **7**, 3297.
69 K. Eichkorn, F. Weigend, O. Treutler and R. Ahlrichs, *Theor. Chem. Acc.*, 1997, **97**, 119.
70 F. Neese, *Wiley Interdiscip. Rev.: Comput. Mol. Sci.*, 2018, **8**, e1327.
71 C. van Wüllen, *J. Chem. Phys.*, 1998, **109**, 392.

3.3 $[SMe_3]_2[Bi_2Ag_2I_{10}]$, a silver iodido bismuthate with an unusually small band gap

Jakob Möbs, Sudip Pan, Ralf Tonner-Zech and Johanna Heine, *Dalton Transactions*, **2022**, *51*, 13771–13778, DOI:10.1039/d2dt02305a.

Abstract

Iodido metalates of heavy main group elements have seen much research interest in the last years due to their possible application as absorbers in photovoltaics. However, for materials based on the non-toxic element bismuth, one challenge lies in narrowing the optical band gap for sufficient solar absorption. Here, we present a new iodido silver bismuthate, $[SMe_3]_2[Bi_2Ag_2I_{10}]$ (**1**), which is prepared from solution and characterized regarding its structure, thermal stability and optical absorption. While compounds with similar anion compositions are known, the band gap of 1.82 eV is the smallest in chain-like Bi/Ag/I-compounds that has been reported to date. To support our experimental findings we carried out computational investigations and were able to reproduce the surprisingly narrow band gap, highlighting the subtle influence of the connectivity of different building units in multinary bismuthates. We also prepared and characterized the simple iodido pentelates $[SMe]_3[E_2I_9]$ (E = Bi, Sb; **2**, **3**) to provide a point of comparison.

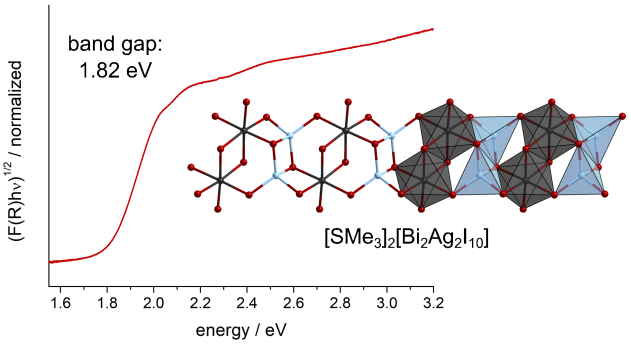

Figure 3.3: Table-of-contents graphic of "$[SMe_3]_2[Bi_2Ag_2I_{10}]$, a silver iodido bismuthate with an unusually small band gap".

Summary

The preparation and properties of a new iodido silver bismuthate, $[SMe_3]_2[Bi_2Ag_2I_{10}]$ (**1**), as well as two homometallic iodido group 15 metalates, $[SMe]_3[E_2I_9]$ (E = Bi (**2**), Sb (**3**)) all featuring the same $[SMe_3]^+$-cation are reported and an overview over all literature known Ag/Bi/I complexes aside elpasolite derivatives is given.

All three compounds are easily synthesized from acetonitrile solutions of the binary metal iodides and trimethyl sulfonium iodide. **1** has a one-dimensional anionic motif made up of $\{Bi_2I_{10}\}$- and $\{Ag_2I_6\}$-subunits of edge-sharing octahedra and tetrahedra, respectively. These subunits are connected *via* shared edges and corners into chains that are very similar to the literature

known anionic motifs of $[NEt_4]_2[Bi_2Ag_2I_{10}]$ and $[1,3,5-Me_3py]_2[Bi_2Ag_2I_{10}]$ with the same nominal composition but still distinctly different. The optical band gap of **1** is significantly smaller than those of the literature compounds, which is surprising given the closely related crystal structures. Furthermore, it is even slightly smaller than the band gaps found for 2d-elpasolites, which also is unexpected, as higher dimensional systems generally lead to smaller band gaps. The optical properties of **2** and **3** on the other hand are well in line with what is generally found for homometallic metalates featuring small, discrete anions. All three compounds are thermally robust and only start to decompose around 200 °C.
To further understand the findings concerning the optical band gap of **1**, computational investigations of the electronic structures of **1** as well as $[NEt_4]_2[Bi_2Ag_2I_{10}]$ for comparison were carried out. No qualitative differences concerning the orbital contributions to the band edges were found. In both cases, the valence band is mostly made up of Ag and I orbitals, while the conduction band comprises Bi and I orbitals. However, in **1**, the charges are more delocalized than in $[NEt_4]_2[Bi_2Ag_2I_{10}]$, which leads to a decrease of the band gap similar to large aromatic systems.

Own contribution

All syntheses were planned by myself and executed by myself, Alena Shlyaykher or Chantsalmaa Berthold under my supervision. Crystallographic measurements, solutions and refinements as well as UV-Vis measurements were done by myself. Thermo-gravimetric measurements were done by Uwe Justus. Computational investigations were carried out by Sudip Pan and Ralf Tonner-Zech. The manuscript was written through contributions of Johanna Heine, Sudip Pan, Ralf Tonner-Zech and myself.

Dalton Transactions

ROYAL SOCIETY OF CHEMISTRY

PAPER

View Article Online
View Journal | View Issue

Cite this: *Dalton Trans.*, 2022, **51**, 13771

$[SMe_3]_2[Bi_2Ag_2I_{10}]$, a silver iodido bismuthate with an unusually small band gap†

Jakob Möbs, [a] Sudip Pan, [b] Ralf Tonner-Zech [b] and Johanna Heine *[a]

Received 15th July 2022,
Accepted 23rd August 2022

DOI: 10.1039/d2dt02305a

rsc.li/dalton

Iodido metalates of heavy main group elements have seen much research interest in the last years due to their possible application as absorbers in photovoltaics. However, for materials based on the non-toxic element bismuth one challenge lies in narrowing the optical band gap for sufficient solar absorption. Here, we present a new iodido silver bismuthate, $[SMe_3]_2[Bi_2Ag_2I_{10}]$ (**1**), which is prepared from solution and characterized regarding its structure, thermal stability and optical absorption. While compounds with similar anion compositions are known, the band gap of 1.82 eV is the smallest in chain-like Bi/Ag/I-compounds that has been reported to date. To support our experimental findings we carried out computational investigations and were able to reproduce the surprisingly narrow band gap, highlighting the subtle influence of the connectivity of different building units in multinary bismuthates. We also prepared and characterized the simple iodido pentelates $[SMe]_3[E_2I_9]$ (E = Bi, Sb; **2**, **3**) to provide a point of comparison.

Introduction

Main group halide metalates have seen strong research interest in the last decade as their semiconductor properties make them suitable for a wide range of applications from photovoltaics and LEDs to X-ray detectors and photocatalysis.[1] The starting point for this interest and still one of the most prominent of these compounds is the lead halide perovskite $CH_3NH_3PbI_3$ (MAPI). With optimized versions of this material record efficiencies of 25.5% were achieved in single-junction solar cells, which nearly matches the performance of the best crystalline silicon based cell,[2] while being cheaper and easier to fabricate.[3] Despite this success, the toxicity of lead[4] in combination with the low stability of $CH_3NH_3PbI_3$ against temperature and moisture[5] remains a serious issue and has led researchers to look beyond Pb toward other heavy main group metals. An obvious choice when trying to substitute lead is its neighbor bismuth as it shows a similar chemistry in its halide compounds[6] and an overall low toxicity.[7] The changed charge of the most stable oxidation state of bismuth compared to lead, however, prevents direct substitution and the formation of the favorable perovskite motif.[8] Efficiencies of photovoltaic cells based on halide bismuthates have remained low due to mostly large and indirect band gaps.[3]

To address this, the electronic structure and optical properties of halide bismuthates can be altered by the introduction of heterometals. In case of monovalent metals like silver, this also allows for the formation of the elpasolite motif, A_2BiMX_6 (A = monovalent organic or inorganic cation, M = monovalent metal, X = Cl, Br, I), which is a superstructure of perovskite, where one half of the bivalent Pb^{2+} is substituted by a monovalent and the other half by a trivalent metal.[9] These compounds, especially $Cs_2BiAgBr_6$, have also been intensely investigated recently and show promising properties for various semiconductor applications in bulk form as well as thin films and nanocrystals.[10] However, overall quite large optical band gaps of around or above 2 eV and short electron diffusion length in $Cs_2BiAgBr_6$, have so far prevented high efficiencies in photovoltaic applications.[11,12] As the trends for other halogenido plumbates and bismuthates show, the band gap should narrow with the transition from chlorido and bromido to iodido compounds.[13–15] Unfortunately though, the corresponding Cs_2BiAgI_6 proved to be unstable and so far could only be synthesized in nanocrystalline form.[16] Instead the related compound Cu_2BiAgI_6 could recently be obtained. It does not feature the elpasolite structure, but 2D layers of edge-sharing BiI_6 and AgI_6 octahedra with a disorder of bismuth and silver atoms.[17] While the band gap of 2.06 eV is still too large for application in single-junction solar cells, its overall optical properties make it a promising candidate for hetero-

[a]*Department of Chemistry and Material Sciences Center, Philipps-Universität Marburg, Hans-Meerwein-Straße 4, 35043 Marburg, Germany. E-mail: johanna.heine@chemie.uni-marburg.de*
[b]*Wilhelm-Ostwald-Institut für Physikalische und Theoretische Chemie, Fakultät für Chemie und Mineralogie, Universität Leipzig, Linnéstraße 2, 04103 Leipzig, Germany*

†Electronic supplementary information (ESI) available: Additional crystallographic details, thermal analysis, optical properties, powder patterns, details of the computational investigations, cif-files. CCDC 2182488–2182491. For ESI and crystallographic data in CIF or other electronic format see DOI: https://doi.org/10.1039/d2dt02305a

junction cells.[17,18] Furthermore, a number of iodido silver bismuthates with crystal structures that feature 2D cut-outs of the elpasolite motif spaced apart by layers of organic cations have been reported.[19,20] These 2D elpasolites show band gaps as small as 1.86 eV.[21] But aside from these elpasolite derivatives only nine iodido silver bismuthates with an anion dimensionality of two or lower are recorded in the Cambridge Structural database,[22] including two overall neutral complexes. These compounds feature optical band gaps between 1.93 eV and 2.29 eV.[14,15,23–25] Fig. 1 gives an overview of their structural motifs.

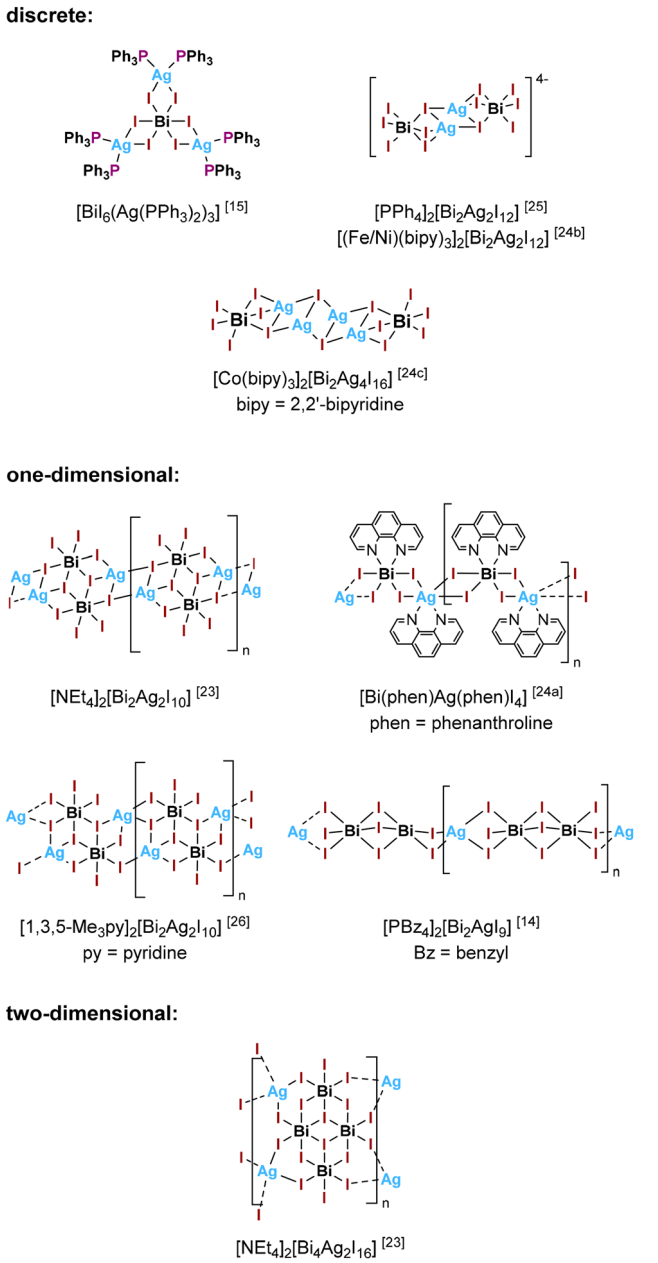

Fig. 1 Overview of the structural motifs of literature-known Bi–Ag–I complexes. Note that the disorder of silver atoms in [1,3,5-$Me_3py]_2[Bi_2Ag_2I_{10}]$[26] is not shown.

Here, we present a new silver iodido bismuthate, $[SMe_3]_2[Bi_2Ag_2I_{10}]$ (**1**), that features a one-dimensional ternary anion. We used the trimethyl sulfonium cation $[SMe_3]^+$, which has been shown to template halogenido metalates with unusual anion motifs, like $[SMe_3][SbCl_4]$, the singular example of a halogenido pentelate with a three-dimensional anion structure,[27] and useful properties, like $[SMe_3][PbI_3]$, an air-stable hexagonal perovskite[28] and $[SMe_3]_4[Pb_3Br_{10}]$, a layered bromido plumbate with a broad red emission.[29] The anion motif in **1** is deceptively similar to the ones found in $[NEt_4]_2[Bi_2Ag_2I_{10}]$ by Chen[23] and $[1,3,5\text{-}Me_3py]_2[Bi_2Ag_2I_{10}]$ by Adonin,[26] however **1** features a band gap of 1.82 eV, much smaller than those found in these previously reported chain-like silver iodido bismuthates. We have also newly prepared the simple iodido pentelates $[SMe]_3[E_2I_9]$ (E = Bi, Sb; **2**, **3**), which serve as a point of comparison.

Experimental

General

BiI_3 and SbI_3, were synthesized from the elements according to literature procedures.[30] AgI and SMe_3I were used as supplied from commercial sources. Solvents were flash distilled prior to use. BiI_3 and SbI_3 were stored under inert conditions. Reactions with AgI were carried out under exclusion of light. The dried products are air-stable.

CHN/S analysis was carried out on an Elementar CHN/S analyser. Thermal analysis was carried out by simultaneous DTA/TG on a NETZSCH STA 409 C/CD in the temperature range of 25–1000 °C with a heating rate of 10 °C min^{-1} in a constant flow of 80 mL min^{-1} N_2. IR spectra were measured on a Bruker Tensor 37 FT-IR spectrometer equipped with an ATR platinum measuring unit. Optical absorption spectra were recorded on a Varian Cary 5000 UV/vis/NIR spectrometer in the range of 300–800 nm in diffuse reflectance mode employing a Praying Mantis accessory (Harrick). The raw data was transformed from reflectance R to absorption according to the Kubelka–Munk function $F(R)$ and then plotted as a Tauc-plot assuming an indirect allowed transition (see ESI† for details).

Synthesis

$[SMe_3]_2[Bi_2Ag_2I_{10}]$ (1). A total of 118 mg of BiI_3 (0.2 mmol, 2 eq.), 23 mg of AgI (0.1 mmol, 1 eq.) and 41 mg of $SMeI_3$ (0.2 mmol, 2 eq.) were suspended in 10 mL of MeCN and heated to 95 °C for 30 min under reflux cooling resulting in a red solution with a yellow precipitate, which could be identified as AgI *via* powder diffraction. While still hot, the solution was filtered through a paper filter and left for crystallization at room temperature. After one day the cover of the crystallization vial was pricked with a needle to allow for slow evaporation of the solvent. After one week reddish black needles of **1** had formed, accompanied by a small number of orange blocks of **2** which were easily separated. Yield: 7 mg (7% with regard to the limiting factor of AgI). CHN/S (calculated): C 3.71 (3.50), H 0.896 (0.88), S 2.88 (3.13).

$[SMe_3]_3[Bi_2I_9]$ (2). A total of 59 mg of BiI_3 (0.1 mmol, 1 eq.) and 31 mg of SMe_3I (0.15 mmol, 1.5 eq.) were suspended in 5 mL of MeCN and heated to 95 °C under reflux cooling. After 30 min an orange precipitate of **2** formed, which was collected and washed twice 3 mL of methanol as well as twice with 3 mL of *n*-pentane. Yield: 61 mg (68%). CHN/S (calculated): C 6.30 (6.03) H 1.582 (1.52) S 5.08 (5.37). Single crystals suitable for X-ray diffraction were grown from filtered reaction solution over the course of two days.

$[SMe_3]_3[Sb_2I_9]$ (3). A total of 100 mg of SbI_3 (0.2 mmol, 1 eq.) and 60 mg of SMe_3I (0.3 mmol, 1.5 eq.) were suspended in 10 mL of acetone and heated to 65 °C. After 30 min an orange precipitate of **3** formed, which was collected and washed twice 3 mL of methanol as well as twice with 3 mL of *n*-pentane. Yield: 133 mg (83%). CHN/S (calculated): C 6.85 (6.68), H 1.696 (1.68), S 5.69 (5.95).

Single crystals suitable for X-ray diffraction were initially grown from a solution of 50 mg SbI_3 (0.1 mmol, 1 eq.), 12 mg AgI (0.05 mmol, 0.5 eq.) and 20 mg SMe_3I (0.1 mmol. 1 eq.) in 10 ml of aqueous hydroiodic acid (c = 2 mol L^{-1}).

X-ray crystallography

Single crystal X-ray determination was performed on a STOE IPDS2 diffractometer equipped with an imaging plate detector system using MoKα radiation with graphite monochromatization or a STOE StadiVari diffractometer using CuKα radiation from an X-ray micro source with X-ray optics and a Pilatus 300 K Si hybrid pixel array detector. The structures were solved using direct methods, refined by full matrix least-squares techniques, and expanded using Fourier techniques, using the ShelX software package[31] within the OLEX2 suite.[32] All non-hydrogen atoms were refined anisotropically unless otherwise indicated. Hydrogen atoms were assigned to idealized geometric positions and included in structure factors calculations. Pictures of the crystal structures were created using DIAMOND.[33] Additional details on individual refinements are reported in the ESI.† The data for compounds **1**, **2** and **3** were deposited as CCDC 2182488–2182491.† Powder patterns were recorded on a STADI MP (STOE Darmstadt) powder diffractometer, with $CuK_{\alpha1}$ radiation with λ = 1.54056 Å at room temperature in transmission mode. Rietveld refinement was carried out using TOPAS-Academic Version 7.[34] Details on individual refinements are given in the ESI.†

Results and discussion

Synthesis

The only reliable method to produce compound **1** proved to be the one described in the Synthesis section. Although trying various stoichiometric ratios and different solvents such as acetone, 1,2-dimethoxyethane, butanone, dimethylformamide and hydroiodic acid to improve the yield of the reaction and the purity of the product we always observed the formation of **2** as the main product alongside unreacted AgI.

In addition we also tried to prepare the corresponding silver-antimony compound, but only observed the formation of **3**.

X-Ray crystallography

1 crystallizes in the monoclinic crystal system in the space group $P2_1/n$ with Z = 2. An excerpt of the crystal structure is shown in Fig. 2. **1** features chain-like $[Bi_2Ag_2I_{10}]^{2-}$-anions oriented in the direction of the *a*-axis and disordered $[SMe_3]^+$-cations. The anionic chains are built from pairs of edge-sharing BiI_6-octahedra forming Bi_2I_{10} sub-units, which are connected into chains by pairs of silver atoms. The silver atoms themselves feature a tetrahedral coordination sphere, which is typical for silver halide complexes. The space in-between the anionic chains is occupied by $[SMe_3]^+$-cations that show a disorder of the sulfur atom over two positions which are occupied with 72.5(12)% and 27.5(12)%.

A very similar anion motif with the same sum formula has already been described by Chen and co-workers.[23] However, this compound features a $[NEt_4]^+$-cation and a different connectivity of the anionic chain. There, the Bi–I–Bi-bridging iodide ligands take part in the coordination of the silver atoms, enforcing additional edge-sharing between BiI_6 and AgI_4 polyhedra, while this is not the case with our compound (see Fig. 3). The interatomic distances of the two compounds are well in line with each other, with Bi–I bond lengths ranging from 2.92 Å to 3.32 Å in **1** and, with a larger range,

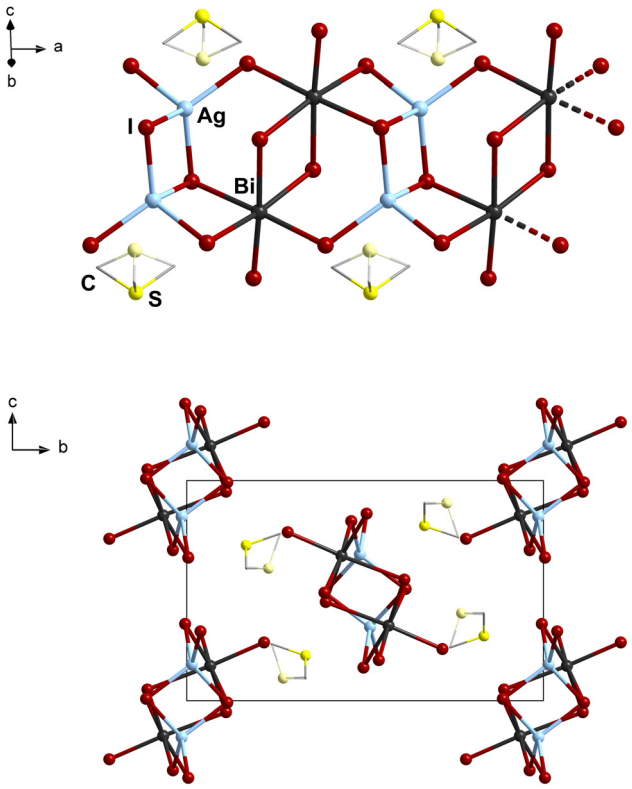

Fig. 2 Excerpt of the crystal structure of **1** (top). Unit cell of **1** (bottom). Lesser occupied positions of disordered sulfur atoms are shown in lighter colors. Hydrogen atoms are omitted for clarity.

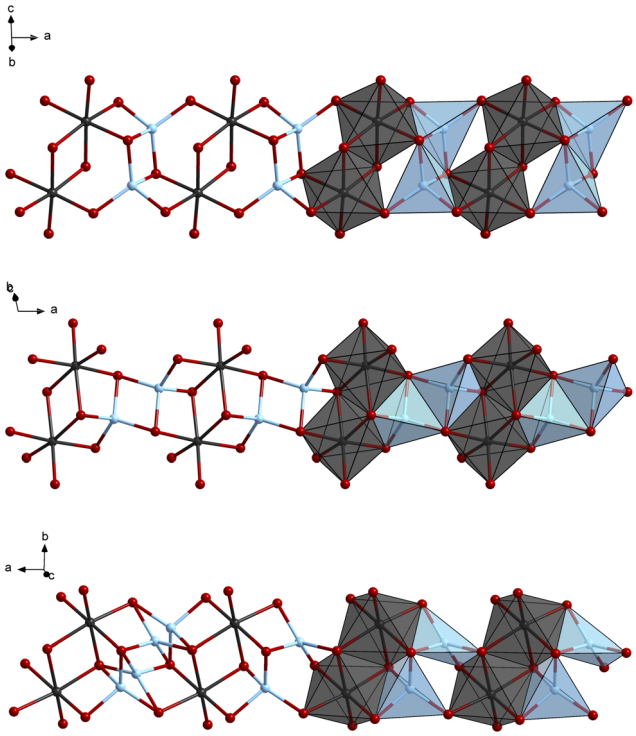

Fig. 3 Comparison of the anionic motifs of **1** (top), $[NEt_4]_2[Bi_2Ag_2I_{10}]$ by Chen and co-workers (center)[23] and $[1,3,5\text{-}Me_3py]_2[Bi_2Ag_2I_{10}]$ by Adonin and co-workers (bottom, only for the leftmost of the repeating units all silver positions are shown).[26]

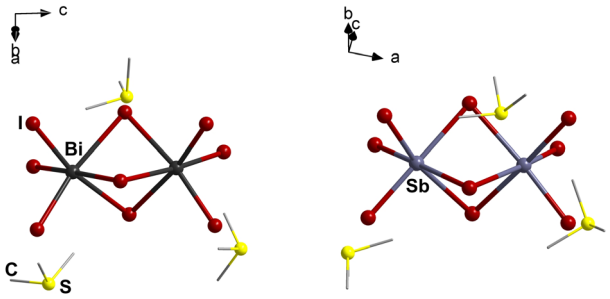

Fig. 4 Excerpts of the crystal structures of **2** (left) and **3** (right). Lesser occupied positions of disordered sulfur atoms as well as hydrogen atoms are omitted for clarity.

from 2.87 to 3.42 Å in the literature compound. Ag–I bond lengths of 2.82 to 2.91 Å and 2.83 to 2.92 Å, respectively, are found in **1** and in $[NEt_4]_2[Bi_2Ag_2I_{10}]$. Secondary bonding interactions show more distinct differences between the two compounds: In the crystal structure of $[NEt_4]_2[Bi_2Ag_2I_{10}]$, argentophilic Ag···Ag (3.32 Å) contacts[35] and I···I (3.85 Å) interactions below the sum of the van der Waals radii are observed,[36] which are absent in **1**. In addition to **1** and $[NEt_4]_2[Bi_2Ag_2I_{10}]$ yet another compound with the nominal anionic formula $[Bi_2Ag_2I_{10}]^{2-}$ has been reported by Adonin and co-workers. It features a $[1,3,5\text{-}Me_3py]^+$-cation and in contrast to the other two compounds the silver atoms are disordered over two equally occupied positions. The Bi–I and Ag–I distances are generally in a similar range but because of the disorder we did not analyze them in detail.

2 crystallizes in the monoclinic crystal system in the space group *C*2/*c* with $Z = 16$. It features the well-known $[Bi_2I_9]^{3-}$-anion which is composed of two face-sharing BiI_6-octaherda and was first described by Chabot *et al.* in 1978 in $Cs_3[Bi_2I_9]$.[37] An excerpt of the crystal structure is shown in Fig. 4. Bi–I distances range from 2.95 Å to 3.35 Å, which is well in line with what is generally found in iodido bismuthates.[38] The $[SMe_3]^+$-cations suffer from a similar disorder as in **1** (see ESI† for details). At room temperature **3** is isostructural to **2** (see ESI† for details). However, when cooled down to 100 K it undergoes a transition to a phase of lower symmetry with the space group *Cc*, which is one of the maximal non-isomorphic subgroups of *C*2/*c*. Additionally, the unit cell of the low temperature phase is only a quarter the size of the room temperature phase's one with two of the axis being cut in half. An excerpt of the crystal structure at 100 K is shown in Fig. 4. Despite the room temperature phase of **3** showing a similar disorder of the $(SMe_3)^+$-cations as **1** and **2** no disorder is observed at 100 K. This phenomenon is also found in the closely related $[SMe_3]_3[Bi_2Br_9]$, although no accompanying phase transition is observed here.[39] Like its bismuth counterpart, the $[Sb_2I_9]^{3-}$ anion is well known throughout the literature and was also first described by Chabot *et al.* in 1978 in $Cs_3[Sb_2I_9]$.[37] The Sb–I distances of 2.87 Å to 3.29 Å at room temperature are well in line with the distances reported there. At 100 K these range from 2.82 Å to 3.42 Å with two quite long contacts between antimony and the μ-bridging iodide ligands of 3.38 Å and 3.42 Å, which are longer than what is typically observed.[40] However, in chlorido antimonates with $[Sb_2Cl_9]^{3-}$ anions similar distortions of the Sb–Cl bond lengths have been reported.[41] Also, $[SMe_3]^+$-cations, as well as the closely related $[NMe_4]^+$-cations are somewhat prone to producing halogenido metalate compounds that feature solid–solid phase transitions, as a number of literature examples show.[28,42]

Thermal analysis

Combined TGA-DSC measurements were carried out for all three compounds. **1** and **2** show a first mass loss of 19.4% and 34.9%, respectively, between 195 °C and 275 °C. This corresponds to the loss of two (**1**) and three (**2**) formula units of SMe_3I (19.8% and 34.2% theoretically). Directly afterwards between 275 °C and 460 °C a second mass loss of 56.9% (**1**) and 65.1% (**2**) is observed which corresponds to the sublimation of BiI_3 (57.3% and 65.8% theoretically). In case of **2** this means the complete decomposition of the product, while for **1** only AgI is left, that slowly decomposes further up to around 940 °C. At this point a final mass 9.3% of the starting material is left which fits the overall share of silver in the compound (10.5% theoretically).

The decomposition of **3** is very similar to the one of **2** with the difference that the two decomposition steps overlap each other and become indistinguishable, due to the lower sublima-

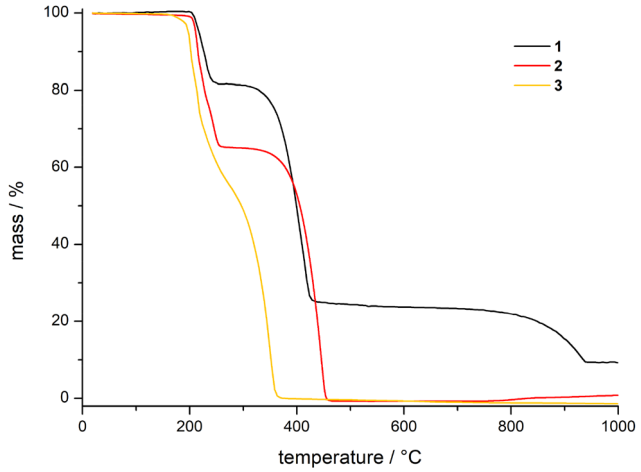

Fig. 5 Thermal decomposition diagrams of **1**, **2** and **3**.

tion temperature of SbI_3. TGA diagrams of **1**, **2** and **3** are shown in Fig. 5. Additional data including the DSC measurements can be found in the ESI.†

UV-Vis spectroscopy

UV-Vis-absorption spectra were obtained for all three compounds. Tauc plots of these measurements are shown in Fig. 6. The optical band gaps of **2** and **3** are estimated from the Tauc-plots to be 2.10 eV and 2.27 eV, respectively, when assuming an indirect allowed transition. This fits well into the ranges that are typically found for iodido antimonates and bismuthates.[43]

1 on the other hand has an optical band gap of 1.82 eV, which is similar to those found in 2D elpasolites, such as $[(3AMPY)_2AgBiI_8{\cdot}H_2O]$ (3AMPY = 3-(aminomethyl) pyridinium)[21] and $(4FPEA)_4AgBiI_8$ (4FPEA = 4-fluorophenethylammonium)[44] with optical band gaps of 1.86 eV and 1.84 eV,

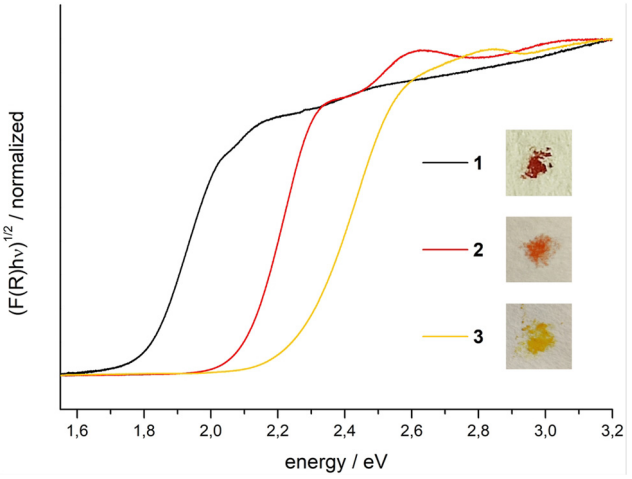

Fig. 6 Tauc-plots from diffuse reflection UV-Vis data of **1**, **2** and **3**. Photographs of corresponding powders smoothed out over filter paper are shown as insets.

respectively. Importantly, the band gap is significantly smaller than the 2.05 eV and 1.92 eV reported for the aforementioned and structurally very similar $[NEt_4]_2[Bi_2Ag_2I_{10}]$[23] and $[1,3,5\text{-}Me_3py]_2[Bi_2Ag_2I_{10}]$,[26] respectively. Generally, structure–property relationships in halogenido pentelates and copper and silver halogenido pentelates are an area of ongoing investigations. Several broad trends are well established. As predicted by the dimensional reduction approach, halogenido pentelates with the same E/X composition will show smaller band gaps upon an increase in anion size and dimensionality.[45] Also, band gaps will decrease within the series Cl → Br → I and antimony compounds will typically display larger band gaps than isostructural bismuth compounds.[46] With regard to copper and silver halogenido pentelates it has been established that while copper significantly contributes states that narrow the band gap, silver does not,[25] a phenomenon that has been described as a difference in structural and electronic dimensionality in double perovskites like $Cs_2AgBiBr_6$ and related compounds.[11,20,47] Judging from these findings, one might assume that $[NEt_4]_2[Bi_2Ag_2I_{10}]$[23] and **1** should have very similar band gaps, as the Bi–I units in each case are the same and the compounds differ only in the connectivity of the silver atoms.

Computational investigations

The puzzling finding of rather strong changes in the band gap upon mere change in the connectivity led us to investigate the electronic structures of the two solids **1** and $[NEt_4]_2[Bi_2Ag_2I_{10}]$ using density functional theory (DFT). We used periodic boundary conditions to account for the translational symmetry of the crystals. Based on our previous experience with similar compounds,[25] we derived a computationally optimized unit cell of **1** starting from the experimental structures with the PBE functional using DFT-D3 dispersion correction in combination with Becke–Johnson (BJ) type damping functions.[48] The resulting structure is in very good agreement with experiment (error in unit cell volume *ca.* 1.3%, see Table S5 in the ESI† for details). We applied the same procedure to the literature-known compound $[NEt_4]_2[Bi_2Ag_2I_{10}]$ achieving similar accuracy (see Table S6†). This agreement in atomic structure lends confidence to the investigation of the electronic structure on the same level of approximation. Although, PBE is notoriously known to underestimate band gaps for elemental and compound semiconductors, it performs much better for ionic compounds.[25] More crucial for an accurate representation of the electronic structure and band gap is the incorporation of spin–orbit coupling (SOC) effects if heavy atoms like Bi are involved.[25]

We thus computed the density of states (DOS) for **1** (Fig. 7) and $[NEt_4]_2[Bi_2Ag_2I_{10}]$ (Fig. S14†). Band structure calculations showed that we find an indirect band gap while the conduction band is slightly (<0.1 eV) higher in energy at the Γ-point compared to the Y and Z points in *k*-space for both compounds. Since we can assume that the transition probability for the direct transition is much higher, we only focus on the difference between valence and conduction band energy as given by the DOS plot. We find a band gap of 1.6 eV for **1**,

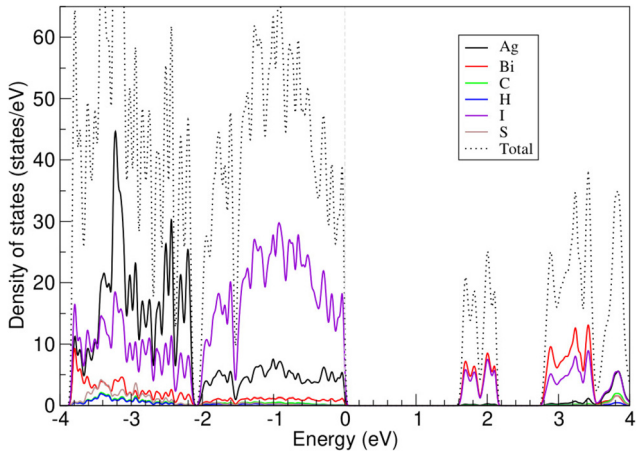

Fig. 7 Density of states (DOS) for **1** computed at PBE-D3(BJ)/SOC. Shown is the total DOS (dotted line) and the contributions from the elements contained (solid lines). The (indirect) band gap is 1.6 eV.

while 1.8 eV is found for $[NEt_4]_2[Bi_2Ag_2I_{10}]$. Although the absolute values are slightly smaller, the trend is in line with the experimental finding of **1** having a significantly smaller band gap than that of previously reported $[NEt_4]_2[Bi_2Ag_2I_{10}]$.

The analysis of the atomic contributions to the DOS highlights the nature of the transition. The valence band is dominated by the contributions from Ag and I atoms – these states thus stem from the Ag–I bonds in the 1D chains. The conduction band on the other hand is clearly dominated by the contributions from Bi and I – thus states resulting from the Bi–I bonds. Therefore, the transition experimentally observed is very likely resulting from an excitation of electrons from the Ag–I into the Bi–I bonding states of the anionic chains. There is no qualitative difference between **1** (Fig. 7) and $[NEt_4]_2[Bi_2Ag_2I_{10}]$ (Fig. S14†) with respect to the atomic contributions to the DOS. Thus, the difference in band gap does not result from a change in nature of the valence or conduction band.

The reason for the difference in band gaps is more subtle. While analyzing the charge density of the valence and conduction bands for **1** (Fig. S15†) and $[NEt_4]_2[Bi_2Ag_2I_{10}]$ (Fig. S16†), we see a significant increase in delocalization for the newly synthesized compound **1**. As is well-known for aromatic systems (*e.g.* oligoacenes or polyacenes), an increase in delocalization leads to a decrease in band gap. Furthermore, the Bi atoms in **1** are significantly more electropositive in nature (charge from AIM analysis: 0.81 and 0.67*e*) compared to the Bi atoms in $[NEt_4]_2[Bi_2Ag_2I_{10}]$ (0.38*e*). This is indicative of a stronger ionic Bi–I interactions in **1** compared to the other complex. This will stabilize the conduction band, lowering the bandgap.

Conclusions

In summary, we show that using $[SMe_3]^+$ as a templating cation, we were able to prepare a new multinary silver iodido bismuthate with a chain-like anion. This compound features a significantly lower band gap than literature-known compounds with chain-like anions of the same composition and a novel connectivity between BiI_6 and AgI_4 units. Using computational investigations, we show that the difference in band gap does not stem from a fundamental difference in the composition of the valence and conduction band, but can be traced back to more subtle effects of delocalization and ionicity.

Conflicts of interest

There are no conflicts to declare.

Acknowledgements

We thank Chantsalmaa Berthold and Alena Shlyaykher for their help with some of the synthetic work and GOETHE-CSC Frankfurt, ZIH Dresden and HLR Stuttgart for computational resources. We also thank the German Research foundation DFG (HE 8018/1) for funding. J. H. thanks Professor Stefanie Dehnen for her support.

References

1 (*a*) A. K. Jena, A. Kulkarni and T. Miyasaka, *Chem. Rev.*, 2019, **119**, 3036–3103; (*b*) L. N. Quan, B. P. Rand, R. H. Friend, S. G. Mhaisalkar, T.-W. Lee and E. H. Sargent, *Chem. Rev.*, 2019, **119**, 7444–7477; (*c*) Y. Zhang, Y. Liu, Z. Xu, H. Ye, Z. Yang, J. You, M. Liu, Y. He, M. G. Kanatzidis and S. F. Liu, *Nat. Commun.*, 2020, **11**, 2304; (*d*) H. Huang, B. Pradhan, J. Hofkens, M. B. J. Roeffaers and J. A. Steele, *ACS Energy Lett.*, 2020, **5**, 1107–1123.

2 M. A. Green, E. D. Dunlop, J. Hohl-Ebinger, M. Yoshita, N. Kopidakis and X. Hao, *Prog. Photovoltaics*, 2022, **30**, 3–12.

3 A. M. Ganose, C. N. Savory and D. O. Scanlon, *Chem. Commun.*, 2016, **53**, 20–44.

4 (*a*) J. Li, H.-L. Cao, W.-B. Jiao, Q. Wang, M. Wei, I. Cantone, J. Lü and A. Abate, *Nat. Commun.*, 2020, **11**, 310; (*b*) A. Babayigit, H.-G. Boyen and B. Conings, *MRS Energy Sustainability*, 2018, **5**, 19.

5 Y. Han, S. Meyer, Y. Dkhissi, K. Weber, J. M. Pringle, U. Bach, L. Spiccia and Y.-B. Cheng, *J. Mater. Chem. A*, 2015, **3**, 8139–8147.

6 L. M. Wu, X. T. Wu and L. Chen, *Coord. Chem. Rev.*, 2009, **253**, 2787–2804.

7 R. Mohan, *Nat. Chem.*, 2010, **2**, 336.

8 Z. Xiao, Z. Song and Y. Yan, *Adv. Mater.*, 2019, **31**, e1803792.

9 N. R. Wolf, B. A. Connor, A. H. Slavney and H. I. Karunadasa, *Angew. Chem., Int. Ed.*, 2021, **60**, 16264–16278.

10 (*a*) E. T. McClure, M. R. Ball, W. Windl and P. M. Woodward, *Chem. Mater.*, 2016, **28**, 1348–1354; (*b*) A. H. Slavney, T. Hu, A. M. Lindenberg and H. I. Karunadasa, *J. Am. Chem. Soc.*, 2016, **138**, 2138–2141; (*c*) X.-F. Cheng, W.-H. Qian, J. Wang, C. Yu, J.-H. He, H. Li, Q.-F. Xu, D.-Y. Chen, N.-J. Li and J.-M. Lu, *Small*, 2019, **15**, e1905731; (*d*) Y. Zhang, T. Shah, F. L. Deepak and B. A. Korgel, *Chem. Mater.*, 2019, **31**, 7962–7969; (*e*) A. Schmitz, L. L. Schaberg, S. Sirotinskaya, M. Pantaler, D. C. Lupascu, N. Benson and G. Bacher, *ACS Energy Lett.*, 2020, **5**, 559–565.

11 C. N. Savory, A. Walsh and D. O. Scanlon, *ACS Energy Lett.*, 2016, **1**, 949–955 **https://pubs.acs.org/doi/pdf/10.1021/acsenergylett.6b00471**.

12 G. Longo, S. Mahesh, L. R. V. Buizza, A. D. Wright, A. J. Ramadan, M. Abdi-Jalebi, P. K. Nayak, L. M. Herz and H. J. Snaith, *ACS Energy Lett.*, 2020, **5**, 2200–2207.

13 (*a*) M. I. Saidaminov, A. L. Abdelhady, B. Murali, E. Alarousu, V. M. Burlakov, W. Peng, I. Dursun, L. Wang, Y. He, G. Maculan, A. Goriely, T. Wu, O. F. Mohammed and O. M. Bakr, *Nat. Commun.*, 2015, **6**, 7586 **https://www.nature.com/articles/ncomms8586** (*b*) K. T. Butler, J. M. Frost and A. Walsh, *Mater. Horiz.*, 2015, **2**, 228–231; (*c*) G. Volonakis, M. R. Filip, A. A. Haghighirad, N. Sakai, B. Wenger, H. J. Snaith and F. Giustino, *J. Phys. Chem. Lett.*, 2016, **7**, 1254–1259.

14 N. Dehnhardt, H. Paneth, N. Hecht and J. Heine, *Inorg. Chem.*, 2020, **59**, 3394–3405.

15 J. Möbs and J. Heine, *Inorg. Chem.*, 2019, **58**, 6175–6183.

16 B. Yang, J. Chen, S. Yang, F. Hong, L. Sun, P. Han, T. Pullerits, W. Deng and K. Han, *Angew. Chem., Int. Ed.*, 2018, **57**, 5359–5363.

17 H. C. Sansom, G. Longo, A. D. Wright, L. R. V. Buizza, S. Mahesh, B. Wenger, M. Zanella, M. Abdi-Jalebi, M. J. Pitcher, M. S. Dyer, T. D. Manning, R. H. Friend, L. M. Herz, H. J. Snaith, J. B. Claridge and M. J. Rosseinsky, *J. Am. Chem. Soc.*, 2021, **143**, 3983–3992.

18 L. R. V. Buizza, A. D. Wright, G. Longo, H. C. Sansom, C. Q. Xia, M. J. Rosseinsky, M. B. Johnston, H. J. Snaith and L. M. Herz, *ACS Energy Lett.*, 2021, **6**, 1729–1739.

19 (*a*) M. K. Jana, S. M. Janke, D. J. Dirkes, S. Dovletgeldi, C. Liu, X. Qin, K. Gundogdu, W. You, V. Blum and D. B. Mitzi, *J. Am. Chem. Soc.*, 2019, **141**, 7955–7964; (*b*) L.-Y. Bi, Y.-Q. Hu, M.-Q. Li, T.-L. Hu, H.-L. Zhang, X.-T. Yin, W.-X. Que, M. S. Lassoued and Y.-Z. Zheng, *J. Mater. Chem. A*, 2019, **131**, 19662–19667; (*c*) M. S. Lassoued, L.-Y. Bi, Z. Wu, G. Zhou and Y.-Z. Zheng, *J. Mater. Chem. C*, 2020, **8**, 5349–5354; (*d*) Y. Yao, B. Kou, Y. Peng, Z. Wu, L. Li, S. Wang, X. Zhang, X. Liu and J. Luo, *Chem. Commun.*, 2020, **56**, 3206–3209.

20 X. Li, B. Traoré, M. Kepenekian, L. Li, C. C. Stoumpos, P. Guo, J. Even, C. Katan and M. G. Kanatzidis, *Chem. Mater.*, 2021, **33**, 6206–6216.

21 D. Fu, S. Wu, Y. Liu, Y. Yao, Y. He and X.-M. Zhang, *Inorg. Chem. Front.*, 2021, **8**, 3576–3580.

22 (*a*) C. R. Groom, I. J. Bruno, M. P. Lightfoot and S. C. Ward, *Acta Crystallogr., Sect. B: Struct. Sci., Cryst. Eng. Mater.*, 2016, **72**, 171–179; (*b*) I. J. Bruno, J. C. Cole, P. R. Edgington, M. Kessler, C. F. Macrae, P. McCabe, J. Pearson and R. Taylor, *Acta Crystallogr., Sect. B: Struct. Sci.*, 2002, **58**, 389–397.

23 W.-X. Chai, L.-M. Wu, J.-Q. Li and L. Chen, *Inorg. Chem.*, 2007, **46**, 1042–1044.

24 (*a*) H. Li, J. Li, M. Wang, S. Huang, A. Gong, H. Wu and Z. Chen, *J. Coord. Chem.*, 2012, **65**, 3851–3859; (*b*) B. Zhang, J. Li, M. Pang, Y.-S. Wang, M.-Z. Liu and H.-M. Zhao, *Inorg. Chem.*, 2022, **61**, 406–413; (*c*) B. Zhang, J. Li, M. Pang, X. Chen and M.-Z. Liu, *Inorg. Chem.*, 2022, **61**, 9808–9815.

25 N. Dehnhardt, H. Borkowski, J. Schepp, R. Tonner and J. Heine, *Inorg. Chem.*, 2018, **57**, 633–640.

26 I. A. Shentseva, A. N. Usoltsev, P. A. Abramov, V. R. Shayapov, P. E. Plyusnin, I. V. Korolkov, M. N. Sokolov and S. A. Adonin, *Polyhedron*, 2022, **216**, 115720.

27 M.-L. Liu and L.-H. Kong, *Acta Crystallogr., Sect. C: Struct. Chem.*, 2014, **70**, 169–172.

28 A. Kaltzoglou, C. C. Stoumpos, A. G. Kontos, G. K. Manolis, K. Papadopoulos, K. G. Papadokostaki, V. Psycharis, C. C. Tang, Y.-K. Jung, A. Walsh, M. G. Kanatzidis and P. Falaras, *Inorg. Chem.*, 2017, **56**, 6302–6309.

29 M. D. Smith, B. L. Watson, R. H. Dauskardt and H. I. Karunadasa, *Chem. Mater.*, 2017, **29**, 7083–7087.

30 G. Brauer, *Handbuch der Präparativen Anorganischen Chemie*, Ferdinand Enke Verlag, Stuttgart, Germany, 3rd edn, 1975, vol. 1.

31 (*a*) G. M. Sheldrick, *Acta Crystallogr., Sect. A: Found. Crystallogr.*, 2008, **64**, 112–122; (*b*) G. M. Sheldrick, *Acta Crystallogr., Sect. C: Struct. Chem.*, 2015, **71**, 3–8; (*c*) G. M. Sheldrick, *Acta Crystallogr., Sect. A: Found. Adv.*, 2015, **71**, 3–8.

32 O. V. Dolomanov, L. J. Bourhis, R. J. Gildea, J. A. K. Howard and H. Puschmann, *J. Appl. Crystallogr.*, 2009, **42**, 339–341.

33 K. Brandenburg, *Diamond*, Crystal Impact GbR, Bonn, Germany, 2005.

34 A. Coelho, *TOPAS-Academic, Coelho Software*, Brisbane, Australia, 2020.

35 H. Schmidbaur and A. Schier, *Angew. Chem., Int. Ed.*, 2015, **54**, 746–784.

36 S. Alvarez, *Dalton Trans.*, 2013, **42**, 8617–8636.

37 B. Chabot and E. Parthé, *Acta Crystallogr., Sect. B: Struct. Crystallogr. Cryst. Chem.*, 1978, **34**, 645–648.

38 S. A. Adonin, M. N. Sokolov and V. P. Fedin, *Coord. Chem. Rev.*, 2016, **312**, 1–21, DOI: **10.1016/j.ccr.2015.10.010**.

39 Y.-Z. Zhang, D.-S. Sun, J.-X. Gao, X.-N. Hua, X.-G. Chen, G.-Q. Mei and W.-Q. Liao, *Chem. – Asian J.*, 2019, **14**, 1028–1033.

40 V. V. Sharutin, V. S. Senchurin, O. K. Sharutina and B. B. Kunkurdonova, *CCDC 864253: Experimental Crystal Structure Determination*, 2013.

41 (*a*) G. R. Willey, L. T. Daly, P. R. Meehan and M. G. B. Drew, *J. Chem. Soc., Dalton Trans.*, 1996, 4045–4053; (*b*) A. Gagor,

M. Wojtaś, A. Pietraszko and R. Jakubas, *Acta Crystallogr., Sect. B: Struct. Sci.*, 2008, **64**, 558–566.
42 (*a*) X.-G. Chen, Y.-Z. Zhang, D.-S. Sun, J.-X. Gao, X.-N. Hua and W.-Q. Liao, *Dalton Trans.*, 2019, **48**, 11292–11297; (*b*) C. Xue, S. Wang, W.-L. Liu and X.-M. Ren, *Chem. – Eur. J.*, 2019, **25**, 5280–5287.
43 A. J. Dennington and M. T. Weller, *Dalton Trans.*, 2018, **47**, 3469–3484.
44 R. Hooijer, A. Weis, A. Biewald, M. T. Sirtl, J. Malburg, R. Holfeuer, S. Thamm, A. A. Y. Amin, M. Righetto, A. Hartschuh, L. M. Herz and T. Bein, *Adv. Opt. Mater.*, 2022, **10**, 2200354.
45 E. G. Tulsky and J. R. Long, *Chem. Mater.*, 2001, **13**, 1149–1166.
46 N. Dehnhardt, M. Axt, J. Zimmermann, M. Yang, G. Mette and J. Heine, *Chem. Mater.*, 2020, **32**, 4801–4807.
47 Z. Xiao, W. Meng, J. Wang, D. B. Mitzi and Y. Yan, *Mater. Horiz.*, 2017, **4**, 206–216.
48 (*a*) J. P. Perdew, K. Burke and M. Ernzerhof, *Phys. Rev. Lett.*, 1996, **77**, 3865–3868; (*b*) S. Grimme, J. Antony, S. Ehrlich and H. Krieg, *J. Chem. Phys.*, 2010, **132**, 154104.

3.4 Establishing Family Relations in Group 15 Halogenido Metalates with the Largest Molecular Antimony Iodide Anion

Jakob Möbs, Gina Stuhrmann, Florian Weigend and Johanna Heine, *Chemistry - A European Journal*, **2023**, *29*, e202202931, DOI:10.1002/chem.202202931.

Abstract

Studying structurally related families of compounds is a valuable tool in understanding and predicting material properties and has been extensively used for metal halide perovskites. Due to the variable anion structures in group 15 halogenido metalates, similar family relations are still largely missing. Herein, we present compounds featuring the $[Sb_{2n}I_{6n+4}]^{4-}$ family of anions, including the first $n = 5$ member in $[Hpyz]_4[Sb_{10}I_{34}]$ (Hpyz = pyrazinium), which contains the largest halogenido pentelate anion reported to date. The optical properties of compounds featuring $n = 1$ - 5 anions show a clear trend as well as an outlier, a low band gap of 1.72 eV for $[Hpyz]_4[Sb_{10}I_{34}]$, that can be well understood using quantum chemical investigations. Also using SbI_3 and $[H_2NMe_2]_3[SbI_6]$, a compound featuring a single octahedral $[SbI_6]^{3-}$-unit, as limiting cases, we show that structure-property relationships can be established in group 15 halogenido metalates in a similar way as in metal halide perovskites, thus providing a framework for understanding new and known compounds in this emerging class of materials.

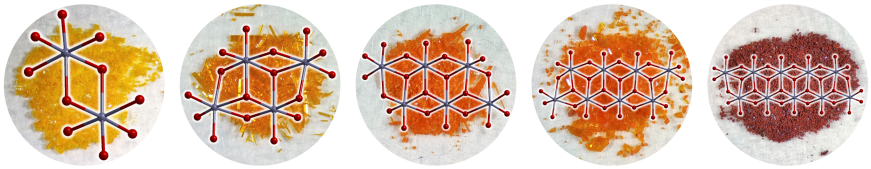

Figure 3.4: Table-of-contents graphic of "Establishing Family Relations in Group 15 Halogenido Metalates with the Largest Molecular Antimony Iodide Anion".

Summary

In this publication, the influence of anion size on the optical properties of group 15 halogenido metalates is investigated. For derivatives of the lead halide perovskites, it is well established that larger anionic motifs or motifs of higher dimensionality lead to smaller band gaps. This trend should continue for group 15 halogenido metalates but the immense structural variety of anions makes it difficult to find families of compounds related closely enough to confirm it. Furthermore, published band gaps for these compounds can vary greatly even for the same exact material due to differences in sample preparation and measurement setups, which further complicates the identification of trends. For $(MeNH_3)_3Sb_2I_9$, for example, values between 1.9 eV and 2.36 eV have been reported.

Here, the newly synthesized compound $[Hpyz]_4[Sb_{10}I_{34}] \cdot MeCN \cdot pyz$ (**2**) is presented. The anion

is the largest discrete halogenido group 15 metalate ion yet and belongs to the $[Sb_{2n}I_{6n+4}]^{4-}$-family ($n = 5$) that features cut-outs of the CdI_2 structure type as the anionic motif. Including compound **2**, examples of that family for n = 1 - 5 are known, making the series suitable to investigate the influence of anion size on the properties. Example compounds for each n were prepared and their optical band gaps determined under the exact same conditions. Additionally, $[H_2NMe_2]_3[SbI_6]$ (**3**) featuring isolated $\{SbI_6\}$-octahedra as well as SbI_3 were synthesized and their band gaps determined as examples of Sb/I-compounds with the smallest and largest possible motifs consisting of $\{SbI_6\}$-octahedra.
3 and SbI_3 have optical band gaps of 2.30 eV and 2.10 eV, respectively, and the values of the $[Sb_{2n}I_{6n+4}]^{4-}$-family fit neatly within that range, with the exception of **2**, which shows a surprisingly low band gap of 1.72 eV. For n = 1 - 3, the optical band gaps follow the expected decreasing trend but the example for $n = 4$ shows a band gap slightly larger than that for $n = 3$.
To unravel these discrepancies, excitation energies for the isolated anions as well as anions with relevant surrounding cations were calculated using quantum chemical methods. For both models, the calculations show a trend of consistently decreasing excitation energies for n = 1 - 4 due to a decrease of the LUMO's energy level. This points to a packing effect of the individual examples for $n = 3$ and $n = 4$ being responsible for the slight increase that was observed with their experimental band gaps. When looking at compound **2** with $n = 5$, however, the models with and without cations differ significantly. The excitation energy of the isolated $[Sb_{10}I_{34}]^{4-}$-anion fits the trend of the smaller ones perfectly and the unexpected drop observed in the experiment is not replicated in the calculations. The inclusion of cations, on the other hand, reveals a pure charge transfer transition from the anion to unoccupied π-orbitals of the pyrazinium cations to be the main mechanism for visible light absorption. This narrows the optical band gap and explains the experimental observations.

Overall, the trend in optical properties found in other classes of semiconductors is confirmed for the $[Sb_{2n}I_{6n+4}]^{4-}$-family and it seems reasonable to at least qualitatively expand it to group 15 halogenido metalates in general. Furthermore, strong deviations from that trend and especially optical band gaps outside the range defined by $[H_2NMe_2]_3[SbI_6]$ and SbI_3 point towards additional absorption mechanisms like charge transfer transitions that are not centered at the anion.

Own contribution

All syntheses were planned by myself and executed by myself or Gina Stuhrmann under my supervision. Crystallographic measurements, solutions and refinements as well as UV-Vis measurements were done by myself. Thermo-gravimetric measurements were done by Uwe Justus. Quantum chemical calculations were carried out by Florian Weigend. The manuscript was written through contributions of Johanna Heine, Florian Weigend and myself.

Chemistry–A European Journal
Research Article
doi.org/10.1002/chem.202202931
Chemistry Europe
European Chemical Societies Publishing
www.chemeurj.org

Establishing Family Relations in Group 15 Halogenido Metalates with the Largest Molecular Antimony Iodide Anion

Jakob Möbs,[a] Gina Stuhrmann,[a] Florian Weigend,[a] and Johanna Heine*[a]

Abstract: Studying structurally related families of compounds is a valuable tool in understanding and predicting material properties and has been extensively used for metal halide perovskites. Due to the variable anion structures in group 15 halogenido metalates, similar family relations are still largely missing. Herein, we present compounds featuring the $[Sb_{2n}I_{6n+4}]^{4-}$ family of anions, including the first $n=5$ member in $[Hpyz]_4[Sb_{10}I_{34}]$ (Hpyz = pyrazinium), which contains the largest halogenido pentelate anion reported to date. The optical properties of compounds featuring $n=1$–5 anions show a clear trend as well as an outlier, a low band gap of 1.72 eV for $[Hpyz]_4[Sb_{10}I_{34}]$, that can be well understood using quantum chemical investigations. Also using SbI_3 and $[H_2NMe_2]_3[SbI_6]$, a compound featuring a single octahedral $[SbI_6]^{3-}$ unit, as limiting cases, we show that structure-property relationships can be established in group 15 halogenido metalates in a similar way as in metal halide perovskites, thus providing a framework for understanding new and known compounds in this emerging class of materials.

Introduction

Metal halide materials are currently being investigated for use in a variety of applications including photovoltaics,[1] solid-state lighting,[2] and catalysis.[3] A prominent group within the larger class are metal halide perovskites AMX_3 (A = alkali metal or small organic cation; M = divalent metal ion, for example, Sn^{2+} or Pb^{2+}; X = F, Cl, Br, I)[4] such as the prototypical $[CH_3NH_3][PbI_3]$ (MAPI).[5] Many metal halide materials can be formally derived from the cubic perovskite aristotype by hypothetical cuts across different planes,[6] leading to distinct families like the ⟨100⟩-oriented layered perovskites with a general formula of $[(RNH_3)_2A_{n-1}][M_nX_{3n+1}]$ (R = organic moiety), for example, $[(CH_3(CH_2)_3NH_3)_2(CH_3NH_3)][Pb_2I_7]$ with $n=2$.[7]

Optical band gaps in related series of perovskite-derived materials can be explained and predicted with the concept of dimensional reduction for changes in anion dimensionality,[8] for example, changing from a "3D" network anion in $[CH_3NH_3][PbI_3]$ to a "2D" layered anion in $[(CH_3(CH_2)_3NH_3)_2(CH_3NH_3)][Pb_2I_7]$ leads to an increase in the optical band gap from 1.50 to 2.17 eV.[7] When comparing anions of the same dimensionality, deliberations regarding quantum confinement derived from the chemistry of nanoparticles[9] and metal chalcogenide clusters[10] can be used, predicting a smaller band gap for thicker or larger anions (for layered or molecular examples, respectively). These predictions are largely confirmed for related series.[11]

Halogenido antimonates and bismuthates $A_xE_yX_z$ (A = organic or inorganic cation; E = Sb, Bi; X = Cl, Br, I) are another class of metal halide materials that are of interest due to their higher stability[12] and low toxicity[13] compared to typical lead halide perovskites.[14] However, the highly variable anion motifs observed here make establishing "family relations" more difficult.[15]

In the current literature on iodido antimonates reported optical band gaps vary broadly in compounds with the same type of anion and even in the same compound. For example, optical band gaps between 1.9 and 2.36 eV have been reported for $(CH_3NH_3)_3Sb_2I_9$.[16] Differences in material preparation, measurement methods and setups typically contribute to the observation of such different values, for example between microcrystalline powders and thin films.[17] In compounds containing $[SbI_4]^-$ anions as chains of *cis*-connected octahedra forming a zigzag chain, optical band gaps between 1.79 and 2.41 eV have been reported.[18] When comparing compounds with the same anion motif but different cations, differences in crystal packing will result. These can lead to differences in the degree of distortion in the anion and halogen-halogen interactions, which are thought to have a distinct influence on the optical band gap in metal halide materials in general, although these effects can be difficult to quantify in a consistent way.[19,20,21]

More direct interactions between the anion and the cation in the form of charge-transfer phenomena can play a key role in determining a material's optical band gap. This is observed, for example, in $[C_7H_7][SbI_4]$, where a charge transfer between the

[a] J. Möbs, G. Stuhrmann, Prof. Dr. F. Weigend, Dr. J. Heine
Department of Chemistry, Philipps-University Marburg
Hans-Meerwein-Straße 4, 35032 Marburg (Germany)
E-mail: johanna.heine@chemie.uni-marburg.de

Supporting information for this article is available on the WWW under https://doi.org/10.1002/chem.202202931

anionic $[SbI_4]^-$ chains and the tropylium cations occurs, resulting in a low optical band gap of 1.55 eV.[22]

All of this can lead to the impression that optical band gaps in iodido antimonates cannot be understood or predicted in a rational way using simple deliberations regarding dimensional reduction and anion size.

To address these issues, we investigated the newly synthesized iodido antimonate $[Hpyz]_4[Sb_{10}I_{34}]\cdot MeCN\cdot pyz$ (**2**), which contains the largest group 15 halogenido metalate anion reported to date and is the largest member of the $[Sb_{2n}I_{6n+4}]^{4-}$ family of anions (Scheme 1). We also prepared literature-known compounds containing anions of the smaller members of the family with $n=1$–4 that have been previously reported and re-determined their optical band gaps to provide consistent measuring conditions. Additionally, we newly synthesized $[H_2NMe_2]_3[SbI_6]$ (**3**), which contains the smallest isolated iodido antimonate unit with octahedral coordination. While this anion has been described before[23] it has never been investigated regarding its optical properties.

Using this well-comparable family of iodido antimonate compounds, we can show that general expectations regarding the correlation between anion size and optical band gap are correct. Using high-level quantum chemical calculations, we elucidate that specific, although sometimes unexpected, factors can explain deviations.

This demonstrates that fundamental optical properties in iodido antimonates can be understood using the same concepts established for other classes of semiconductor materials, like metal chalcogenide clusters or lead halide perovskites. Quantum chemical calculations can provide a solid baseline to quantify these expectations and help to understand when deviations are observed due to additional effects such as charge-transfer phenomena.

Results and Discussion

Synthesis

Hpyzl (**1 a**) was synthesized by treating stoichiometric amounts of concentrated hydriodic acid with pyrazine (pyz) in diethyl ether, resulting in a bright yellow powder. In air **1 a** absorbs water to form the hydrate $Hpyzl\cdot H_2O$ (**1 b**). **1 a** and **1 b** both are sensitive to light – especially when not thoroughly dry – and turn from a bright yellow to a brown color, likely due to the formation of iodine or polyiodides. We did not find any evidence that the doubly protonated pyrazinium ion forms under these conditions. Instead any excess of hydroiodic acid during the preparation of **1 a** also results in a contamination of the product with iodine/poly-iodides, as the acid decomposes during workup.

Compound **2** crystallizes from a solution of **1 a** (Hpyzl) and SbI_3 in acetonitrile. A summary of the synthesis is given in Scheme 2.

$[H_2NMe_2]_3[SbI_6]$ (**3**) is prepared as a powder by evaporation of a stoichiometric solution of H_2NMe_2I and SbI_3 in MeCN. Details are given in the Supporting Information.

Description of crystal structures

As compounds **1 a**, **1 b** and **3** are structurally of less interest, they are described in the Supporting Information.

Compound **2** crystallizes in the triclinic space group $P\bar{1}$ with one formula unit per unit cell as very dark red blocks. It consists of discrete $[Sb_{10}I_{34}]^{4-}$ anions and pyrazinium cations as well as acetonitrile and pyrazine solvent molecules. The anionic motif is the largest discrete halogenido pentelate anion reported in the CCDC[24] to this point. It is composed of a double row of edge-sharing SbI_6 octahedra and represents the largest member of a series of iodido antimonates with the general formula $[Sb_{2n}I_{6n+4}]^{4-}$.

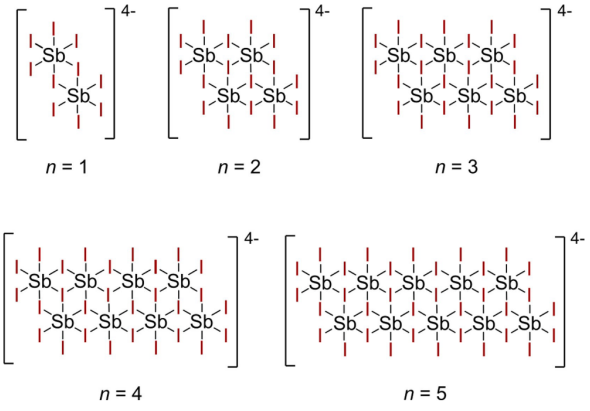

Scheme 1. Overview of the $n=1$ to $n=5$ members of the $[Sb_{2n}I_{6n+4}]^{4-}$ family of anions.

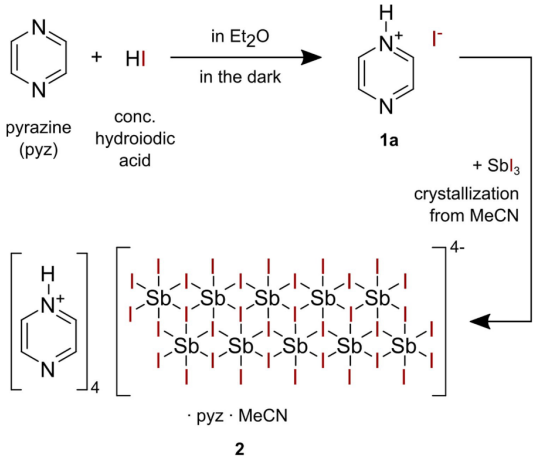

Scheme 2. Overview of the synthesis of **1 a** and **2**.

The singly protonated pyrazinium cations form four-part chains that are linked by hydrogen bonds and lie parallel to the double row of the anion (Figure 1). Similar N–H···N interactions have also been reported in pyridine-pyridinium dimers.[25] Centroid-to-iodine distances as short as 3.75 Å are observed, significantly less than the corresponding distance of 3.84 Å found in the iodido argentate $[Hpyz]_2[Ag_2I_4]\cdot H_2O$.[26] Additionally, one molecule of acetonitrile and free pyrazine crystallize per formula unit. These solvate molecules as well as the pyrazinium cations show disorder over two equally populated positions (see the Supporting Information for details).

The $[Sb_{2n}I_{6n+4}]^{4-}$ series: Anion structures and optical band gaps

Similar to related families in perovskite-derived materials, the $[Sb_{2n}I_{6n+4}]^{4-}$ series can be established for iodido antimonates. In addition to **2**, featuring the $n=5$ member, we have prepared known examples with the $n=1$–4 members of the series: $[C_8H_{11}NF]_4[Sb_2I_{10}]$,[27] $[C_6H_{14}N_2]_2[Sb_4I_{16}]\cdot 2H_2O$,[28] $[C_5H_{12}NO]_4[Sb_6I_{22}]$,[28] and $[PPh_4]_4[Sb_8I_{28}]$.[29] The metalate ions in the series can be viewed as cut-outs of the CdI_2 structure type.[30] Starting from the smallest representative, the $[Sb_2I_{10}]^{4-}$ anion, the next larger member can always be constructed by the hypothetical addition of two neutral SbI_3 molecules on opposing sides of the previous ion (Figure 2). This understanding of the motif is also underlined by the strong distortion of the outmost SbI_6 octahedra, where the original SbI_3 molecule is still recognizable. In general the distortion of the octahedra is very uniform throughout the series. For each octahedron aside from the central $\{Sb_2I_{10}\}$ units three long bonds of above 3 Å and three short bonds well below 3 Å are observed with the long Sb–I bonds pointing towards the center of the ion. Therefore all "previously attached" SbI_3 units remain recognizable in every ion (see Figures S11 and S12 on the Supporting Information for details). The reason for these observations can be found in the well-known structural *trans* effect in main group halogenido metalates.[31] Sb–I bonds *trans* to terminal ones are elongated. The distortions in bond length caused by the presence of three or two terminal Sb–I bonds at the outer edges of the anion propagate to neighboring $\{SbI_6\}$ octahedra, with bond length of Sb–I bonds not *trans* to terminal ones becoming more uniform in the central octahedra, for example in $[Sb_{10}I_{34}]^{4-}$ (Figure S12).

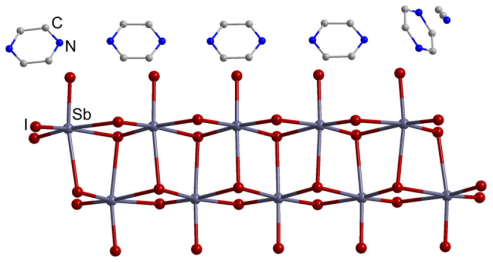

Figure 1. Formula unit of **2**. All nitrogen and carbon positions are only half occupied due to disorder. The second positions are not shown. Hydrogen atoms are omitted for clarity.

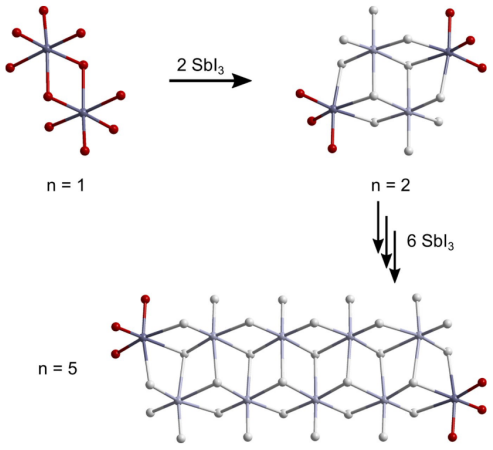

Figure 2. Building scheme of the $[Sb_{2n}I_{6n+4}]^{4-}$ series. The distinct SbI_3 molecules at the outermost octahedra are highlighted.

We note that the description of iodido antimonates as cut-outs of the CdI_2 structure type has been established very early by Pohl and co-workers.[29] Using the building principle above, members of the $[Sb_{2n}I_{6n+4}]^{4-}$ series that cannot be derived from the CdI_2 structure type can be generated as well, depending on where additional SbI_3 units are attached. For example, five different isomers of the $[Sb_6I_{22}]^{4-}$ anion are known that differ only in the point of attachment of two SbI_3 units to the $[Sb_4I_{16}]^{4-}$ anion.[32,33] We also want to mention $[Cu(MeCN)_4]_4[Sb_7I_{25}]$, a iodido antimonate that can be understood as part of the $[Sb_{2n}I_{6n+4}]^{4-}$ series with $n=3.5$, although unfortunately, its optical band gap could not be determined due to the compound's sensitivity toward solvent loss outside the mother liquor.[32] The $[Sb_{2n}I_{6n+4}]^{4-}$ series also represents a specific case of the $[E_{2n}X_{6n+4}]^{4-}$ (E = Sb, Bi; X = Cl, Br, I) family of compounds with examples reported for all combinations of E and X.[34] This suggests that our findings for the $[Sb_{2n}I_{6n+4}]^{4-}$ series can be extended towards other E/X combinations. The end member of the series when n approaches infinity would be a hypothetical SbI_3 polymorph featuring neutral double chains. This is, of course, not the structure of SbI_3 at standard conditions. Here, honeycomb layers of edge-sharing octahedra are observed.[35] However, infinite double chains have been reported in halogenido cadmates[36] and plumbates,[37] showing that in principle the motif can be realized.

Although in all five compounds of the $[Sb_{2n}I_{6n+4}]^{4-}$ series the antimony and iodine atoms form discrete complex anions, there are significant I···I contacts connecting the individual ions. When considering all contacts below the double van der Waals radius of iodine of 4.08 Å[38] different one- to three-dimensional connections are observed (see the Supporting Information for details). Halogen-halogen interactions in general[39] and iodine-iodine interactions especially play a role in the packing and subsequent optical properties of metal halide materials.[20,21,40] However, quantifying their effect in a series of compounds

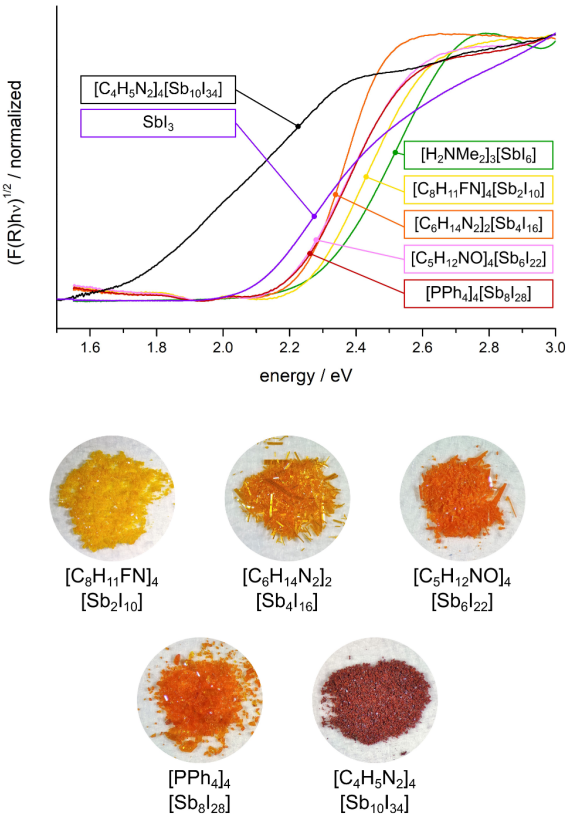

Figure 3. Top: Tauc plots from diffuse reflectance UV-Vis measurements against $BaSO_4$ of the compounds of the $[Sb_{2n}I_{6n+4}]^{4-}$ series as well as SbI_3 and $[H_2NMe_2]_3[SbI_6]$ for comparison. Note that the optical band gap of $[C_6H_{14}N_2]_2[Sb_4I_{16}]$ is actually larger than it seems from the plot due to the quite steep absorption edge. Bottom: Photographs of the crystalline compounds.

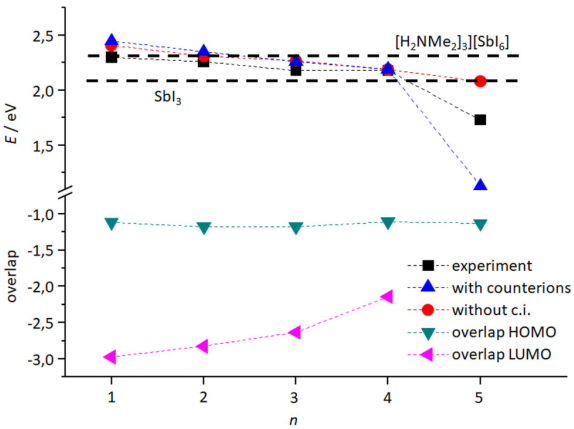

Figure 4. Experimental and calculated lowest excitation energies E (with and without counter ions, shifted by 1 eV) as well as Mulliken overlap (sum of nondiagonal elements as a measure for the antibonding character) for the HOMO and the LUMO of the systems without counter ions for $n=1$ to 5 of the $[Sb_{2n}I_{6n+4}]^{4-}$ series. The excitation energies of the limiting cases of $[H_2NMe_2]_3[SbI_6]$ and SbI_3 are drawn as dashed lines that do not correspond to a specific n, defining the borders of expected values.

featuring different dimensionalities of the interaction, as well as different I···I distances and Sb—I···I angles is beyond the scope of the present work.

For each compound diffuse reflectance UV-Vis spectra were recorded against a $BaSO_4$ standard as a 5% mixture of the compound in $BaSO_4$. When looking at the optical band gaps estimated from Tauc plots of these measurements a trend of narrowing gaps with increasing anion size is observed (Figures 3 and 4). This trend is very clear for the compounds featuring the bi-, tetra- and hexanuclear ions with optical band gap energies of 2.25, 2.23, and 2.19 eV, respectively. The value for the octanuclear complex of 2.20 eV seems slightly too high. This might be an effect of the reduced dimensionality of the network formed through I···I contacts which is only 1D for $[PPh_4]_4[Sb_8I_{28}]$, compared to 2D or 3D for the other compounds.

All the optical band gap energies neatly fit within the boundaries defined by the optical band gaps of $[H_2NMe_2]_3[SbI_6]$ (**3**) and SbI_3, which are 2.30 and 2.10 eV, respectively. As these are the compounds featuring the smallest and largest antimony-iodide motifs composed of $\{SbI_6\}$ octahedra, their optical band gaps can serve as the upper and lower limits for molecular and chain-like iodido antimonates in general following the anion size and dimensional reduction approaches.

Surprisingly, at 1.71 eV the onset of absorption of **2** is far lower than what is expected from the trend in the rest of the $[Sb_{2n}I_{6n+4}]^{4-}$ series, the theoretical prediction for the isolated anion (see below), and the lower limit set by the optical band gap of SbI_3. Further investigations, described below, reveal that this decrease stems from an additional charge-transfer (CT) excitation from the anion into the π-system of the cation. Generally, pyrazine and its derivatives are well known for their electron-deficient character that enables electron transfer reactions, for example when used as a bridging ligand in multinuclear metal complexes.[41] This character is increased in alkylated pyrazinium cations, which have been used prepare halogenido metalates such as $[MepyzH]_3[BiBr_6]_2$ or $[Me_2pyz][Pb_2Br_6]$,[42] where CT phenomena were observed. However, only a single example of CT in a salt featuring $[Hpyz]^+$ has been reported.[26] This suggests that despite their enhanced electron-deficiency, protonated pyrazinium cations can only act as charge acceptors under very specific circumstances.

Generally, the changes in the onset of absorption observed and calculated for the $[Sb_{2n}I_{6n+4}]^{4-}$ family are noticeable, but fairly small. This is well in line with expectations, as the structural changes as n increases are less drastic here than in ⟨100⟩ perovskites $(RNH_3)_2A_{n-1}M_nX_{3n+1}$, where, for example, a decrease in the optical band gap from 2.42 to 2.16 and 2.00 eV is observed going from $n=1$ to 3 as the layer thickness is doubled or tripled in the $[(mPDA)MA_{n-1}][Pb_nI_{3n+1}]$ series (mPDA = *m*-phenylenediammonium; MA = CH_3NH_3).[43]

Quantum chemistry

Quantum chemical calculations[44] (PBE0[45] /def2-TZVP,[46] together with corresponding effective core potentials[47] and auxiliary basis sets[48]) were carried out for the rationalization of

the experimentally observed UV-VIS spectra. Detailed data are given in the Supporting Information, for PBE0 as well as for PBE[49] and a recently developed local hybrid functional,[50] which shows similar results as PBE0. For each species, we calculated the isolated anion as well as the anion together with a set of cations ensuring charge neutrality. Data were done for the experimental structure, shown and listed in the Supporting Information; the conductor-like screening model (COSMO)[51] was used throughout. The main experimental observations for the $[Sb_{2n}I_{6n+4}]^{4-}$ series are a slight decrease of the onset of the absorption from $n=1$ to $n=4$ and a significantly lower onset for $n=5$. In Figure 4 we show the calculated lowest excitation energies (shifted by 1 eV). The slight decrease from $n=1$ to $n=4$ is well reproduced both for the calculations without and with counterions, the significantly lower onset for $n=5$ only for the latter.

The reason for this is evident when inspecting the difference densities between the first excited state and the ground state, exemplarily shown for $n=1$ to 5 together with the dominantly involved orbitals, which are HOMO and LUMO in all cases, in Figure 5. For all species except $n=5$, the lowest excitations take place within the iodido antimonate anion without involving the cations, whereas for $n=5$ a pure charge transfer from the anion to the unoccupied orbitals of the π-systems of the cations is observed, which is lower in energy than the unoccupied orbitals of the anion. This charge transfer is observed also for the other values of n, as soon as doubly protonated pyrazinium ions are employed as counterions, as shown for $n=2$ in Figure 5 (bottom). It has to be noted that

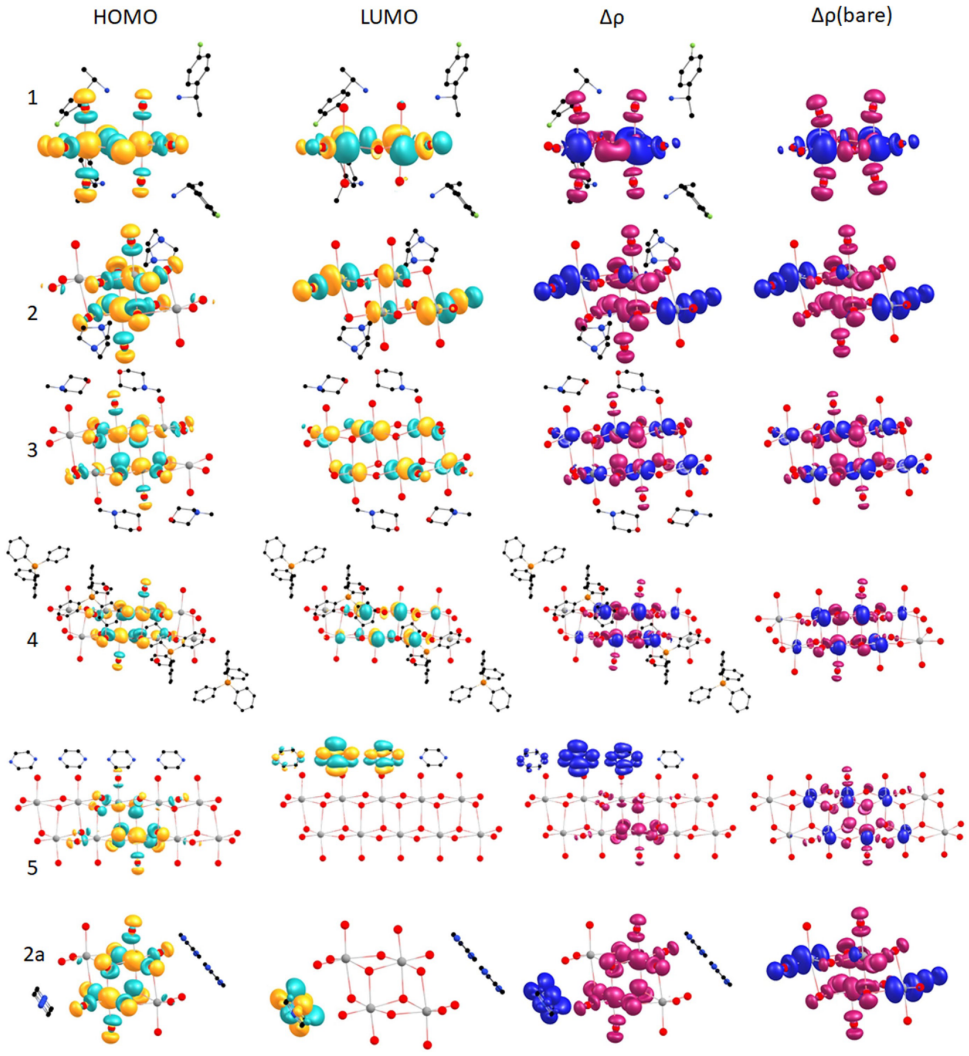

Figure 5. Images of the HOMO, LUMO, and difference density $\Delta\rho$ between first excited and ground states for $n=1$–5 of the $[Sb_{2n}I_{6n+4}]^{4-}$ series calculated in presence of counterions, as well as $\Delta\rho$ for the excitations of the bare SbI units. 2a denotes the anion for $n=2$ with the cations of $n=5$. Iso-surfaces are drawn at 0.03 a.u. for the orbitals and at 0.001 a.u. for $\Delta\rho$, where magenta indicates a density surplus for the ground state and blue for the excited state.

even with the hybrid functional PBE0 the change in excitation energies from $n=4$ to $n=5$ is overestimated (ca. 1 eV vs. ca. 0.45 eV); this can at least partly be addressed to spin-orbit coupling, see below.

The subtle decrease of excitation energies from $n=1$ to $n=4$ is rather due to changes in the unoccupied than in the occupied orbitals: The band of highest occupied orbitals is formed mainly by the lone pairs at the iodine atoms, with slight antibinding contributions from the central Sb atoms. This yields to a negative value for the Mulliken overlap (sum of the nondiagonal elements of the Mulliken overlap matrix) for the HOMO, which is about the same (−1.2) for all choices of n, see Figure 4. Matters are different for the LUMOs, which are (much more) anti-bonding combinations of the p(I) orbitals with the p(Sb) orbitals. For $n=1$ one gets a Mulliken overlap of −3.0. For increasing n, higher (less negative) values are observed, for example, −2.0 for $n=4$. This decrease of the antibonding character of the LUMO with increasing size of the anion leads to smaller HOMO-LUMO gaps and thus to decreasing excitation energies. We finally note that spin-orbit coupling reduces energies for excitation within the anion by about 0.5 eV, and for the charge-transfer excitation by 0.2 eV, as calculated at two-component level[52] with the PBE functional for $n=1$ and $n=5$, see the Supporting Information. Thus, the size of the change of the excitation energy from $n=4$ to $n=5$ is smaller by 0.3 eV than without spin-orbit coupling and thus amounts to 0.7 eV, which is reasonably close to the experiment (0.45 eV).

Conclusion

In summary, we have prepared compounds featuring the $n=1$–5 members of the $[Sb_{2n}I_{6n+4}]^{4-}$ family of anions, including $[Hpyz]_4[Sb_{10}I_{34}]\cdot MeCN\cdot pyz$ (**2**), with $n=5$, the largest molecular halogenido pentelate ion reported to date. We established that the optical properties in this series can be understood with familiar concepts used in the description of other semiconductor materials and that deviations from expected trends can and should be rationalized: DFT calculations for the $[Sb_{2n}I_{6n+4}]^{4-}$ series show that the comparably low excitation energy for $n=5$ is due to the different character of the excitation for this system (charge transfer from the anion to cations) compared to the others (excitations within anion from the lone pairs of I to orbitals that are anti-bonding combinations of p(I) and p(Sb)). Furthermore, the slight decrease in excitation energies from $n=1$ to $n=4$ is due to the decreasing antibonding character of the LUMOs with increasing n. By investigating the optical band gaps of the limiting cases of a compound with a mononuclear anion, $[H_2NMe_2]_3[SbI_6]$ (**3**), and the parent halide SbI_3, we established that a range of expected values can be defined. If a compound's optical band gap lies significantly outside of this range, additional phenomena like the charge-transfer effect found in **2** might be present and should be investigated. In future work, this approach could also be used for other metal-halide combinations.

Acknowledgements

The authors thank Dr. Philip Klement for his help with the UV-Vis measurements and Sarah Critchley for her help with the preparation of the compounds. This research was funded by the German Research Foundation DFG (HE 8018/1). J.H. thanks Prof. Stefanie Dehnen for her support. Open Access funding enabled and organized by Projekt DEAL.

Conflict of Interest

The authors declare no conflict of interest.

Data Availability Statement

The data that support the findings of this study are available in the supplementary material of this article.

Keywords: anions · antimony · density functional calculations · iodine · UV/Vis spectroscopy

[1] A. K. Jena, A. Kulkarni, T. Miyasaka, *Chem. Rev.* **2019**, *119*, 3036.
[2] J. Chen, H. Xiang, J. Wang, R. Wang, Y. Li, Q. Shan, X. Xu, Y. Dong, C. Wei, H. Zeng, *ACS Nano* **2021**, *15*, 17150.
[3] H. Huang, B. Pradhan, J. Hofkens, M. B. J. Roeffaers, J. A. Steele, *ACS Energy Lett.* **2020**, *5*, 1107.
[4] L. Chouhan, S. Ghimire, C. Subrahmanyam, T. Miyasaka, V. Biju, *Chem. Soc. Rev.* **2020**, *49*, 2869.
[5] a) D. Weber, *Z. Naturforsch. B* **1978**, *33*, 1443; b) A. Kojima, K. Teshima, Y. Shirai, T. Miyasaka, *J. Am. Chem. Soc.* **2009**, *131*, 6050.
[6] B. Saparov, D. B. Mitzi, *Chem. Rev.* **2016**, *116*, 4558.
[7] C. C. Stoumpos, D. H. Cao, D. J. Clark, J. Young, J. M. Rondinelli, J. I. Jang, J. T. Hupp, M. G. Kanatzidis, *Chem. Mater.* **2016**, *28*, 2852.
[8] a) G. C. Papavassiliou, *Prog. Solid State Chem.* **1997**, *25*, 125; b) E. G. Tulsky, J. R. Long, *Chem. Mater.* **2001**, *13*, 1149.
[9] A. M. Smith, S. Nie, *Acc. Chem. Res.* **2010**, *43*, 190.
[10] a) V. N. Soloviev, A. Eichhöfer, D. Fenske, U. Banin, *J. Am. Chem. Soc.* **2000**, *122*, 2673; b) V. N. Soloviev, A. Eichhöfer, D. Fenske, U. Banin, *J. Am. Chem. Soc.* **2001**, *123*, 2354.
[11] I. W. H. Oswald, A. A. Koegel, J. R. Neilson, *Chem. Mater.* **2018**, *30*, 8606.
[12] B.-W. Park, B. Philippe, X. Zhang, H. Rensmo, G. Boschloo, E. M. J. Johansson, *Adv. Mater.* **2015**, *27*, 6806.
[13] D. M. Griffith, H. Li, M. V. Werrett, P. C. Andrews, H. Sun, *Chem. Soc. Rev.* **2021**, *50*, 12037.
[14] J. Li, H.-L. Cao, W.-B. Jiao, Q. Wang, M. Wei, I. Cantone, J. Lü, A. Abate, *Nat. Commun.* **2020**, *11*, 310.
[15] a) G. A. Fisher, N. C. Norman, *Adv. Inorg. Chem.* **1994**, *41*, 233; b) L.-M. Wu, X.-T. Wu, L. Chen, *Coord. Chem. Rev.* **2009**, *253*, 2787; c) N. Mercier, N. Louvain, W. Bi, *CrystEngComm* **2009**, *11*, 720; d) S. A. Adonin, M. N. Sokolov, V. P. Fedin, *Russ. J. Inorg. Chem.* **2017**, *62*, 1789.
[16] a) J.-C. Hebig, I. Kühn, J. Flohre, T. Kirchartz, *ACS Energy Lett.* **2016**, *1*, 309; b) D. Ju, X. Jiang, H. Xiao, X. Chen, X. Hu, X. Tao, *J. Mater. Chem. A* **2018**, *6*, 20753; c) M. Scholz, M. Morgenroth, K. Oum, T. Lenzer, *J. Phys. Chem. C* **2018**, *122*, 5854; d) S. Chatterjee, J. Payne, J. T. S. Irvine, A. J. Pal, *J. Mater. Chem. A* **2020**, *8*, 4416.
[17] R. Hooijer, A. Weis, A. Biewald, M. T. Sirtl, J. Malburg, R. Holfeuer, S. Thamm, A. A. Y. Amin, M. Righetto, A. Hartschuh, L. M. Herz, T. Bein, *Adv. Opt. Mater.* **2022**, *10*, 2200354.
[18] a) G. A. Mousdis, N.-M. Ganotopoulos, H. Barkaoui, Y. Abid, V. Psycharis, A. Savvidou, C. P. Raptopoulou, *Eur. J. Inorg. Chem.* **2017**, *2017*, 3401; b) P.-F. Li, Y.-Y. Tang, W.-Q. Liao, H.-Y. Ye, Y. Zhang, D.-W. Fu, Y.-M. You, R.-G. Xiong, *NPG Asia Mater.* **2017**, *9*, e342–e342; c) J.-X. Gao, X.-N. Hua, X.-G. Chen, G.-Q. Mei, W.-Q. Liao, *Inorg. Chem.* **2019**, *58*, 4337; d) Y. Li, T. Yang, X. Liu, S. Han, J. Wang, Y. Ma, W. Guo, J. Luo, Z. Sun, *Inorg. Chem. Front.* **2020**, *7*, 2770.

[19] a) J. L. Knutson, J. D. Martin, D. B. Mitzi, *Inorg. Chem.* **2005**, *44*, 4699; b) X. Li, J. M. Hoffman, M. G. Kanatzidis, *Chem. Rev.* **2021**, *121*, 2230; c) E. I. Marchenko, V. V. Korolev, S. A. Fateev, A. Mitrofanov, N. N. Eremin, E. A. Goodilin, A. B. Tarasov, *Chem. Mater.* **2021**, *33*, 7518.
[20] N. Louvain, N. Mercier, F. Boucher, *Inorg. Chem.* **2009**, *48*, 879.
[21] D. B. Mitzi, P. Brock, *Inorg. Chem.* **2001**, *40*, 2096.
[22] I. W. H. Oswald, E. M. Mozur, I. P. Moseley, H. Ahn, J. R. Neilson, *Inorg. Chem.* **2019**, *58*, 5818.
[23] a) M. Bujak, *Acta Crystallogr. B* **2017**, *73*, 432; b) C. Shi, H. Yu, Q.-W. Wang, Le Ye, Z.-X. Gong, J.-J. Ma, J.-Y. Jiang, M.-M. Hua, C. Shuai, Y. Zhang, H.-Y. Ye, *Angew. Chem. Int. Ed.* **2020**, *59*, 167.
[24] C. R. Groom, I. J. Bruno, M. P. Lightfoot, S. C. Ward, *Acta Crystallogr. B* **2016**, *72*, 171.
[25] A. A. Gurinov, S. B. Lesnichin, H.-H. Limbach, I. G. Shenderovich, *J. Phys. Chem. A* **2014**, *118*, 10804.
[26] P. Hao, H. Li, T. Yu, Y. Fu, *Dyes Pigm.* **2017**, *136*, 825.
[27] N. Dehnhardt, M. Axt, J. Zimmermann, M. Yang, G. Mette, J. Heine, *Chem. Mater.* **2020**, *32*, 4801.
[28] A. J. Dennington, M. T. Weller, *Dalton Trans.* **2018**, *47*, 3469.
[29] S. Pohl, W. Saak, D. Haase, *Z. Naturforsch. B* **1987**, *42*, 1493.
[30] R. M. Bozorth, *J. Am. Chem. Soc.* **1922**, *44*, 2232.
[31] H.-L. Sheu, J. Laane, *Inorg. Chem.* **2013**, *52*, 4244.
[32] N. Dehnhardt, A. Böth, J. Heine, *Dalton Trans.* **2019**, *48*, 5222.
[33] a) S. Pohl, D. Haase, R. Lötz, W. Saak, *Z. Naturforsch. B* **1988**, *43*, 1033; b) S. Pohl, R. Lotz, W. Saak, D. Haase, *Angew. Chem. Int. Ed. Engl.* **1989**, *28*, 344; c) S. Pohl, M. Peters, D. Haase, W. Saak, *Z. Naturforsch. B* **1994**, *49*, 741; d) J. Möbs, J.-N. Luy, A. Shlyaykher, R. Tonner, J. Heine, *Dalton Trans.* **2021**, *50*, 15855.
[34] a) K. Kozawa, T. Uchida, *Acta Crystallogr. C* **1990**, *46*, 1006; b) L. Antolini, A. Benedetti, A. C. Fabretti, A. Giusti, *Dalton Trans.* **1988**, 2501; c) W.-Y. Yin, Y.-G. Weng, M. Jiang, S.-K. Yu, Q.-Y. Zhu, J. Dai, *Inorg. Chem.* **2020**, *59*, 5161; d) I. A. Ahmed, R. Blachnik, G. Kastner, W. Brockner, *Z. Anorg. Allg. Chem.* **2001**, *627*, 2261; e) H. Krautscheid, *Z. Anorg. Allg. Chem.* **1994**, *620*, 1559.
[35] H. C. Hsueh, R. K. Chen, H. Vass, S. J. Clark, G. J. Ackland, W. C.-K. Poon, J. Crain, *Phys. Rev. B* **1998**, *58*, 14812.
[36] H. Brasseur, L. Pauling, *J. Am. Chem. Soc.* **1938**, *60*, 2886.
[37] D. M. Trots, S. V. Myagkota, *J. Phys. Chem. Solids* **2008**, *69*, 2520.
[38] S. Alvarez, *Dalton Trans.* **2013**, *42*, 8617.
[39] G. Cavallo, P. Metrangolo, R. Milani, T. Pilati, A. Priimagi, G. Resnati, G. Terraneo, *Chem. Rev.* **2016**, *116*, 2478.
[40] N. Dehnhardt, J.-N. Luy, M. Szabo, M. Wende, R. Tonner, J. Heine, *Chem. Commun.* **2019**, *55*, 14725.
[41] W. Kaim, *Angew. Chem. Int. Ed. Engl.* **1983**, *22*, 171.
[42] a) D. Umeyama, L. Leppert, B. A. Connor, M. A. Manumpil, J. B. Neaton, H. I. Karunadasa, *Angew. Chem. Int. Ed.* **2020**, *59*, 19087; b) V. Y. Kotov, A. B. Ilyukhin, P. A. Buikin, N. P. Simonenko, A. A. Korlyukov, A. F. Smol'yakov, K. E. Yorov, A. V. Gavrikov, *Dalton Trans.* **2019**, *48*, 7602.
[43] L. Gao, X. Li, B. Traoré, Y. Zhang, J. Fang, Y. Han, J. Even, C. Katan, K. Zhao, S. Liu, et al., *J. Am. Chem. Soc.* **2021**, *143*, 12063.
[44] *TURBOMOLE Version 7.6*, TURBOMOLE GmbH, University of Karlsruhe and Forschungszentrum Karlsruhe (Germany), **2022**.
[45] J. P. Perdew, M. Ernzerhof, K. Burke, *J. Chem. Phys.* **1996**, *105*, 9982.
[46] F. Weigend, R. Ahlrichs, *Phys. Chem. Chem. Phys.* **2005**, *7*, 3297.
[47] B. Metz, H. Stoll, M. Dolg, *J. Chem. Phys.* **2000**, *113*, 2563.
[48] F. Weigend, *Phys. Chem. Chem. Phys.* **2006**, *8*, 1057.
[49] J. P. Perdew, K. Burke, M. Ernzerhof, *Phys. Rev. Lett.* **1996**, *77*, 3865.
[50] C. Holzer, Y. J. Franzke, *J. Chem. Phys.* **2022**, *157*, 034108.
[51] A. Schäfer, A. Klamt, D. Sattel, J. C. W. Lohrenz, F. Eckert, *Phys. Chem. Chem. Phys.* **2000**, *2*, 2187.
[52] a) M. Kühn, F. Weigend, *J. Chem. Theory Comput.* **2013**, *9*, 5341; b) F. Weigend, A. Baldes, *J. Chem. Phys.* **2010**, *133*, 174102.

Manuscript received: September 19, 2022
Accepted manuscript online: October 4, 2022
Version of record online: November 14, 2022

3.5 Optical Properties and Metal-Dependent Charge Transfer in Iodido Pentelates

Jakob Möbs, Gina Stuhrmann, Stefan Wippermann and Johanna Heine, *ChemPlusChem*, **2023**, e202200403, DOI:10.1002/cplu.202200403.

Abstract

Lead-free heavy halogenido metalates are currently under intense investigation, as they show similar promising semiconducting properties as their famous but toxic lead relatives. A major interest in this regard is the understanding and control of optical properties with the goal of designing highly efficient photoconducting materials. Here, we present two isostructural iodido pentelates $(Hpyz)_3E_2I_9 \cdot 2\,H_2O$ (pyz = pyrazine; E = Sb, Bi). Both compounds are stable up to 100 °C. We observe an inverted order of band gap sizes, 1.91 eV and 1.98 eV for the antimony and bismuth compound, respectively, compared to similar pairs of compounds. We use DFT calculations to confirm that this surprising finding can be traced back to the presence of charge transfer excitations in both compounds.

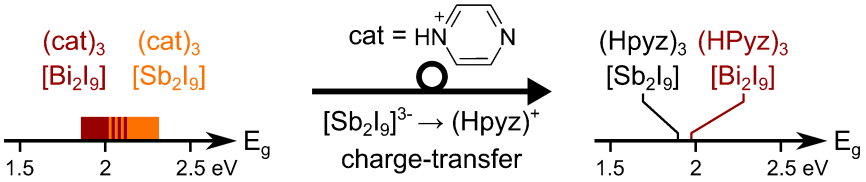

Figure 3.5: Table-of-contents graphic of "Optical Properties and Metal-Dependent Charge Transfer in Iodido Pentelates".

Summary

The preparation and properties of two isostructural group 15 iodido metalates, $(Hpyz)_3E_2I_9 \cdot 2\,H_2O$ (pyz = pyrazine; E = Sb (**1**), Bi (**2**)), are reported. They feature binuclear $[E_2I_9]^{3-}$-anions of two face-sharing $\{EI_6\}$-octahedra and singly protonated pyrazinium cations that are interconnected by hydrogen bonds and co-crystallized water. There are short contacts between the iodine atoms and the pyrazinium cations with centroid to iodine distances as low as 3.737 Å for **1** and 3.574 Å for **2**. These distances are very close to those found in similar compounds, where anion-to-pyrazinium charge transfer has been observed.

When looking at examples of pairs of isostructural antimonates and bismuthates in the literature, the bismuth compounds generally show optical band gaps that are 0.08 eV to 0.20 eV smaller than those of the antimony compounds. For **1** and **2**, however, this order is inverted with **1** having an optical band gap of 1.91 eV and **2** of 1.98 eV. Similar to what was observed with $[Hpyz]_4[Sb_{10}I_{34}]$, the close proximity of pyrazinium ions to the anion should give rise to an anion-to-cation charge transfer excitation that narrows the optical band gap in both cases. Computational investigations confirmed this hypothesis, and for both compounds the CBM is composed mostly of iodine *p*-states, while VBM comprises the pyrazinium π*-orbitals. Due to

differences in the absolute energies, however, the effect of this charge transfer on the band gap is much larger for the antimony compound explaining the reverse order observed experimentally.

Own contribution

All syntheses were planned by myself and executed by myself or Gina Stuhrmann under my supervision. Crystallographic measurements, solutions and refinements as well as UV-Vis measurements were done by myself. Thermo-gravimetric measurements were done by Uwe Justus. Quantum chemical calculations were carried out by Stefan Wippermann. The manuscript was written through contributions of Johanna Heine Stefan Wippermann and myself.

ChemPlusChem

Research Article
doi.org/10.1002/cplu.202200403

Chemistry Europe
European Chemical Societies Publishing

www.chempluschem.org

Special Issue

Optical Properties and Metal-Dependent Charge Transfer in Iodido Pentelates

Jakob Möbs,[a] Gina Stuhrmann,[a] Stefan Wippermann,[b] and Johanna Heine*[a]

Lead-free heavy halogenido metalates are currently under intense investigation, as they show similarly promising semiconducting properties as their famous but toxic lead relatives. A major interest in this regard is the understanding and control of optical properties with the goal of designing highly efficient photoconducting materials. Here, we present two isostructural iodido pentelates $(Hpyz)_3E_2I_9 \cdot 2H_2O$ (pyz=pyrazine; E=Sb, Bi). Both compounds are stable up to 100 °C. We observe an inverted order of band gap sizes, 1.91 eV and 1.98 eV for the antimony and bismuth compound, respectively, compared to similar pairs of compounds. We use DFT calculations to confirm that this surprising finding can be traced back to the presence of charge transfer excitations in both compounds.

Introduction

Inspired by the success of lead halide perovskites as solar absorber materials,[1] main group halogenido metalates have developed into an active field of semiconductor material research encompassing applications such as solid state lighting,[2] detector materials for X-rays and high energy particles[3] and novel photocatalysts.[4] Antimony and bismuth based materials provide the added benefit of avoiding the environmental instability[5] and significant toxicity of lead halide perovskites[6] and have been used in memristors,[7] remote thermography[8] and battery materials.[9]

Heavy halogenido pentelates with $[E_xX_y]^{q-}$ anions (E=Sb, Bi; X=Cl, Br, I) display a highly variable structural chemistry with molecular, chain-like, layered and network anions typically based on $\{EX_6\}$ units connected via corner-, edge- or face-sharing.[10] The dinuclear ions $[E_2X_9]^{3-}$, $[E_2X_{10}]^{4-}$ and $[E_2X_{11}]^{5-}$, shown in Scheme 1, are especially ubiquitous species and constitute important species in the solution chemistry of halogenido pentelates.[11]

The first examples of compounds featuring them have been reported as early as 1897,[12] with single crystal determinations following in 1955.[13] Despite this long history, methods to rationally modify the optical properties of these compounds are of continuing interest. The use of organic cations functioning as cationic acceptors can dramatically change the light absorption of the respective material through charge-transfer (CT) effects.[14] This has been studied for viologens[15] and tetrathiafulvalenes[16] in some depth, however, CT phenomena in materials featuring other cations have remained under-explored, especially across series of isostructural compounds.[17]

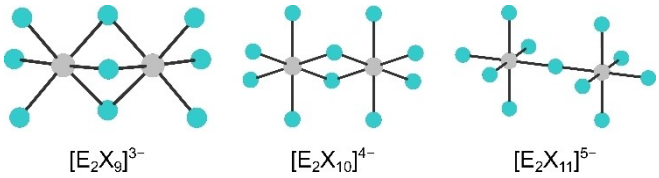

Scheme 1. Ball and stick models of the halogenido pentelates anions $[E_2X_9]^{3-}$, $[E_2X_{10}]^{4-}$ and $[E_2X_{11}]^{5-}$ with halogen atoms shown in cyan and metal atoms shown in grey.

Here, we present the synthesis and characterization of two isostructural iodido pentelates $(Hpyz)_3E_2I_9 \cdot 2H_2O$ (pyz = pyrazine; E=Sb (**1**), Bi (**2**)). UV-Vis spectroscopy and the comparison with selected literature examples reveals that CT effects lower the optical band gap in the two materials and reverse the typically observed order of optical band gaps in isostructural antimony and bismuth iodide materials. This highlights the potential for using electron acceptors as templating organic cations in halogenido pentelates materials, but also underlines that CT may be found beyond the prototypical viologens and tetrathiafulvalenes.

Results and Discussion

Description of crystal structures

$(Hpyz)_3Sb_2I_9 \cdot 2H_2O$ (**1**) and $(Hpyz)_3Bi_2I_9 \cdot 2H_2O$ (**2**) crystallize from solutions of pyrazine and Sb_2O_3/Bi_2O_3 with the ratios corresponding to the target compositions in dilute hydroiodic acid.

[a] J. Möbs, G. Stuhrmann, Dr. J. Heine
Department of Chemistry
Philipps-University Marburg
Hans-Meerwein-Straße 4, 35032 Marburg (Germany)
E-mail: johanna.heine@chemie.uni-marburg.de
[b] Prof. Dr. S. Wippermann
Department of Physics
Philipps-University Marburg
Renthof 5, 35032 Marburg (Germany)

Supporting information for this article is available on the WWW under https://doi.org/10.1002/cplu.202200403

Special Issue *Part of a Special Collection: "From Light to Heavy: Advancing the Chemistry of Pnictogen Compounds"*

1 and **2** are isostructural and crystallize in the tetragonal crystal system with 8 formula units per unit cell. Note that the structures of **1** and **2** have been solved in the different but isomorphic space groups $P4_12_12$ and $P4_32_12$, respectively, from data collected at 230 K. Upon cooling to 100 K both compounds undergo a phase transition to the orthorhombic space group $P2_12_12_1$. Since the datasets collected at 100 K are of significantly worse quality than those collected at 230 K and the optical properties of the compounds were investigated at room temperature only the structures of the high temperature phases will be discussed.

The $[E_2I_9]^{3-}$-anions are composed of two face-sharing $\{EI_6\}$-octahedra. For **1** Sb–I-distances range from 2.820 Å to 2.879 Å for terminating iodido ligands and from 3.201 Å to 3.365 Å for bridging ones. The respective values for **2** are 2.893 Å to 2.950 Å and 3.234 Å to 3.366 Å. In both cases this is well in line with what is found for other compounds featuring the same anionic motif measured at similar temperatures.[18–20] The anions are surrounded by pyrazinium cations, which are interconnected via hydrogen bonding with co-crystallized water (see Figure 1A/B). Although, it was not possible to reliably locate the hydrogen position in the electron density map, we assume that each pyrazine moiety is singly protonated, as this fits the overall charge. Additionally, we observed in previous works that pyrazine does not form di-cations under the reaction conditions employed in the synthesis of **1** and **2**.[21] One of the three crystallographically independent pyrazinium ions is disordered over two positions. For both **1** and **2** the occupancies were refined freely to about $^3/_4$ and $^1/_4$ for the two parts.

Furthermore, significantly short iodine to pyrazine contacts are observed with the shortest centroid-to-iodine distance being 3.72 Å for **1** and 3.57 Å for **2** (see Figure 1C/D). For the antimony compound this is very close to the corresponding distance of 3.75 Å observed in $(Hpyz)_4Sb_{10}I_{34}$ where it gives rise to a charge-transfer excitation between the anions and cations.[21]

Optical Properties

When looking at the optical properties, specifically the optical band gap E_g, of isostructural iodido pentelates, a typical observation can be made: The bismuthates will generally display smaller values of E_g than the antimonates. This is shown for a number of examples in Table 1. We note that the absolute values of E_g can depend significantly on the specific technique used for measuring and whether single crystals, powders or thin films are investigated.[22] Thus, we only selected examples were measurements were conducted under the same conditions by the same group. Across these examples, the optical band gap of the respective bismuth compounds is 0.08–0.20 eV smaller than that of the isostructural antimony compound. This fits well with dimensional reduction deliberations[23] regarding the parent halides, which show optical band gaps of 2.2 eV for SbI_3[24] and 1.7 eV for BiI_3,[25] which are isostructural as well.[26] Interestingly, the opposite order of optical band gaps is typically observed in isostructural iodido stannates and plumbates, for example in $(CH_3NH_3)SnI_3$ (1.2 eV) and $(CH_3NH_3)PbI_3$ (1.5 eV), but also in more complex compounds[27] and is

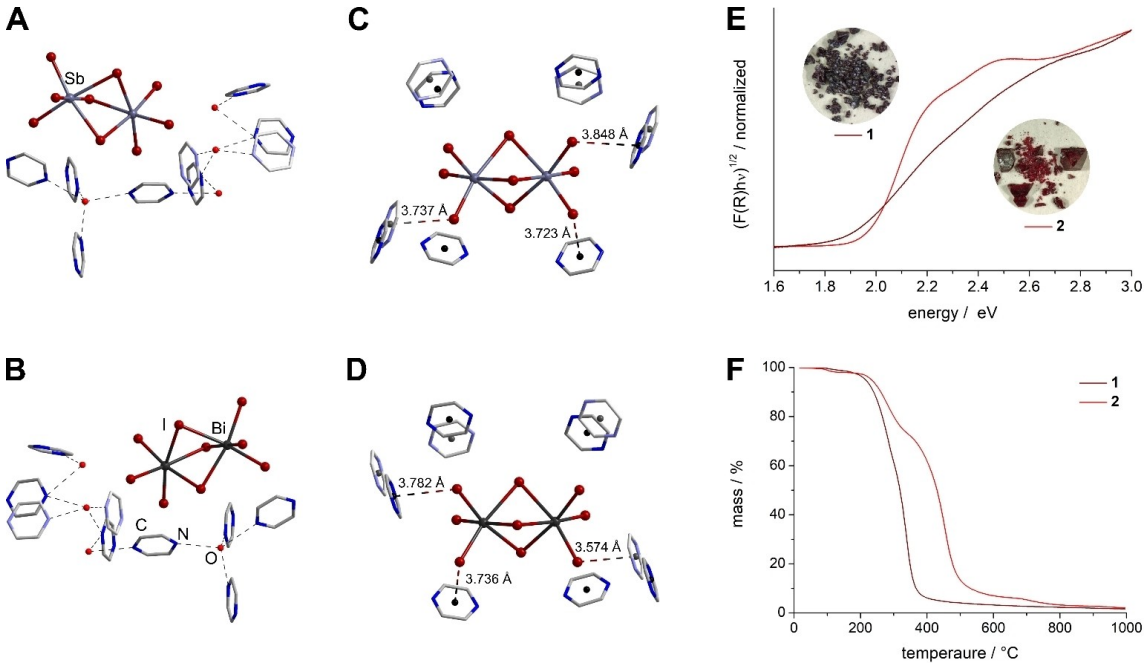

Figure 1. A/B: Structural motifs of **1** and **2**. Hydrogen bonds indicated as fragmented lines. **C/D**: Anions of **1** and **2** with surrounding pyrazine moieties, centroids shown as black balls. Centroid-to-iodine contacts of below 4 Å are highlighted. **A–D**: All hydrogen atoms are omitted for clarity, less occupied parts of disordered pyrazine molecules shown in lighter colours. **E**: Tauc-plots of diffuse reflection UV-Vis data of **1** and **2**. Photographs of crystals of the compounds shown as insets. **F**: Thermo-gravimetric measurements of **1** and **2**.

Table 1. Comparison of optical band gaps of isostructural antimony and bismuth compounds.

Compound	Optical band gap (in eV; E=Sb)	Optical band gap (in eV; E=Bi)	Ref.
$(C_3N_2H_5)_3E_2I_9$	2.10	1.97	[30]
$(CH_3NH_3)_3E_2I_9$	2.36	2.16	[31]
$(NH_2CHNH_2)_3E_2I_9$	1.99	1.85	[18,19]
$(S(CH_3)_3)_3E_2I_9$	2.27	2.10	[20]
$(C_8H_{11}FN)_4E_2I_{10}$	2.26	2.09	[32]
$(C_6H_9N_2O)EI_4$[a]	2.13	2.05	[33]
$Rb_3E_2I_9$[b]	2.03	1.93	[34]
$(Hpyz)_3E_2I_9 \cdot 2H_2O$	1.91	1.98	This work

[a] These compounds feature a chain-like anion. [b] These compounds feature a layered anion.

attributed to the higher electronegativity of tin compared to lead.[28] These deliberations should hold true for the pair Sb/Bi, where electronegativity differences are similar,[29] but apparently, other considerations are needed here.

We recorded diffuse reflectance UV-Vis spectra of both compounds against a $BaSO_4$-standard as a 5% mixture of the compound in $BaSO_4$. From Tauc-plots of these measurements (see Figure 1E) optical band gaps E_g of 1.91 eV for **1** and 1.98 eV for **2** could be extracted.

In contrast to the typically observed difference between isostructural iodido antimonates and bismuthates, optical band gaps in **1** and **2** show an inverse order, with the antimony compound featuring the smaller band gap. We assign this phenomenon to a low energy CT-excitation from the antimonate to the pyrazinium ion, which has been observed before in pyrazinium iodido metallates. Quantum chemical investigations of the related $(Hpyz)_4Sb_{10}I_{34}$ revealed the HOMO to be mostly situated at the antimonate ion, while the LUMO is composed of π-orbitals of the pyrazinium ion. The relation of **1** and $(Hpyz)_4Sb_{10}I_{34}$ is also supported by the shape of the Tauc-plot. In both cases a very slow incline of the absorption with increasing energy is observed, in contrast to the generally quite sharp absorption edges found for other iodido pentelates.[21] For the bismuth compound the similarly small pyrazine–iodine contacts suggest that CT is also the main mechanism of absorption in this case. However, as shown by *Neilson* and co-workers for a series of tropylium halogenido pentelates the effect of the metalate-to-cation-CT on the optical band gap of bismuthates is weaker than for antimonates due to the energetically lower lying valence band maximum.[17]

Stability and Thermal Decomposition

Combined TG-DSC measurements were performed on both compounds. The TG data is shown in Figure 1F. Both compounds are stable up to around 100 °C, where the first step of decomposition occurs. For **2** this first step is finished at 130 °C after 1.9% of the initial mass are lost. This corresponds well to the overall part of 1.9% water in the compound. For **1** no distinct end of the first decomposition can be identified as it overlaps with the second and main decomposition step, which is mostly finished at 500 °C and corresponds to the complete evaporation of the compound. For **2** the main decomposition occurs between 180 °C and 600 °C as a combination of two overlapping steps. Small endothermic peaks can be found in the DSC-data (see Supporting Information) at 180 °C for **1** and 205 °C for **2** indicating the melting of both compounds at the beginning of decomposition.

Computational Investigations

Density-functional theory (DFT) simulations were performed, starting from the crystallographically determined structures. We observed only minor deviations during structural relaxation via the DFT-calculated forces, cf. supplemental information. Figure 2a/c shows the projected densities of states (PDOS) of $(Hpyz)_3Sb_2I_9$ and $(Hpyz)_3Bi_2I_9$, respectively.

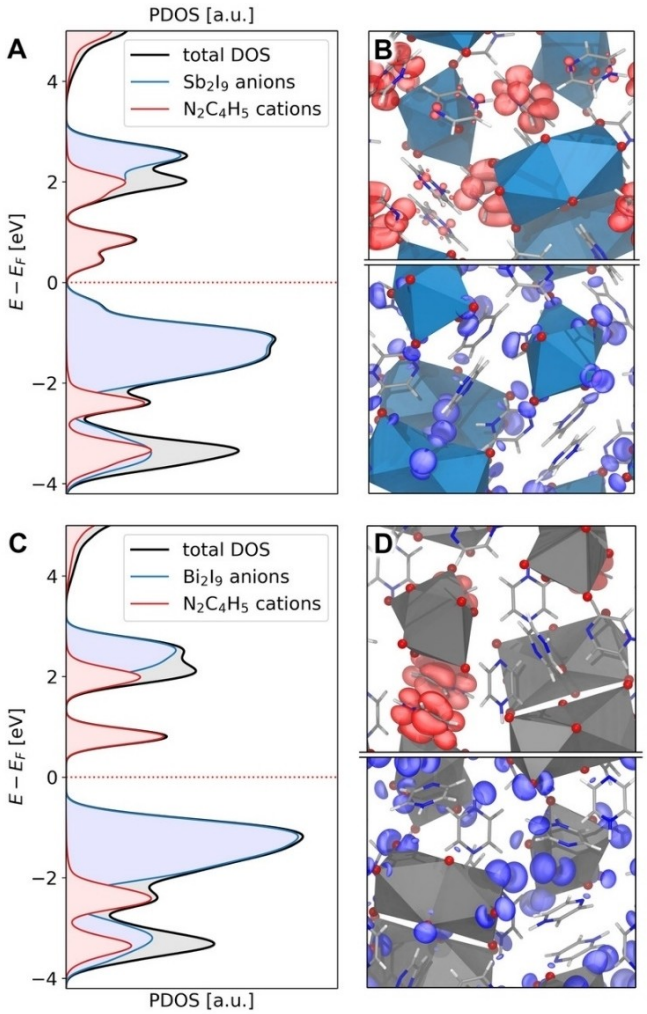

Figure 2. A/C: Projected densities of states (PDOS) of $(Hpyz)_3Sb_2I_9$ and $(Hpyz)_3Bi_2I_9$, respectively. In both cases, the valence band maxima (VBM) are located at the metalate anions, whereas the conduction band minima are localized to the pyrazinium cations. **B/D**: Isodensity plots of the VBM and CBM square wavefunction moduli at an isodensity value of 0.003 e^-/A^3, respectively.

Both compounds feature indirect band gaps of 0.81 eV and 1.41 eV, respectively. The valence bands consist predominantly of iodine *p* states in both cases. The conduction bands are comprised of localized π* states, originating from the pyrazinium cations. Figure 2b/d shows the square moduli of the wavefunctions associated with the band edges for each of the compounds, indicating that the fundamental excitations involve a charge transfer from the metalate anions to the pyrazinium cations. Our findings are in line with an analogous charge transfer reported by Neilson for tropylium iodido pentelates.[17]

Conclusion

To summarize our work, we have prepared two new pyrazinium iodido metalates and discussed their crystal structures including a phase transition upon cooling to 100 K. A discrepancy in the optical absorption of these compounds compared to similar literature-known materials revealed that a metalate-to-cation charge transfer is responsible for the narrower band gap of the antimony compound. This highlights the need to further investigate the effect of smaller cations beyond the classical acceptors like viologens or tetrathiafulvalenes on the optical properties and electronic structure of heavy halogenido metalates. This approach can provide a powerful tool to tune the absorption properties in halogenido pentelate materials.

Experimental Section

General: Sb_2O_3, Bi_2O_3, pyrazine and HI (57% solution in water, stabilizer: 0.75% H_3PO_2) were used as supplied from commercial sources. Pyrazinium iodide was synthesized according to our previously published method.[21] Acetonitrile was generally flash-distilled prior to use. For filtration cellulose filters with a pore size of 5–8 μm were used. Reactions and crystallizations were performed under inert conditions to avoid the formation of polyiodides. CHN analysis was carried out on an Elementar CHN-analyzer. Thermal analysis was carried out by simultaneous DSC/TG on a NETZSCH STA 409C/CD in the temperature range of 25 °C to 1000 °C with a heating rate of 10 °C min^{-1} in a constant flow of 80 mL min^{-1} N_2. Powder patterns were recorded on a STADI MP (STOE Darmstadt) powder diffractometer, with CuKα1 radiation with λ = 1.54056 Å at room temperature in transmission mode. Optical absorption spectra were recorded on a Varian Cary 5000 UV/Vis/NIR spectrometer in the range of 200–800 nm in diffuse reflectance mode employing a Praying Mantis accessory (Harrick). The raw data was transformed from reflectance R to absorption according to the Kubelka-Munk function *F*(*R*) and then plotted as a Tauc-plot, assuming an indirect allowed transition (see Supporting Information for details).

Synthesis

$(Hpyz)_3Sb_2I_9 \cdot 2H_2O$ (1). A total of 58 mg of Sb_2O_3 (0.2 mmol) and 48 mg pyrazine (0.6 mmol) were dissolved into 10 mL of hydroiodic acid (c = 2 mol/L) by stirring at 110 °C for 30 min. The resulting clear orange solution was filtered while still hot and left for crystallization at room temperature. Over the course of a week, large dark red crystals were formed. The crystals were collected and rinsed twice with 2 mL of cold acetone and twice with 2 mL of pentane. Yield: 103 mg (31%). CHN (calculated): C 8.70 (8.66), H 1.17 (1.15), N 4.98 (5.05).

$(Hpyz)_3Bi_2I_9 \cdot 2H_2O$ (2): A total of 47 mg of Bi_2O_3 (0.1 mmol) and 24 mg pyrazine (0.3 mmol) were dissolved into 5 mL of hydroiodic acid (c = 1 mol/L) by stirring at 110 °C for 30 min. The resulting clear red solution was filtered while still hot and left for crystallization at room temperature. After one day, large red crystals had formed, which were collected and dried on filter paper in air. Yield: 126.5 mg (69%). CHN (calculated): C 7.69 (7.84), H 1.10 (1.04), N 4.39 (4.57).

Crystallography: Single crystal X-ray determination was performed on a Bruker Quest D8 diffractometer with microfocus MoK_α radiation and a Photon 100 (CMOS) detector or a STOE StadiVari diffractometer with MoK_α radiation and a Detectris Pilatus 100 K detector. The structures were solved using direct methods, refined by full-matrix least-squares techniques and expanded using Fourier techniques, using the ShelX software package[35] within the OLEX2 suite.[36] Pictures of the crystal structures were created using DIAMOND.[37] For additional details on individual refinements, including disorder and twinning found in a number of structures, we refer the reader to the Supporting Information.

Deposition Number(s) 2213023, 2213024, 2213025 contain(s) the supplementary crystallographic data for this paper. These data are provided free of charge by the joint Cambridge Crystallographic Data Centre and Fachinformationszentrum Karlsruhe Access Structures service.

Microscopic Theory: Density-functional theory (DFT) simulations were performed within the generalized gradient approximation (GGA-PBE)[38] as implemented within the *Vienna* ab initio *simulation package* (VASP).[39] The electronic structure was described by projector-augmented wave potentials with a plane-wave basis set limited to a cutoff energy of $E_C = 550$ eV. We used periodic boundary conditions and an 8x8x8 Monkhorst-Pack mesh was used to sample the Brillouin zone. The structural data obtained from the crystallographical measurements were used as starting points for structural relaxations. We relaxed the forces until a threshold of < 0.01 eV/A was reached. Illustrations of the charge densities were created using VMD.[40]

Acknowledgements

This research was funded by the German Research Foundation DFG (HE 8018/1 and 505757318). J. H. thanks Prof. Stefanie Dehnen for her support. Open Access funding enabled and organized by Projekt DEAL.

Conflict of Interest

The authors declare no conflict of interest.

Data Availability Statement

The data that support the findings of this study are available in the supplementary material of this article.

Keywords: antimony · band gaps · bismuth · charge transfer · iodine

[1] a) A. Kojima, K. Teshima, Y. Shirai, T. Miyasaka, *J. Am. Chem. Soc.* **2009**, *131*, 6050; b) A. K. Jena, A. Kulkarni, T. Miyasaka, *Chem. Rev.* **2019**, *119*, 3036; c) L. Chouhan, S. Ghimire, C. Subrahmanyam, T. Miyasaka, V. Biju, *Chem. Soc. Rev.* **2020**, *49*, 2869.
[2] J. Chen, H. Xiang, J. Wang, R. Wang, Y. Li, Q. Shan, X. Xu, Y. Dong, C. Wei, H. Zeng, *ACS Nano* **2021**, *15*, 17150.
[3] X. Yu, H. N. Tsao, Z. Zhang, P. Gao, *Adv. Opt. Mater.* **2020**, *8*, 2001095.
[4] K. Ren, S. Yue, C. Li, Z. Fang, K. A. M. Gasem, J. Leszczynski, S. Qu, Z. Wang, M. Fan, *J. Mater. Chem. A* **2022**, *10*, 407.
[5] R. L. Z. Hoye, R. E. Brandt, A. Osherov, V. Stevanović, S. D. Stranks, M. W. B. Wilson, H. Kim, A. J. Akey, J. D. Perkins, R. C. Kurchin, J. R. Poindexter, E. N. Wang, M. G. Bawendi, V. Bulović, T. Buonassisi, *Chem. Eur. J.* **2016**, *22*, 2605.
[6] a) G. Schileo, G. Grancini, *J. Mater. Chem. C* **2021**, *9*, 67; b) S. Sundar, J. Chakravarty, *Int. J. Environ. Res. Public Health* **2010**, *7*, 4267; c) D. M. Griffith, H. Li, M. V. Werrett, P. C. Andrews, H. Sun, *Chem. Soc. Rev.* **2021**, *50*, 12037.
[7] X.-F. Cheng, W.-H. Qian, J. Wang, C. Yu, J.-H. He, H. Li, Q.-F. Xu, D.-Y. Chen, N.-J. Li, J.-M. Lu, *Small* **2019**, *15*, e1905731.
[8] V. Morad, S. Yakunin, B. M. Benin, Y. Shynkarenko, M. J. Grotevent, I. Shorubalko, S. C. Boehme, M. V. Kovalenko, *Adv. Mater.* **2021**, *33*, e2007355.
[9] K. Roy, T. Li, S. Ogale, N. Robertson, *J. Mater. Chem. A* **2021**, *9*, 2689.
[10] a) G. A. Fisher, N. C. Norman, *Adv. Inorg. Chem.* **1994**, *41*, 233; b) L.-M. Wu, X.-T. Wu, L. Chen, *Coord. Chem. Rev.* **2009**, *253*, 2787; c) N. Mercier, N. Louvain, W. Bi, *CrystEngComm* **2009**, *11*, 720; d) S. A. Adonin, M. N. Sokolov, V. P. Fedin, *Coord. Chem. Rev.* **2016**, *312*, 1; e) S. A. Adonin, M. N. Sokolov, V. P. Fedin, *Russ. J. Inorg. Chem.* **2017**, *62*, 1789.
[11] R. Rowe, K. R. J. Lovelock, P. A. Hunt, *J. Chem. Phys.* **2021**, *155*, 14501.
[12] H. Wells, H. W. Foote, *Am. J. Sci.* **1897**, *s4–3*, 461.
[13] L. Cavalca, M. Nardelli, A. Braibanti, *Gazz. Chim. Ital.* **1955**, *85*, 1239.
[14] a) J. K. Pious, M. G. Basavarajappa, C. Muthu, N. Krishna, R. Nishikubo, A. Saeki, S. Chakraborty, C. Vijayakumar, *J. Phys. Chem. Lett.* **2020**, *11*, 6757; b) J. K. Pious, C. Muthu, C. Vijayakumar, *Acc. Chem. Res.* **2022**, *55*, 275.
[15] a) G. Xu, G.-C. Guo, M.-S. Wang, Z.-J. Zhang, W.-T. Chen, J.-S. Huang, *Angew. Chem. Int. Ed.* **2007**, *46*, 3249; b) N. Leblanc, M. Allain, N. Mercier, L. Sanguinet, *Cryst. Growth Des.* **2011**, *11*, 2064; c) N. Leblanc, N. Mercier, M. Allain, O. Toma, P. Auban-Senzier, C. Pasquier, *J. Solid State Chem.* **2012**, *195*, 140; d) C. Sun, M.-S. Wang, P.-X. Li, G.-C. Guo, *Angew. Chem. Int. Ed.* **2017**, *56*, 554.
[16] W.-Y. Yin, Y.-G. Weng, M. Jiang, S.-K. Yu, Q.-Y. Zhu, J. Dai, *Inorg. Chem.* **2020**, *59*, 5161.
[17] I. W. H. Oswald, E. M. Mozur, I. P. Moseley, H. Ahn, J. R. Neilson, *Inorg. Chem.* **2019**, *58*, 5818.
[18] P. Szklarz, A. Gągor, R. Jakubas, P. Zieliński, A. Piecha-Bisiorek, J. Cichos, M. Karbowiak, G. Bator, A. Ciżman, *J. Mater. Chem. C* **2019**, *7*, 3003.
[19] P. Szklarz, R. Jakubas, A. Gągor, G. Bator, J. Cichos, M. Karbowiak, *Inorg. Chem. Front.* **2020**, *7*, 1780.
[20] J. Möbs, S. Pan, R. Tonner-Zech, J. Heine, *Dalton Trans.* **2022**, *51*, 13771.
[21] J. Möbs, G. Stuhrmann, F. Weigend, J. Heine, *Chem. Eur. J.* **2022**, *29*, e2022029.
[22] R. Hooijer, A. Weis, A. Biewald, M. T. Sirtl, J. Malburg, R. Holfeuer, S. Thamm, A. A. Y. Amin, M. Righetto, A. Hartschuh, L. M. Herz, T. Bein, *Adv. Opt. Mater.* **2022**, *10*, 2200354.
[23] E. G. Tulsky, J. R. Long, *Chem. Mater.* **2001**, *13*, 1149.
[24] K. A. Mady, A. H. Eid, W. Z. Soliman, *Czech. J. Phys.* **1979**, *29*, 907.
[25] N. J. Podraza, W. Qiu, B. B. Hinojosa, M. A. Motyka, S. R. Phillpot, J. E. Baciak, S. Trolier-McKinstry, J. C. Nino, *J. Appl. Phys.* **2013**, *114*, 33110.
[26] H. C. Hsueh, R. K. Chen, H. Vass, S. J. Clark, G. J. Ackland, W. C.-K. Poon, J. Crain, *Phys. Rev. B* **1998**, *58*, 14812.
[27] X. Li, Y. He, M. Kepenekian, P. Guo, W. Ke, J. Even, C. Katan, C. C. Stoumpos, R. D. Schaller, M. G. Kanatzidis, *J. Am. Chem. Soc.* **2020**, *142*, 6625.
[28] D. B. Straus, C. R. Kagan, *J. Phys. Chem. Lett.* **2018**, *9*, 1434.
[29] A. L. Allred, E. G. Rochow, *J. Inorg. Nucl. Chem.* **1958**, *5*, 264.
[30] P. Szklarz, R. Jakubas, W. Medycki, A. Gągor, J. Cichos, M. Karbowiak, G. Bator, *Dalton Trans.* **2022**, *51*, 1850.
[31] S. Chatterjee, J. Payne, J. T. S. Irvine, A. J. Pal, *J. Mater. Chem. A* **2020**, *8*, 4416.
[32] N. Dehnhardt, M. Axt, J. Zimmermann, M. Yang, G. Mette, J. Heine, *Chem. Mater.* **2020**, *32*, 4801.
[33] A. J. Dennington, M. T. Weller, *Dalton Trans.* **2018**, *47*, 3469.
[34] K. M. McCall, C. C. Stoumpos, S. S. Kostina, M. G. Kanatzidis, B. W. Wessels, *Chem. Mater.* **2017**, *29*, 4129.
[35] a) G. M. Sheldrick, *Acta Crystallogr. Sect. A* **2008**, *64*, 112; b) G. M. Sheldrick, *Acta Crystallogr.* **2015**, *71*, 3; c) G. M. Sheldrick, *Acta Crystallogr. Sect. A* **2015**, *71*, 3.
[36] O. V. Dolomanov, L. J. Bourhis, R. J. Gildea, J. A. K. Howard, H. Puschmann, *J. Appl. Crystallogr.* **2009**, *42*, 339.
[37] K. Brandenburg, *Diamond*, Crystal Impact GbR, Bonn, Germany, **2005**.
[38] J. P. Perdew, K. Burke, M. Ernzerhof, *Phys. Rev. Lett.* **1996**, *77*, 3865.
[39] a) G. Kresse, J. Furthmüller, *Phys. Rev. B* **1996**, *54*, 11169; b) G. Kresse, J. Hafner, *Phys. Rev. B* **1993**, *47*, 558.
[40] W. Humphrey, A. Dalke, K. Schulten, *J. Mol. Graphics* **1996**, *14*, 27–8.

Manuscript received: November 14, 2022
Revised manuscript received: March 10, 2023
Accepted manuscript online: March 20, 2023

3.6 Enhanced Circular Dichroism and Polarized Emission in an Achiral, Low Bandgap Bismuth Iodide Perovskite Derivative

Jakob Möbs, Gina Stuhrmann, Stefan Wippermann and Johanna Heine, *J. Am. Chem. Soc.*, **2023**, *published online*, DOI:10.1021/jacs.3c06141.

Abstract

Lead halide perovskites and related main group halogenido metalates offer unique semiconductor properties and diverse applications in photovoltaics, solid-state lighting, and photocatalysis. Recent advances in incorporating chiral organic cations have led to the emergence of chiral metal-halide semiconductors with intriguing properties such as chiroptical activity and chirality-induced spin selectivity, enabling the generation and detection of circularly polarized light and spin-polarized electrons for applications in spintronics and quantum information. However, understanding the structural origin of chiroptical activity remains challenging due to macroscopic factors and experimental limitations. In this work, we present an achiral perovskite derivative $[Cu_2(pyz)_3(MeCN)_2][Bi_3I_{11}]$ (**CuBiI**; pyz = pyrazine; MeCN = acetonitrile), which exhibits remarkable circular dichroism attributed to the material's non-centrosymmetric nature. **CuBiI** features a unique structure as a poly-threaded iodido bismuthate, with $[Bi_3I_{11}]^{2-}$ chains threaded through a cationic two-dimensional coordination polymer. The material possesses a low, direct optical band gap of 1.70 eV. Notably, single crystals display both linear and circular optical activity, with a large anisotropy factor of up to 0.16. Surprisingly, despite the absence of chiral building blocks, CuBiI exhibits a significant degree of circularly-polarized photoluminescence, reaching 4.9 %. This value is comparable to the results achieved by incorporating chiral organic molecules into perovskites, typically ranging from 3 – 10 % at zero magnetic field. Our findings provide insights into the macroscopic origin of circular dichroism and offer design guidelines for developing materials with high chiroptical activity.

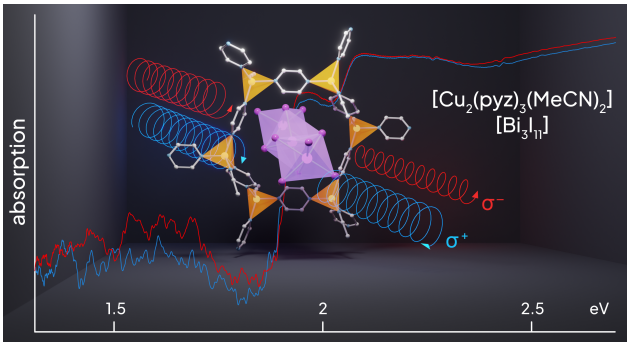

Figure 3.6: Table-of-contents graphic of "Enhanced Circular Dichroism and Polarized Emission in an Achiral, Low Bandgap Bismuth Iodide Perovskite Derivative".

Summary

This publication is focused on the compound $[Cu_2(pyz)_3(MeCN)_2][Bi_3I_{11}]$ (**CuBiI**), which shows a variety of interesting features. It crystallizes in the non-centrosymmetric, but achiral space group *Cc*, giving rise to a series of chiroptical properties like circular dichroism or circularly polarized emission. Such properties are generally associated with compounds where chirality and non-centrosymmetry are enforced through chiral organic molecules or ions. However, they are not the effect of these chiral building blocks but rather the complete macroscopic single crystal. Therefore, they can, in theory, be observed in all compounds that crystallize in a suitable non-centrosymmetric and non-enantiomorphous crystal class like m, $mm2$, $\overline{4}$ or $\overline{4}2m$. Although this has long been known, it is mostly overlooked in modern research and chiroptical properties are generally only investigated for compounds with chiral building blocks.

In **CuBiI**, {Cu(MeCN)}-units are connected via pyrazine ligands into cationic, honeycomb-like 2d layers, which are stacked in an AB-fashion. Through these layers, chain-like $[Bi_3I_{11}]^{2-}$-anions are threaded. The anions are built up of trimers of face sharing $\{BiI_6\}$-octahedra that are connected via shared corners into chains. This is similar to the connectivity of $\{RuO_6\}$-octahedra in $BaRuO_3$, a stacking variant of the perovskite structure family in between the hexagonal and cubic perovskite structures. The structure of **CuBiI** can be understood as a distorted and vacancy-ordered derivative of the $BaRuO_3$ structure type.
CuBiI has a direct band gap of 1.70 eV at room temperature, which is quite narrow compared to other compounds with similar 1d-anionic motifs. This is most likely due to a charge transfer excitation between the iodido and pyrazine ligands, as there are significantly short I-pyz distances, similar to those described in sections 3.4 and 3.5, connecting the cations and anions. At 4 K the band gap is widened to 1.89 eV and the compound also shows a sharp photoluminescence peak centered around 1.93 eV. Both absorption and photoluminescence show dependence on the polarization of the light, linearly as well as circularly. The circular dichroism is especially strong with an optical anisotropy factor of $g_{CD} = 0.16$, which is the largest value in the context of halide perovskites and their derivatives reported to date. The reason for this lies in the high quality of the single crystals as well as a very precise measurement setup with high spatial resolution, thus, eliminating errors from differently oriented neighbouring domains. To ensure the reliability of the data great care was taken to extract the genuine circular dichroism from the measurement which also includes contributions of linear dichroism and linear birefringence.

Overall, the results show that it is not strictly necessary to use chiral cations to obtain products with strong chiroptical properties—as long as the crystal symmetry allows for such—but that high quality of the crystals is greatly beneficial. Several lead halide perovskites or their derivatives are known that crystallize in the needed space groups. In combination with the experience in fabrication of high-quality crystalline materials in the halide perovskite community, this is a great opportunity for future applications in the detection or generation of circularly polarized light or electron spin in the field of spintronics.

Own contribution

All syntheses were planned by myself and executed by myself or Gina Stuhrmann under my supervision. Crystallographic measurements, solutions and refinements as well as initial diffuse reflectance UV-Vis measurements at room temperature were done by myself. Temperature- and polarization-dependent UV-Vis and luminescence measurements were carried out by Philip Klement, Lukas Gübel and Marius Müller. Thermo-gravimetric measurements were done by Uwe Justus. The manuscript was written through contributions of Philip Klement, Sangam Chatterjee, Johanna Heine and myself.

JACS
JOURNAL OF THE AMERICAN CHEMICAL SOCIETY
pubs.acs.org/JACS
Article

Enhanced Circular Dichroism and Polarized Emission in an Achiral, Low Band Gap Bismuth Iodide Perovskite Derivative

Jakob Möbs, Philip Klement, Gina Stuhrmann, Lukas Gümbel, Marius J. Müller, Sangam Chatterjee, and Johanna Heine*

Cite This: https://doi.org/10.1021/jacs.3c06141
Read Online

ABSTRACT: Lead halide perovskites and related main-group halogenido metalates offer unique semiconductor properties and diverse applications in photovoltaics, solid-state lighting, and photocatalysis. Recent advances in incorporating chiral organic cations have led to the emergence of chiral metal-halide semiconductors with intriguing properties, such as chiroptical activity and chirality-induced spin selectivity, enabling the generation and detection of circularly polarized light and spin-polarized electrons for applications in spintronics and quantum information. However, understanding the structural origin of chiroptical activity remains challenging due to macroscopic factors and experimental limitations. In this work, we present an achiral perovskite derivative $[Cu_2(pyz)_3(MeCN)_2][Bi_3I_{11}]$ (**CuBiI**; pyz = pyrazine; MeCN = acetonitrile), which exhibits remarkable circular dichroism (CD) attributed to the material's noncentrosymmetric nature. **CuBiI** features a unique structure as a poly-threaded iodido bismuthate, with $[Bi_3I_{11}]^{2-}$ chains threaded through a cationic two-dimensional coordination polymer. The material possesses a low, direct optical band gap of 1.70 eV. Notably, single crystals display both linear and circular optical activity with a large anisotropy factor of up to 0.16. Surprisingly, despite the absence of chiral building blocks, **CuBiI** exhibits a significant degree of circularly polarized photoluminescence, reaching 4.9%. This value is comparable to the results achieved by incorporating chiral organic molecules into perovskites, typically ranging from 3−10% at zero magnetic field. Our findings provide insights into the macroscopic origin of CD and offer design guidelines for the development of materials with high chiroptical activity.

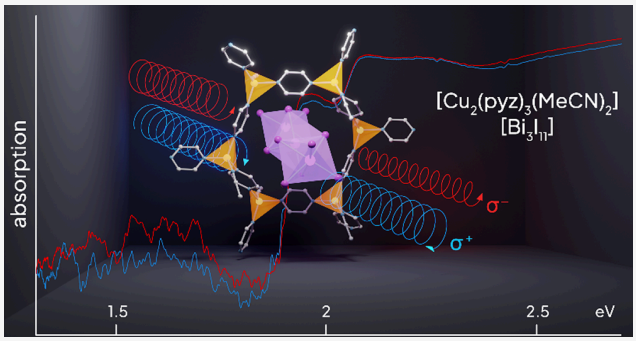

INTRODUCTION

Chirality refers to the property that an object is not superimposable in its mirror image.[1] Common macroscopic examples of so-called enantiomers are the human hands, leading to the term handedness for distinction. Chirality has profound implications in various fields such as pharmacology, biology, and medicine,[2] where the correct handedness of drugs is crucial.[3] In spintronics, chirality enables the manipulation of spins for information processing, particularly in quantum technology.[4,5] Chiral materials exhibit distinct behavior when interacting with circularly polarized light, manifesting as optical activity in the forms of circular birefringence (CB) and circular dichroism (CD), where CD refers to the differential absorption of clockwise and counterclockwise circularly polarized light.

These chiroptical phenomena,[6,7] including optical rotation (OR) and circularly polarized luminescence (CPL), are commonly associated with chirality in molecules. In solution, OR and CD are routinely utilized to investigate the stereochemistry of chiral molecules and metal complexes.[8] While chiral molecules or ions typically crystallize in one of the 65 enantiomorphous Sohncke space groups,[9] it is noteworthy that achiral molecules or ions can also adopt these groups,[10] sometimes exhibiting spontaneous resolution.[11] Interestingly, chiroptical phenomena can arise in certain achiral compounds with unique symmetries, crystallizing in selected noncentrosymmetric, nonenantiomorphous crystal classes, namely *m*, *mm*2, $\bar{4}$, $\bar{4}2m$.[12,13] This property is predominantly observed in single crystals[14] and has been recognized for some time.[12,13,15] Its utilization remains limited due to the practical challenges of investigating nonenantiomorphous single crystals[14] and the traditional association of chiroptical phenomena with chirality,[7] although the latter has also been challenged by investigations in 2D and metamaterials.[16,17]

Main group halogenido metalates, represented by the formula $A_xE_yX_z$ (A = organic or inorganic cation; E = main

Received: June 12, 2023

group metal; X = halogen), are a class of semiconductors that have gained significant attention, particularly the widely studied lead halide perovskites.[18] These materials possess a diverse range of useful properties and find applications in areas such as photovoltaics,[19] solid-state lighting,[20] catalysis,[21] and ion conduction.[22] By employing different types of cations A, it is possible to control the metalate anion dimensionalities, which can vary from molecular species (0D) to chains (1D), layers (2D), and networks (3D).[23] The introduction of cationic metal complexes and coordination polymers into the chemistry of halogenido metalates offers exciting prospects for introducing additional functionalities, including specific magnetic properties,[24] luminescence,[25] or modified optical absorption behavior.[26]

Although there have been significant advances in the study of molecular metal complexes,[27,28] achieving the simultaneous formation of cationic coordination polymers and halogenido metalate anions remains a challenging task. Moreover, identifying compounds that exhibit coordination polymers and higher-dimensional halogenido metalate anions poses an even greater challenge. In theory, it is possible to observe mechanically interlocking motifs in such systems, which expands upon the concept of mechanical bonds[29] and their application in coordination polymers and metal−organic frameworks.[30] Additionally, the phenomena of polycatenation, polyknotting and polythreading, which are fundamental to the understanding of coordination polymers, come into play.[31]

Recently, there has been a growing interest in studying the chiroptical activity of chiral perovskites and other metal-halide materials that incorporate chiral organic cations.[32−35] This research has shed light on the possibility of observing chiroptical activity in compounds that lack chiral building blocks and do not crystallize in one of the 65 Sohncke groups.[36,37] Notable examples of such materials include $[K(dibenzo\text{-}18\text{-}crown\text{-}6)]_2MnX_4$ (X = Cl, Br), which crystallizes in the space group *Cc* and exhibits CPL.[38] Another example is $(4\text{-}AMP)BiI_5$ (4-AMP = 4-(aminomethyl)-piperidinium), which also crystallizes in the space group *Cc*, and displays CD and a circularly polarized light-dependent anomalous bulk photovoltaic effect.[39] These recent findings have motivated the investigation of the chiroptical properties of single crystals of **CuBiI**.

In this study, we synthesized single crystals of the achiral perovskite $[Cu_2(pyz)_3(MeCN)_2][Bi_3I_{11}]$ (**CuBiI;** pyz = pyrazine; MeCN = acetonitrile). **CuBiI** exhibits a unique structure, where $[Bi_3I_{11}]^{2-}$ chains are threaded through a cationic 2D coordination polymer, resulting in a poly-threaded iodido bismuthate. Remarkably, **CuBiI** single crystals display CD with a large anisotropy factor of 0.16, which originates in the material's noncentrosymmetric nature. The CD is free from linear contributions that we eliminate through rigorous methodology. Furthermore, the degree of circularly polarized photoluminescence is 4.9%, a surprisingly high value considering the absence of chiral building blocks. This finding is comparable to the approach of incorporating chiral organic molecules into perovskites, which resulted in 3−10% circularly polarized photoluminescence at zero magnetic field.[32,40]

RESULTS

Crystal Structure. We successfully synthesized an iodido bismuthate compound, $[Cu_2(pyz)_3(MeCN)_2][Bi_3I_{11}]$, through the reaction of BiI_3, CuI, and pyrazine (pyz) in an acetonitrile solution with a slight excess of pyrazine. Upon cooling the solution, the compound crystallizes as thick, dark red, hexagonally shaped plates in the noncentrosymmetric monoclinic spacegroup *Cc*. The product is obtained with a 40% yield.

The cationic part in **CuBiI** consists of a layer-like coordination polymer, where Cu^+ ions are tetrahedrally coordinated by three pyrazine molecules and one acetonitrile molecule. The pyrazine ligands interconnect the Cu atoms in such a way that topologically, a 6^3 honeycomb lattice results (Figure 1). The acetonitrile molecules are oriented above and

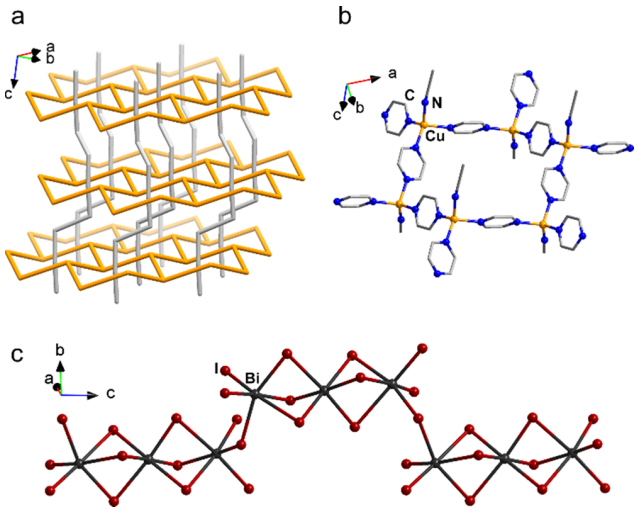

Figure 1. (a) Topology of the poly-threaded motif in **CuBiI**. Topology of the cationic coordination polymer shown in orange (Cu atoms directly connected), topology of the metalate chains shown in gray (Bi atoms directly connected). (b) Motif of the cationic 2D coordination polymer of **CuBiI**. (c) Motif of the anionic 1D-coordination polymer of **CuBiI**.

below the layers in an alternating fashion. Overall, waved layers parallel to the *ab*-plane result, akin to the arrangement found in gray arsenic. Layers show AB stacking; although dissimilar to gray arsenic, layers are only displaced with respect to each other along one and not both crystallographic directions normal to the stacking direction. Generally, due to their flexible coordination spheres, Cu(I) and Ag(I) have been intensely explored in early investigations of coordination polymers, especially when combined with pyrazine or the larger 4,4′-bipyridine ligand.[41−43] Interestingly, the same cationic coordination polymer found in **CuBiI** has been observed once before in $[Cu(pyz)_{3/2}(MeCN)][PF_6]\cdot 0.5(C_3H_6O)$.[44] With regard to the combination of Cu(I)-pyrazine coordination polymers and metalate anions, a number of compounds are known where these types of coordination polymers are combined with polyoxometalate anions.[45]

The anion motif in **CuBiI** is composed of trinuclear units where $\{BiI_6\}$ octahedra are connected through *trans* face-sharing—a fairly common anion type in iodido bismuthates.[46] In **CuBiI**, these units are further connected through corner-sharing into chains, a motif that has not been previously observed in main group halogenido metalate chemistry before. However, a number of compounds with anions of the same composition have been reported, including the condensed molecular anion $[Bi_3I_{11}]^{2-}$,[27] the larger molecular anion $[Bi_6I_{22}]^{4-}$, of which five different isomers are known,[47−51] and two different types of chain-like $[Bi_3I_{11}]^{2-}$ anions,[52,53]

https://doi.org/10.1021/jacs.3c06141
J. Am. Chem. Soc. XXXX, XXX, XXX−XXX

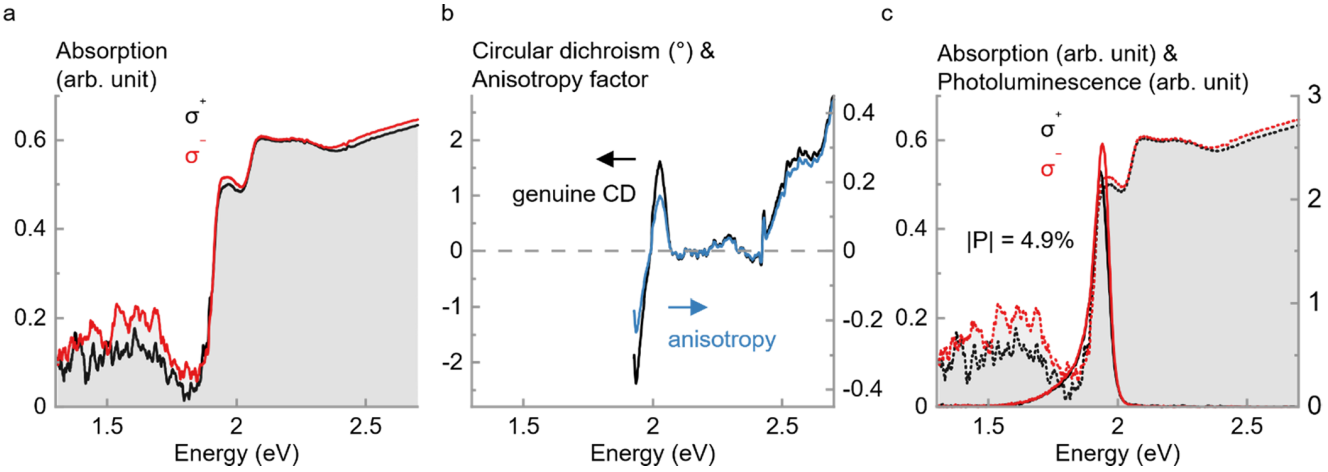

Figure 2. CD of CuBiI. (a) Absorption spectra for clockwise (σ^+, black) and counterclockwise (σ^-, red) circular polarization. (b) Genuine CD and anisotropy factor calculated from (a). (c) Photoluminescence spectra for clockwise (σ^+, black) and counterclockwise (σ^-, red) circular polarization showing a degree of circular polarization of 4.9%.

where a wider chain motif is formed entirely through edge-sharing of $\{BiI_6\}$ octahedra. A combination of face- and corner-sharing connections, as seen in **CuBiI** has been observed in $[M(tpy)_2][Bi_2I_8]$ (M = Fe, Cu; tpy = 2,2′:6′2″-terpyridine). Here, dinuclear $\{Bi_2I_9\}$ units, where two octahedra are connected through face-sharing, are further connected into a chain via corner-sharing.[54]

The structure of **CuBiI** can be understood as a distorted, vacancy-ordered derivative of the $BaRuO_3$ perovskite structure with two-thirds of the $\{RuO_6\}$ octahedra missing. The $BaRuO_3$ structure type is a stacking variant in between hexagonal and cubic perovskite, where for every two layers of hexagonally close packed Ba^{2+} and O^- ions, there is one layer of cubic closest packing.[55] This packing leads to units of three face-sharing octahedra, connected together via shared corners like in **CuBiI** (Figures S5−S7).

The cationic honeycomb layers and anionic chains in **CuBiI** combine into a poly-threaded motif, where the chains are threaded through the windows of each layer (Figure 1). This creates an entangled array that can hypothetically be separated without breaking any bonds, although, of course, the ionic nature of both components will prevent this. The specific topology of a 2D honeycomb lattice poly-threaded by 1D chains to form an overall 3D pseudopolyrotaxane has been observed before in a silver coordination polymer.[56] The anionic chains in **CuBiI** are further interconnected by I···I-contacts below the sum of the van der Waals radius of I into another set of 2D-layers parallel to the *bc*-plane, which can be described as 4^4 square nets.[57] If this secondary interaction is taken into account, the resulting topology can be described as a polycatenated motif with two inclined 2D nets of different topologies combining into an overall 3D assembly (Figure S3), a type of polycatenation that has remained rare in coordination polymers.[58−60] Halogen−halogen contacts like this are commonly found in halogenido metalates and generally thought to have a significant influence on the electronic properties of the compounds, although a systematic analysis of their effects is yet to be done.[61,62]

A second type of intermoiety connections is found in the form of very short I···pyrazine contacts that connect the anionic and cationic sublattices. Its centroid-to-I distance of 3.58 Å is significantly smaller than in pyrazinium iodide itself or the pyrazinium iodido antimonate $[Hpyz]_4[Sb_{10}I_{34}]$ (see Supporting Information for details).[63] The I···pyrazine contacts give rise to charge transfer excitations in these two compounds and significantly alter their electronic properties. Therefore, we expect similar effects and a strong interaction between anion and cation of **CuBiI**.

The combination of halogenido bismuthate anions and cationic coordination polymers has remained very rare, with only two examples featuring molecular anions up to now.[25,64] For the related halogenido plumbates, some examples featuring metalate chains threaded through 2D or 3D coordination polymers have been reported.[25,65,66]

Thermal Analysis. CuBiI is stable up to 100 °C, indicating the material's suitability for additional investigations. At higher temperatures, it starts to lose the organic ligands without prior melting or solid−solid phase transitions indicated. It decomposes in four consecutive steps, losing pyrazine, acetonitrile, BiI_3, and residual iodine. The full thermal analysis is available in the Supporting Information.

Optical Activity. We investigated the optical properties of **CuBiI** single crystals by microreflectance and microphotoluminescence spectroscopy to confirm the chiroptical activity originating from the noncentrosymmetric crystal structure. Careful consideration is given to the measurement of CD in these anisotropic single crystals to mitigate artifacts arising from linear dichroism and linear birefringence (LDLB). Both contribute to a background signal superimposing the genuine CD.[67,68] To minimize these artifacts, we spectroscopically deconvolve LDLB contributions from genuine CD by using virtually perfectly circular-polarized light. We confirm the polarization state by Stokes polarimetry. In addition, a small spot size and precise position control of the sample are crucial for repeated measurements at the same location on a crystal facet. By determining the optic axes of the crystal facet and acquiring optical spectra along one axis, we effectively eliminate any contribution from LD′LB′.[67,69] To extract genuine CD and LDLB contributions, we rotate the azimuth by 90° and acquire the corresponding optical spectra.[33] The 90° rotation from the optic axis leads to a sign inversion of the LDLB terms, enabling the isolation of the CD by averaging (semisum) the 0 and 90° spectra:

https://doi.org/10.1021/jacs.3c06141
J. Am. Chem. Soc. XXXX, XXX, XXX−XXX

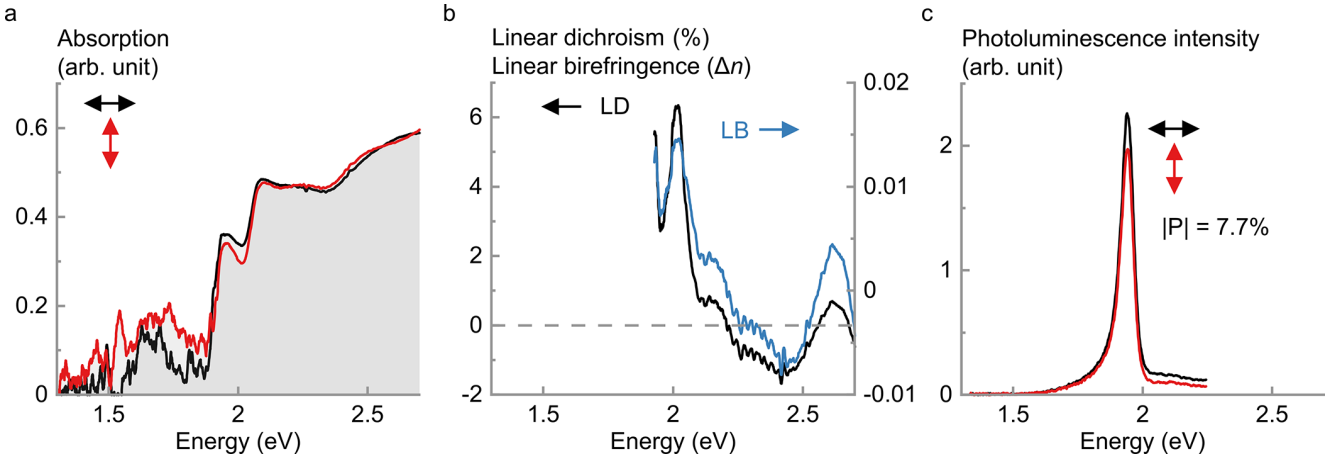

Figure 3. Linearly polarized optical properties of CuBiI. (a) Absorption spectra parallel (↔, black) and perpendicular (↕, red) to the main optic axis of the crystal. (b) LDLB spectra. (c) Photoluminescence spectra for parallel (↔) excitation and parallel (↔, black) and perpendicular (↕, red) detection showing a degree of linear polarization of 7.7%.

$$\mathrm{CD}_{\mathrm{genuine}} = \frac{1}{2} \times (\mathrm{CD}_{\mathrm{apparent}}(0°) + \mathrm{CD}_{\mathrm{apparent}}(90°))$$

Similarly, this allows us to extract the LDLB contribution.

$$\mathrm{LDLB} = \frac{1}{2} \times (\mathrm{CD}_{\mathrm{apparent}}(0°) - \mathrm{CD}_{\mathrm{apparent}}(90°))$$

Additional details are given in the Supporting Information. Circularly polarized absorption spectra parallel to the main optic axis at 4 K temperature (Figure 2a) show the onset of absorption near 1.89 eV (656 nm) and a clearly defined resonance at 1.97 eV (629 nm), which we identify with the fundamental bright exciton. A local minimum is at 2.02 eV (614 nm) and absorption peaks are at 2.10 eV (590 nm). The weak residual absorption below 1.89 eV could indicate additional states, e.g., due to disorder. A Tauc analysis yields a direct band gap with 1.89 eV band gap energy at 4 K, which decreases to 1.70 eV at room temperature (Figure S11). Many iodido bismuthates show overall optical absorption properties and thermochromism similar to that of **CuBiI**.[70] However, the band gap energy is quite small compared to other iodido bismuthates featuring similar 1D-anionic motifs, in which energies range from 1.9 to 2.2 eV.[71−73] Band gap energies can be as low as 1.62 eV in more condensed 1D-motifs featuring wider chains.[74] In **CuBiI**, however, we attribute the narrow band gap to additional electronic states resulting from the interaction of iodido ligands of the anion with pyrazine ligands of the cation, similar to what we observed recently in $[Hpyz]_4[Sb_{10}I_{34}]$.[63]

Absorption may indicate CD in **CuBiI** as it is stronger for counterclockwise circular polarization (σ^-). In contrast, the spectral shape is independent of light helicity. Using the methods outlined above, we confirm and quantify the intrinsic chiroptical activity of **CuBiI** (Figure 2b). CD is negative at low energies and crosses 0 at 1.99 eV, which is close to the exciton absorption edge and can be interpreted as the positive Cotton effect. It peaks as high as 1.62° at 2.03 eV, which coincides with the local minimum in absorption, and rises again above 2.4 eV. The preferential absorption of counterclockwise circularly polarized light verifies the chiroptical activity in **CuBiI**. Further, linear effects are significant in the material (vide infra), and we calculated the LDLB contributions to the apparent CD (Figure S12a). The ratio of the integrated area of LDLB to genuine CD is 6.3, indicating the major contribution of LDLB to apparent CD.

Different CD measurements are not comparable, as CD depends on sample density (or concentration) and thickness (or optical path length). The optical anisotropy factor g_{CD} is the widely accepted quantitative figure-of-merit for chiroptical activity and normalizes CD by absorption:

$$g_{CD} = \frac{\mathrm{CD}\ [°]}{32.98 \times \mathrm{Absorption\ [OD]}}$$

The factor g_{CD} of **CuBiI** is 0.16 at 2.03 eV (Figure 2b), which is the largest reported value to date in a metal-halide perovskite derivative and several orders of magnitude greater than what has been observed in other bismuth halide-based compounds.[75−77] We ascribe the large g_{CD} to two advantageous circumstances: (1) the sample is of excellent quality with large and flat single crystal domains (Figures 4 and S13a), and (2) microspectroscopy addresses one single crystal domain while larger spots inevitably average many neighboring domains with different polarization orientations (Figure S13b,c). g_{CD} is 1.6 times larger than in 0D chiral methylbenzylammonium copper chloride $(R\text{-}MBA)_2CuCl_4$ ($g_{CD} \approx 0.1$)[78] and 1 order of magnitude larger than in 1D phenylethylamin lead iodide $(R/S\text{-}\alpha\text{-}PEA)PbI_3$ ($g_{CD} \approx 0.02$)[79] and 1D naphthylethylamine lead iodide $(R/S\text{-}NEA)PbI_3$ ($g_{CD} \approx 0.04$).[80] However, these g_{CD} factors are greatly inflated due to significant LDLB contributions to CD.[33] For instance, Zhang et al. calculated an overestimation of g_{CD} by at least a factor of 1.83 and a genuine g_{CD} of 2.5×10^{-3} in the $(R\text{-}MBA)_2CuCl_4$ thin films.[33] This is 2 orders of magnitude smaller than the initial report. We also note that g_{CD} values of the same order of magnitude as observed in our measurements have been reported for single crystals of simple metal complexes[81,82] as well as polymer materials.[83]

The zero-crossing of the Cotton effect close to the exciton absorption edge supports our interpretation as an electronic transition. Thus, we anticipate circularly polarized photoluminescence in **CuBiI**. PL spectra parallel to the main optic axis at 4 K temperature show a narrow emission in the red part of the electromagnetic spectrum (Figure 2c). The PL peaks at 1.93 eV (642 nm) and features a full width at half-maximum (fwhm) of 0.068 eV. It is Stokes-shifted by 0.04 eV from the

https://doi.org/10.1021/jacs.3c06141
J. Am. Chem. Soc. XXXX, XXX, XXX−XXX

exciton absorption resonance at 1.97 and 0.17 eV from the absorption maximum at 2.10 eV at 4 K temperature. The emission features a significant low-energy tail, mirroring the onset of absorption. Circularly polarized PL spectra with cocircular excitation and detection exhibit a distinct intensity difference between clockwise (σ^+) and counterclockwise (σ^-) circular polarization with σ^- PL being more intense. We quantify the degree of circular polarization with $P = \frac{I(\sigma^-) - I(\sigma^+)}{I(\sigma^-) + I(\sigma^+)}$, where $I(\sigma^\pm)$ is the clockwise (counterclockwise) circularly polarized PL intensity. We extract a degree of circular polarization of 4.9%, which is on the same order of magnitude as in the reduced-dimensional perovskite $(R/S\text{-}MBA)_2PbBr_4$ (3% under zero magnetic field).[40] This is consistent with the CD and further confirms the chiroptical activity in **CuBiI**.

Next, we determined the linear optical activity in **CuBiI**. This is important as most single crystals and thin films show macroscopic anisotropies in their optical properties in the forms of linear dichroism (LD) and linear birefringence (LB). They define the optic axes of the crystal along which light suffers no birefringence and propagates independent of its polarization state. We perform angle-dependent absorption measurements of single crystals, i.e., by rotating the azimuth angle (θ) between the propagation projection vector and the reference vector.

Linearly polarized absorption spectra at 4 K temperature display optical anisotropy, as the absorption depends on the incident light polarization (Figure 3a). We determine the crystal anisotropy axis from the cosine dependence of the absorption on the azimuth angle (Figure S12b). The polarization angle of 30° is the main optic axis of optical anisotropy, along which the absorption is strongest (red line in Figure 3a). The spectral shape and peak positions are identical with the circularly polarized absorption spectra (Figure 2a) and independent of polarization. The difference of absorption, parallel and perpendicular to the main optic axis, is maximum at the local absorption minimum at 2.02 eV, which we also observed in the circularly polarized absorption spectra (Figure 2a).

To further understand the linear optical activity in **CuBiI**, we define the LD as $\frac{A_\perp - A_\parallel}{A_\perp + A_\parallel}$, where $A_\perp$ ($A_\parallel$) is the absorption perpendicular (parallel) to the main optic axis. In other words, this is the difference of the absorption perpendicular and parallel to the main optic axis normalized to the total unpolarized absorption. From this, we quantify the LD spectrum in the absorptive spectral region (Figure 3b). LD ranges from 6.34% at 2.02 eV to −1.33% at 2.42 eV. The spectrum exhibits multiple peaks, and LD peaks at higher energies are lower.

We measured the dielectric function of **CuBiI** by spectroscopic ellipsometry (Figure S14a,b) to determine LB from the linearly polarized absorption spectra on a large bulk crystal (≈1 mm size) with a spot size of 200 μm at room temperature and derive the refractive index values n and k directly from the pseudodielectric function. The refractive indices parallel and perpendicular to the main optic axis $n_\parallel$ and $n_\perp$ can be derived from reflectance spectra by using the Fresnel equation for normal reflection at the air-material interface:

$$R = \left|\frac{\hat{n} - 1}{\hat{n} + 1}\right|^2$$

where $\hat{n} = n + ik$ is complex. We neglect the imaginary part ($k \approx 0.28$) as it is much smaller than the real part ($n \approx 2.01$) at the fundamental bright exciton resonance (Figure S14b), which simplifies the analysis and allows us to estimate the real $n_\parallel$ and $n_\perp$ from

$$n_{\parallel/\perp} = \frac{1 - \sqrt{R_{\parallel/\perp}}}{1 + \sqrt{R_{\parallel/\perp}}}$$

where $R_\parallel$ ($R_\perp$) is the reflectance spectrum parallel and perpendicular to the main optic axis of the crystal. The birefringence is $\Delta n = n_\parallel - n_\perp$, and we provide the exact calculation in the Supporting Information (Figure S15). This estimation does not consider differences in the extinction coefficients (Δk) parallel and perpendicular to the main optic axis due to the limitations of our spectroscopic ellipsometry setup in spot size and temperature control. This procedure results in an estimation of the birefringence spectrum (Δn) of **CuBiI** (Figure 3b). The LB spectrum resembles the LD spectrum and ranges from 0.015 at 2.02 eV to −0.007 at 2.42 eV. LB crosses 0 twice, from positive to negative at 2.21 eV and back at 2.56 eV, possibly indicating the presence of additional optical resonances like in the 2D antiferromagnet $FePS_3$.[84]

We further investigated the linear polarization of the PL to provide information about the relationship between crystal anisotropy and emission properties. The linearly polarized PL spectra at 4 K temperature (Figure 3c) feature a narrow emission centered at 1.93 eV (642 nm) with fwhm of 0.06 eV. This is very similar to the circularly polarized PL spectra (Figure 2c). Both are Stokes-shifted by 0.04 eV from the exciton resonance at 1.97 and 0.17 eV from the absorption maximum at 2.10 eV, respectively. The PL intensity is stronger under colinear polarization detection along the main optic axis, yielding a degree of linear polarization of 7.7%. This is consistent with LD and confirms the linear optical activity in **CuBiI**.

The power dependence of the PL is linear over 4 orders of magnitude (Figure S16a,b). We observe no threshold for the onset of PL due to nonradiative recombination through defects at low excitation power densities, and the damage threshold for thermal decomposition at high excitation power densities is above 130 $\mu W\ cm^{-2}$. We do not observe additional states in the low-energy tail of the PL even at very low excitation power densities (Figure S16c).

Optical microscopy images of **CuBiI** with crossed linear polarizers in the illumination and reflection light path visualize good crystal quality and the presence of optical anisotropy through LD and LB. LD and LB rotate the linear polarization of light, and bright and dark spots appear for this polarization geometry. Conversely, when optical anisotropy is absent, the image appears homogeneously bright under crossed polarizers. The latter is what we observe in the optical microscopy images of a single crystal domain of **CuBiI**. The surface appears homogeneously bright under unpolarized light illumination (Figure 4a) and switches to homogeneously dark for cross-linear polarized image detection (Figure 4b). Only a few local spots of higher brightness appear on the surface presumably due to imperfections, and their locations do not correlate with the unpolarized image. Consequently, the crystal domain is homogeneous, with some residual contribution from LD and LB.

https://doi.org/10.1021/jacs.3c06141
J. Am. Chem. Soc. XXXX, XXX, XXX−XXX

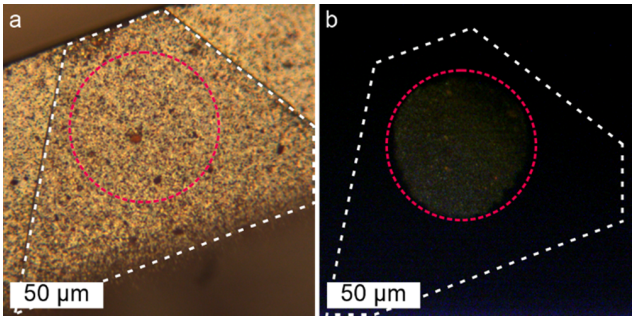

Figure 4. Optical microscopy of CuBiI. (a) Microscopy image of a trapezoidal shaped single crystal domain under unpolarized light. The dashed white line highlights the crystal domain and the dashed red circle highlights the white-light spot. (b) The same crystal domain with crossed linear polarizers.

DISCUSSION

The study of **CuBiI** reveals the existence of poly-threaded iodido bismuthate structures, indicating the potential for mechanically interlocking motifs in metal-halide materials. This opens opportunities to stabilize unusual anion motifs and introduce additional properties. Importantly, our results demonstrate that chiral cations are not a strict requirement to achieve halogenido metalates with remarkable chiroptical properties. While chiral cations facilitate the synthesis of metal-halide materials in noncentrosymmetric space groups, there are a number of examples of lead halide perovskites and halogenido metalates without chiral cations that still crystallize in crystal classes that exhibit chiroptical phenomena.[85−89] Materials displaying nonpolarized luminescence are $(BZA)_2PbX_4$ (BZA = benzylammonium, X = Cl, Br),[90,91] and $(C_mH_{2m+1}NH_3)_2(CH_3NH_3)Pb_2Br_7$ (m = 6−8),[92] crystallizing in the space groups $Cmc2_1$ and Cc, respectively. Overall, this suggests that more compounds may be suitable for CPL and subsequent spintronics applications than previously anticipated.[40,93] However, the analysis of chiroptical properties necessitates the use of single crystals or single-crystalline films as opposed to randomly oriented polycrystalline films or powders. Fortunately, protocols for growing high-quality single crystals are available,[94,95] and devices based on perovskite single crystals have already been explored.[96] We demonstrate that, by utilizing such single crystals, it is possible to uncover anisotropy factors and degrees of circularly polarized photoluminescence comparable to perovskite materials containing chiral cations, thus holding significant promise for future spintronics applications.

CONCLUSIONS

In conclusion, our study demonstrates the unique properties of the achiral perovskite derivative $[Cu_2(pyz)_3(MeCN)_2][Bi_3I_{11}]$ (**CuBiI**) as a poly-threaded iodido bismuthate material. Despite the absence of chiral building blocks, **CuBiI** exhibits remarkable CD and a significant degree of circularly polarized photoluminescence comparable to those of chiral organic molecule-incorporated perovskites. The material's noncentrosymmetric nature and the interplay between its layered coordination polymer and threaded $[Bi_3I_{11}]^{2-}$ chains contribute to these properties. The low optical band gap and the large anisotropy factor further enhance its potential for applications in spintronics and quantum information.

Our findings highlight that chiroptical activity can be achieved in halogenido metalates without the use of chiral cations, expanding the range of materials suitable for circularly polarized light generation and detection. By utilizing high-quality single crystals, our study reveals the macroscopic origin of CD and emphasizes the importance of careful analysis of the chiroptical properties in material design.

Overall, the unique combination of chirality, low band gap, and strong chiroptical activity in **CuBiI** opens up new possibilities for the development of advanced optoelectronic devices and highlights the potential for further exploration of metal-halide materials with enhanced chiroptical properties. These findings contribute to a deeper understanding of the relationship between molecular structure and optical properties, paving the way for future advancements in chiroptics and related fields.

METHODS

Synthesis. To synthesize **CuBiI**, a suspension of 89 mg of BiI_3 (0.15 mmol), 19 mg of CuI (0.1 mmol), and 16 mg of pyrazine (0.2 mmol) was prepared in 10 mL of acetonitrile (MeCN). The suspension was heated to 95 °C for 30 h under reflux cooling. After completion, the resulting clear red solution was filtered and allowed to crystallize for several days. Dark red blocks of **CuBiI** crystals formed and were separated from the solution. The crystals were washed twice with 3 mL of cold MeCN and dried under a vacuum of 10^{-3} mbar. The yield of **CuBiI** obtained was 48 mg (40%). The composition of **CuBiI** was confirmed by elemental analysis (CHN). The measured (calculated) composition was as follows: C 7.96 (7.77); H, 0.72 (0.73); N, 4.47 (4.53).

Optical Measurements. All optical measurements were carried out at a low temperature of 4 K with the samples in vacuum. For μ-reflectance measurements, we utilized unpolarized light emitted from a tungsten lamp. The light was focused onto the sample using a 40× objective with a numerical aperture of 0.6, resulting in an 80 μm spot size. The reflected light was collected by the same objective and directed to the spectrometer. To obtain reflectance spectra, we subtracted the background reflectance intensity (R_{bg}) from the sample reflectance intensity (R_{sample}) and normalized it using the reflectance intensity from a silicon plate (R_{ref}). The normalized reflectance was calculated as $R = \frac{R_{sample} - R_{bg}}{R_{ref} - R_{bg}}$. For μ-photoluminescence measurements, the samples were excited by using a 532 nm (2.33 eV) laser. The beam was focused into a 1.31 μm spot size, and the excitation power density was set at 0.83 μW cm^{-2}.

Polarization Measurements. The unpolarized light from the tungsten lamp was initially polarized by a linear polarizer and subsequently converted into circularly polarized light by a quarter-wave plate oriented at ±45° relative to the linear polarizer. The normalized Stokes vector of the circularly polarized light at the sample location was determined to be $S = (S_0, S_1, S_2, S_3) = (1, 0.054, 0.036, 0.856)$. The reflected light underwent depolarization upon passing through the same quarter-wave plate and was then analyzed by a linear polarizer before reaching the spectrometer. CD is the difference in reflectance of clockwise (σ^+) and counterclockwise (σ^-) circularly polarized light according to $CD = R(\sigma^+) - R(\sigma^-)$, and radians can be converted to degrees according to [°] = [rad] 180°/π. For linear polarization measurements, the quarter-wave plate was repositioned in front of the spectrometer and oriented at 45° relative to the second linear polarizer. This adjustment was made to compensate for the polarization dependence of the spectrometer.

Detailed methods are given in the Supporting Information.

ASSOCIATED CONTENT

Supporting Information

The Supporting Information is available free of charge at https://pubs.acs.org/doi/10.1021/jacs.3c06141.

https://doi.org/10.1021/jacs.3c06141
J. Am. Chem. Soc. XXXX, XXX, XXX−XXX

Detailed methods, crystallographic details, powder diffraction, thermal analysis, CD calibration, absorption spectra and band gap energies, apparent CD and LD polar plots, sample microphotography, spectroscopic ellipsometry, LDLB, photoluminescence excitation-power dependence (PDF)

Accession Codes

CCDC 2264618 contains the supplementary crystallographic data for this paper. These data can be obtained free of charge via www.ccdc.cam.ac.uk/data_request/cif, or by emailing data_request@ccdc.cam.ac.uk, or by contacting The Cambridge Crystallographic Data Centre, 12 Union Road, Cambridge CB2 1EZ, UK; fax: +44 1223 336033.

AUTHOR INFORMATION

Corresponding Author

Johanna Heine − *Department of Chemistry and Material Sciences Center, Philipps-Universität Marburg, Marburg D-35043, Germany;* orcid.org/0000-0002-6795-5288; Email: johanna.heine@chemie.uni-marburg.de

Authors

Jakob Möbs − *Department of Chemistry and Material Sciences Center, Philipps-Universität Marburg, Marburg D-35043, Germany;* orcid.org/0000-0001-9618-5975

Philip Klement − *Institute of Experimental Physics I and Center for Materials Research, Justus Liebig University Giessen, Giessen D-35392, Germany;* orcid.org/0000-0001-7044-713X

Gina Stuhrmann − *Institute of Nanotechnology (INT) and Karlsruhe Nano Micro Facility (KNMF), Karlsruhe Institute of Technology (KIT), Eggenstein-Leopoldshafen 76344, Germany;* orcid.org/0009-0007-0660-2298

Lukas Gümbel − *Institute of Experimental Physics I and Center for Materials Research, Justus Liebig University Giessen, Giessen D-35392, Germany*

Marius J. Müller − *Institute of Experimental Physics I and Center for Materials Research, Justus Liebig University Giessen, Giessen D-35392, Germany;* orcid.org/0009-0005-2187-0122

Sangam Chatterjee − *Institute of Experimental Physics I and Center for Materials Research, Justus Liebig University Giessen, Giessen D-35392, Germany;* orcid.org/0000-0002-0237-5880

Complete contact information is available at: https://pubs.acs.org/10.1021/jacs.3c06141

Funding

We gratefully acknowledge funding by the German Research Foundation DFG (HE 8018/1, 505757318 and via the Collaborative Research Center No. 223848855-SFB 1083) and the European Regional Development Fund (ERDF) through the innovation laboratory high-performance materials FPG990 0005/2018.

Notes

The authors declare no competing financial interest.

REFERENCES

(1) Moss, G. P. Basic terminology of stereochemistry (IUPAC Recommendations 1996). *Pure Appl. Chem.* **1996**, *68* (12), 2193−2222.

(2) Guijarro, A.; Yus, M. *The Origin of chirality in the molecules of life*; Royal Society of Chemistry, 2009.

(3) Lin, G.-Q.; You, Q.-D.; Cheng, J.-F. *Chiral drugs: Chemistry and biological action*, 1st edition; Wiley, 2011.

(4) Yang, S.-H.; Naaman, R.; Paltiel, Y.; Parkin, S. S. P. Chiral spintronics. *Nat. Rev. Phys.* **2021**, *3* (5), 328−343.

(5) Wei, Q.; Ning, Z. Chiral Perovskite Spin-Optoelectronics and Spintronics: Toward Judicious Design and Application. *ACS Mater. Lett.* **2021**, *3* (9), 1266−1275.

(6) Berova, N.; Polavarapu, P.; Nakanishi, K.; Woody, R. *Comprehensive Chiroptical Spectroscopy, Vol. 1: Instrumentation, Methodologies, and Theoretical Simulations*; John Wiley & Sons, Inc.: Hoboken, NJ, 2012.

(7) Claborn, K.; Isborn, C.; Kaminsky, W.; Kahr, B. Optical rotation of achiral compounds. *Angew. Chem., Int. Ed.* **2008**, *47* (31), 5706−5717.

(8) Berova, N.; Polavarapu, P.; Nakanishi, K.; Woody, R. *Comprehensive Chiroptical Spectroscopy, Vol. 2: Applications in Stereochemical Analysis of Synthetic Compounds, Natural Products, and Biomolecules*; John Wiley & Sons, Inc.: Hoboken, NJ, 2012.

(9) Sohncke, L. *Entwickelung einer Theorie der Krystallstruktur*; B.G. Teubner, 1879.

(10) Pidcock, E. Achiral molecules in non-centrosymmetric space groups. *Chem. Commun.* **2005**, *27*, 3457−3459.

(11) Pérez-García, L.; Amabilino, D. B. Spontaneous resolution, whence and whither: from enantiomorphic solids to chiral liquid crystals, monolayers and macro- and supra-molecular polymers and assemblies. *Chem. Soc. Rev.* **2007**, *36* (6), 941−967.

(12) Gibbs, J. W. ART. LIV.–Notes on the Electromagnetic Theory of Light. *Am. J. Sci.* **1880**, *23*, 460.

(13) Pockels, F. *Lehrbuch der Kristalloptik*; Teubner, 1906.

(14) Kahr, B.; Martin, A. T.; Ernst, K.-H. On the chiroptical properties of racemic crystals. *Chirality* **2018**, *30* (4), 378−382.

(15) O'Loane, J. K. Optical activity in small molecules, non-enantiomorphous crystals, and nematic liquid crystals. *Chem. Rev.* **1980**, *80* (1), 41−61.

(16) Plum, E.; Liu, X.-X.; Fedotov, V. A.; Chen, Y.; Tsai, D. P.; Zheludev, N. I. Metamaterials: optical activity without chirality. *Phys. Rev. Lett.* **2009**, *102* (11), 113902.

(17) Cheng, J.; Di Huang; Jiang, T.; Shan, Y.; Li, Y.; Wu, S.; Liu, W.-T. Chiral selection rules for multi-photon processes in two-dimensional honeycomb materials. *Opt. Lett.* **2019**, *44* (9), 2141−2144.

(18) Chouhan, L.; Ghimire, S.; Subrahmanyam, C.; Miyasaka, T.; Biju, V. Synthesis, optoelectronic properties and applications of halide perovskites. *Chem. Soc. Rev.* **2020**, *49* (10), 2869−2885.

(19) Jena, A. K.; Kulkarni, A.; Miyasaka, T. Halide Perovskite Photovoltaics: Background, Status, and Future Prospects. *Chem. Rev.* **2019**, *119* (5), 3036−3103.

(20) Chen, J.; Xiang, H.; Wang, J.; Wang, R.; Li, Y.; Shan, Q.; Xu, X.; Dong, Y.; Wei, C.; Zeng, H. Perovskite White Light Emitting Diodes: Progress, Challenges, and Opportunities. *ACS Nano* **2021**, *15*, 17150.

(21) Huang, H.; Pradhan, B.; Hofkens, J.; Roeffaers, M. B. J.; Steele, J. A. Solar-Driven Metal Halide Perovskite Photocatalysis: Design, Stability, and Performance. *ACS Energy Lett.* **2020**, *5* (4), 1107−1123.

(22) Kim, G. Y.; Senocrate, A.; Yang, T.-Y.; Gregori, G.; Grätzel, M.; Maier, J. Large tunable photoeffect on ion conduction in halide perovskites and implications for photodecomposition. *Nat. Mater.* **2018**, *17* (5), 445−449.

(23) Saparov, B.; Mitzi, D. B. Organic-Inorganic Perovskites: Structural Versatility for Functional Materials Design. *Chem. Rev.* **2016**, *116* (7), 4558−4596.

(24) Mishra, S.; Jeanneau, E.; Iasco, O.; Ledoux, G.; Luneau, D.; Daniele, S. Heterometallic, Hybrid, Heavy Main-Group Iodometallates Containing Lanthanide Complexes: Template Synthesis, Structures, Thermal, Optical, Luminescent and Magnetic Properties. *Eur. J. Inorg. Chem.* **2012**, *2012* (16), 2749−2758.

(25) He, Y.; Huang, Y.-R.; Li, Y.-L.; Li, H.-H.; Chen, Z.-R.; Jiang, R. Encapsulating Halometallates into 3-D Lanthanide-Viologen Frame-

works: Controllable Emissions, Reversible Thermochromism, Photocurrent Responses, and Electrical Bistability Behaviors. *Inorg. Chem.* **2019**, *58* (20), 13862−13880.
(26) Zhang, Z.-X.; Zhang, H.-Y.; Zhang, W.; Chen, X.-G.; Wang, H.; Xiong, R.-G. Organometallic-Based Hybrid Perovskite Piezoelectrics with a Narrow Band Gap. *J. Am. Chem. Soc.* **2020**, *142* (41), 17787−17794.
(27) Goforth, A. M.; Tershansy, M. A.; Smith, M. D.; Peterson, L.; Kelley, J. G.; DeBenedetti, W. J. I.; zur Loye, H.-C. Structural diversity and thermochromic properties of iodobismuthate materials containing d-metal coordination cations: observation of a high symmetry Bi3I112- anion and of isolated I- anions. *J. Am. Chem. Soc.* **2011**, *133* (3), 603−612.
(28) Yue, C.-Y.; Yue, Y.-D.; Sun, H.-X.; Li, D.-Y.; Lin, N.; Wang, X.-M.; Jin, Y.-X.; Dong, Y.-H.; Jing, Z.-H.; Lei, X.-W. Transition metal complex dye-sensitized 3D iodoplumbates: syntheses, structures and photoelectric properties. *Chem. Commun.* **2019**, *55* (48), 6874−6877.
(29) Stoddart, J. F. The chemistry of the mechanical bond. *Chem. Soc. Rev.* **2009**, *38* (6), 1802−1820.
(30) Wilson, B. H.; Loeb, S. J. Integrating the Mechanical Bond into Metal-Organic Frameworks. *Chem.* **2020**, *6* (7), 1604−1612.
(31) Carlucci, L.; Ciani, G.; Proserpio, D. M. Polycatenation, polythreading and polyknotting in coordination network chemistry. *Coord. Chem. Rev.* **2003**, *246* (1−2), 247−289.
(32) Ma, J.; Fang, C.; Chen, C.; Jin, L.; Wang, J.; Wang, S.; Tang, J.; Li, D. Chiral 2D Perovskites with a High Degree of Circularly Polarized Photoluminescence. *ACS Nano* **2019**, *13* (3), 3659−3665.
(33) Zhang, Z.; Wang, Z.; Sung, H. H.-Y.; Williams, I. D.; Yu, Z.-G.; Lu, H. Revealing the Intrinsic Chiroptical Activity in Chiral Metal-Halide Semiconductors. *J. Am. Chem. Soc.* **2022**, *144* (48), 22242−22250.
(34) Huang, P.-J.; Taniguchi, K.; Miyasaka, H. Bulk Photovoltaic Effect in a Pair of Chiral-Polar Layered Perovskite-Type Lead Iodides Altered by Chirality of Organic Cations. *J. Am. Chem. Soc.* **2019**, *141* (37), 14520−14523.
(35) Ahn, J.; Lee, E.; Tan, J.; Yang, W.; Kim, B.; Moon, J. A new class of chiral semiconductors: chiral-organic-molecule-incorporating organic−inorganic hybrid perovskites. *Mater. Horiz.* **2017**, *4* (5), 851−856.
(36) Gautier, R.; Klingsporn, J. M.; van Duyne, R. P.; Poeppelmeier, K. R. Optical activity from racemates. *Nat. Mater.* **2016**, *15* (6), 591−592.
(37) Li, X.; Wu, F.; Yao, Y.; Wu, W.; Ji, C.; Li, L.; Sun, Z.; Luo, J.; Liu, X. Robust Spin-Dependent Anisotropy of Circularly Polarized Light Detection from Achiral Layered Hybrid Perovskite Ferroelectric Crystals. *J. Am. Chem. Soc.* **2022**, *144* (31), 14031−14036.
(38) Zhao, J.; Zhang, T.; Dong, X.-Y.; Sun, M.-E.; Zhang, C.; Li, X.; Zhao, Y. S.; Zang, S.-Q. Circularly Polarized Luminescence from Achiral Single Crystals of Hybrid Manganese Halides. *J. Am. Chem. Soc.* **2019**, *141* (40), 15755−15760.
(39) Zhu, T.; Bie, J.; Ji, C.; Zhang, X.; Li, L.; Liu, X.; Huang, X.-Y.; Fa, W.; Chen, S.; Luo, J. Circular polarized light-dependent anomalous photovoltaic effect from achiral hybrid perovskites. *Nat. Commun.* **2022**, *13* (1), 7702.
(40) Long, G.; Jiang, C.; Sabatini, R.; Yang, Z.; Wei, M.; Quan, L. N.; Liang, Q.; Rasmita, A.; Askerka, M.; Walters, G.; Gong, X.; Xing, J.; Wen, X.; Quintero-Bermudez, R.; Yuan, H.; Xing, G.; Wang, X. R.; Song, D.; Voznyy, O.; Zhang, M.; Hoogland, S.; Gao, W.; Xiong, Q.; Sargent, E. H. Spin control in reduced-dimensional chiral perovskites. *Nat. Photonics* **2018**, *12* (9), 528−533.
(41) Hoskins, B. F.; Robson, R. Infinite polymeric frameworks consisting of three dimensionally linked rod-like segments. *J. Am. Chem. Soc.* **1989**, *111* (15), 5962−5964.
(42) Carlucci, L.; Ciani, G.; Proserpio, D. M.; Sironi, A. Interpenetrating diamondoid frameworks of silver(I) cations linked by N,N′-bidentate molecular rods. *J. Chem. Soc., Chem. Commun.* **1994**, No. 24, 2755−2756.
(43) MacGillivray, L. R.; Subramanian, S.; Zaworotko, M. J. Interwoven two- and three-dimensional coordination polymers through self-assembly of Cu I cations with linear bidentate ligands. *J. Chem. Soc., Chem. Commun.* **1994**, *11*, 1325.
(44) Kitagawa, S.; Munakata, M.; Tanimura, T. Synthesis of the novel infinite-sheet and -chain copper(I) complex polymers {[Cu(C4H4N2)3/2(CH3CN)](PF)6).cntdot.0.5C3H6O}.infin. and {[Cu2(C8H12N2)3](ClO4)2}.infin. and their x-ray crystal structures. *Inorg. Chem.* **1992**, *31* (9), 1714−1717.
(45) Qi, M.-L.; Yu, K.; Su, Z.-H.; Wang, C.-X.; Wang, C.-M.; Zhou, B.-B.; Zhu, C.-C. Three new three-dimensional organic-inorganic hybrid compounds based on PMo12O40(n-) (n = 3 or 4) polyanions and Cu(I)-pyrazine/Cu(I)-pyrazine-Cl porous coordination polymers. *Dalton Trans.* **2013**, *42* (21), 7586−7594.
(46) Geiser, U.; Wade, E.; Wang, H. H.; Williams, J. M. Structure of a new iodobismuthate: tetra(n-butyl)ammonium 1,2;1,2;1,2;2,3;2,3;2,3-hexa-μ-iodo-1,1,1,3,3,3-hexaiodotribismuthate-(III) (3:1). *Acta Crystallogr., C: Cryst. Struct. Commun.* **1990**, *46* (8), 1547−1549.
(47) Krautscheid, H. Synthese und Kristallstrukturen von [Li(thf)-4]2[Bi4I14(thf)2], [Li(thf)4]4[Bi5I19] und (Ph4P)4[Bi6I22]. *Z. Anorg. Allg. Chem.* **1994**, *620* (9), 1559−1564.
(48) Pohl, S.; Peters, M.; Haase, D.; Saak, W. Bildung von Iodoantimonaten und -bismutaten. Kristallstrukturen von (PhCH 2 NEt 3) 4 [Sb 6 I 22], (PhCH 2 NEt 3) 4 [Bi 6 I 22] und (Ph 4 P) 3 [Bi 5 I 18]/Formation of iodoantim onates and bismutates. crystal structures of (PhCH 2 NEt 3) 4 [Sb 6 I 22], (PhCH 2 NEt 3) 4 [Bi 6 I 22] and (Ph 4 P) 3 [Bi 5 I 18]. *Z. Naturforsch., B: J. Chem. Sci.* **1994**, *49* (6), 741−746.
(49) Möbs, J.; Luy, J.-N.; Shlyaykher, A.; Tonner, R.; Heine, J. The influence of copper on the optical band gap of heterometallic iodido antimonates and bismuthates. *Dalton Trans.* **2021**, *50* (43), 15855−15869.
(50) Fu, M.-Y.; Wang, H.-Y.; Zhai, H.-L.; Zhu, Q.-Y.; Dai, J. Assembly of a Titanium-Oxo Cluster and a Bismuth Iodide Cluster, a Single-Source Precursor of a p-n-Type Photocatalyst. *Inorg. Chem.* **2021**, *60* (13), 9589−9597.
(51) Goforth, A. M.; Tershansy, M. A.; Smith, M. D.; Peterson, L.; Zur Loye, H.-C. Tetrakis2-(2-pyridyl)pyridinium tetra-mu3-iodo-hexa-mu2-iodo-dodecaiodohexabismuthate and bistris(2,2'-bipyridine)ruthenium(II) di-mu4-iodo-octa-mu2-iodo-dodecaiodo-hexabismuthate. *Acta Crystallogr., C: Cryst. Struct. Commun.* **2006**, *62* (Pt 9), m381−m385.
(52) Krautscheid, H. Synthese und Kristallstrukturen von (Ph4P)-4[Bi8I28], (nBu4N)[Bi2I7] und (Et3PhN)2[Bi3I11] - Iodobismutate mit isolierten bzw polymeren Anionen. *Z. Anorg. Allg. Chem.* **1995**, *621* (12), 2049−2054.
(53) Goforth, A. M.; Peterson, L.; Smith, M. D.; zur Loye, H.-C. Syntheses and crystal structures of several novel alkylammonium iodobismuthate materials containing the 1,3-bis-(4-piperidinium)-propane cation. *J. Solid State Chem.* **2005**, *178* (11), 3529−3540.
(54) Tershansy, M. A.; Goforth, A. M.; Peterson, L.; Burns, M. C.; Smith, M. D.; zur Loye, H.-C. Syntheses and crystal structures of new chain-containing iodometallate compounds: [H1,10-phen](H2O)-1.41[AgI2], [H1,10-phen](H2O)1.42[CuI2]; [Co(tpy)2][Bi2I8], [Fe(tpy)2][Bi2I8]; [Co(1,10-phen)3][Pb3I8]·H2O, and [Fe(1,10-phen)3][Pb3I8]·0.5(H2O). *Solid State Sci.* **2007**, *9* (10), 895−906.
(55) Müller, U. *Anorganische Strukturchemie, 6*; aktualisierte Aufl; Studienbücher Chemie: Vieweg + Teubner, 2008.
(56) Tong, M.-L.; Wu, Y.-M.; Ru, J.; Chen, X.-M.; Chang, H.-C.; Kitagawa, S. Pseudo-polyrotaxane and beta-sheet layer-based three-dimensional coordination polymers constructed with silver salts and flexible pyridyl-type ligands. *Inorg. Chem.* **2002**, *41* (19), 4846−4848.
(57) Alvarez, S. A cartography of the van der Waals territories. *Dalton Trans.* **2013**, *42* (24), 8617−8636.
(58) Carlucci, L.; Ciani, G.; Proserpio, D. M. Three-dimensional architectures of intertwined planar coordination polymers: the first case of interpenetration involving two different bidimensional polymeric motifs. *New J. Chem.* **1998**, *22* (12), 1319−1321.
(59) Tian, Z.; Lin, J.; Su, Y.; Wen, L.; Liu, Y.; Zhu, H.; Meng, Q.-J. Flexible Ligand, Structural, and Topological Diversity: Isomerism in

https://doi.org/10.1021/jacs.3c06141
J. Am. Chem. Soc. XXXX, XXX, XXX−XXX

Zn(NO 3) 2 Coordination Polymers. *Cryst. Growth Des.* **2007**, *7* (9), 1863−1867.
(60) Carlucci, L.; Ciani, G.; Proserpio, D. M.; Mitina, T. G.; Blatov, V. A. Entangled two-dimensional coordination networks: a general survey. *Chem. Rev.* **2014**, *114* (15), 7557−7580.
(61) Dehnhardt, N.; Luy, J.-N.; Szabo, M.; Wende, M.; Tonner, R.; Heine, J. Synthesis of a two-dimensional organic-inorganic bismuth iodide metalate through in situ formation of iminium cations. *Chem. Commun.* **2019**, *55* (98), 14725−14728.
(62) Louvain, N.; Mercier, N.; Boucher, F. Alpha- to beta-(dmes)BiI(5) (dmes = dimethyl(2-ethylammonium)sulfonium dication): umbrella reversal of sulfonium in the solid state and short I···I interchain contacts−crystal structures, optical properties, and theoretical investigations of 1D iodobismuthates. *Inorg. Chem.* **2009**, *48* (3), 879−888.
(63) Möbs, J.; Stuhrmann, G.; Weigend, F.; Heine, J. Establishing Family Relations in Group 15 Halogenido Metalates with the Largest Molecular Antimony Iodide Anion. *Chem.—Eur. J.* **2023**, *29* (2), No. e202202931.
(64) Wang, D.-H.; Zhao, L.-M.; Lin, X.-Y.; Wang, Y.-K.; Zhang, W.-T.; Song, K.-Y.; Li, H.-H.; Chen, Z.-R. Iodoargentate/iodobismuthate-based materials hybridized with lanthanide-containing metalloviologens: thermochromic behaviors and photocurrent responses. *Inorg. Chem. Front.* **2018**, *5* (5), 1162−1173.
(65) Liu, J.-J.; Guan, Y.-F.; Li, L.; Chen, Y.; Dai, W.-X.; Huang, C.-C.; Lin, M.-J. Construction of a bicontinuous donor-acceptor hybrid material at the molecular level by inserting inorganic nanowires into porous MOFs. *Chem. Commun.* **2017**, *53* (32), 4481−4484.
(66) Liu, J.-J.; Shan, Y.-B.; Dai, W.-X.; Huang, C.-C.; Lin, M.-J. Assembly of donor-acceptor hybrid heterostructures based on iodoplumbates and viologen coordination polymers. *Dalton Trans.* **2017**, *46* (35), 11556−11560.
(67) Jensen, H. P.; Schellman, J. A.; Troxell, T. Modulation Techniques in Polarization Spectroscopy. *Appl. Spectrosc.* **1978**, *32* (2), 192−200.
(68) Shindo, Y.; Nishio, M. The effect of linear anisotropies on the CD spectrum: Is it true that the oriented polyvinylalcohol film has a magic chiral domain inducing optical activity in achiral molecules? *Biopolymers* **1990**, *30* (1−2), 25−31.
(69) Buffeteau, T.; Lagugné-Labarthet, F.; Sourisseau, C. Vibrational circular dichroism in general anisotropic thin solid films: measurement and theoretical approach. *Appl. Spectrosc.* **2005**, *59* (6), 732−745.
(70) Pandey, S.; Andrews, A. P.; Venugopal, A. Manifestation of helicity in one-dimensional iodobismuthate. *Dalton Trans.* **2016**, *45* (21), 8705−8707.
(71) Mitzi, D. B.; Brock, P. Structure and optical properties of several organic-inorganic hybrids containing corner-sharing chains of bismuth iodide octahedra. *Inorg. Chem.* **2001**, *40* (9), 2096−2104.
(72) Li, T.; Hu, Y.; Morrison, C. A.; Wu, W.; Han, H.; Robertson, N. Lead-free pseudo-three-dimensional organic−inorganic iodobismuthates for photovoltaic applications. *Sustainable Energy Fuels* **2017**, *1* (2), 308−316.
(73) Hu, Y.-Q.; Hui, H.-Y.; Lin, W.-Q.; Wen, H.-Q.; Yang, D.-S.; Feng, G.-D. Crystal and Band-Gap Engineering of One-Dimensional Antimony/Bismuth-Based Organic-Inorganic Hybrids. *Inorg. Chem.* **2019**, *58* (24), 16346−16353.
(74) Notter, S.; Donsbach, C.; Feldmann, C. On iodido bismuthates, bismuth complexes and polyiodides with bismuth in the system BiI 3 /18-crown-6/I 2. *Z. Naturforsch., B: J. Chem. Sci.* **2021**, *76* (10−12), 765−774.
(75) Zhao, J.; Huo, H.; Zhao, Y.; Guo, Y.; Dong, M.; Fu, Y.; Zhang, J.; Gao, Z.; Kang, L. Chiral Hybrid Perovskites (R -/ S -CLPEA) 4 Bi 2 I 10 with Enhanced Chirality and Spin−Orbit Coupling Splitting for Strong Nonlinear Optical Circular Dichroism and Spin Selectivity Effects. *Chem. Mater.* **2023**, *35* (11), 4347−4354.
(76) Rajput, P. K.; Poonia, A. K.; Mukherjee, S.; Sheikh, T.; Shrivastava, M.; Adarsh, K. V.; Nag, A. Chiral Methylbenzylammonium Bismuth Iodide with Zero-Dimensional Perovskite Derivative Structure. *J. Phys. Chem. C* **2022**, *126* (23), 9889−9897.
(77) Moon, T. H.; Oh, S.-J.; Ok, K. M. ((R)-C8H12N)4Bi2Br10 and ((S)-C8H12N)4Bi2Br10: Chiral Hybrid Bismuth Bromides Templated by Chiral Organic Cations. *ACS omega* **2018**, *3* (12), 17895−17903.
(78) Hao, J.; Lu, H.; Mao, L.; Chen, X.; Beard, M. C.; Blackburn, J. L. Direct Detection of Circularly Polarized Light Using Chiral Copper Chloride-Carbon Nanotube Heterostructures. *ACS Nano* **2021**, *15* (4), 7608−7617.
(79) Chen, C.; Gao, L.; Gao, W.; Ge, C.; Du, X.; Li, Z.; Yang, Y.; Niu, G.; Tang, J. Circularly polarized light detection using chiral hybrid perovskite. *Nat. Commun.* **2019**, *10* (1), 1927.
(80) Ishii, A.; Miyasaka, T. Direct detection of circular polarized light in helical 1D perovskite-based photodiode *Sci. Adv.* **2020**, *6*(46), eabd3274, DOI: 10.1126/sciadv.abd3274.
(81) Burkov, V.; Lysenko, O. Absorption and circular-dichroism spectra of LaBGeO5−Cr4+ single crystal. *Opt. Mater.* **2010**, *33* (1), 63−65.
(82) Moran, D. M.; Richardson, F. S. Measurement and analysis of circular dichroism in the 4f-4f transitions of holmium(3+) in sodium tris(oxydiacetato)holmate(3-) bis(sodium perchlorate) hexahydrate. *Inorg. Chem.* **1992**, *31* (5), 813−818.
(83) Kawagoe, Y.; Fujiki, M.; Nakano, Y. Limonene magic: noncovalent molecular chirality transfer leading to ambidextrous circularly polarised luminescent π-conjugated polymers. *New J. Chem.* **2010**, *34* (4), 637.
(84) Zhang, H.; Ni, Z.; Stevens, C. E.; Bai, A.; Peiris, F.; Hendrickson, J. R.; Wu, L.; Jariwala, D. Cavity-enhanced linear dichroism in a van der Waals antiferromagnet. *Nat. Photonics* **2022**, *16* (4), 311−317.
(85) Zeng, Y.; Hu, C.-L.; Xu, W.-J.; Zeng, T.-W.; Zhu, Z.-X.; Chen, X.-X.; Liu, D.-X.; Chen, Y.-J.; Zhang, Y.-B.; Zhang, W.-X.; Chen, X.-M. An Exceptional Thermally Induced Four-State Nonlinear Optical Switch Arising from Stepwise Molecular Dynamic Changes in a New Hybrid Salt. *Angew. Chem., Int. Ed.* **2022**, *61* (2), No. e202110082.
(86) Passarelli, J. V.; Mauck, C. M.; Winslow, S. W.; Perkinson, C. F.; Bard, J. C.; Sai, H.; Williams, K. W.; Narayanan, A.; Fairfield, D. J.; Hendricks, M. P.; Tisdale, W. A.; Stupp, S. I. Tunable exciton binding energy in 2D hybrid layered perovskites through donor-acceptor interactions within the organic layer. *Nat. Chem.* **2020**, *12* (8), 672−682.
(87) Li, X.; Traoré, B.; Kepenekian, M.; Li, L.; Stoumpos, C. C.; Guo, P.; Even, J.; Katan, C.; Kanatzidis, M. G. Bismuth/Silver-Based Two-Dimensional Iodide Double and One-Dimensional Bi Perovskites: Interplay between Structural and Electronic Dimensions. *Chem. Mater.* **2021**, *33* (15), 6206−6216.
(88) Li, J.-Y.; Wang, C.-F.; Wu, H.; Liu, L.; Xu, Q.-L.; Ye, S.-Y.; Tong, L.; Chen, X.; Gao, Q.; Hou, Y.-L.; Wang, F.-M.; Tang, J.; Chen, L.-Z.; Zhang, Y. Eco-Friendly and Highly Efficient Light-Emission Ferroelectric Scintillators by Precise Molecular Design. *Adv. Funct. Mater.* **2021**, *31* (35), 2102848.
(89) Gao, Y.; Chen, N.; Tian, Y.; Zhang, J.; Jia, D. Polymeric Iodoargentate Hybrids Incorporating Octakis- or Heptakis-Solvated Lanthanide Complexes: Syntheses, Crystal Structures, and Photocatalysis. *Inorg. Chem.* **2021**, *60* (6), 3761−3772.
(90) Jung, M.-H. White-Light Emission from the Structural Distortion Induced by Control of Halide Composition of Two-Dimensional Perovskites ((C6H5CH2NH3)2PbBr4- xCl x). *Inorg. Chem.* **2019**, *58* (10), 6748−6757.
(91) Liao, W.-Q.; Zhang, Y.; Hu, C.-L.; Mao, J.-G.; Ye, H.-Y.; Li, P.-F.; Huang, S. D.; Xiong, R.-G. A lead-halide perovskite molecular ferroelectric semiconductor. *Nat. Commun.* **2015**, *6*, 7338.
(92) Vasileiadou, E. S.; Hadar, I.; Kepenekian, M.; Even, J.; Tu, Q.; Malliakas, C. D.; Friedrich, D.; Spanopoulos, I.; Hoffman, J. M.; Dravid, V. P.; Kanatzidis, M. G. Shedding Light on the Stability and Structure−Property Relationships of Two-Dimensional Hybrid Lead Bromide Perovskites. *Chem. Mater.* **2021**, *33* (13), 5085−5107.

https://doi.org/10.1021/jacs.3c06141
J. Am. Chem. Soc. XXXX, XXX, XXX−XXX

(93) Aiello, C. D.; Abendroth, J. M.; Abbas, M.; Afanasev, A.; Agarwal, S.; Banerjee, A. S.; Beratan, D. N.; Belling, J. N.; Berche, B.; Botana, A.; Caram, J. R.; Celardo, G. L.; Cuniberti, G.; Garcia-Etxarri, A.; Dianat, A.; Diez-Perez, I.; Guo, Y.; Gutierrez, R.; Herrmann, C.; Hihath, J.; Kale, S.; Kurian, P.; Lai, Y.-C.; Liu, T.; Lopez, A.; Medina, E.; Mujica, V.; Naaman, R.; Noormandipour, M.; Palma, J. L.; Paltiel, Y.; Petuskey, W.; Ribeiro-Silva, J. C.; Saenz, J. J.; Santos, E. J. G.; Solyanik-Gorgone, M.; Sorger, V. J.; Stemer, D. M.; Ugalde, J. M.; Valdes-Curiel, A.; Varela, S.; Waldeck, D. H.; Wasielewski, M. R.; Weiss, P. S.; Zacharias, H.; Wang, Q. H. A Chirality-Based Quantum Leap. *ACS Nano* **2022**, *16* (4), 4989−5035.
(94) Lei, Y.; Chen, Y.; Zhang, R.; Li, Y.; Yan, Q.; Lee, S.; Yu, Y.; Tsai, H.; Choi, W.; Wang, K.; Luo, Y.; Gu, Y.; Zheng, X.; Wang, C.; Wang, C.; Hu, H.; Li, Y.; Qi, B.; Lin, M.; Zhang, Z.; Dayeh, S. A.; Pharr, M.; Fenning, D. P.; Lo, Y.-H.; Luo, J.; Yang, K.; Yoo, J.; Nie, W.; Xu, S. A fabrication process for flexible single-crystal perovskite devices. *Nature* **2020**, *583* (7818), 790−795.
(95) Capitaine, A.; Sciacca, B. Monocrystalline Methylammonium Lead Halide Perovskite Materials for Photovoltaics. *Adv. Mater.* **2021**, *33* (52), No. e2102588.
(96) Battula, R. K.; Sudakar, C.; Bhyrappa, P.; Veerappan, G.; Ramasamy, E. Single-Crystal Hybrid Lead Halide Perovskites: Growth, Properties, and Device Integration for Solar Cell Application. *Cryst. Growth Des.* **2022**, *22*, 6338−6362.

https://doi.org/10.1021/jacs.3c06141
J. Am. Chem. Soc. XXXX, XXX, XXX−XXX

Chapter 4

Summary and future prospects

4.1 Summary in the English language

In this work, the synthesis and properties of new halogenido antimonates and bismuthates were investigated. The focus lay on iodido complexes and heterometallic compounds that feature coinage metal atoms in the anionic motif alongside antimony or bismuth. The motivation for this line of research is based on the success of halogenido plumbates in semiconductor applications. With methyl ammonium lead iodide, for example, outstanding efficiencies in a new generation of solar cells have been achieved, but issues of stability as well as the toxicity of lead are obstacles for large-scale application. The heavy group 15 elements present a good alternative to lead since they show similar chemistry with regard to halogenido metalates while being less toxic and the resulting materials being generally more stable in terms of temperature and moisture resistance. The inclusion of coinage metals can further improve the optical and electrical properties of the heavy group 15 metalates.

This class of heterometallic compounds is still quite small and especially structure-property relationships are not yet well understood. Therefore, different reaction conditions and a variety of small organic cations were explored to synthesize new heterometallic metalates. Here, especially the use of cations derived by protonation of secondary amines and tertiary phosphines proved successful. Either by direct use or *in situ* deprotonation, the parent bases are available in the reaction and can coordinate to the coinage metal, which stabilizes heterometallic motifs. This led to the discovery of several stable and easy to prepare heterometallic compounds.

For the pair pyridine/pyridinium a copper iodido bismuthate with a chain-like anion and a remarkably small optical band gap was found. It also shows photoconductivity which makes this compound a prime candidate for experimental solar cells in the future. The use of P(*o*-tol)$_3$/HP(*o*-tol)$_3$ yielded a series of discrete heterometallic compounds for various of group 11 and group 15 elements. These compounds are structurally very similar to a series of PPh_3-complexes, which are the result of previous work but differ greatly in optical properties.

This allowed for a computational comparison of the absorption mechanisms, which revealed the electronic states involved to be strongly dependent on the fine changes in the coordination environment of the coinage metal atoms. This high sensitivity was further highlighted in the investigation of the also newly synthesized bismuth/silver compound $[SMe_3]_2[Bi_2Ag_2I_{10}]$. Here all ligands are the same, namely iodide ions, as in a small number of previously known compounds with the same nominal composition of the anion. Still, the optical band gap of $[SMe_3]_2[Bi_2Ag_2I_{10}]$ is significantly smaller than observed for the comparable compounds, simply due to a slightly different connectivity of the $\{BiI_6\}$ and $\{AgI_4\}$ building blocks.

Aside from these heterometallic compounds, metalates featuring interesting homometallic anionic motifs have been prepared as well. The discovery of $[Hpyz]_4[Sb_{10}I_{34}]$, which contains the largest discrete halogenido pentelate anion reported to date, allowed for the experimental as well as computational investigation of the relationship between anion size and optical band gap in a series of closely related antimonates. With these results, the concept that larger anionic motifs lead to smaller optical band gaps, which is well established for other classes of semiconductors, could be expanded to group 15 iodido metalates. It was also shown that seemingly contrasting cases can be traced back to additional effects like charge-transfer excitation.
Furthermore, a new iodido bismuthate with a chain-like anionic motif threaded through a 2d-network of a cationic copper/pyrazine coordination polymer was discovered. Although it does not feature any chiral building blocks, it crystallizes in a non-centrosymmetric space group. In addition to a narrow band gap, it shows non-linear optical properties like strong circular dichroism and circularly polarized emission. These properties are generally overlooked for this class of compounds and associated only with metalates featuring chiral organic cations. An oversight that should be avoided in the future.

To further broaden the class of heterometallic metalates in the future and especially towards anions with higher dimensionality, the group of cations used in this work should be expanded to still small but doubly charged ions. This leaves more room for the anionic framework as less space is occupied by the cations. Exploratory experiments with piperazinium derivatives have already yielded promising results, which, however, are not part of this thesis.

In figure 4.1 the results of this work are graphically summarized.

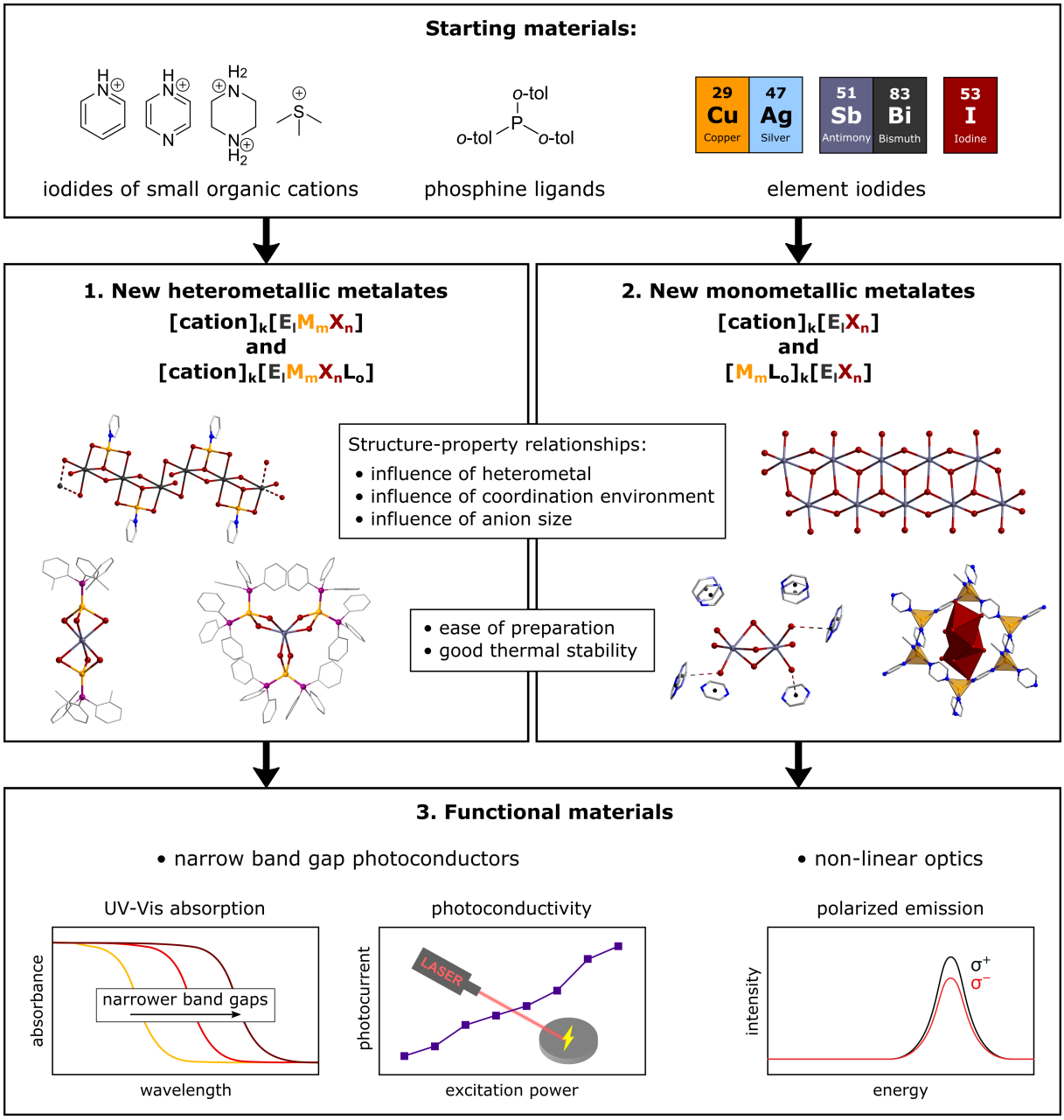

Figure 4.1: Graphical summary.

4.2 Zusammenfassung in deutscher Sprache

In dieser Arbeit wurden die Bildung und die Eigenschaften von neuen Halogenidoantimonaten und -bismutaten untersucht. Der Schwerpunkt lag dabei auf Iodidokomplexen und heterometallischen Verbindungen, die neben Antimon oder Bismut auch Münzmetallatome im Anion aufweisen. Die Motivation für dieses Forschungsgebiet beruht auf dem Erfolg von Halogenidoplumbaten in Hableiteranwendungen. Mit Methylammoniumbleiiodid beispielsweise wurden hervorragende Wirkungsgrade in einer neuen Generation von Solarzellen erreicht, aber Probleme mit der Stabilität der Verbindungen sowie die Toxizität von Blei verhindern die großtechnische Anwendung. Die schweren Elemente der Gruppe 15 stellen eine gute Alternative zu Blei dar, da sie eine ähnliche Chemie bezüglich der Halogenidokomplexe aufweisen, aber weniger toxisch und die resultierenden Materialien im Allgemeinen stabiler sind. Durch den Einbau von Heterometallen können die optischen und elektronischen Eigenschaften der Metallate der Gruppe 15 weiter verbessert werden.
Die Klasse der Heterometallverbindungen ist jedoch noch recht klein und insbesondere Beziehungen zwischen Struktur und Eigenschaften sind noch nicht gut verstanden. Daher wurden verschiedene Reaktionsbedingungen und kleine organische Kationen getestet, um neue heterometallische Metallate zu synthetisieren. Dabei erwies sich vor allem die Verwendung von Kationen, die durch Protonierung von sekundären Aminen und tertiären Phosphinen gebildet werden, als erfolgreich. Die zugrundeliegenden Basen sind entweder durch direkten Einsatz oder *in-situ*-Deprotonierung der Kationen im Reaktionsgemisch verfügbar und können an das Münzmetall koordinieren, wodurch heterometallische Motive stabilisiert werden. Dies führte zur Entdeckung einer Reihe von stabilen und leicht herzustellenden heterometallischen Verbindungen. Für das Paar Pyridin/Pyridinium wurde ein Kupferiodidobismutat mit kettenartigem Anion und einer bemerkenswert kleinen optischen Bandlücke gefunden. Es zeigt darüber hinaus Photoleitfähigkeit, was diese Verbindung zu einem vielverspechenden Kandidaten für experimentelle Solarzellen in der Zukunft macht. Die Verwendung von P(*o*-tol)$_3$/HP(*o*-tol)$_3$ führte zu einer Reihe von diskreten heterometallischen Verbindungen für verschiedene Elemente der Gruppen 11 und 15. Diese sind strukturell sehr ähnlich zu einer Serie von PPh_3-Komplexen, die das Ergebnis von vorherigen Arbeiten waren, unterscheiden sich jedoch stark in ihren optischen Eigenschaften. Dies ermöglichte einen theoretischen Vergleich der Absorptionsmechanismen, der zeigte, dass die an der Absorption beteiligten energetischen Zustände stark durch kleine Änderungen in der Koordinationsumgebung der Heterometallatome beeinflusst werden. Diese Empfindlichkeit wurde ebenfalls bei der Untersuchung der neu synthetisierten Bismut/Silber-Verbindung $[SMe_3]_2[Bi_2Ag_2I_{10}]$ beobachtet. Hier sind alle Liganden die gleichen wie in einer kleinen Reihe bereits zuvor bekannter Verbindungen mit Anionen derselben Summenformel. Dennoch ist die optische Bandlücke von $[SMe_3]_2[Bi_2Ag_2I_{10}]$ deutlich kleiner als bei den Vergleichsverbindungen, was auf eine nur leicht andere Konnektivität der $\{BiI_6\}$- und $\{AgI_4\}$-Grundbausteine zurückzuführen ist.

Neben diesen heterometallischen Verbindungen wurden auch einige Metallate mit interessan-

ten monometallischen Anionenmotiven hergestellt. Die Entdeckung von $[Hpyz]_4[Sb_{10}I_{34}]$, welche das größte bisher gefundene diskrete Halogenidopentelatanion enthält, ermöglichte die experimentelle und theoretische Untersuchung der Beziehung zwischen Anionengröße und optischer Bandlücke in einer Reihe eng verwandter Antimonate. Mit den erzielten Ergebnissen konnte das Konzept, dass größere Anionenmotive zu kleineren optischen Bandlücken führen, welches für andere Halbleiterklassen gut etabliert ist, auf Iodidometallate der Gruppe 15 ausgedehnt werden. Auch konnte gezeigt werden, dass sich vermeintliche Widersprüche zu den bekannten Trends auf zusätzliche Effekte wie etwa Charge-Transfer-Übergange zurückführen lassen.
Darüber hinaus wurde ein neues Iodidobismutat mit einem kettenartigen Anionenmotiv synthetisiert, das durch ein 2d-Netzwerk eines kationischen Kupfer/Pyrazin-Koordinationspolymers gewoben ist. Obwohl sie keine chiralen Bausteine aufweist, kristallisiert die Verbindung in einer nicht-zentrosymmetrischen Raumgruppe und zeigt neben einer engen Bandlücke nicht-lineare optische Eigenschaften wie starken Zirkulardichroismus und zirkular polarisierte Emission. Diese Eigenschaften werden bei dieser Verbindungsklasse im Allgemeinen übersehen und nur mit Metallaten in Verbindung gebracht, die chirale organische Kationen aufweisen.

Um die Klasse der heterometallischen Metallate in Zukunft weiter auszubauen, insbesondere hin zu Anionen mit höherer Dimensionalität, sollte die Gruppe der in dieser Arbeit verwendeten Kationen auf immer noch kleine, aber zweifach geladene Ionen erweitert werden. Dadurch steht mehr Platz für das anionische Gerüst zur Verfügung, da weniger Raum von den Kationen eingenommen wird. In ersten Versuchen mit Piperazinium-Derivaten wurden hier bereits vielversprechende Ergebnisse erzielt, die jedoch nicht mehr Teil dieser Arbeit sind.

In Abbildung 4.2 sind die Ergebnisse dieser Arbeit grafisch zusammengefasst.

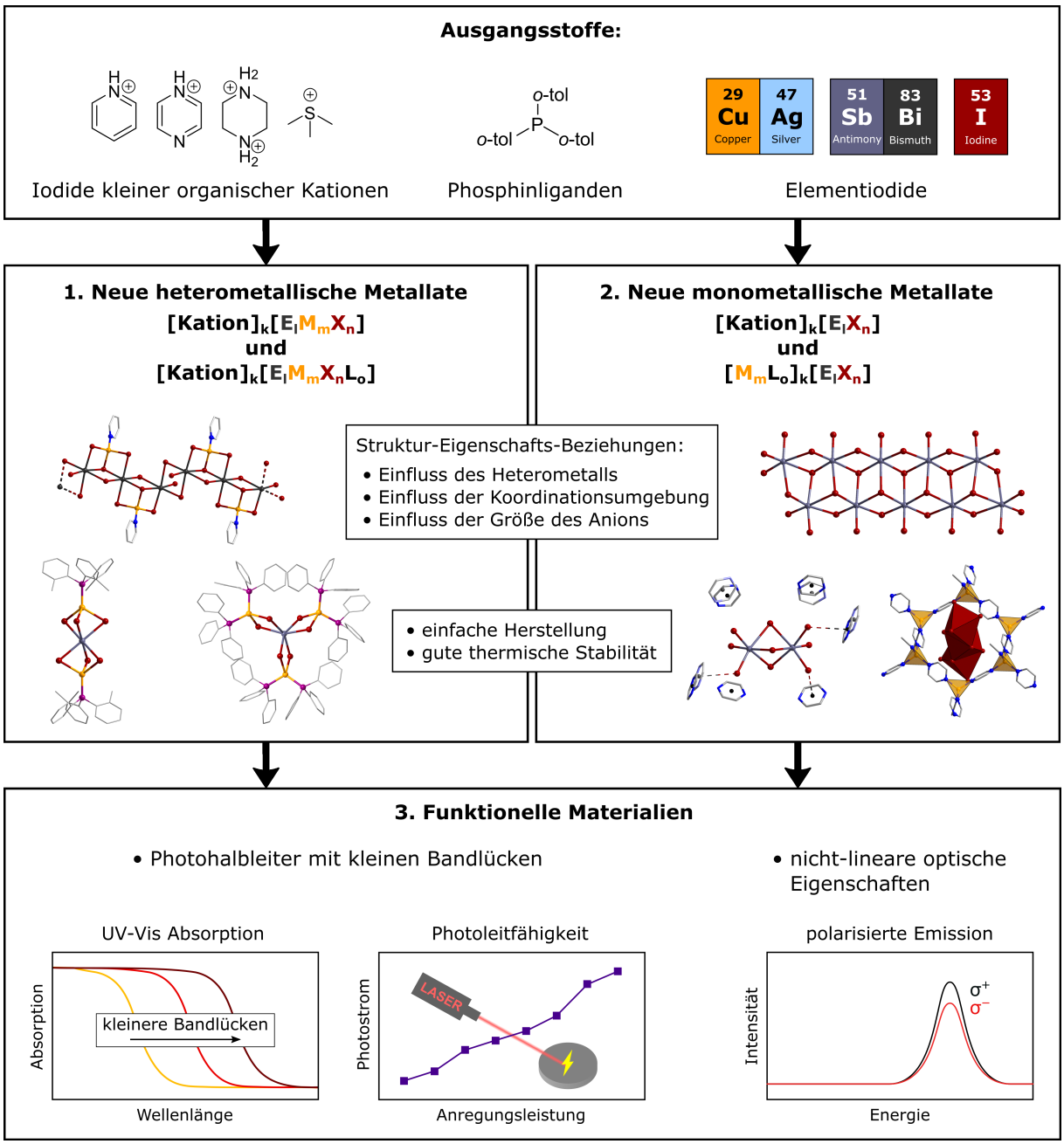

Figure 4.2: Graphische Zusammenfassung.

Bibliography

[1] D. Adams, *Mostly harmless: The Hitch Hiker's guide to the galaxy 5*, Pan, London, **1992**.

[2] D. M. Chapin, C. S. Fuller, G. L. Pearson, *Journal of Applied Physics* **1954**, *25*, 676–677.

[3] G. Celotti, D. Nobili, P. Ostoja, *Journal of Materials Science* **1974**, *9*, 821–828.

[4] K. Seeger, *Semiconductor Physics: An Introduction*, Ninth Edition, Springer, Berlin and Heidelberg, **2004**.

[5] R. Müller, *Grundlagen der Halbleiter-Elektronik*, 7., durchgesehene Auflage, Springer Berlin Heidelberg, Berlin, Heidelberg and s.l., **1995**.

[6] R. Sauer, *Halbleiterphysik: Lehrbuch für Physiker und Ingenieure*, Oldenbourg, München, **2010**.

[7] M. B. Prince, *Journal of Applied Physics* **1955**, *26*, 534–540.

[8] M. A. Green in *Clean Electricity from Photovoltaics*, (Eds.: M. D. Archer, M. A. Green), Series on Photoconversion of Solar Energy, Imperial College Press, **2014**, pp. 87–137.

[9] W. Shockley, H. J. Queisser, *Journal of Applied Physics* **1961**, *32*, 510–519.

[10] S. Rühle, *Solar Energy* **2016**, *130*, 139–147.

[11] M. A. Green, E. D. Dunlop, J. Hohl–Ebinger, M. Yoshita, N. Kopidakis, K. Bothe, D. Hinken, M. Rauer, X. Hao, *Progress in Photovoltaics: Research and Applications* **2022**, *30*, 687–701.

[12] D. E. Carlson, C. R. Wronski, *Applied Physics Letters* **1976**, *28*, 671–673.

[13] B. O'Regan, M. Grätzel, *Nature* **1991**, *353*, 737–740.

[14] K. Sharma, V. Sharma, S. S. Sharma, *Nanoscale Research Letters* **2018**, *13*, 381.

[15] S. Ferrere, A. Zaban, B. A. Gregg, *The Journal of Physical Chemistry B* **1997**, *101*, 4490–4493.

[16] H. J. Snaith, *Advanced Functional Materials* **2010**, *20*, 13–19.

[17] R. Amadelli, R. Argazzi, C. A. Bignozzi, F. Scandola, *Journal of the American Chemical Society* **1990**, *112*, 7099–7103.

[18] U. Bach, D. Lupo, P. Comte, J. E. Moser, F. Weissörtel, J. Salbeck, H. Spreitzer, M. Grätzel, *Nature* **1998**, *395*, 583–585.

[19] O. Moudam, S. Villarroya-Lidon, *Journal of Solar Energy* **2014**, *2014*, 1–7.

[20] M. Tathavadekar, M. Biswal, S. Agarkar, L. Giribabu, S. Ogale, *Electrochimica Acta* **2014**, *123*, 248–253.

[21] A. Kojima, K. Teshima, Y. Shirai, T. Miyasaka, *Journal of the American Chemical Society* **2009**, *131*, 6050–6051.

[22] L. K. Ono, E. J. Juarez-Perez, Y. Qi, *ACS Applied Materials & Interfaces* **2017**, *9*, 30197–30246.

[23] M. M. Lee, J. Teuscher, T. Miyasaka, T. N. Murakami, H. J. Snaith, *Science* **2012**, *338*, 643–647.

[24] C.-S. Jiang, M. Yang, Y. Zhou, B. To, S. U. Nanayakkara, J. M. Luther, W. Zhou, J. J. Berry, J. van de Lagemaat, N. P. Padture, K. Zhu, M. M. Al-Jassim, *Nature communications* **2015**, *6*, 8397.

[25] A. K. Jena, A. Kulkarni, T. Miyasaka, *Chemical Reviews* **2019**, *119*, 3036–3103.

[26] L. Etgar, P. Gao, Z. Xue, Q. Peng, A. K. Chandiran, B. Liu, M. K. Nazeeruddin, M. Grätzel, *Journal of the American Chemical Society* **2012**, *134*, 17396–17399.

[27] M. Jeong, I. W. Choi, E. M. Go, Y. Cho, M. Kim, B. Lee, S. Jeong, Y. Jo, H. W. Choi, J. Lee, J.-H. Bae, S. K. Kwak, D. S. Kim, C. Yang, *Science* **2020**, *369*, 1615–1620.

[28] A. Babayigit, A. Ethirajan, M. Muller, B. Conings, *Nature materials* **2016**, *15*, 247–251.

[29] A. Babayigit, D. Duy Thanh, A. Ethirajan, J. Manca, M. Muller, H.-G. Boyen, B. Conings, *Scientific Reports* **2016**, *6*, 18721.

[30] A. Babayigit, H.-G. Boyen, B. Conings, *MRS Energy & Sustainability* **2018**, *5*, 19.

[31] A. M. A. Leguy, Y. Hu, M. Campoy-Quiles, M. I. Alonso, O. J. Weber, P. Azarhoosh, M. van Schilfgaarde, M. T. Weller, T. Bein, J. Nelson, P. Docampo, P. R. F. Barnes, *Chemistry of Materials* **2015**, *27*, 3397–3407.

[32] A. Zohar, N. Kedem, I. Levine, D. Zohar, A. Vilan, D. Ehre, G. Hodes, D. Cahen, *The Journal of Physical Chemistry Letters* **2016**, *7*, 191–197.

[33] W. Kong, A. Rahimi-Iman, G. Bi, X. Dai, H. Wu, *The Journal of Physical Chemistry C* **2016**, *120*, 7606–7611.

[34] R. Brenes, D. Guo, A. Osherov, N. K. Noel, C. Eames, E. M. Hutter, S. K. Pathak, F. Niroui, R. H. Friend, M. S. Islam, H. J. Snaith, V. Bulović, T. J. Savenije, S. D. Stranks, *Joule* **2017**, *1*, 155–167.

[35] N. Aristidou, I. Sanchez-Molina, T. Chotchuangchutchaval, M. Brown, L. Martinez, T. Rath, S. A. Haque, *Angewandte Chemie (International ed. in English)* **2015**, *54*, 8208–8212.

[36] E. Smecca, Y. Numata, I. Deretzis, G. Pellegrino, S. Boninelli, T. Miyasaka, A. La Magna, A. Alberti, *Physical Chemistry Chemical Physics* **2016**, *18*, 13413–13422.

[37] S.-W. Lee, S. Kim, S. Bae, K. Cho, T. Chung, L. E. Mundt, S. Lee, S. Park, H. Park, M. C. Schubert, S. W. Glunz, Y. Ko, Y. Jun, Y. Kang, H.-S. Lee, D. Kim, *Scientific Reports* **2016**, *6*, 38150.

[38] T. Leijtens, G. E. Eperon, S. Pathak, A. Abate, M. M. Lee, H. J. Snaith, *Nature communications* **2013**, *4*, 2885.

[39] B. Roose, J.-P. C. Baena, K. C. Gödel, M. Graetzel, A. Hagfeldt, U. Steiner, A. Abate, *Nano Energy* **2016**, *30*, 517–522.

[40] Y. Yuan, J. Chae, Y. Shao, Q. Wang, Z. Xiao, A. Centrone, J. Huang, *Advanced Energy Materials* **2015**, *5*, 1500615.

[41] Y. Yuan, Q. Wang, Y. Shao, H. Lu, T. Li, A. Gruverman, J. Huang, *Advanced Energy Materials* **2016**, *6*, 1501803.

[42] X. Zhao, T. Liu, Q. C. Burlingame, T. Liu, R. Holley, G. Cheng, N. Yao, F. Gao, Y.-L. Loo, *Science* **2022**, *377*, 307–310.

[43] A. R. Chakhmouradian, P. M. Woodward, *Physics and Chemistry of Minerals* **2014**, *41*, 387–391.

[44] U. Müller, *Anorganische Strukturchemie*, 6., aktualisierte Aufl., Vieweg + Teubner, Wiesbaden, **2008**.

[45] R. Ali, M. Yashima, *Journal of Solid State Chemistry* **2005**, *178*, 2867–2872.

[46] S. Geller, *The Journal of Chemical Physics* **1956**, *24*, 1236–1239.

[47] V. M. Goldschmidt, T. F. W. Barth, G. Lunde, W. H. Zachariasen, *Geochemische Verteilungsgesetze der Elemente: 7. Die Gesetze der Krystallochemie*, I Kommission Hos Jacob Dybwad, Oslo, **1926**.

[48] T. F. W. Barth, E. Posnjak, *Zeitschrift für Kristallographie - Crystalline Materials* **1934**, *88*, 265–270.

[49] J. J. Lander, *Acta Crystallographica* **1951**, *4*, 148–156.

[50] V. M. Goldschmidt, *Die Naturwissenschaften* **1926**, *14*, 477–485.

[51] H. L. Wells, *Zeitschrift für anorganische Chemie* **1893**, *3*, 195–210.

[52] C. K. Møller, *Nature* **1957**, *180*, 981–982.

[53] C. K. Møller, *Nature* **1958**, *182*, 1436.

[54] D. B. Mitzi in *Progress in Inorganic Chemistry*, (Ed.: K. D. Karlin), Wiley, New York, **1999**, pp. 1–121.

[55] D. Weber, *Zeitschrift für Naturforschung B* **1978**, *33*, 1443–1445.

[56] A. Poglitsch, D. Weber, *The Journal of Chemical Physics* **1987**, *87*, 6373–6378.

[57] D. Weber, *Zeitschrift für Naturforschung B* **1978**, *33*, 862–865.

[58] R. E. Brandt, V. Stevanović, D. S. Ginley, T. Buonassisi, *MRS Communications* **2015**, *5*, 265–275.

[59] W.-J. Yin, T. Shi, Y. Yan, *The Journal of Physical Chemistry C* **2015**, *119*, 5253–5264.

[60] G. Xing, N. Mathews, S. Sun, S. S. Lim, Y. M. Lam, M. Grätzel, S. Mhaisalkar, T. C. Sum, *Science* **2013**, *342*, 344–347.

[61] S. D. Stranks, G. E. Eperon, G. Grancini, C. Menelaou, M. J. P. Alcocer, T. Leijtens, L. M. Herz, A. Petrozza, H. J. Snaith, *Science* **2013**, *342*, 341–344.

[62] M. Szafrański, A. Katrusiak, *The Journal of Physical Chemistry Letters* **2016**, *7*, 3458–3466.

[63] Q. Chen, N. de Marco, Y. Yang, T.-B. Song, C.-C. Chen, H. Zhao, Z. Hong, H. Zhou, *Nano Today* **2015**, *10*, 355–396.

[64] S. Sun, T. Salim, N. Mathews, M. Duchamp, C. Boothroyd, G. Xing, T. C. Sum, Y. M. Lam, *Energy & Environmental Science* **2014**, *7*, 399–407.

[65] A. Binek, F. C. Hanusch, P. Docampo, T. Bein, *The Journal of Physical Chemistry Letters* **2015**, *6*, 1249–1253.

[66] C. C. Stoumpos, C. D. Malliakas, M. G. Kanatzidis, *Inorganic Chemistry* **2013**, *52*, 9019–9038.

[67] Z. Zhao, F. Gu, Y. Li, W. Sun, S. Ye, H. Rao, Z. Liu, Z. Bian, C. Huang, *Advanced Science* **2017**, *4*, 1700204.

[68] F. Hao, C. C. Stoumpos, D. H. Cao, R. P. H. Chang, M. G. Kanatzidis, *Nature Photonics* **2014**, *8*, 489–494.

[69] M. Konstantakou, T. Stergiopoulos, *Journal of Materials Chemistry A* **2017**, *5*, 11518–11549.

[70] J. Breternitz, S. Schorr, *Advanced Energy Materials* **2018**, *8*, 1802366.

[71] N. Mercier, *Angewandte Chemie (International ed. in English)* **2019**, *58*, 17912–17917.

[72] Q. A. Akkerman, L. Manna, *ACS Energy Letters* **2020**, *5*, 604–610.

[73] B. Saparov, D. B. Mitzi, *Chemical Reviews* **2016**, *116*, 4558–4596.

[74] D. B. Mitzi, *Chemistry of Materials* **1996**, *8*, 791–800.

[75] C. C. Stoumpos, D. H. Cao, D. J. Clark, J. Young, J. M. Rondinelli, J. I. Jang, J. T. Hupp, M. G. Kanatzidis, *Chemistry of Materials* **2016**, *28*, 2852–2867.

[76] C. C. Stoumpos, C. M. M. Soe, H. Tsai, W. Nie, J.-C. Blancon, D. H. Cao, F. Liu, B. Traoré, C. Katan, J. Even, A. D. Mohite, M. G. Kanatzidis, *Chem* **2017**, *2*, 427–440.

[77] C. M. M. Soe, G. P. Nagabhushana, R. Shivaramaiah, H. Tsai, W. Nie, J.-C. Blancon, F. Melkonyan, D. H. Cao, B. Traoré, L. Pedesseau, M. Kepenekian, C. Katan, J. Even, T. J. Marks, A. Navrotsky, A. D. Mohite, C. C. Stoumpos, M. G. Kanatzidis, *Proceedings of the National Academy of Sciences* **2019**, *116*, 58–66.

[78] S. N. Ruddlesden, P. Popper, *Acta Crystallographica* **1957**, *10*, 538–539.

[79] S. N. Ruddlesden, P. Popper, *Acta Crystallographica* **1958**, *11*, 54–55.

[80] M. Dion, M. Ganne, M. Tournoux, *Materials Research Bulletin* **1981**, *16*, 1429–1435.

[81] D. H. Cao, C. C. Stoumpos, O. K. Farha, J. T. Hupp, M. G. Kanatzidis, *Journal of the American Chemical Society* **2015**, *137*, 7843–7850.

[82] J. Ye, H. Zheng, L. Zhu, G. Liu, X. Zhang, T. Hayat, X. Pan, S. Dai, *Solar Rapid Research Letters* **2017**, *1*, 1700125.

[83] J. Lu, L. Jiang, W. Li, F. Li, N. K. Pai, A. D. Scully, C.-.-M. Tsai, U. Bach, A. N. Simonov, Y.-.-B. Cheng, L. Spiccia, *Advanced Energy Materials* **2017**, *7*, 1700444.

[84] D. H. Cao, C. C. Stoumpos, T. Yokoyama, J. L. Logsdon, T.-B. Song, O. K. Farha, M. R. Wasielewski, J. T. Hupp, M. G. Kanatzidis, *ACS Energy Letters* **2017**, *2*, 982–990.

[85] L. R. Morss, *Journal of Inorganic and Nuclear Chemistry* **1974**, *36*, 3876–3878.

[86] A. H. Slavney, T. Hu, A. M. Lindenberg, H. I. Karunadasa, *Journal of the American Chemical Society* **2016**, *138*, 2138–2141.

[87] A. Kaltzoglou, M. Antoniadou, A. G. Kontos, C. C. Stoumpos, D. Perganti, E. Siranidi, V. Raptis, K. Trohidou, V. Psycharis, M. G. Kanatzidis, P. Falaras, *The Journal of Physical Chemistry C* **2016**, *120*, 11777–11785.

[88] K. Yamada, H. Sera, S. Sawada, H. Tada, T. Okuda, H. Tanaka, *Journal of Solid State Chemistry* **1997**, *134*, 319–325.

[89] A. M. Ganose, C. N. Savory, D. O. Scanlon, *Chemical Communications* **2016**, *53*, 20–44.

[90] Z. Xiao, K.-Z. Du, W. Meng, J. Wang, D. B. Mitzi, Y. Yan, *Journal of the American Chemical Society* **2017**, *139*, 6054–6057.

[91] G. Volonakis, M. R. Filip, A. A. Haghighirad, N. Sakai, B. Wenger, H. J. Snaith, F. Giustino, *The Journal of Physical Chemistry Letters* **2016**, *7*, 1254–1259.

[92] E. T. McClure, M. R. Ball, W. Windl, P. M. Woodward, *Chemistry of Materials* **2016**, *28*, 1348–1354.

[93] F. Wei, Z. Deng, S. Sun, F. Zhang, D. M. Evans, G. Kieslich, S. Tominaka, M. A. Carpenter, J. Zhang, P. D. Bristowe, A. K. Cheetham, *Chemistry of Materials* **2017**, *29*, 1089–1094.

[94] F. Wei, Z. Deng, S. Sun, N. T. P. Hartono, H. L. Seng, T. Buonassisi, P. D. Bristowe, A. K. Cheetham, *Chemical Communications* **2019**, *55*, 3721–3724.

[95] T. T. Tran, J. R. Panella, J. R. Chamorro, J. R. Morey, T. M. McQueen, *Materials Horizons* **2017**, *4*, 688–693.

[96] F. Giustino, H. J. Snaith, *ACS Energy Letters* **2016**, *1*, 1233–1240.

[97] C. N. Savory, A. Walsh, D. O. Scanlon, *ACS Energy Letters* **2016**, *1*, 949–955.

[98] E. Greul, M. L. Petrus, A. Binek, P. Docampo, T. Bein, *Journal of Materials Chemistry A* **2017**, *5*, 19972–19981.

[99] B. Lee, C. C. Stoumpos, N. Zhou, F. Hao, C. Malliakas, C.-Y. Yeh, T. J. Marks, M. G. Kanatzidis, R. P. H. Chang, *Journal of the American Chemical Society* **2014**, *136*, 15379–15385.

[100] B. Saparov, F. Hong, J.-P. Sun, H.-S. Duan, W. Meng, S. Cameron, I. G. Hill, Y. Yan, D. B. Mitzi, *Chemistry of Materials* **2015**, *27*, 5622–5632.

[101] R. Mohan, *Nature Chemistry* **2010**, *2*, 336.

[102] S. Sundar, J. Chakravarty, *International Journal of Environmental Research and Public Health* **2010**, *7*, 4267–4277.

[103] N. Dehnhardt, M. Axt, J. Zimmermann, M. Yang, G. Mette, J. Heine, *Chemistry of Materials* **2020**, *32*, 4801–4807.

[104] P. Klement, N. Dehnhardt, C.-D. Dong, F. Dobener, S. Bayliff, J. Winkler, D. M. Hofmann, P. J. Klar, S. Schumacher, S. Chatterjee, J. Heine, *Advanced Materials* **2021**, *33*, e2100518.

[105] W. Bi, N. Louvain, N. Mercier, J. Luc, I. Rau, F. Kajzar, B. Sahraoui, *Advanced Materials* **2008**, *20*, 1013–1017.

[106] Y. Wei, W. Wang, Z. Wang, H. Yang, X. You, Y. Zhao, P. Dang, H. Lian, J. Hao, G. Li, J. Lin, *Advanced Functional Materials* **2023**, *33*, 2205829.

[107] Y. Jing, Y. Liu, M. Li, Z. Xia, *Advanced Optical Materials* **2021**, *9*, 2002213.

[108] K. Liu, C. Deng, C. Li, X. Zhang, J. Cao, J. Yao, J. Zhao, X. Jiang, Z. Lin, Q. Liu, *Advanced Optical Materials* **2021**, *9*, 2101333.

[109] J.-H. Wei, J.-F. Liao, X.-D. Wang, L. Zhou, Y. Jiang, D.-B. Kuang, *Matter* **2020**, *3*, 892–903.

[110] Z. Zhang, Da Cao, Z. Huang, E. O. Danilov, C.-.-C. Chung, D. Sun, G. Yang, *Advanced Optical Materials* **2021**, *9*, 2001575.

[111] S. A. Adonin, M. N. Sokolov, V. P. Fedin, *Coordination Chemistry Reviews* **2016**, *312*, 1–21.

[112] N. Dehnhardt, A. Böth, J. Heine, *Dalton Transactions* **2019**, *48*, 5222–5229.

[113] U. Müller, H. Bärnighausen, *Acta Crystallographica Section B* **1970**, *26*, 1671–1679.

[114] S. L. Lawton, R. A. Jacobson, *Inorganic Chemistry* **1968**, *7*, 2124–2134.

[115] M. Bujak, *Acta Crystallographica Section B* **2017**, *73*, 432–442.

[116] G. A. Fisher, N. C. Norman in *Advances in Inorganic Chemistry, Vol. 41*, (Ed.: A. G. Sykes), Academic Press, Orlando, FL, **1994**, pp. 233–271.

[117] R. A. Wheeler, P. N. V. P. Kumar, *Journal of the American Chemical Society* **1992**, *114*, 4776–4784.

[118] M. Lindsjö, A. Fischer, L. Kloo, *Zeitschrift für anorganische und allgemeine Chemie* **2005**, *631*, 1497–1501.

[119] V. Morad, S. Yakunin, B. M. Benin, Y. Shynkarenko, M. J. Grotevent, I. Shorubalko, S. C. Boehme, M. V. Kovalenko, *Advanced Materials* **2021**, *33*, e2007355.

[120] F. Lazarini, *Acta Crystallographica Section C* **1987**, *43*, 875–877.

[121] A. Benedetti, A. C. Fabretti, W. Malavasi, *Journal of Crystallographic and Spectroscopic Research* **1992**, *22*, 145–149.

[122] J. Matuszewski, R. Jakubas, L. Sobczyk, T. Głowiak, *Acta Crystallographica Section C* **1990**, *46*, 1385–1388.

[123] U. Ensinger, W. Schwarz, A. Schmidt, *Zeitschrift für Naturforschung B* **1982**, *37*, 1584–1589.

[124] N. Dehnhardt, Dissertation, Philipps-Universität Marburg, Marburg, **2020**.

[125] O. Hassel, *Zeitschrift für Physikalische Chemie* **1933**, *22B*, 333–334.

[126] R. D. Pike, N. E. Marshall, A. L. Martucci, *Journal of Crystallographic and Spectroscopic Research* **2022**, *52*, 161–173.

[127] S. Pohl, R. Lotz, W. Saak, D. Haase, *Angewandte Chemie (International ed. in English)* **1989**, *28*, 344–345.

[128] S. Pohl, D. Haase, R. Lötz, W. Saak, *Zeitschrift für Naturforschung B* **1988**, *43*, 1033–1037.

[129] S. Pohl, M. Peters, D. Haase, W. Saak, *Zeitschrift für Naturforschung B* **1994**, *49*, 741–746.

[130] N. Leblanc, M. Allain, N. Mercier, L. Sanguinet, *Crystal Growth & Design* **2011**, *11*, 2064–2069.

[131] S. Pohl, W. Saak, P. Mayer, A. Schmidpeter, *Angewandte Chemie (International ed. in English)* **1986**, *25*, 825.

[132] A. J. Lehner, D. H. Fabini, H. A. Evans, C.-A. Hébert, S. R. Smock, J. Hu, H. Wang, J. W. Zwanziger, M. L. Chabinyc, R. Seshadri, *Chemistry of Materials* **2015**, *27*, 7137–7148.

[133] D. B. Mitzi, *Inorganic Chemistry* **2000**, *39*, 6107–6113.

[134] N. Dehnhardt, J.-N. Luy, M. Szabo, M. Wende, R. Tonner, J. Heine, *Chemical Communications* **2019**, *55*, 14725–14728.

[135] J. Beck, T. Hilbert, *Zeitschrift für anorganische und allgemeine Chemie* **2000**, *626*, 837–844.

[136] K. M. McCall, C. C. Stoumpos, S. S. Kostina, M. G. Kanatzidis, B. W. Wessels, *Chemistry of Materials* **2017**, *29*, 4129–4145.

[137] I. W. H. Oswald, A. A. Koegel, J. R. Neilson, *Chemistry of Materials* **2018**, *30*, 8606–8614.

[138] S. Notter, C. Donsbach, C. Feldmann, *Zeitschrift für Naturforschung B* **2021**, *76*, 765–774.

[139] A. Khan, S. Han, X. Liu, K. Tao, D. Dey, J. Luo, Z. Sun, *Inorganic Chemistry Frontiers* **2018**, *5*, 3028–3032.

[140] J. K. Pious, C. Muthu, S. Dani, A. Saeki, C. Vijayakumar, *Chemistry of Materials* **2020**, *32*, 2647–2652.

[141] T. Li, Y. Hu, C. A. Morrison, W. Wu, H. Han, N. Robertson, *Sustainable Energy & Fuels* **2017**, *1*, 308–316.

[142] S. M. Jain, D. Phuyal, M. L. Davies, M. Li, B. Philippe, C. de Castro, Z. Qiu, J. Kim, T. Watson, W. C. Tsoi, O. Karis, H. Rensmo, G. Boschloo, T. Edvinsson, J. R. Durrant, *Nano Energy* **2018**, *49*, 614–624.

[143] C. Feldmann, *Inorganic Chemistry* **2001**, *40*, 818–819.

[144] W.-X. Chai, L.-M. Wu, J.-Q. Li, L. Chen, *Inorganic Chemistry* **2007**, *46*, 8698–8704.

[145] W.-X. Chai, L.-M. Wu, J.-Q. Li, L. Chen, *Inorganic Chemistry* **2007**, *46*, 1042–1044.

[146] M.-W. Yuan, L.-H. Li, L. Chen, *Zeitschrift für anorganische und allgemeine Chemie* **2009**, *635*, 1645–1649.

[147] N. Dehnhardt, J.-.-N. Luy, P. Klement, L. Schipplick, S. Chatterjee, R. Tonner, J. Heine, *Angewandte Chemie (International ed. in English)* **2021**, *60*, 3906–3911.

[148] S. A. Adonin, M. N. Sokolov, A. I. Smolentsev, S. G. Kozlova, V. P. Fedin, *Dalton Transactions* **2013**, *42*, 9818–9821.

[149] N. Dehnhardt, H. Borkowski, J. Schepp, R. Tonner, J. Heine, *Inorganic Chemistry* **2018**, *57*, 633–640.

[150] N. Dehnhardt, P. Klement, S. Chatterjee, J. Heine, *Inorganic Chemistry* **2019**, *58*, 10983–10990.

[151] N. Dehnhardt, H. Paneth, N. Hecht, J. Heine, *Inorganic Chemistry* **2020**, *59*, 3394–3405.

[152] A. W. Kelly, A. M. Wheaton, A. D. Nicholas, F. H. Barnes, H. H. Patterson, R. D. Pike, *European Journal of Inorganic Chemistry* **2017**, *2017*, 4990–5000.

[153] Y. Cai, A. M. Chippindale, R. J. Curry, P. Vaqueiro, *Inorganic Chemistry* **2021**, *60*, 5333–5342.

[154] H. Sommer, A. Eichhöfer, D. Fenske, *Zeitschrift für anorganische und allgemeine Chemie* **2009**, *635*, 1997–2001.

[155] J. Möbs, J. Heine, *Inorganic Chemistry* **2019**, *58*, 6175–6183.

[156] A. V. Paderina, I. O. Koshevoy, E. V. Grachova, *Dalton Transactions* **2021**, *50*, 6003–6033.

[157] Z. Xu, H. Wu, D. Li, W. Wu, L. Li, J. Luo, *Journal of Materials Chemistry C* **2021**, *9*, 13157–13161.

[158] L.-Y. Bi, T.-L. Hu, M.-Q. Li, B.-K. Ling, M. S. Lassoued, Y.-Q. Hu, Z. Wu, G. Zhou, Y.-Z. Zheng, *Journal of Materials Chemistry A* **2020**, *8*, 7288–7296.

[159] L.-Y. Bi, Y.-Q. Hu, M.-Q. Li, T.-L. Hu, H.-L. Zhang, X.-T. Yin, W.-X. Que, M. S. Lassoued, Y.-Z. Zheng, *Journal of Materials Chemistry A* **2019**, *7*, 19662–19667.

[160] J. Möbs, M. Gerhard, J. Heine, *Dalton Transactions* **2020**, *49*, 14397–14400.

Appendix A

List of publications

7. Jakob Möbs, Gina Stuhrmann, Stefan Wippermann and Johanna Heine "Enhanced Circular Dichroism and Polarized Emission in an Achiral, Low Band Gap Bismuth Iodide Perovskite Derivative", *J. Am. Chem. Soc.*, **2023**, *in print*, DOI:10.1021/jacs.3c06141.[4]

6. Jakob Möbs, Gina Stuhrmann, Stefan Wippermann and Johanna Heine "Optical Properties and Metal-Dependent Charge Transfer in Iodido Pentelates", *ChemPlusChem*, **2023**, e202200403, DOI:10.1002/cplu.202200403.[4]

5. Jakob Möbs, Gina Stuhrmann, Florian Weigend and Johanna Heine "Establishing Family Relations in Group 15 Halogenido Metalates with the Largest Molecular Antimony Iodide Anion", *Chemistry*, **2023**, 29, e202202931, DOI:10.1002/chem.202202931.[4]

4. Jakob Möbs, Sudip Pan, Ralf Tonner-Zech and Johanna Heine "$[SMe_3]_2[Bi_2Ag_2I_{10}]$, a silver iodido bismuthate with an unusually small band gap", *Dalton Transactions*, **2022**, 51, 13771–13778, DOI:10.1039/d2dt02305a.[4]

3. Jakob Möbs, Jan-Niclas Luy, Alena Shlyaykher, Ralf Tonner and Johanna Heine "The influence of copper on the optical band gap of heterometallic iodido antimonates and bismuthates", *Dalton Transactions*, **2021**, 50, 15855-15869, DOI:10.1039/d1dt02828f.[4]

2. Jakob Möbs, Marina Gerhard and Johanna Heine "$(HPy)_2(Py)CuBi_3I_{12}$, a low bandgap metal halide photoconductor", *Dalton Transactions*, **2020**, 49, 14397-14400, DOI:10.1039/d0dt03427d.[4]

1. Jakob Möbs, Johanna Heine "11/15/17 Complexes as Molecular Models for Metal Halide Double Perovskite Materials", *Inorganic Chemistry*, **2019**, 58, 6175, DOI:10.1021/acs.inorgchem.9b00429.

[4]Part of this dissertation.